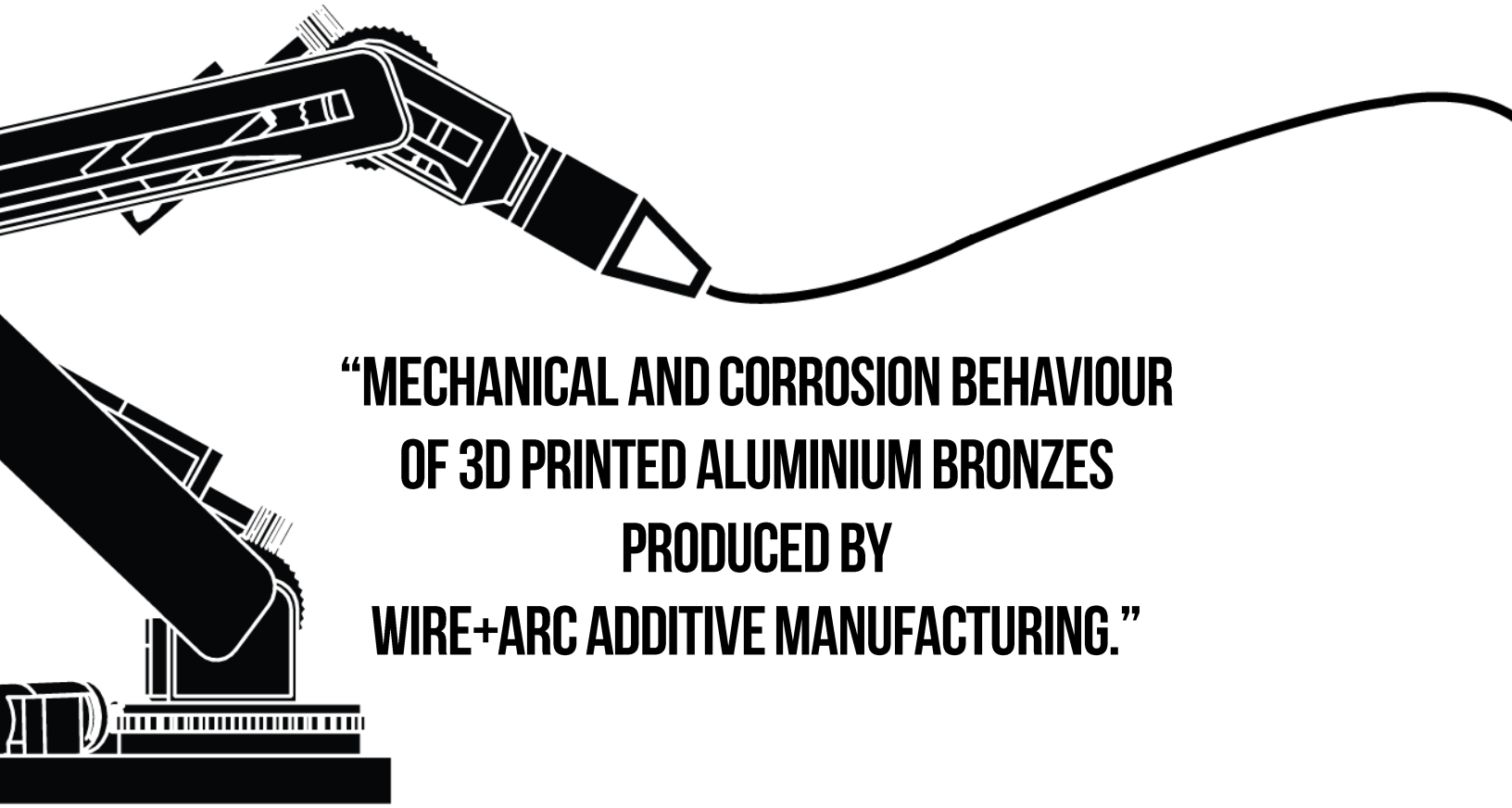

“MECHANICAL AND CORROSION BEHAVIOUR OF 3D PRINTED ALUMINIUM BRONZES PRODUCED BY WIRE+ARC ADDITIVE MANUFACTURING.”

STAMATIS KIAKIDIS

MSc. MATERIALS SCIENCE AND ENGINEERING

TU Delft

RAMLAB

Master thesis project on

“Mechanical and corrosion behaviour of 3D printed aluminium bronzes produced by wire+arc additive manufacturing”

(in collaboration with RAMLAB)

by

Stamatis Kiakidis

in partial fulfilment of the requirements for the degree of MSc. Materials Science and Engineering

at Delft University of Technology,

to be defended publicly on Thursday Augoust 3, 2017 at 14:00.

Student number:	4501519	
Project duration:	November, 2017 – Augoust, 2017	
Thesis committee:	Dr. Ir. M. Hermans (Supervisor)	Delft University of Technology
	Prof. Dr. I. Richardson	Delft University of Technology
	Ir. K. Goulas	Delft University of Technology
	Dr. Ir. Wei Ya	University of Twente

ACKNOWLEDGEMENTS

This piece of work is the result of my fruitful collaboration with a considerable number of people. First of all, I would like to thank my supervisor, Dr. Marcel Hermans for his assistance. He was willing to help me and provide the necessary means to complete the project successfully. Moreover, the laboratory staff of the department of Materials Science and Engineering helped me to perform all the required experiments. Thus, I would like to thank Agnieszka Kooijman, Jurriaan van Slingerland, Ton Riemslag and Sander van Asperen for their contribution to extract reliable data. Regarding to the corrosion part, I would like to thank Dr. Yaiza Gonzalez Garcia for helping to interpret the experimental results. I could not forget the workshop owner Michalis Noukaris, who was willing to manufacture my specimens at the lowest possible cost.

Of course, I would also like to thank the RAMLAB members Wei Ya and Konstantinos Goulas, who were willing to help me to deposit the 3D printed walls within the deadline. They read, together with Prof. Ian Richardson, the thesis report and were the exam committee of my thesis defence. I would like to thank all three of them for their useful comments.

Moreover, I would like to thank Elise for making the last year of my studies unforgettable and for helping me with the layout of the report. Furthermore, I would like to thank all my friends in the Netherlands for making this study period unique.

Finally, I would like to thank my parents for their endless support throughout my academic life. Even this thesis project would not have been possible without them.

ABSTRACT

The emerging field of 3D printing has expanded to the fabrication of metallic components during the last decade. Among the most prominent applications is the production of aluminium bronze marine propellers by the Wire+Arc Additive Manufacturing (WAAM) method. This method incorporates a welding system attached to a robotic arm. The final product results after sequential bead depositions. The main assets of the method are the efficient material usage and the minimization of lead time, which both have a positive environmental and economic impact.

The aim of this project is to evaluate the feasibility to produce 3D printed aluminium bronze (CMA and NAB alloys) blocks with the WAAM method and compare the mechanical and corrosion properties of the blocks with the market requirements. In order to achieve that, rectangular blocks were manufactured at the facilities of Delft University of Technology and at Rotterdam Additive Manufacturing Fieldlab (RAMLAB). Cross sectional areas were extracted and used for microstructural investigation and for hardness measurement. Subsequently, the blocks were machined to produce tensile and Charpy specimens along the built height. Finally, corrosion tests were performed, including open circuit potential measurements, polarization experiments and Scanning Kelvin Probe (SKP) tests.

The microstructural investigation revealed that the 3D printed CMA block consisted of a banded structure. The deposited layers consisted of two dominant phases, α and β, and a variety of precipitates. The Widmanstätten α phase nucleates at the grain boundaries mainly. The tempering promotes the growth of the α phase, making the grain boundaries more indistinguishable, while the β phase decomposes.

The mechanical testing results depicted that the hardness, the tensile strength and the absorption energy of the 3D printed blocks exceeded the specifications of the cast products, according to the ASTM standards. The built height direction is weaker than the welding direction; however, the deposition height plays no significant role in the mechanical properties. Samples were also tested after a heat treatment of 675 °C for 6 hours, as recommended in the literature. The result was a 25% reduction of the tensile yield strength and a 10% reduction of the ultimate tensile strength. However, the scatter in the measured values was reduced too.

Regarding the corrosion results, the built height has little effect on the corrosion susceptibility, according to the polarization curves. The material exhibits a remarkable low corrosion rate, which justifies its use in marine applications. The Scanning Kelvin Probe (SKP) tests illustrated the beneficial aspect of the tempering heat treatment, which alleviates the large potential differences of adjacent deposited areas.

It can be concluded that the CMA alloys are tolerable to the oscillations of the production parameters, making them appealing to the additive manufacturing industry. The mechanical properties achieved, outmatch not only the specifications for the cast CMA products, but also the performance of similar 3D printed aluminium bronze structures, found in the literature.

ABBREVIATIONS

AM:	Additive Manufacturing
AMF:	Additive Manufacturing Format
ASTM	American Society for Testing and Material
BCC:	Body Centred Cubic
BTF:	Buy to Fly
CAM	Computer Aided Manufacturing
CMA:	Copper Manganese Aluminium
CNC:	Computer Numerical Control
DED:	Directed Electron Deposition
EBF:	Electron Beam Fabrication
EDS:	Electron Dispersive Spectroscopy
FCC:	Face Centred Cubic
FEM:	Finite Elements Model
FOM:	Flat-top Overlapping Model
GMAW:	Gas Metal Arc Welding
GTAW:	Gas Tungsten Arc Welding
HCP:	Hexagonal Close Packed
MAT:	Medial Axis Transformation
NAB:	Nickel Aluminium Bronze
OM:	Optical Microscopy
PAW:	Plasma Arc Welding
PBF:	Powder Bed Fusion
PWHT:	Post Weld Heat Treatment
SCC:	Stress Corrosion Cracking
SEM:	Scanning Electron Microscopy
SKP	Scanning Kelvin Probe
SLM:	Selective Laser Melting
SLS:	Selective Laser Sintering
SPA:	Selective Phase Attack
STL:	Stereo Lithography
TEM:	Transmitted Electron Microscopy
TOM:	Tangent Overlapping Model
WAAM:	Wire Arc Additive Manufacturing

TABLE OF CONTENTS

1. INTRODUCTION

Aluminium bronzes are used in a diverse spectrum of applications, due to their unique properties. Their combination of high strength, corrosion resistance and low cavitation susceptibility, makes these copper alloys appealing to the marine industry [1]–[10]. Furthermore, the aircraft industry takes advantage of the excellent wear resistance of the aluminium bronzes, using them for gear bushing and bearings. The density of the alloy is 10% lower than that of the one of steel, while the damping capacity is twice that of steel [1]. The latter feature is important for the submarine's propellers, where the sound suppression is critical in silent operation. Good stress corrosion resistance has also been reported together with a high resistance to biofouling, properties closely related to high static loading applications in seawater environment. Moreover, the aluminium bronzes present low magnetic permeability and acceptable cryogenic properties [1].

The aluminium bronzes were first patented in 1887 by Paul Heroult, who produced aluminium by electrolyzing alumina as the anode and copper as the cathode. In 1893, engineers in the USA selected the alloy for corrosion applications, while in 1913 the Durville process was patented for the production of the aluminium bronzes, eliminating the oxide inclusions. Finally, the second world war acted as a catalyst for the mass production of the nickel aluminium bronzes [1].

The aforementioned copper alloys are mainly used in the following industries: aerospace, architecture, marine, offshore and water condenser or desalination systems. This thesis report focuses on the application of nickel aluminium bronzes (NAB) and copper manganese aluminium alloys (CMA) in the marine industry. The piping and valve systems together with the propellers are the areas where these alloys are mostly applied.

Figure 1: (left) Submarine propeller [1]*, (right) Adjustable, bolted propeller from the Queen Elizabeth class aircraft carrier* [1].

1.1 THESIS PURPOSE AND STRUCTURE

The present work is conducted in collaboration with the companies Promarin and RAMLAB. Promarin is a propeller manufacturer, while RAMAB is involved in the 3D printing of metallic structures. The aim of this thesis is to evaluate the mechanical properties of CMA and NAB components produced by the wire+arc additive manufacturing method. Mechanical and corrosion tests in conjunction with characterization techniques will be used to evaluate the feasibility to produce three-dimensional (3D) printed parts with similar mechanical and corrosion properties such as the cast products. The results will

assist these companies in the production and repair of propellers using the additive manufacturing technology.

In the literature review part (chapters 2 & 3), the necessary background information is presented to familiarize the reader with the basic concepts of the additive manufacturing and the aluminium bronzes. Subsequently, the experimental procedures are documented to enable the reproducibility of the obtained results. The mechanical and corrosion characterisation involve hardness, tensile, and instrumented Charpy tests, and open circuit potential (OCP) measurements, together with polarization experiments and Scanning Kelvin Probe tests. The hardness test is chosen as the easiest way to get a first approximation of the anticipated mechanical behaviour of the sample. Then, the tension test is the most established way to evaluate the strength and ductility of the materials, and compare them with the application requirements. The Charpy V-impact test will provide information of the response of the material in impact load, which is the load case scenario of ice-breaking propellers. In addition, the use of the propellers in seawater environment imply the execution of polarization tests, which will provide corrosion rate results. The SKP test assist in the determination of the deposition height effect on the potential differences of adjacent areas. Furthermore, in the results section, the mechanical and the corrosion behaviour of the printed alloys are analysed, giving an overview on the influence of the different processing parameters. At the end of the report, the most important observations are discussed and explained.

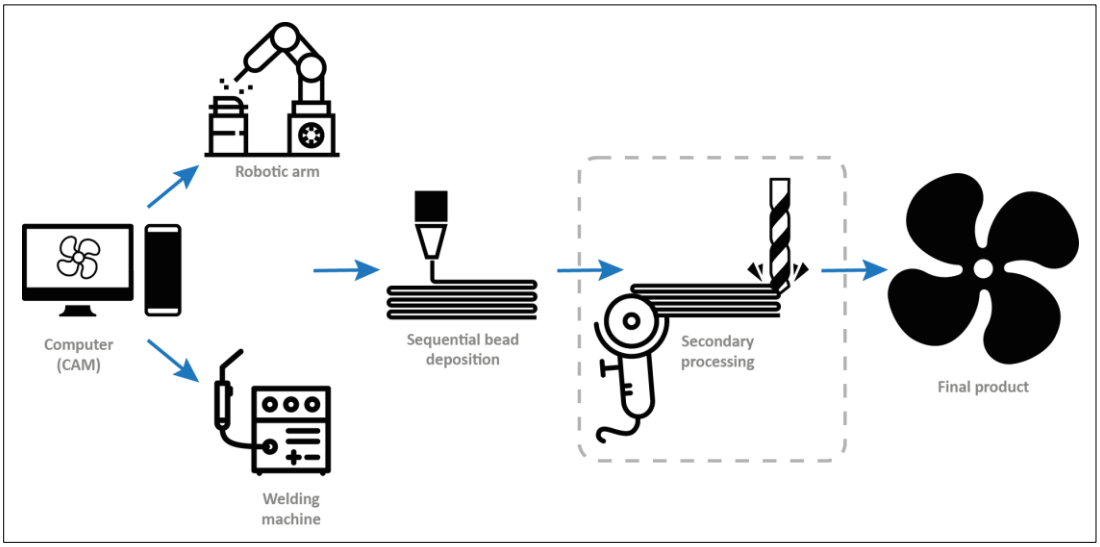

Figure 2: Schematic representation of the WAAM process.

Table 1: Comparison between AM techniques [12].

Additive materials	*Process*	*ASTM group*	*Layer thickness (µm)*	*Deposition rate (g/min)*	*Dimensional accuracy (mm)*	*Surface roughness (µm)*
Powder	SLM	PBF[1]	20-100	N/A	±0.04	9-10
	SLS	PBF	75	~0.1	±0.05	14-16
Wire	**WAAM**	DED[2]	**~1500**	**12**	**±0.2**	**200**
	EBF	DED	N/A	Up to 330	Low	High

[1] Powder Bed Fusion
[2] Directed Energy Deposition

2. ADDITIVE MANUFACTURING

2.1 GENERAL INFORMATION

Additive Manufacturing (AM) processes produce physical three-dimensional objects from digital information piece-by-piece, line-by-line, surface-by surface, or layer-by-layer, with the first attempts dated more than 150 years ago [13], [14]. The above definition of the process highlights the difference of additive manufacturing with the subtractive manufacturing methodologies, such as milling or lathing. Additive manufacturing methods may be reported in the literature with the following synonyms, additive fabrication, additive process, freeform fabrication, direct digital manufacturing and 3D printing [15]. The AM field exhibits a double-digit growth for 18 of the past 27 years, transforming from a non-commercial technology in the early 1980s to an over $4 billion market in 2014. It is expected that the AM market will reach the level of $21 billion by 2020 [13].

During any AM process, there is a digital dataflow generating the instructions for the AM machine followed by a physical workflow transforming the raw materials into final parts. The first part is supported by software formats, developed and standardized specifically for AM purposes. The most common one is the AMF format, which incorporates colour, material, lattice, and constellation information, and which is intended to replace the STL format [13], [15]. Similar formats such as STEP, STEP-NC, and 3MF have adopted AM concepts to compete with AM dedicated formats. On the other hand, the physical workflow incorporates one of the seven currently recognized groups of AM technologies, binder jetting, material extrusion, material jetting, powder, bed fusion, sheet lamination, vat polymerization and directed energy deposition [13]. The Wire+Arc Additive manufacturing (WAAM) process, which this project deals with, belongs to the last group.

2.2 WIRE+ARC ADDITIVE MANUFACTURING

The material plays a major role during the AM process. In case of metals, the different deposition techniques may be divided into powder bed systems, powder feed systems and wire feed systems [16]. Depending on the energy source, further classification of the wire feed systems leads to the following categories: laser-based, arc welding-based and electron beam-based [12]. The current study is focusing on the arc welding-based WAAM method, due to its assets concerning the maritime application, with the main ones being the high deposition rate (50-150 g/min) [17], [18]. A schematic of a WAAM process is shown in Figure 2. The feedstock filler wire melts due to heat generated by a gas tungsten arc welding (GTAW) or a gas metal arc welding (GMAW) or a plasma arc welding (PAW) torch. These arc-based techniques offer up to 90% energy efficiency, whereas the laser and the electron beam based methods offer less than 20% [12]. The different alternatives of WAAM torches are presented in Figure 3. There are three main material transfer modes, short-circuiting, globular and spray [12], [16]. The mode preferred in AM is the short-circuit mode, because it minimizes the heat input into the rest of the 3D printed component [16]. Nowadays, the sputter formation caused by the short-circuit is reduced by optimized waveform patterns. Initially, a single bead of metal is deposited and upon subsequent passes a three-dimensional structure is developed. In general, all the wire feed systems provide a high deposition rate and are ideal to produce large volumes. However, the product usually requires substantially more machining than the powder systems [15], but also offers less porosity [12]. Secondary processing may include grinding, milling or even high pressure interpass rolling to limit porosity. At this point, it should be highlighted that the application of every component indicates if and which process is suitable. For example, components subjected to high cycle fatigue should have a smoother surface than components

under low cycle fatigue or static loads [14]. Typical values of deposition rate, dimensional accuracy and surface roughness for different types of AM processes are shown in Table 1.

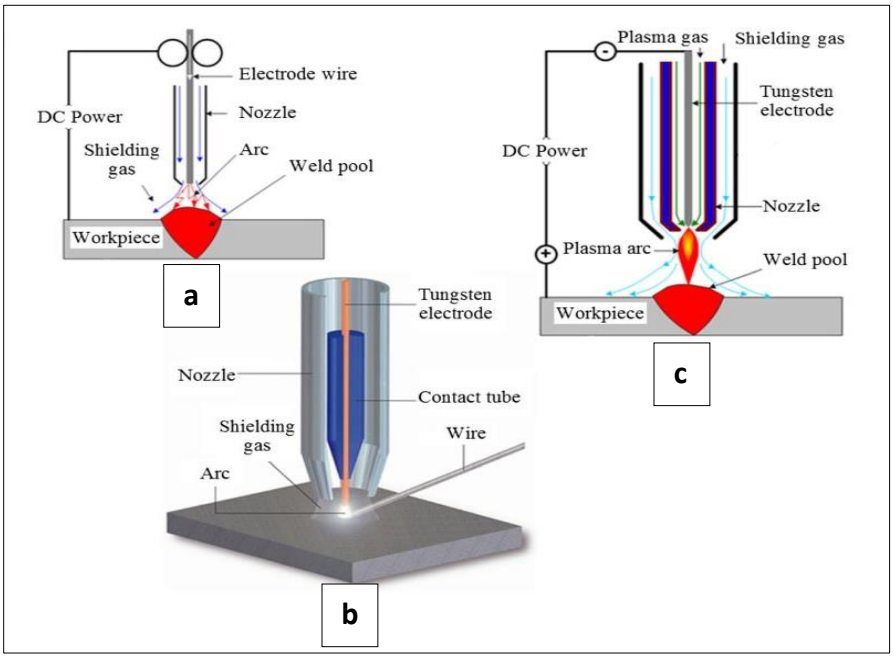

Figure 3: Schematic of WAAM process equipped with different welding torches: (a) GMAW, (b) GTAW, (c) PAW [12].

2.3 ADDITIVE MANUFACTURING ADVANTAGES AND COST

Additive manufacturing involves many assets which make it an appealing production method for low production volumes or high materials cost cases [12], [15]. Products may be tailored to a significantly greater extent than in conservative manufacturing techniques, meaning that the design limitations are substantially reduced. AM method creates both object's material and geometry, thus it can be used to produce custom alloys and composite materials. The lead time and raw material quantity are also reduced, decreasing the transportation and logistics cost, and the environmental impact [15], [16]. In more detail, AM produces near to net shape components, a characteristic quantified by the "buy to fly" indicator (BTF), which is defined as the ratio of the volume or mass of the initial work piece to that of the finished product [14]. Additionally, AM is an automated process, like the CNC machining. Nevertheless, the complex geometries may demand multiple re-fixturing in the case of classical subtractive manufacturing, resulting in time-consuming calibration procedures [12].

The cost of AM is one of the biggest barriers for the industrialization of the process. However, there are many examples where the assets of AM outweigh the costs [15]. Martina [14] published a study proposing a simple model for calculating and comparing the cost of a subtractive and an additive manufacturing method (WAAM). While the developed model is presented for titanium, it can be applied to any other case, provided that the cost of raw material, the deposition and the material removal rates are known. The following results show the sensitivity of the cost to the process parameters. In case of AM, increasing the deposition rate above 1 kg/hour has no significant economic benefit, regardless of the BTF ratio. Furthermore, as the equipment cost increases, a higher deposition rate leads to a lower specific cost of deposition. Generally, AM is cost effective in the case of production of a limited number of components. Currently, conventional manufacturing methods are always favoured over AM for mass production.

2.4 STEP-OVER DISTANCE AND PATH PATTERNS

Ding et al. investigated the profile of the welding beads' cross section and the distance between them, the step-over distance [11]. The cross-sectional geometry of a single bead is strongly correlated with the wire-feed rate and the travel speed [19]. In his work, three models are presented for the cross-sectional profile, simulating the shape as a circular arc or as a parabola or with a cosine function, presented in Table 2. Currently, these are considered outdated models, producing an error in the range of 15% to 20% [11]. Moreover, before Ding's work, the flat top overlapping model (FOM) was used to calculate a step-over distance for a flat top surface. With respect to this model, as the centre distance (d) between adjacent beads decreases to a certain value; the overlapping area becomes equal to the area of the geometrical valley shaped between the beads and the overlapped surface. The model results in the following relationship; $d_{critical}$ =0.667w (, where w is the bead width). Unfortunately, a wavy surface instead of a flat top one is produced. Ding proposes an alternative way, the tangent overlapping model (TOM), see Figure 4, in which the following formula holds; $d_{critical}$=0.738w. In this case, the height of the second bead is bigger when the centre distance is smaller than the critical distance. The error in the prediction of the bead height in the TOM model is approximately 5%. The difference between the above critical values has a major impact on the BTF ratio. Any component built by overlapping beads is subjected to a secondary machining process to remove the scallops. For the FOM model (d=0.667w), the BTF is 75.7%, whereas for the TOM model (d=0.738w), the BTF is 84.1% [11].

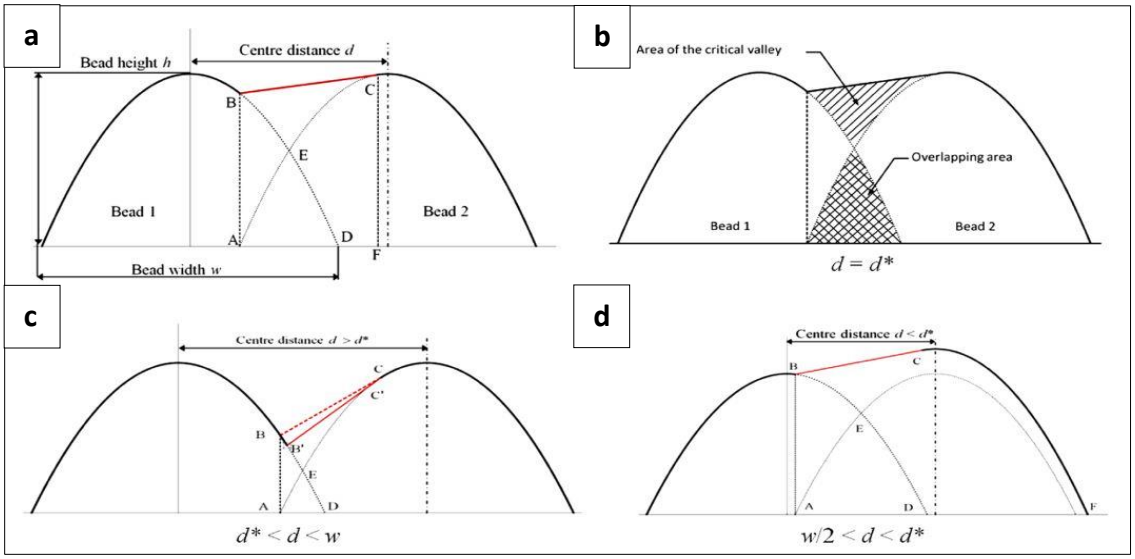

Figure 4: Schematic presentation of the four cases in the tangent overlapping model (TOM) [11].

Table 2: Formulas for the model describing the bead cross-sectional geometry [11].

Models	*Model function*	*Bead height, h*	*Bead width, w*	*Bead area, A*
Parabola model	$y = ax^2 + c$	c	$2\sqrt{-\frac{c}{a}}$	$A_p = \frac{4c}{3}\sqrt{-\frac{c}{a}}$
Cosine model	$y = \mathrm{acos}(bx)$	a	$\frac{\pi}{b}$	$A_c = \frac{2a}{b}$
Arc model	$y = \sqrt{a^2 - x^2} + b$	$a - b$	$2\sqrt{a^2 - b^2}$	$A_a = \arccos\left(-\frac{b}{a}\right) - b\sqrt{a^2 - x^2}$

In the WAAM method, the welding torch is driven by a robotic arm and must follow a specific path for shaping the desired geometry. The path planning in WAAM is more complex than in powder-based AM, due to constraints from the weld bead and the layer geometry [19]. There are two kinds of paths, the raster and the contour paths [17]. The first category includes patterns which offset parallel to a given direction, whereas the second category describes patterns which offset parallel to the boundary of the geometry. The above path options may produce gaps in cases of complex shapes, thus Ding [17] proposes the medial axis transformation (MAT) procedure to produce the robotic arm's path. This raster pattern method uses the medial axis of the contour of every deposition layer and generates the offset curves by starting at the inside and heading towards the outside. The disadvantage of the method is the extra material deposition beyond the geometrical boundary limits, which however, can be overcome by grinding or milling of the excess material. In addition, the small step-over distance provides high efficiency but in expense of productivity [17]. In posterior work, Ding proposed the adaptive MAT model, reducing even further the excess material deposition [19]. In short, the model takes advantage of the ability of the WAAM process to produce deposits with different widths within a layer by varying travel speed and wire feed rate, while maintaining a constant deposit height. A qualitative comparison of the different models is illustrated in Figure 5.

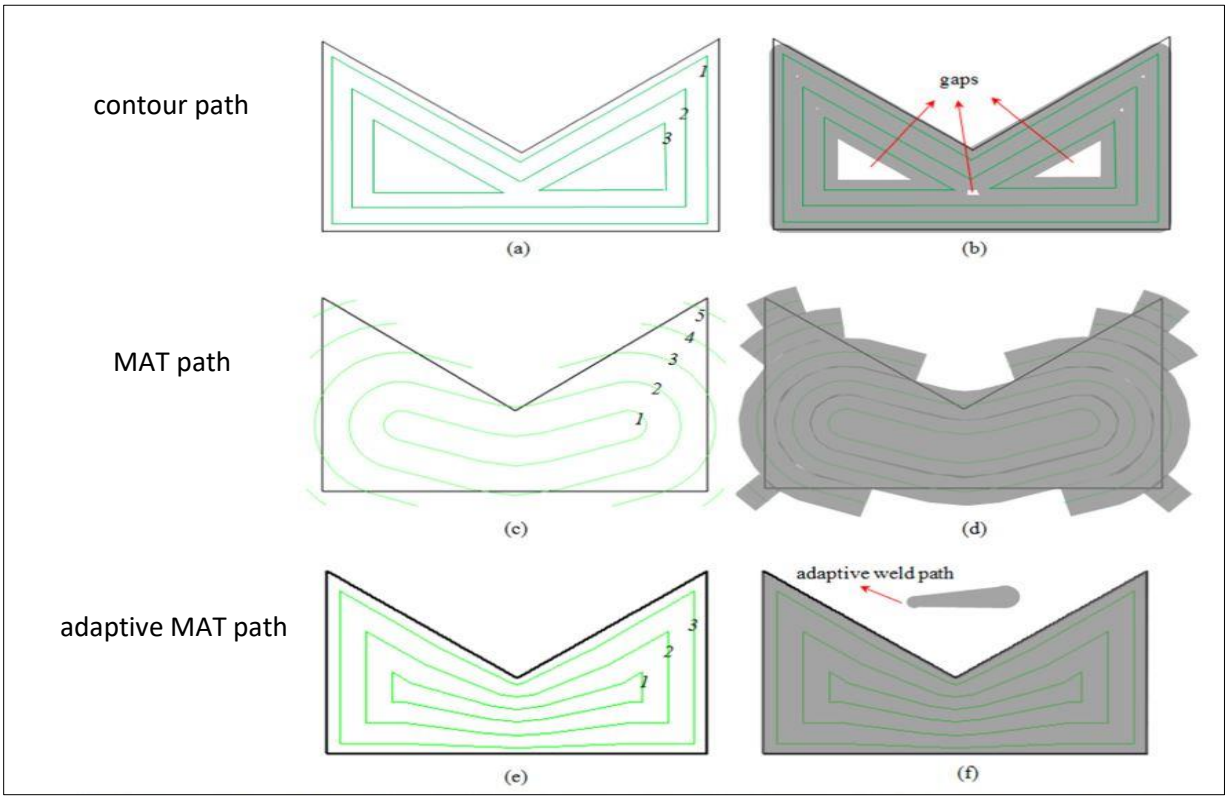

Figure 5: External lines: boundary of the geometry; internal lines: deposition paths; numbers: order of the deposition paths; grey regions: area by the relevant paths. (a) Contour path patterns; (b) The predicted high accuracy deposition but with internal gaps; (c) MAT path patterns; (d) The predicted void-free deposition, but with extra material deposited along the boundary; (e) Adaptive MAT path patterns with varying step-over distance; (f) The predicted void-free deposition with high accuracy at the boundary [19].

2.5 PROCESS PARAMETERS

The dimensions of the deposit, namely the width and the height, are affected mainly by the heat source power[3], the wire feed rate and the welding speed [12]. The deposition width is determined by the heat source power, whereas the height is influenced more by the welding speed. The deposition area is only determined by the ratio of the wire feed rate to the welding speed (λ). The table depicts that with increasing heat source power, the deposition height decreases and the deposition width increases. Furthermore, the increase in the welding speed raises the deposition height and narrows the width. Finally, an increase in the ratio λ gives rise to both the deposition area and height, while the width remains intact. Table 3 summarizes the effect of the above process parameters on the bead geometry.

Table 3: Effect of process parameters on the geometry of a single bead [12]. *↑: significant increase, ↓: significant decrease, 0: no significant influence.*

	Bead area, A	*Bead height, h*	*Bead width, w*
Heat source power, $\boldsymbol{P}$ ↑	0	↓	↑
Welding speed, $\boldsymbol{V_w}$ ↑	0	↑	↓
Wire feed rate / welding speed, $\boldsymbol{\lambda}$ ↑	↑	↑	0

2.6 ANISOTROPY

In the WAAM process, the metal alloy is cast upon a previous layer resulting in complex, time dependent temperature profiles within the part being fabricated. Thus, the alloy may experience repeated thermal cycles leading to solid state and liquid-solid phase transformations. The relatively higher cooling rates, than in the case of large castings, achieved in many of the AM processes, reduce segregation and cause grain refinement. Anisotropy in microstructural and mechanical properties cannot be easily predicted in AM, with the height direction generally being the weakest. Nevertheless, static mechanical properties, like tensile strength, of AM metallic products are comparable to conventionally fabricated components [15], [16]. In general, superior tensile properties are observed along the weld line direction than across the wall building direction. Tensile properties exhibit stronger correlation with the anisotropy rather than with the process parameters [12].

2.7 THERMOMECHANICAL ANALYSIS OF WAAM USING NUMERICAL METHODS

The WAAM process could be represented as subsequent depositions of GMAW or GTAW welds. Thus, from the welding point of view, the process induces residual stresses and distortion to the product [12]. If macroscopic distortion is hindered, then microscopic distortion (yield, cracks) or residual stresses development will take place [12]. These phenomena are limited by the selective deposition approaches. A series of small patches are deposited first and subsequently they are connected to form the complete structure [12]. The concept behind this technique is that it allows for deformation during cooling before the deposit is fully constrained.

Ding et al. [20] uses a finite element method (FEM) software package, ABAQUS, to construct thermal and mechanical models. In his study, coupled thermo-mechanical simulations are carried out for the calculation of the temperature distribution, which is the input to the mechanical analysis of a four-layer wall produced by WAAM. The first model is transient and uses a Lagrange reference frame, while the second model is a steady state one, using an Eulerian reference frame. Both FEM models can

[3] Heat source power: P=VI [W], where V: potential difference (V), I: current (A).

accurately predict the heating and cooling cycles during the WAAM process, but the Eulerian model is 80% quicker, and thus can deal easier with the multi-layer welding process. The results most worth mentioning indicates that the stress across the deposit is uniform, with little influence of the preceding layers on the subsequent ones. Moreover, a significant stress redistribution is observed after unclamping the jiggs. Finally, the stress at the top of the wall has a lower value than in the interface due to the bending distortion of the sample.

The simulation of the heat source is one of the most troublesome parts in the thermomechanical analyses mentioned above. The study of Montevecchi [18] presents the Goldak model which is the most commonly used. Concerning this model, the heat input is delivered over the moving double ellipsoid region, following the Gaussian distribution. Despite the accurate prediction of the shape of the weld pool, the Goldak model does not consider the correct heat distribution between filler and base material, and clearly leads to higher temperature predictions. In the WAAM process, the heat energy is mainly transferred to the molten pool by two ways. The first one is the direct transfer from electric arc to the base metal and the second one incorporates the filler metal heat capacity. According to the Goldak model, the power consumed in melting the filler metal is about 50% of the total arc power. On the other hand, in the model proposed by Montevecchi, part of the total power is delivered to the base material by the Goldak method and the remaining part is distributed over the filler material with a constant distribution, see Figure 6. The advantage is the ability to capture the steep temperature gradients in the molten pool. Furthermore, the WAAM simulation involves specific elements activation techniques to simulate material deposition and the “quiet element method” is the technique used in the work of Montevecchi.

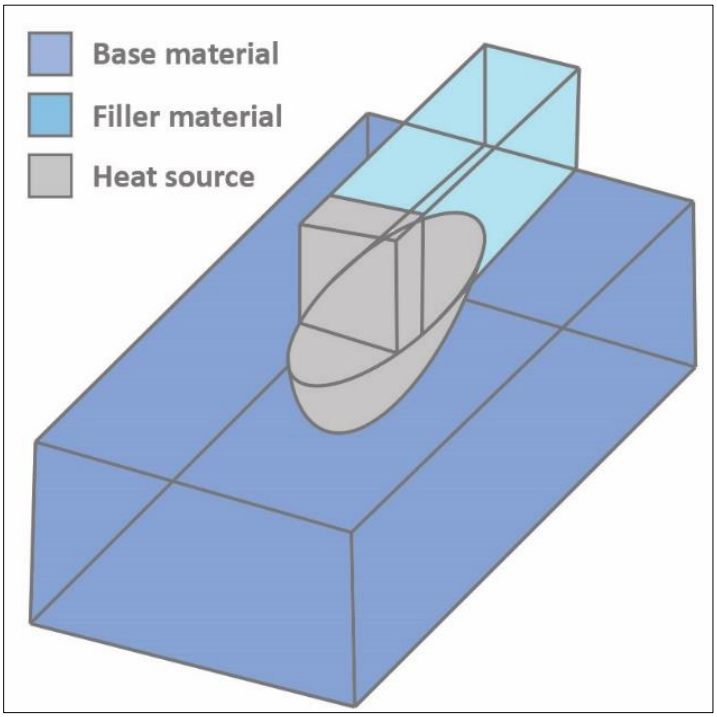

Figure 6: Heat source model by Montevecchi [18].

3. ALUMINIUM BRONZES

The aluminium bronzes are copper based alloys and contain up to 14 wt% aluminium (Al) [21]. The main alloying elements include nickel (Ni), iron (Fe), manganese (Mn) and silicon (Si). Nevertheless, the predominate nomenclature may be misleading for the alloy composition. The term "Aluminium Bronzes" is the first used, but indicates the presence of Al in conjunction with the standard alloying elements of bronze, copper (Cu) and tin (Sn). Thus, the alternative name "Cupro-aluminium" is used but is established only in the French speaking countries. The most common designation, used also in this report, is "aluminium bronzes". This study deals with two categories of aluminium bronzes, the nickel aluminium bronzes (NAB alloys) and the aluminium manganese bronzes (CMA alloys).

Copper (Cu), the main constituent of the aluminium bronzes, has atomic number 29 and atomic weight 63.546 amu. Its name comes from the Latin word cuprum, meaning "from the island of Cyprus", and the first time it was used dates back to more than 10,000 years ago. More than 400 copper alloys are in use nowadays [22]. As an element, copper is vital to the health of humans, animals and plants and thus it should be incorporated into the human diet (29). Taking conductivity into consideration, copper has high electrical and thermal conductivity, allowing for the usage of smaller conductors, saving space and cost [22]. Focusing on the biomechanical sector, copper is antimicrobial, therefore is used on the surfaces at public transportations. From a mechanical point of view, this element is durable, corrosion resistant and ductile. Thus, it can be formed and processed into many shapes and sizes. In addition, copper is 100% recyclable without any compromise in performance. Sustainability estimations reveal that 33% of today's world annual copper demand is supplied by recycled copper. Finally, copper alloys are aesthetically pleasing, being the only metals other than gold that have a natural colour. The rest of the metals are either grey or white [22]. Many architects selected copper structural elements as a part of their architectural design, see Figure 7 [22].

Figure 7: Nickel aluminium bronze window frames, Portcullis House (London) [1].

3.1 MICROSTRUCTURE OF NICKEL ALUMINIUM BRONZES (NAB)

3.1.1 CHARACTERISTICS OF THE CONSTITUENT PHASES

The NAB alloy is going to be used as substrate material at the experimental procedures, which are presented in the following chapters. The microstructure of NAB alloys is characterized by a variety of different phases and precipitates, see Figure 8. The structure and properties of the different microstructures will be analysed based on the work of Meigh [21], where their chemical compositions can be found as well. Furthermore, the microstructural development is strongly correlated with the cooling rate. At low cooling rates, the equilibrium phases are observed, while at high cooling rates, the diffusional transformations may be limited and martensitic transformation may take place. In this chapter, but also in the rest of the report, expressions like "slow" or "fast" cooling rate are mentioned. Therefore, it should be highlighted that a value in the range 10^{-3}-10^{-2} °C/sec characterises a slow cooling rate and every other case is compared to this magnitude. As a reference handbook for NAB alloys, the reader is advised to use the "Guide to Nickel Aluminium Bronze for Engineers" [1].

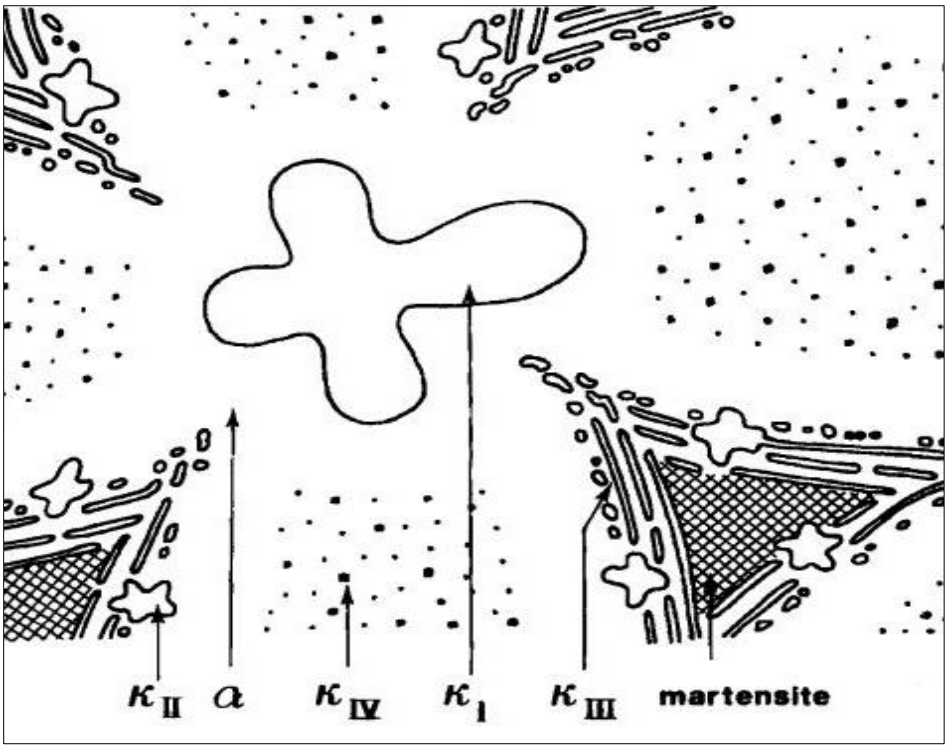

Figure 8: Schematic representations of the various phases in a type CuAl10Ni5Fe5 NAB alloy [23].

The **α phase** is a copper-rich stable solid solution with a face centred cubic (FCC) structure and a lattice of 3.64±0.04 Å. The solubility of iron decreases in this phase as the temperature drops resulting in the formation of κ phase precipitates. The α phase is evident by optical microscopy as the white areas in the microstructure and provides ductility at the expense of hardness [4]. In addition, α phase has a Widmanstätten[4] morphology [3], [4], [6], [10], [24], [25] and may occur intergranually or intragranually according to Nabach [10].

[4] Widmanstätten ferrite grains grow directly from a prior austenite grain boundary or from inclusions, having a needle or plate like appearance.

The **β phase** is stable at elevated temperatures and is a solid solution with a body centred cubic (BCC) structure. The solubility of aluminium is higher than the average value in the alloy and together with nickel, iron, manganese and κ_1 precipitates, constitute the chemical composition. Another variant of the β phase is present at low temperatures. **Retained β**, martensitic β phase or β' is the most common used nomenclature for this phase as suggested by Culpan and Rose [23], despite that other researchers like Fuller et al. highlighted the possibility of a bainitic β phase [6]. The structure of β' is hexagonal closed packed (HCP) and it is a needle like martensitic phase, appeared as dark etched intergranular areas. Electron diffraction patterns reveal that the β' phase may appear as either 3R or 2H martensite, containing small particles of spherical or cubic morphology based on NiAl ordering, according to Hasan [23]. Moreover, the 3R version of the structure, contains a high number of B2 precipitates, the size of which depends on the cooling rate [23]. This phase contributes to hardness but may lead to dealloying, deteriorating the corrosion resistance [4].

Another phase that may appear at low temperatures is **γ_2**, which forms a eutectoid with the $\alpha+\kappa_3$ phase. The characteristics of this phase include high corrosion susceptibility, excellent wear properties and brittleness.

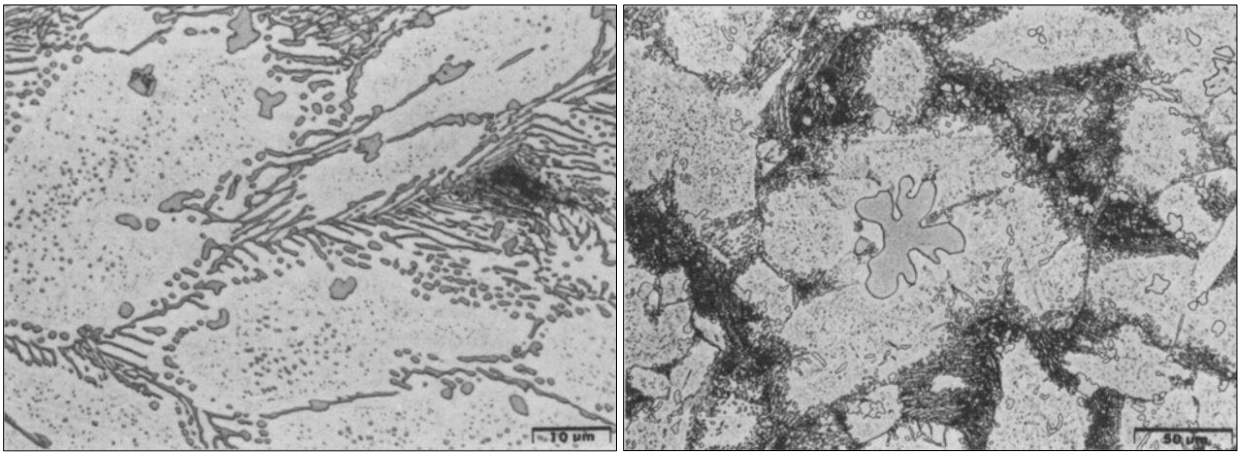

Figure 9: Micrographs of cast NAB showing (left) the phase distribution in CuAl9.4Ni4.9Fe4.4 NAB alloy, (right) a large κ_1 particle in a CuAl9Ni4.4Fe5.1 NAB alloy.[23]

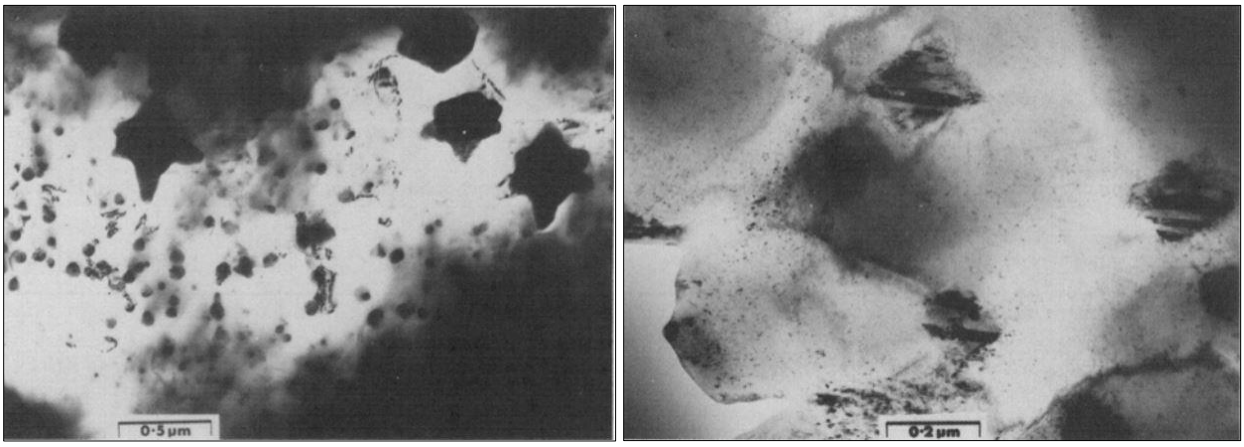

Figure 10: Transmission electron micrographs of a thin foil specimen showing (left) κ_4 particles of various sizes and (right) internally twinned κ_4 particles. [23]

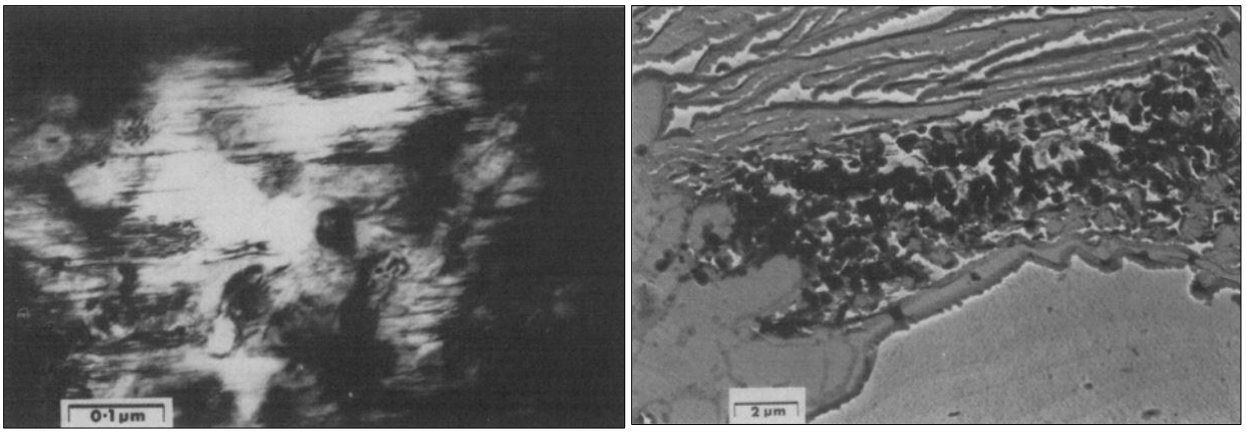

Figure 11: (left) Transmission electron micrograph of the retained β region showing martensite. (right) Fine precipitates extracted from the martensite are shown on the left. [23]

3.1.2 K PRECIPITATES: STRUCTURE, GEOMETRY, ORIENTATION

The precipitates in NAB alloys, κ particles, are intermetallic compounds which differ from the solid solution in that the constituent metals have reacted chemically to form a definite combination. They have either Fe_3Al, NiAl, FeAl or a disordered structure, and the substitution between the metallic elements is allowed. This means that one of the constituent metals can be partially replaced by another metal of the alloy. Their index number indicates the order that they appear as the alloy cools from the liquid state. Furthermore, κ precipitates absorb aluminium of the matrix, extending the range of the α field in the phase diagram (Figure 14) and increase the mechanical strength, deteriorating the ductility. However, the embrittlement is not as detrimental as in the case of the β' contribution. The classification of the κ phase is not a straightforward procedure for two main reasons. Various researchers have designated κ particles in different ways and their appearance and chemical composition is strongly correlated with the cooling rate. The following paragraphs attempt to give a detailed description incorporating all the types that have been observed [4], [6], [8]–[10], [21], [23], [25].

The **pre-primary κ_1** phase is the first precipitate formed in the liquid during cooling and can be divided into two types [21]. A worth mentioning fact is that as the iron content of the alloy is increased, the number of both types of particles also increases. Type 1 κ_1 particles appear white with a coarse globular morphology. Their iron content is around 71 wt% and as this value rises, the precipitation temperature becomes higher. This phenomenon is observed but not scientifically proven yet. If the ratio of nickel to iron content is less than unity the number of type 1 particles is minimized. If the iron content is less than 4.5 wt% these particles are eliminated. Type 2 κ_1 phase appear dark and has a dendritic faceted structure. The iron content is 64 wt% and their solubility changes more rapidly with temperature. Type 2 particles precipitate at lower temperatures than type 1 particles. Moreover, the β phase crystals nucleate heterogeneously on type 2 particles and thus their contribution to the microstructure of the alloy is beneficial due to their grain refining function.

Post solidification κ_1 phase consists of iron-rich intermetallic particles. Initially they are formed in the β phase of alloys with high iron levels, around 5 wt% [21], [26]. Upon further cooling, these particles nucleate at α grains, thus at room temperature they appear in the form of large dendritic rosettes in the centre of the α phase [23]. With respect to their structure, κ_1 particles have an ordered BCC Fe_3Al (DO_3)

[7], an ordered FeAl (B2), or a disordered iron rich solid solution BCC structure. Their diameter ranges from 20-50 μm and are cored, meaning that their geometrical centre is copper-rich.

As discussed previously, **κ_2** particles should appear second during cooling and they precipitate at the β phase. However, they may be enveloped in the α phase as the β phase breaks down into α+β+κ at 900 °C. The κ_2 particles continue to form below 840 °C at the α/β interface together with κ_3. The geometry of the κ_2 particles varies from coarse and rounded to dendritic rosettes of size between 5-10 μm. Other researchers support that these particles have a small cruciform shape [25]. The structure is ordered BCC Fe_3Al (DO_3) [6], with copper, manganese and nickel as possible substitutes for iron, and silicon for aluminium. The lattice parameter is 5.71±0.06 Å [7], [23]. Finally, they do not contribute to the corrosion properties of the alloy, except that they may cause superficial oxidation.

At lower temperatures, 840-600 °C, the **κ_3** particles precipitate. They have a lamellar, pearlitic or a globular form and grow at a 90° angle to the α/β boundary or at the boundary of large κ_1 rosettes [25]. Their composition is nickel-rich and their structure is ordered BCC NiAl (B2), allowing iron, copper or manganese for substitution of the nickel atoms. The lattice parameter is significantly lower than κ_2 particles, 2.88±0.03 Å [7].

The **κ_4** particles precipitate at low cooling rates and at temperatures below 850 °C. They are iron-rich, with 2 μm diameter, located in the α phase, causing a precipitate depleted zone near the grain boundary. Their structure is ordered BCC Fe_3Al (DO_3) with lattice parameter 5.77±0.06 Å [7], similar to κ_2 particles. According to Hasan [23], some of the κ_4 particles are internally twinned. Hazra et al. [26] claimed that κ_4 particles have spheroidal or cruciform morphology [25]. However, their size is very small, not allowing for chemical composition characterization via SEM-EDX equipment [26].

The last category (**κ_5** precipitates) is the most controversial one because it is not accepted by the entire scientific community. The κ_5 particles are defined by Brezina, together with Culpan and Rose who mention that these particles might be absent in the as cast structure and become evident as a result of heat treatments. They claim that κ_5 particles have ordered BCC NiAl (DO_3) structure, whereas other researchers support that the actual structure is a modified κ_3 one.

There are several remarks on the orientation and structure of these precipitates that should be clarified. Hasan et al. [23] also investigated the orientation relationships between the κ particles and the α matrix, concluded that κ_1, κ_2 and κ_3 precipitates exhibit the Kurdjumov-Sachs (K-S) orientation, whereas in the κ_4 particles a more complicated behaviour is observed. The smaller sized κ_4 particles are oriented, with respect to the matrix, according to the Nishiyama-Wasserman (N-W) type relationship, while the larger particles' orientation lies between N-W and K-S. This phenomenon may be explained by the internal twinning of the larger κ_4 particles. The κ_2 and κ_4 particles could be expected to have the same orientation relationship with the matrix as they have a similar structure (Fe_3Al). However, κ_2 particles nucleate in the pre-existing β phase and are enveloped subsequently by the α phase, while the κ_4 particles grow directly at the α phase. Therefore, the orientation of κ_2 particles depends on the orientation of the β phase with respect to the α matrix.

As far as the structure is concerned, the NiAl and the Fe_3Al are the most common configurations, see Figure 12. In the NiAl, all the BCC positions are occupied by aluminium, whereas in Fe_3Al half of these positions are occupied by transition elements. The Fe_3Al phase can contain 25-35 wt% of aluminium and a limited amount of iron can be substituted by nickel and copper atoms. On the contrary, NiAl phase

exhibits a wide composition range in iron, copper and aluminium. Alternatively, the DO_3 structure is characterized as an ordered BCC superlattice containing eight cells according to Nabach [10], while the B2 structure for NiAl is an ordered CsCl crystal structure.

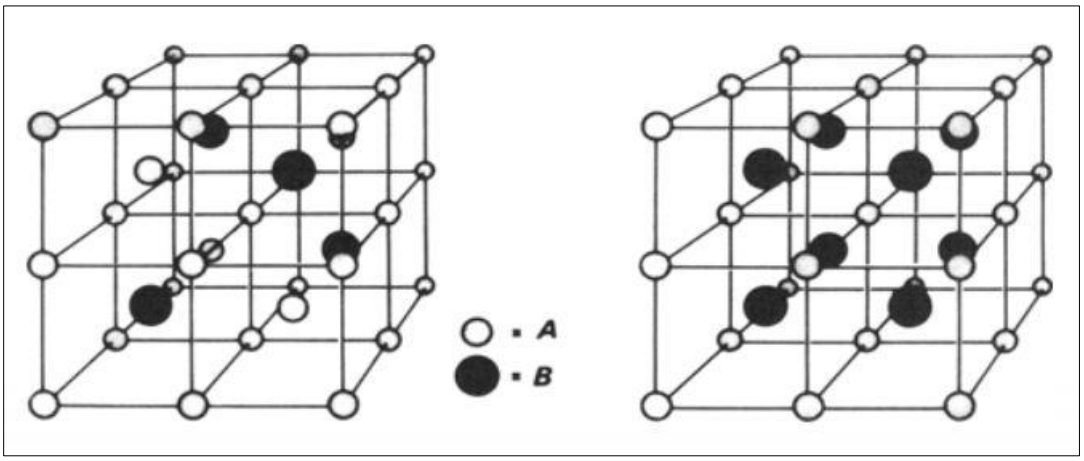

Figure 12: Schematic representation of the crystal structures of the κ phases: (left) Fe_3Al structure of $κ_2$ and $κ_4$. The positions A are occupied by the Fe (or Ni or Cu or Mn) and positions B by Al (or Si). (right) NiAl structure of $κ_3$ phase. The positions A are occupied by Ni (or Fe or Cu or Mn) and positions B by Al. Eight unit cells of NiAl structure are shown to illustrate its similarity with Fe_3Al [23].

Nishiyama states in his work [27] that most β phases of noble-metal alloys are BCC. Copper, gold or silver based alloys, alternatively called Hume-Rothery phases, belong to this category. The close packed layers are transformed from the $\{110\}_{bcc}$ plane, which is the martensitic transformation shear plane. There are two possibilities, namely ± $[1\bar{1}0]$ on each plane. In the case shear takes place in the same direction on every plane parallel to (110) plane, the resulting structure is FCC. If alternate shear on every other plane takes place, the resulting structure is HCP. In any other case, there is a combination of the two structures.

Nishiyama explains also the 2H and 3R Ramsdell notation, according to which the Arabic numerical indicates the number of layers in one period and the letter (H or R) following, stands for hexagonal or rhombohedral symmetry, see Figure 13. Concerning the superlattice structure, it is formed because the product phase in the martensitic transformation inherits the atomic ordering of the parent phases. Confirming the observation from other researchers, which is mentioned in previous paragraphs, most β phases in noble metal-based alloys have the Fe_3Al type (DO_3) superlattice or CsCl-type (B2) superlattice [27].

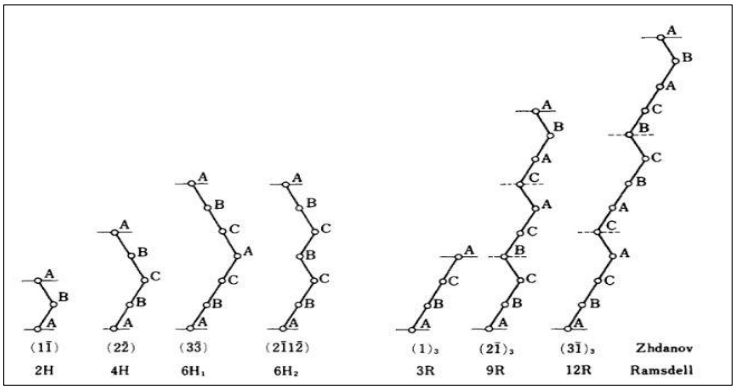

Figure 13: Various kinds of close-packed layer structures, designated by two different notations. [27]

3.1.3 EFFECTS OF ALLOYING ELEMENTS

Alloying elements are mainly used to enhance the properties of metals which would be of limited use if they remained pure. This paragraph describes the effect of the major alloying elements in NAB alloys, on the bases of mechanical and corrosion properties and weldability.

Aluminium (Al) is the main alloying element tremendously affecting the properties of NAB alloys. It is reported that small variations in aluminium content have a greater influence on the properties than similar variations of the other alloying elements [25]. The excellent tensile properties of NAB alloys are attributed to Al. Weston designates that with increasing the aluminium content within the range of 8.8-10 wt%, the hardness rises and the elongation drops. Indicatively, the proof stress increases from 200 MPa to 277 MPa and the tensile strength from 700 MPa to 708 MPa [25]. Together with Ni, Al determines whether α+κ (excellent corrosion resistance) or α+κ+β (higher tensile, but lower corrosion properties) appears. In most cases, the 9.4-9.5% aluminium content gives the best compromise between mechanical and corrosion properties [21], [25]. Above 12 wt% Al the elongation drops dramatically and welding is not advisable [21], because of the danger of hot tearing. Moreover, while the high aluminium content enhances the corrosion resistance of single α phase, amounts larger than 10 wt% may give rise to a continuous grain boundary β' phase increasing the corrosion susceptibility [25].

Nickel (Ni) contributes to the precipitation strengthening mechanism, the corrosion and erosion resistance [1]. In more detail, the nickel-rich κ precipitates give rise to the precipitation strengthening mechanism in the α+κ alloys. However, there is no significant advantage if the nickel content exceeds 5 wt% and above 7 wt% welding becomes impossible. In addition, if the value of iron content exceeds the nickel concentration, on slow cooling, the eutectoid structure may break down and be replaced by a (semi-) continuous grain boundary network of κ_3, deteriorating the corrosion properties and the elongation. Moreover, it has been reported that increasing the Ni content retards the β phase transformation and provides elevated hardness in both hypoeutectoid and eutectoid NAB alloys [25].

Iron (Fe) has a similar function as nickel with respect to the mechanical properties. The iron-rich precipitates provide mechanical strength to the α+κ alloys. Moreover, iron acts as a grain refiner [21], [25]. Sustaining the iron content in the range of 3-5 wt% assists to maintain the mechanical properties at elevated temperatures, improves wear and abrasion resistance, and increases the fatigue endurance limit [25]. Nevertheless, its content should be below 4 wt%, otherwise cavitation problems may arise. According to Weston, 4 wt% is the optimum value [25]. Welding is not affected by the iron content variation in the composition range that this report is focused on.

Manganese (Mn) enhances the fluidity, facilitating the casting of thin or complex sections. In addition, acts as a deoxidant and a scavenger for dross [25]. Manganese content above 2 wt% should be avoided because β' is stabilized [21], [25] and the decomposition to α+κ is hindered. Thus, this element improves the weldability of NAB alloys but deteriorates the corrosion resistance by selective phase attack.

Unfortunately, impurities cannot be completely avoided. Lead and phosphorus may cause hot tearing, while magnesium decreases the ductility. The content of these elements must be limited below 0.01 wt%. [1]

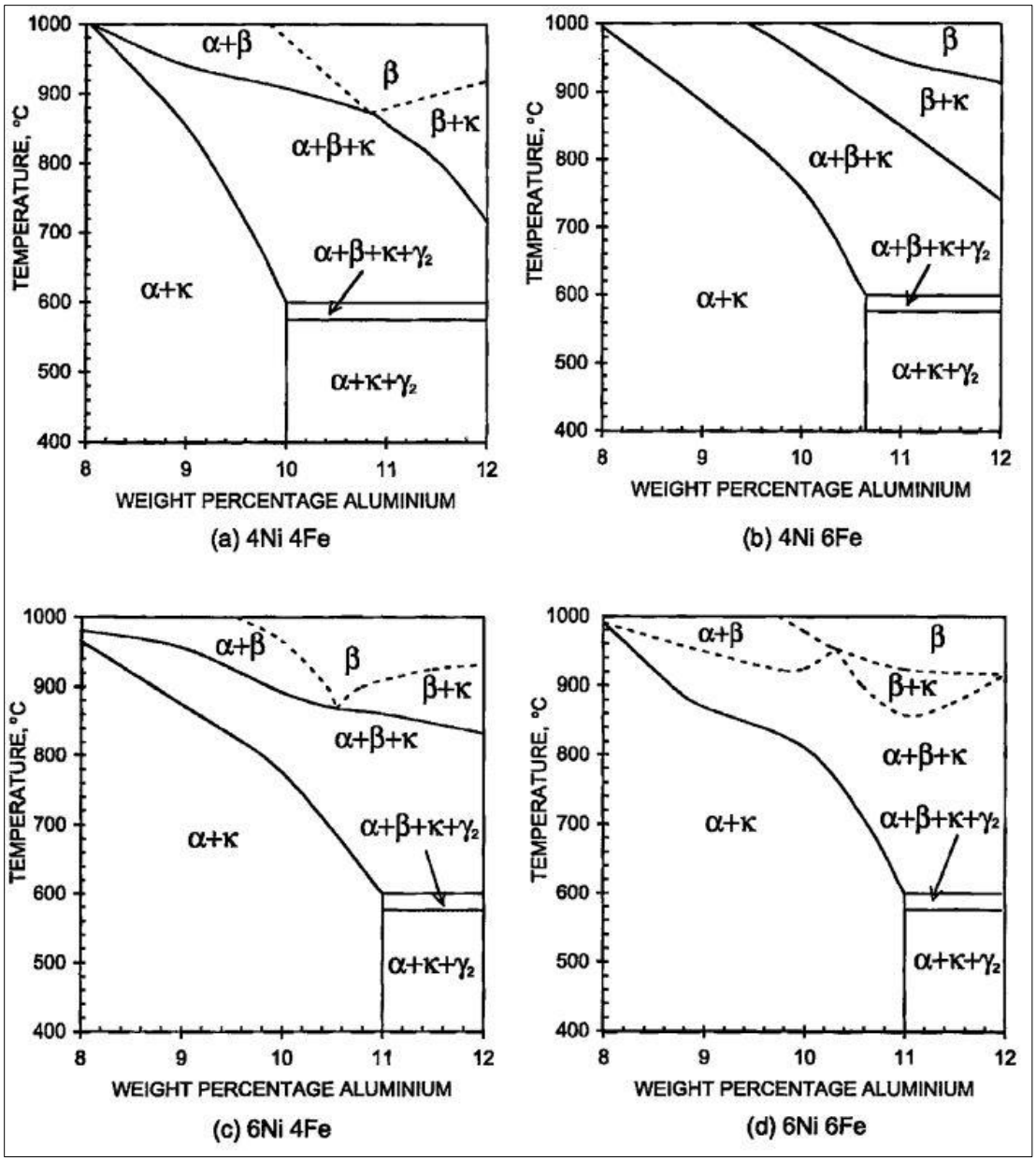

Figure 14: Vertical cross sections of the Cu-Al-Ni-Fe system with various amounts of iron, nickel and aluminium [21].

3.1.4 MICROSTRUCTURAL DEVELOPMENT

In the previous session, all the constituents present in NAB alloys were described. This paragraph focuses on the different phases which may appear upon cooling from the liquid state. Understanding of this evolution is of vital importance to predict the final microstructure at room temperature. Initially, the microstructural development of the nominal composition CuAl10Ni5Fe5 is going to be presented based on the work done by Meigh [21] and Jahanafrooz [28], but in subsequent paragraphs, a more weld-oriented approach will be followed.

It should be highlighted that phase changes tend to occur at lower temperatures than the phase diagram indicates. The reasoning behind yields to the fact that equilibrium conditions cannot be achieved by slow cooling [21]. The only way to achieve them is by quenching at high temperature and subsequent annealing at the desired temperature. Thus, there are significant differences between the equilibrium state and the microstructure resulting from slow cooling.

Between **1080 °C and 1050 °C** the Cu-rich **β** phase nucleates and grows in the form of dendrites. Some dendrites nucleate at the **type 2 κ_1** particles, while their simultaneous formation acts as an obstacle for their growth and triggers a grain refinement mechanism eventually. On the contrary, at **type 1 κ_1** phase there is no nucleation of other phases and thus they accumulate in the last to solidify area between the dendritic arms. Upon slow cooling, it is possible to re-dissolve some of these precipitates in the solid-state.

At 1010 °C a distinction should be made between alloys with iron content lower or higher than 5 wt%. The first category transforms entirely into β phase, which in case of quenching becomes the martensitic retained β phase. The second category, transforms into a β+κ_1 type 2 phase.

Below **1010 °C** the microstructure breaks down progressively into **α+β**. At first steps, the α phase nucleates at β phase grain boundaries in a needle-like, Widmanstätten form, as mentioned in the previous chapter. In addition, the aluminium and iron content plays an important role to the nucleation of this phase. In case of a low aluminium or high iron content, the nucleation of α phase is observed at elevated temperatures. If iron content exceeds 5 wt%, the nucleation site of the α phase is at the κ_1 particles.

Once the temperature reaches below 1000 °C, the nucleation of the rest of the κ particles is triggered. More specifically, between **1000 °C and 900 °C** the **κ_2** particles appear in the β phase. The higher aluminium content lowers the nucleation temperature of these particles. At the range of **940-840 °C** the solubility limit of iron in the α phase is reached and tiny **κ_4** particles nucleate at the centre of α grains. The nickel and iron content strongly affects the nucleation of the **κ_4**. The higher the nickel to iron ratio, the higher the nucleation temperature of κ_4 particles, whereas the increase of iron content has an adverse effect. At an even lower temperature range, between **840 °C and 800 °C** the remaining β transforms to a finely divided eutectoid **α+κ_3 phase**. The **κ_3** particles may be initially globular but become lamellar or pearlitic in form at the α/β interface.

The eutectoid transformation of α+κ_3 stops at **660 °C**, leaving substantial amount of β regions, which transform into **β'** martensitic structure at medium cooling rates. A temperature of **415 °C** is the limit below which no appreciable change takes place. Between **660 °C and 415 °C** the precipitation of **κ_5** particles is responsible for the dark etching of the β phase.

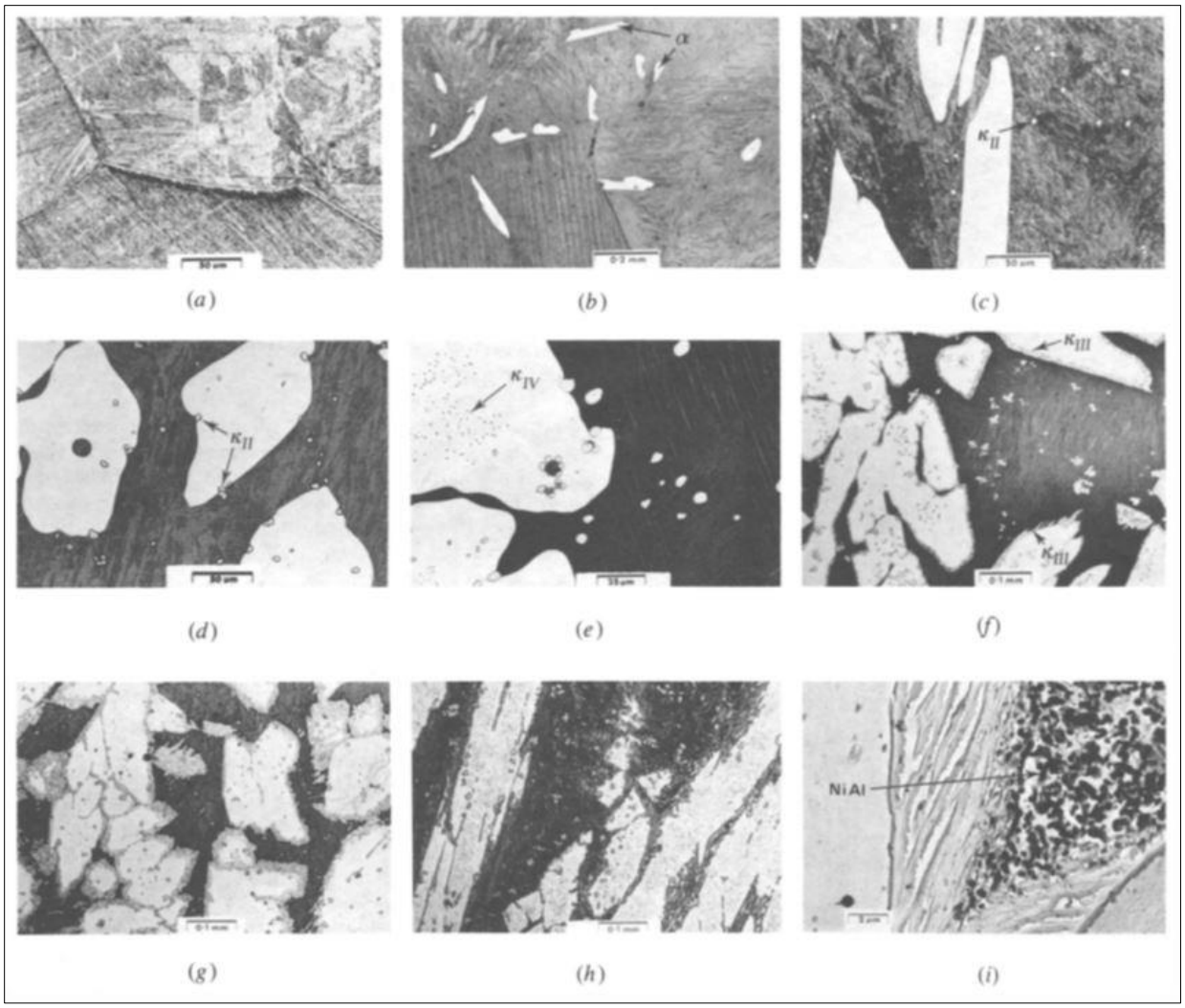

Figure 15: (a) 1010 °C: fully β structure, (b) 900 °C: β(dark) and α(white), (c) 880 °C: α and β (with κ_2 formed in β). (d) 880 °C: growing α envelopes some κ_2 particles, (e) 850 °C: tiny κ_4 particles formed at α phase, (f) 800 °C: decomposition of β into eutectoid α+κ_3 at the α/β boundaries, (g) 660 °C: eutectoid decomposition of β has been ceased, (h) 415 °C: dark etched β region due to κ_5 precipitates, (i) higher magnification of (h) showing the κ_5 particles which have a NiAl order. [28]

Different researchers designated alternative theories to the one presented above for the microstructural development of NAB alloys. Thomson and Edwards [29] claimed that only a single κ phase was formed with just two different morphologies, one plate like nickel rich and one nodular iron rich. On the contrary, the work of Rowlands and Brown [30], and that of Culpan and Rose [31], are in closer agreement with the study of Jahanafrooz [23]. The main difference yields to the classification of the various precipitates. These two studies designated the 5-10 μm κ particles as κ_1 and the first formed κ_3 particles as κ_2. Concerning the sequence of nucleation, they reported that κ_4 particles appear after the eutectoid reaction of α+κ_3, which comes into conflict with the work of Jahanafrooz, who clearly observed the early formation of κ_4 particles well above the eutectoid reaction temperature. However, these initial observations and reports are responsible for the misleading numerical index of κ particles, having κ_4 particles formed after κ_3 ones. Finally, Culpan and Rose [31] stated that κ_2 particles nucleate randomly in both α and β phase, while more recent studies showed that κ_2 particles may be enveloped by the α phase [28].

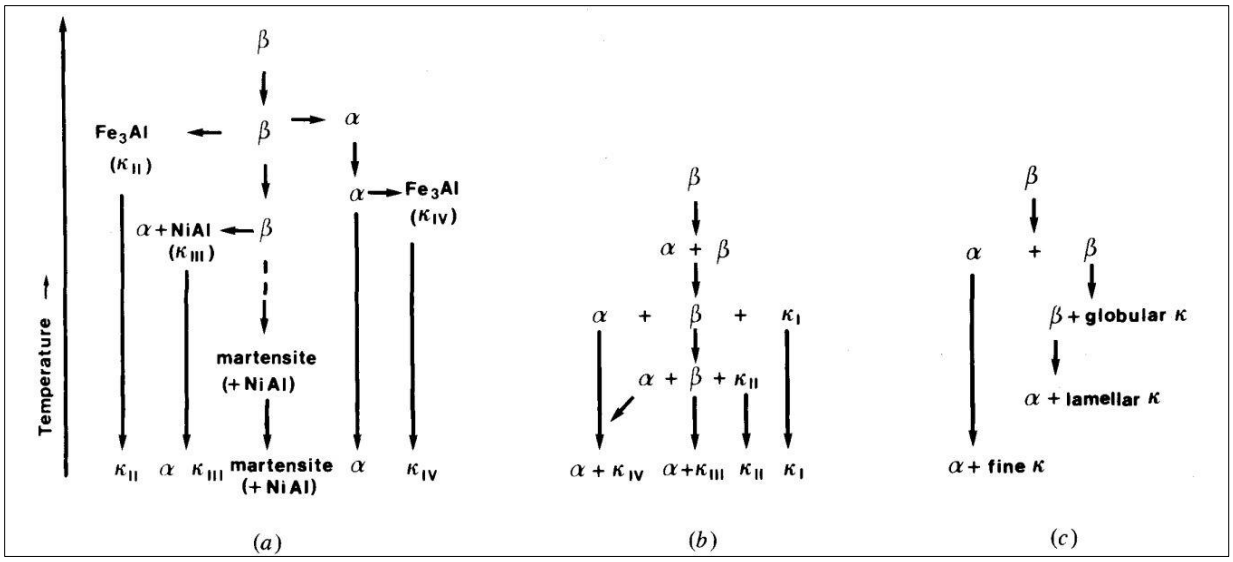

Figure 16: Schematic representation of the sequence of microstructural development, according to (a) Jahanafrooz and Hazan, (b) Rowlands and Brown and (c) Culpan and Rose.

Pisarek attempts to create a model for NAB alloys crystallization [32]. According to him, the addition of extra alloying elements makes no differences in the phase transformation procedure, while in case these elements are among the basic constituents of the alloy, meaning Ni, Al, Fe, the effect is significant. Using the Thermal and Derivative Analysis method, Pisarek exports the following schematic for the microstructural development of hypoeutectoid NAB alloys, based on observations presented in Table 4.

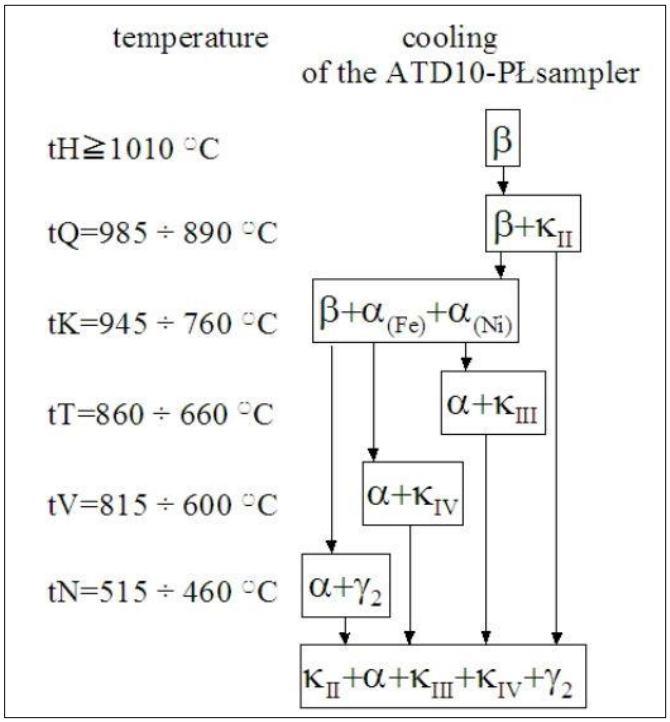

Figure 17: Phase transformation during cooling of hypoeutectoid NAB alloys with limited additions of Cr, Mo, W, Si [32].

Table 4: Observed temperatures with TDA during phase transformations. [32]

Transformation	*Temperature (°C)*
liquidus (L→β)	1082.6
Solidus (β)	1023.3
κ_2 phase crystallization	89704
α phase crystallization $\alpha_{(Ni)}$, $\alpha_{(Fe)}$	81202
κ_3 Phase crystallization α(Ni)→α+κ_3	736.6
κ_4 Phase crystallization α(Fe)→α+κ_4	702.7
Eutectoid transformation β(Al)→α+γ_2	461.7

3.2 MICROSTRUCTURE OF COPPER MANGANESE ALUMINIUM ALLOYS (CMA)

3.2.1 COMPARISON BETWEEN NAB AND CMA ALLOYS

The microstructure of aluminium manganese bronzes (CMA) is similar to the one of NAB alloys. In the coming paragraphs, an attempt is made to clarify and highlight the structural differences of the phases and their microstructural development [21]. The reason behind this behaviour is the presence of manganese, which has a similar effect as aluminium. It is reported that 6 wt% Mn equals to 1 wt% Al, meaning that the CuAl10Ni5Fe5 has many similarities to the CuMn13Al7. Moreover, manganese contributes to the strength of the alloy and stabilizes BCC β phase [9]. Thus, in aluminium manganese bronzes, the β phase is retained even at low temperatures, whereas in NAB alloys there is the martensitic transformation resulting in the formation of β'.

Manganese also acts as a stabilizer for the FCC form of iron, enhancing the formation of FCC precipitates. In addition, it has a detrimental effect on the solubility of iron in copper and decreases the temperature at which the β→α+γ_2 transformation takes place.

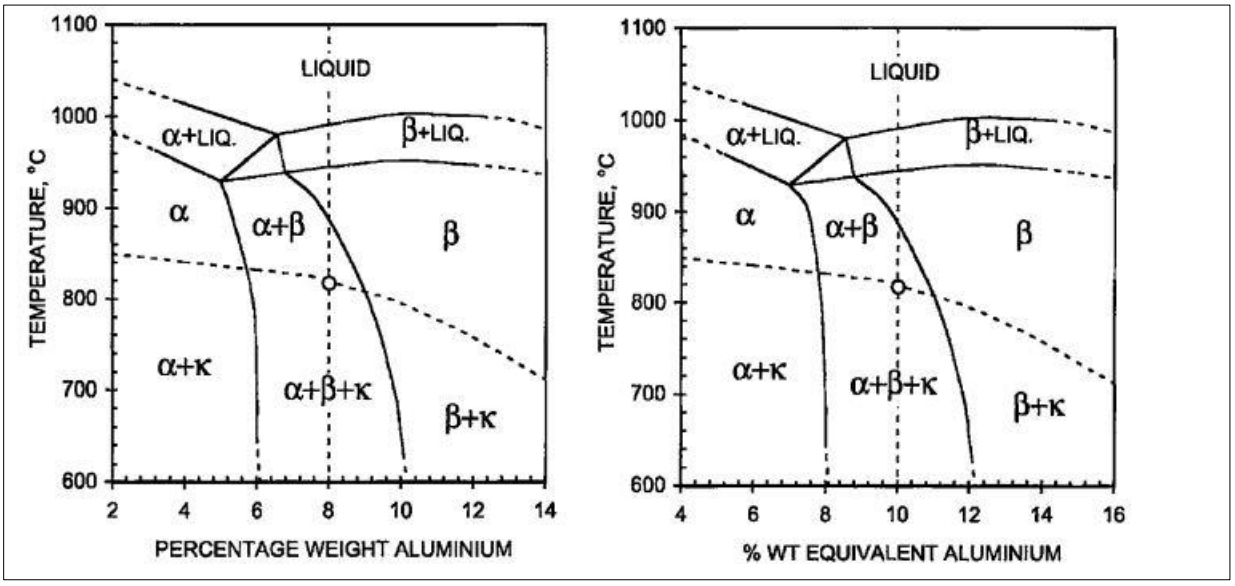

Figure 18: Phase diagram of Cu-Mn-Al-Ni-Fe alloy containing 12% manganese, 8% aluminium, 2.8% iron and 2% nickel. (a) Plotted against actual aluminium content, (b) Plotted against equivalent aluminium content.

3.2.2 CHARACTERISTICS OF THE CONSTITUENT PHASES

The alloy consists of four phases, one of which is in the form of precipitates of various morphologies. The copper-rich **α phase** is the light etched one, as in the case of the NAB alloys and its structure is FCC. The lattice parameter is 3.61±0.04 Å [9]. On the contrary, the **β phase** has an ordered BCC structure, based on Cu_3Al. This phase is evident as the dark etched areas in the microstructure and is also copper rich, but with twice the level of aluminium content than the α phase. The lattice parameter of the phase is 2.97±0.03 Å [9]. According to Iqbal [9], the orientation of α grains with respect to the β grains resembles the Nishiyama-Wasserman relationship, meaning [001]β//[011]α and [110]β/[111]α. Finally, the γ_2 phase is part of the eutectoid transformation and forms at 400 °C, at very slow cooling rates.

3.2.3 K PRECIPITATES: STRUCTURE, GEOMETRY, ORIENTATION

The precipitates of as cast CMA alloys are designated also as κ phase following the index numbering system from 1 to 5. The geometrical characteristics are similar to the ones of NAB alloys, while their composition differs significantly. The characteristics of these particles are investigated by Iqbal [9].

The **κ_1** particles are dendritic in shape, γ(Fe) FCC regarding the structure and with 20-40 μm diameter. They are located at the centre of the α grains and consist mainly of iron and manganese. According to Meigh [21], these particles are observed in the microstructure after quenching just below the solidus (950 °C), indicating that they might be formed in the melt. Their lattice parameter is 3.69±0.03 Å [9].

The **κ_2** particles are a smaller version of the κ_1, meaning that they have a dendritic shape and a diameter between 5 to 10 μm. These particles are observed in the β phase at 750 °C and become enveloped by the growing α phase as the temperature falls. Their composition consists mainly of iron, manganese and significantly more aluminium than the κ_1 particles. The structure of κ_2 particles is ordered BCC (based on Fe_3Al) allowing for substitutions. In more detail, manganese, copper and nickel may partially substitute iron, while silicon may replace aluminium. The lattice parameter is 2.94±0.04 Å and exhibit the Kurdjumov-Sachs orientation relationship with the α matrix, ([111]precipitate//[011]α and [101]precipitate//[111]α) [9].

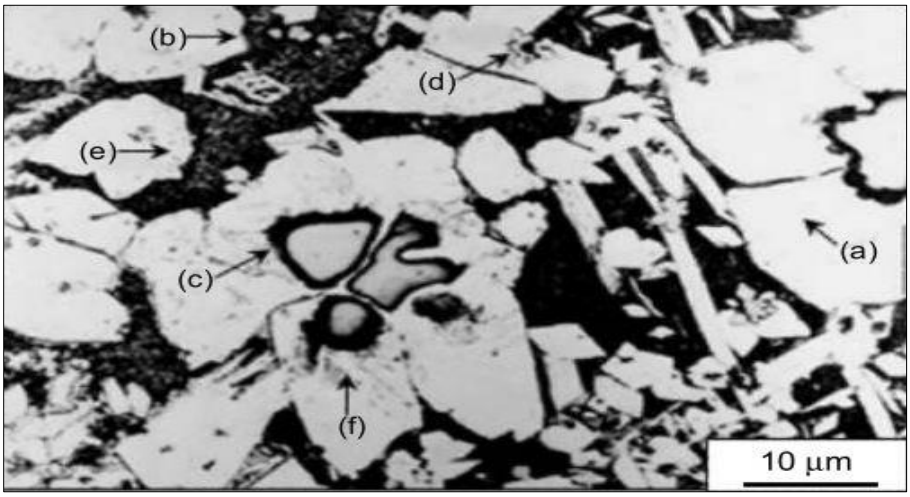

Figure 19: Microstructure of an as-cast CMA alloy, where the (a) α phase, (b) β phase, (c) large dendritic particles, (d) smaller dendritic particles, (e) globular precipitates, (f) cuboid precipitates are evident [9].

On the contrary, **κ_3** particles are globular and appear close to boundaries of α and β grains at 730 °C. They are also enveloped by the growing α phase as the temperature drops. Iron, manganese, copper and aluminium are incorporated in the composition, with the first element being the main constituent, whereas the last has the smallest amount. The structure of these particles is also ordered BCC, based on Fe_3Al (DO_3). Their lattice parameter is 2.95±0.04 Å and for their orientation relationship with the α matrix holds the following [011]precipitate//[011]α and [001]precipitate//[111]α [9].

Finally, the cuboid shaped **κ_4** particles precipitate in the α phase at a temperature between 730 °C and 670 °C. They have a γ(Fe) structure with a FCC lattice, and are richer in iron than the globular particles, while their aluminium level is lower. Their size varies from 0.1 to 0.2 μm [9], their lattice parameter is 3.7±0.04 Å and they show a cube-cube orientation with the α matrix ([100]precipitate//[001]α). According to Iqbal [9], it is possible to observe tiny cuboid precipitates inside the β phase, which have higher aluminium and lower silicon percentage than the κ_4 particles. In addition, these **κ_5** particles are evident only by TEM and are based on Fe_3Al (DO_3) structure.

Despite the similarities of the κ phase between the two alloys, there is also a characteristic which clearly distinguish the precipitates of manganese aluminium alloys. Sparkle phase inter-metallic particles are needle-like in appearance and are formed due to the excess of carbon during prolonged overheating of the melt. Contamination is the source of the excess carbon and occurs primarily inside the furnaces. This phase is evident when the alloy cools at very slow rate and occurs around 400°C, requiring a very long transformation time. The composition of the sparkle phase has many similarities with the one of the κ_1 particles but has more iron and less aluminium. Considering the structure, this unique phase is similar to cementite (Fe_3C) with an approximate composition of Fe_2Mn, in which a substantial proportion of iron is replaced by manganese. It has a detrimental effect on the mechanical properties of the alloy, making it more brittle.

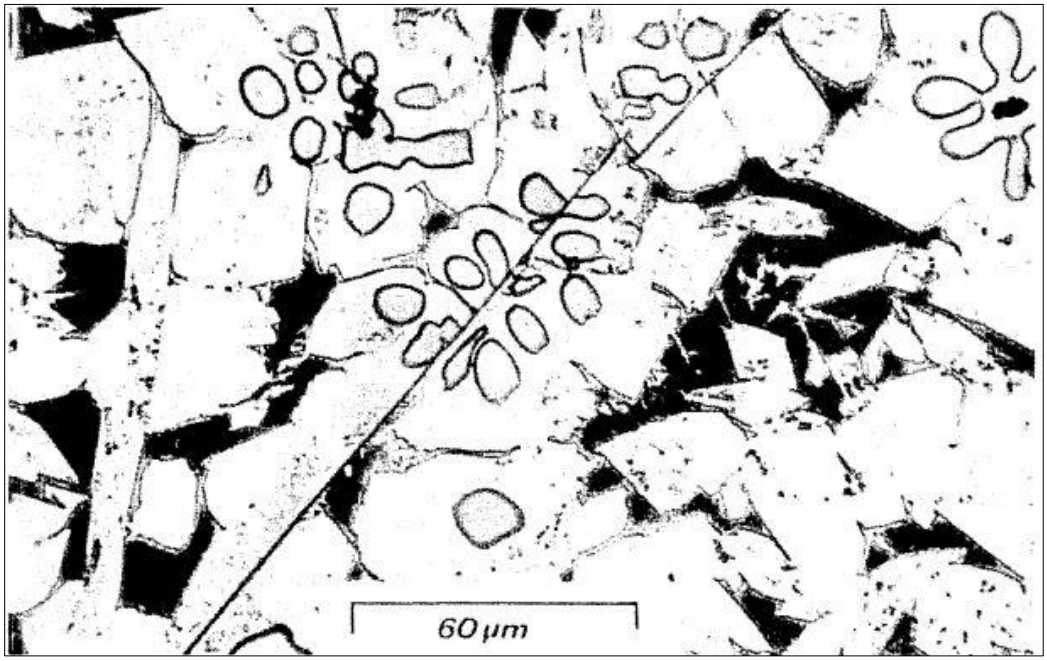

Figure 20: Microstructure of an as-cast CMA alloy illustrating the "sparkle phase" [21].

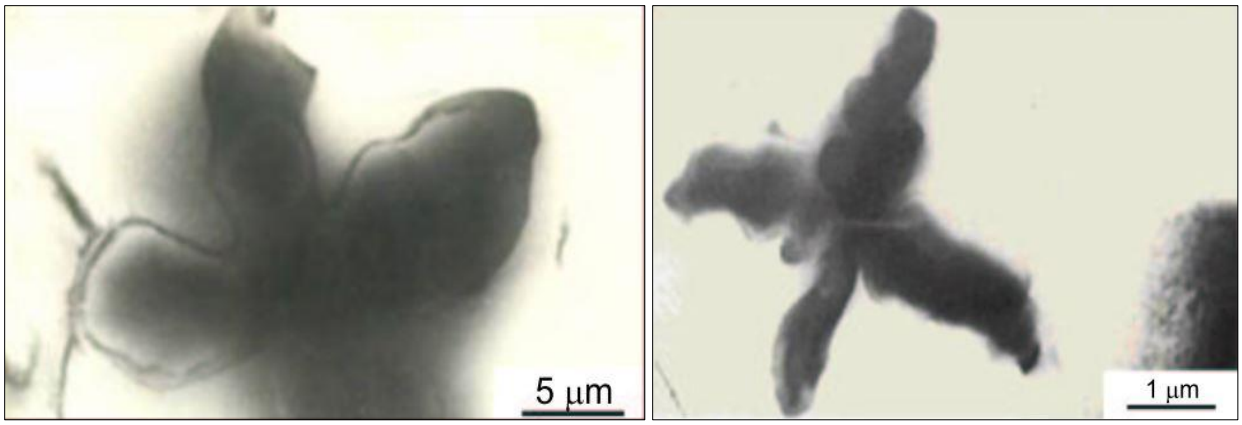

Figure 21: Transmission electron micrograph showing a large, κ_1, (left) and a small, κ_2, (right) dendritic-shaped particle in the α-grain [9].

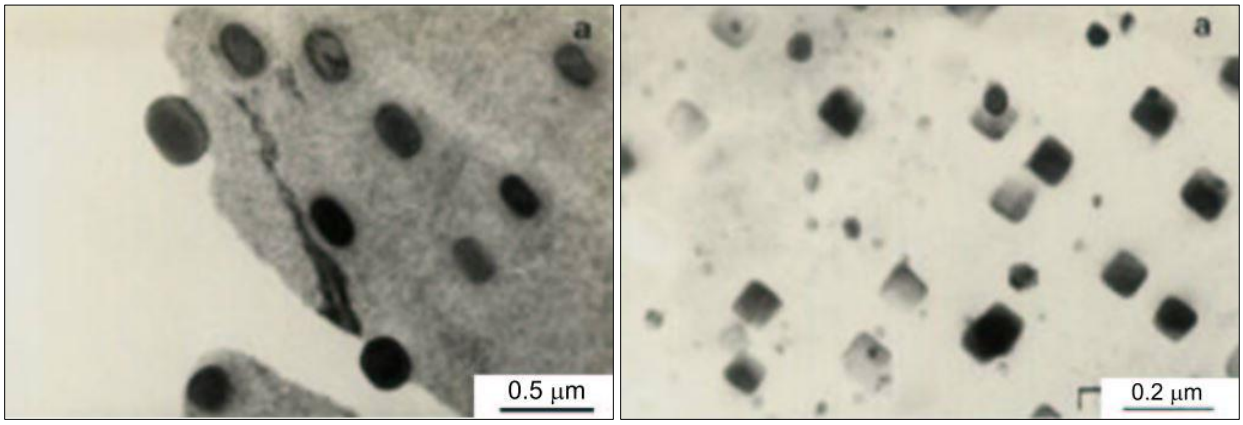

Figure 22: Transmission electron micrograph showing globular, κ_3, (left) and cuboid-shaped, κ_4, (right) precipitates in α-phase [9].

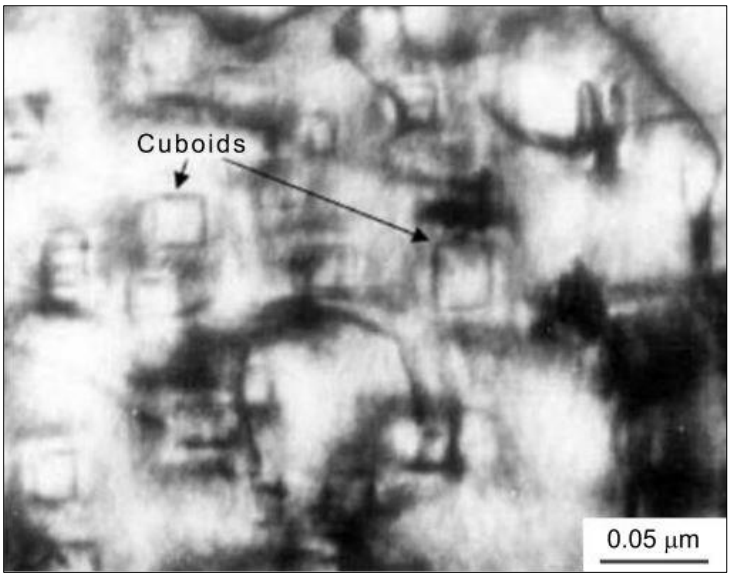

Figure 23: Transmission electron micrograph showing the cuboid κ_4 precipitates in the β-phase [9].

3.3 WELDING OF ALUMINIUM BRONZES

The aluminium bronzes are classified into four main categories with respect to welding [33]. Groups 2 and 4 are of great importance due to their exceptional behaviour in maritime applications. Alloys with 8-11 wt% Al and additions of nickel and iron belong to group 2, and are designated as AB1 or AB2, according to BS 1400 specifications [21]. On the contrary, alloys with manganese as the main alloying element and additions of aluminium belong to group 4, and are classified as CMA1 or CMA2. Group 1 incorporates single phase alloys with less than 8 wt% Al, which are most vulnerable to cracking due to a wide ductility dip, a term explained in the subsequent paragraph. Finally, group 3 contains aluminium silicon bronzes of low magnetic permeability [33]. Table 5 contains information on the chemical composition of these alloys.

Table 5: Compositions of cast copper aluminium alloys. Impurities are specified by the BS 1400 standard [33].

BS 1400	*Alloy Composition (wt%) – Cu: balanced*				
Designation	*Al*	*Fe*	*Ni*	*Mn*	*Si*
AB1	8.5 - 10.5	1.5 - 3.5	1.0 max	1.0 max	
AB2	8.5 - 10.5	3.5 - 5.5	4.5 - 6.5	1.5 max	
AB3	6.0 - 6.4	0.5 - 0.7			2.0 – 2.4
CMA1	7.5 - 8.5	2.0 - 4.0	1.5 - 4.5	11.0 - 14.0	
CMA2	8.5 - 9.0	2.0 - 4.0	1.5 - 4.5	11.0 - 14.0	

This paragraph highlights the most significant welding characteristics of aluminium bronzes. The aluminium oxide film, which forms on the surface of these alloys provides a high corrosion resistance. However, oxide may be entrapped in the weld, a phenomenon which can be annihilated by pre-weld and inter-run cleaning of the metal. In addition, the thermal conductivity of the aluminium bronzes is higher than in low carbon steels and provides a faster dissipation of the heat generated during welding. As a consequence, the solidification proceeds faster and the HAZ is wider. The above property, together with the high thermal expansion of the alloy cause considerable shrinkage and expansion, which must not be restricted when it is possible [21]. Finally, aluminium bronzes of low aluminium content are characterized by a ductility dip, which describes the shape of Figure 24, where the elongation versus the temperature is plotted. At the ductility dip, the alloys are less ductile and are most prone to fracture. The temperature range where the phenomenon is observed is 600 °C to 400 °C for 9 to 10 wt% Al, and 650 °C to 300 °C for 7.6 wt% Al. The implications caused by the ductility dip are mainly correlated with the restraints caused by the welding jigs. If the weld elongation due to restrained shrinkage is greater than the fracture elongation, cracks may appear in the specimen. Moreover, any impurities and inclusion might lower the fracture elongation.

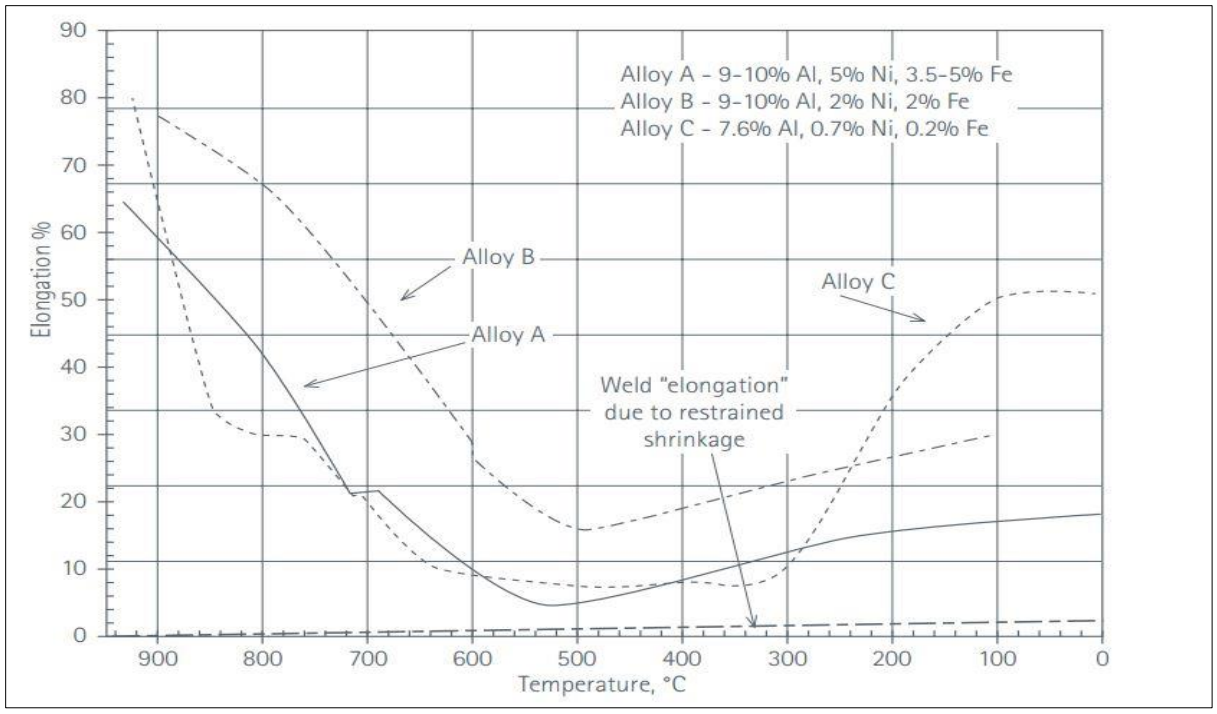

Figure 24: Maximum elongation versus temperature of various aluminium bronzes in the as-cast condition, showing the ductility drop [1].

3.3.1 WELDING TECHNIQUE AND FILLER MATERIAL

The recommended welding processes are presented in Table 6 with descending order of applicability [1]. The most suitable welding methods for the aluminium bronzes are the GTAW and GMAW. GTAW may be also used as initial pass before the application of the GMAW method. Both welding processes may be applied with a pulsed arc. In the pulsed arc method, a lower average current is used, interrupted by a high current at regular intervals. In this case the weld pool is not overheated, and the extension of HAZ is limited. On the contrary, the use of the manual metal arc (MMA) method with aluminium bronzes filler material is restricted to facilitate welding of dissimilar metals. Finally, the EBW is not recommended because the rapid cooling may give rise to the unwanted martensitic transformation, and therefore deteriorate the corrosion properties [1].

Table 6: Order of welding process according to the easiness of joining the aluminium bronzes [1].

order	*Welding method*
1	Gas Tungsten Arc Welding (GTAW)
2	Gas Metal Arc Welding (GMAW)
3	Manual Metal Arc (MMA)
4	Electron Beam Welding (EBW)
5	Friction Welding (FW)
6	Laser Welding (LW)

The filler material selection should be done with respect to the following rules [1], [33]. The composition of the parent and the weld metal should be matched as closely as possible. The aluminium and the nickel contents should follow the relations, Al<8.2+Ni/2 and Ni>Fe+0.5 to prevent the formation of brittle phases. According to Weill-Couly [1] the aluminium percentage should be between 9.4 wt% and

9.8 wt% for optimum mechanical properties. The initial pass in large welds must be carried out by the ductile Cu6100 filler, followed by a capping pass with one of the following filler metals, Cu 6325, Cu 6327, and Cu 6328. In case of CMA alloys, the filler Cu3668 should be applied [1].

Concerning the additive manufacturing, the aluminium bronze fillers are already used for repairing of castings. In general, the same recommendations as in the case of welding may be applied [1], [4]. It should be highlighted, that matching fillers are of high importance and pre-heat together with inter-run temperatures should be below 200 °C [1], [4]. Obviously, the final bead geometry must be over-sized to allow for machining to the exact desired geometry.

The preheating procedure is not necessary for the welding of NAB or CMA alloys, unless the substrate is a high conductivity metal. A preheat at a temperature of 120 °C is used to eliminate the moisture but the temperature should be kept below 400 °C to avoid the embrittlement of the alloy.

3.3.2 MICROSTRUCTURAL OBSERVATIONS IN NAB ALLOYS PRODUCED BY WAAM

Additive manufacturing of aluminium bronzes has started to be investigated in recent years by many researchers, paying special attention to the NAB alloys. This paragraph summarizes the most significant microstructural results of these studies. Li et al. [4] investigated welding of a NAB alloy of 8.8 wt% aluminium, 5.2 wt% nickel and 4.4 wt% iron with a matching filler. In the parent metal, the continuous nature of the κ_3 phase promotes a large proportion of closely adjacent cathodic and anodic regions, resulting in the formation of micro-galvanic cells. Concerning the HAZ, the width is less than 1 mm for the different heat inputs and a transformation of eutectic structure to martensitic occurred in the areas adjacent to the fusion line [2]. If the peak temperature in the HAZ exceeded the eutectic point, β phase was formed. Fuller [6] remarks that there is a distinct region of low ductility in the HAZ of the weld, where fracture may initiate at the β phase or at the κ particles. The different temperature gradient with respect to the distance to the fusion line resulted in areas of a partially transformed eutectic structure. Finally, concerning the weld metal, a fine and uniform microstructure with Widmanstätten α phase and various non-equilibrium transformation products of β is reported. [6].

Special attention should be given to the work of Ding [2], who investigated the tensile strength of NAB alloys produced by WAAM method. In more detail, he used a GMAW and a synergic pulse spray transfer mode with argon as a shielding gas. The base metal has a cast structure according to the Australian Defence Standard NES 747 specifications and the wire is the ALUNOX AX-CuAl8Ni6 with 1.2 mm diameter. Moreover, he studied three different welding set ups, presented in Table 7, and all his specimens had a heat treatment at 675 °C for 6 hours. The tensile specimens were manufactured from different regions of the 3D printed walls by a 2 mm wire saw, as the Figure 25 illustrates. The mechanical testing results are presented in chapter 8 for comparison with the results of the present study. The microstructural results of the report depict the banded nature of the weld metal microstructure, with band thickness of 200 μm and the final height of each weld bead after the deposition of the subsequent layer is at the order of 2 mm. Specifically, the weld metal contains Widmanstätten α phase and very fine martensite. In addition, the HAZ characteristics are in complete agreement with the ones mentioned in the previous paragraph and the base metal microstructure resembles the as cast morphology which has already been analysed. Finally, an X-ray diffraction (XRD) analysis was conducted in the cross-section of the component for the phase structure identification. The diffraction patterns showed an abundance of α phase and a certain amount of NiAl or Fe_3Al precipitates. The volume fraction of precipitates decreased significantly in the weld metal due to the suppression of the eutectoid reaction $\beta \rightarrow \alpha+\kappa_3$ by the rapid

cooling rate. The banded morphology is mentioned also in the work of Hazelhuhn [16], together with the fact that the layers do not perfectly coincide with each deposited layer, thus there is a slight curvature to the banded regions at the specimen edges, presumably due to a faster cooling rate.

Table 7: Welding parameters of the different test conducted by Ding [2].

Test No.	*Wire Feed Rate (m/min)*	*Travel Speed (mm/min)*	*Average Current (A)*	*Average Voltage (V)*	*Heat Input (J/mm)*
1	5.4	400	175.5	24.8	653
2	6.7	400	218.3	26.7	874
3	8	400	256.1	29.0	1114

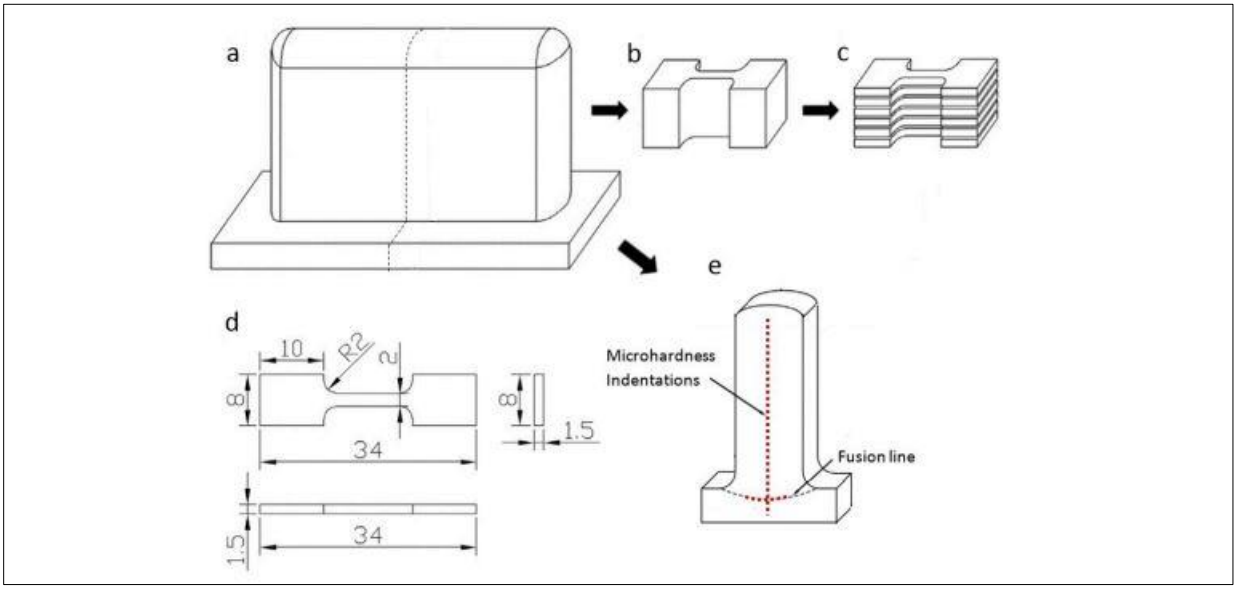

Figure 25: (a) Wall structure and middle cutting trajectory; (b) Tensile sample machined from the wall; (c) Tensile specimens after slicing machined tensile sample; (d) Dimensions of tensile specimens in mm; (e) Wire-cut cross-section [2].

3.4 POST WELD HEAT TREATMENT (PWHT)

3.4.1 STRESS RELIEVING

Stress-relief annealing of the CMA alloys involves heating to 500 °C to 550 °C for two hours [21], while for the NAB alloys the temperature should be kept between 300 °C to 350 °C for at least one hour [1]. Meigh in his work mentions even higher temperatures for the stress relief of NAB alloy, ranging from 400 °C to 600 °C [21]. In addition, stress-relief enhances the stress corrosion cracking (SCC) resistance in NAB alloys according to Richardson [1], but has no effect on mechanical properties of either the NAB or CMA alloys.

3.4.2 QUENCHING AND TEMPERING AFTER HOT WORKING

This method is among the most frequently used heat treatments to control the mechanical properties of the aluminium bronzes. It involves quenching from a high temperature and subsequent tempering at moderate temperature. Quenching from elevated temperatures increases the hardness, while the high tempering temperature has an adverse effect. Moreover, the extended tempering time decreases the hardness and improves the ductility. Both NAB and CMA alloys may be quenched from a temperature in the order of 900 °C and subsequently be tempered in a temperature region of 550 °C. In more detail, Richardson [1] recommends, full anneal of the NAB and CMA alloys at 650 °C to 750 °C for 6 hours at a rate of 100 °C/hour and subsequent air cooling. The same author highlights also that the UK Navy standardized a procedure of 675 °C for NAB alloys for 6 hours, which is a heat treatment adopted by Li et at. [4] and Ding et al. [2]. Li and Ding report, that the parent metal remains unaffected because of the stable casting structure, but the HAZ and weld bead, where martensite was present, is refined. More specifically, in the HAZ the large sections of α phase could still be observed, while closer to the fusion line the α phase appeared partially decomposed. The retained β phase was replaced with a fine grain α phase and κ precipitates. The weld bead, which consisted primarily of Widmanstätten α and small amount of β', after PWHT, had a fine, homogenized microstructure of α phase and κ precipitates. In general, the refining that occurred in both the HAZ and the weld metal due to PWHT is favourable from both mechanical and corrosion point of view.

3.4.3 ANNEALING OF LARGE PROPELLERS

In the case of icebreaker propellers, which are used to plough up the ice, allowing the ship to proceed, the deterioration of impact toughness may be detrimental. The most effective heat treatment, concerning the enhancement of impact toughness, is annealing at 720 °C for 7 hours and subsequent cooling at 55 °C/hour, according to Meigh [21]. This heat treatment increases the Charpy test's result by a factor of 2 to 3. Alternatively, in order to avoid distortion at high temperatures, the recommended annealing process is at 720 °C for 24 hours, followed by quenching.

3.5 CORROSION SUSCEPTIBILITY

Corrosion of metals takes place when positively charged ions are created and discharged into a corrosive liquid or a moist atmosphere. The corrosion rate is affected by the electrical potential difference between the metal and the corrosive medium. Any substance has a unique electrode potential value relative to a medium. The galvanic series are lists containing this information, illustrating the electro-potential of different metals in a specific environment, in millivolts relative to a reference electrode. Apparently, most metals show a great range of values in sea water, depending on the environmental conditions, like temperature, aeration, turbulences, pH values and biofouling.

Aluminium bronzes present remarkable resistance to corrosion [21], [34], attributed to three factors: the formation of a stable oxide film, the restriction of corrosion prone phases, and the discontinuity of the corrodible phases, in case these phases are unavoidable.

3.5.1 PASSIVITY

The oxide film has good adhesion properties, is relatively impermeable to most liquid corrodents and may reform in case of its disruption. The damage of the film may be caused by an impact of an object of higher hardness, by internal stresses or by chemical attack. Furthermore, the oxide is abrasion resistant, because of the high hardness of alumina, the main constituent of the oxide film. Concerning the chemical composition, the film contains both aluminium oxide (Al_2O_3) and copper oxide (Cu_2O) [21]. The area close to the parent metal is aluminium-rich, while the surface is rich in copper oxides, such as copper hydroxide $Cu(OH)_2$. Initially, aluminium will oxidise preferentially in the oxide-free surface, but subsequently it will hinder the diffusion of aluminium from the bulk, leaving copper to oxidise preferentially on the surface of the corrosion product. In addition, the presence of copper oxide prevents the deposition of marine organisms on the surface and thus eliminates biofouling [1]. Oxides of iron, nickel and magnesium and traces of copper salts and copper hydro-chlorides have been also observed at the surface. The higher the nickel and the iron percentages of the film, the more protective it is. Correspondingly, the higher the aluminium content, the greater the protectiveness of the oxide film. However, any increase of aluminium beyond 6 wt% has no significant result [21].

3.5.2 SELECTIVE PHASE ATTACK (SPA)

If anodic and cathodic areas are electrically connected in the presence of an electrolyte, then a galvanic couple occurs. This configuration may be formed by dissimilar metals in contact or when adjacent phases in a metallic component have a great difference in electro-potential. The second case is of major interest for the NAB and CMA components, investigated in this thesis. An electrolytic cell is created, meaning that positively charged ions flow through the electrolyte from the anode to the cathode and a corresponding stream of electrons passes directly from the anode to the cathode via the metal connection. As a result, the anodic area corrodes. Unfortunately, it is not predetermined which phase is the anode and which the cathode, due to the effect of the environment on the galvanic series. In case of sea water, the electrolyte contains salts, such as sodium chloride, which are anodic to the metal anode. Thus, these salts will remain unaffected and the ions from the anode will displace hydrogen from the water, which will be collected on the surface of the cathode.

In the case of aluminium bronze alloys, the (anodic) aluminium ions are attracted to the cathode, whereas the (cathodic) copper ions redeposit at the anodic corroded phase. This procedure is referred in the literature as selective phase attack or de-alloying or de-aluminification [21]. The re-deposited copper is characterized by a weak and porous honeycomb structure. The appearance of the aluminium bronze components is essentially unchanged, except for a slight discoloration. Aluminium is not the only alloying element which is reduced by selective phase attack, thus the term de-aluminification must be used with caution. However, this is a galvanic effect and the reduction of oxygen at the copper cathode takes place. Thus, the redeposition is happening due to dissolution of aluminium around the copper rich phase. As a result, the Cu-particles can detach from the material and become oxidized due to their contact with the environment. Subsequently they may deposit again on the surface.

The cast structure of WAAM produced components indicates that the alloy solidifies as a mass of crystals which are strongly held together by the last solidified film of metal. The different phases of such

a structure vary in composition due to the difference in melting point of the elements, and thus, have different electrochemical potentials. Consequently, there is always a tendency for the most anodic phase to corrode preferentially. In the single phase aluminium bronzes, the last metal to solidify, forming a boundary around the crystals is richer in aluminium because of its lower melting point. Thus, the grain boundaries are anodic to the adjoining crystal and are therefore prone to corrode. The extent of corrosion depends upon how great the potential difference is between the anode and the cathode, and upon their respective exposed surface areas. In case the cathode is large relative to the anode, the latter will corrode severely. Moreover, if the anode is fragmented, the effect of corrosion may be negligible, whereas a continuous form may deteriorate the integrity of the structure.

In the NAB alloys, the most corrosion susceptible phase is the aluminium-rich γ_2 phase. Subsequently, the less aluminium-rich but still prone to corrode is the β' phase. Furthermore, the eutectoid $\alpha+\kappa_3$ is less corrodible than the aforementioned phases, but still gives rise to selective phase attack. This phenomenon is evident especially in the heat affected zone of welds and in the case of crevice corrosion. For good corrosion resistance, the formation of these phases should be avoided by careful choice of the composition of the alloy and by controlling the cooling rate. The γ_2 phase can normally be avoided by keeping the composition percentages within a certain range and the κ_3 phase can be reduced or fragmentized by heat treatments. The detrimental effect of SPA is presented in the work of Hazra, who investigated the failure of a NAB pump impeller [26]. The CMA alloys, consist essentially of two phases, namely α and β, where the β phase is more prone to corrode. It has to be highlighted that the phenomenon is limited under free exposure and rapidly flowing water conditions, which are encountered in marine propellers. However, severe selective phase corrosion of the β phase is observed in static sea water environment. The susceptibility of CMA alloys to selective phase dealloying corrosion is greater than NAB alloys.

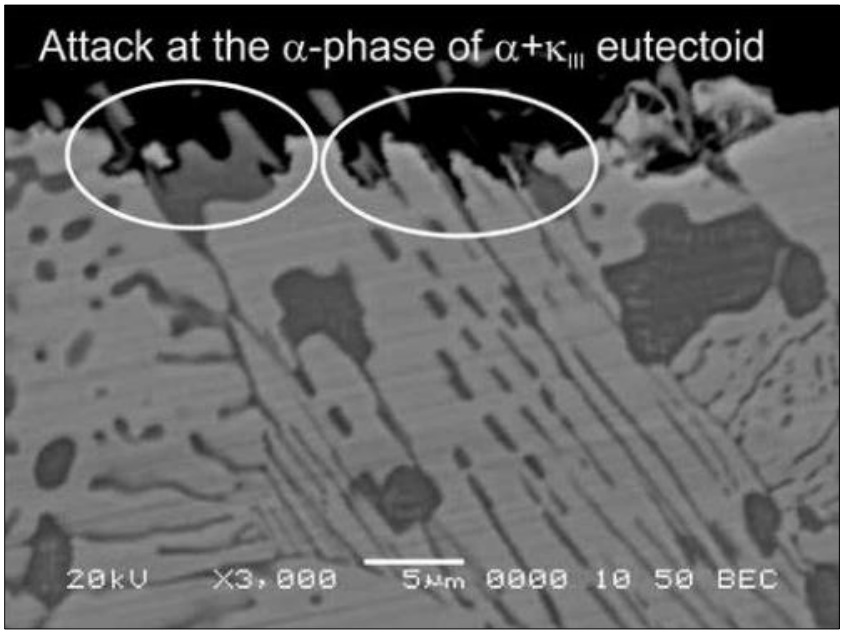

Figure 26: Microstructure showing the low rate corrosion of the copper-rich a phase within the α+κ3 eutectoid [1].

3.5.3 METALLOGRAPHIC OBSERVATIONS IN NAB AND CMA ALLOYS IN SEA WATER ENVIRONMENT

The corroded NAB alloys facilitate dark etched martensitic β areas in their microstructure when they are exposed to sea water. The eutectoid regions are also prone to corrosion while the κ_2 particles show no significant attack. More specifically, the α constituent of the eutectoid phase is anodic to the κ_3 phase and thus is preferentially attacked. However, the α grains are less attacked due to absence of large cathodic counterparts. Rowlands and Brown [30] reported that the lamellar κ_3 precipitates are cathodic to α under aerated sea water conditions, while the situation holds vice versa for crevice conditions. A crevice is formed in close-fitting areas between metallic or non-metallic components. The absence of aeration allows for alternation on the pH values during the corrosion process within the restricted areas and may accelerate the dissolution of the more electronegative phases [34]. Weston claims that κ_3 phase may have a wide range of compositions which affects the possibility of being anodic or cathodic to α phase [34]. Furthermore, Nakhaie indicated the anodic character of κ phases mapping the Volta potential relative to the copper rich α phase. Volta potential represents the difference in potential between a point close to the surface of the metal under investigation and a point close to the surface of a second metal. According to his study, the κ_1 precipitates have the most negative Volta potential among all the κ intermetallics [8].

Concerning the CMA alloys, the β grains are the ones more susceptible to corrosion, along with the large dendritic and the cuboid particles in the α phase. Both types of particles are anodic to α phase. On the contrary, the small dendritic particles evident in the β phase remain intact, because they are cathodic to the surrounding matrix.

3.5.4 CORROSION OF WELD REPAIRS

In the case of welding, the HAZ is the most problematic area in terms of corrosion. The metal in this region is subjected to a thermal cycle able to dissolve the κ particles and form a martensitic phase upon rapid cooling, in the case of NAB alloys. These β’ regions are preferentially attacked by corrosion, especially in case the κ particles are partially dissolved, causing greater difference in size between the cathodic and the anodic areas. [34]

Weston observed initiation of the corrosion in the HAZ in a zone 1-3 mm from the fusion line and a subsequent propagation as a wedge into the parent metal. He also reports cases in which the corrosion propagates as a very narrow continuous or semi-continuous, 1-2 mm wide band in the parent metal, adjacent to the HAZ boundary. [25]

3.5.5 EFFECT OF HEAT-TREATMENT ON CORROSION RESISTANCE

Heat-treated NAB alloys, at either 775 °C for 6 hours or 830 °C for 2 hours, present significantly enhanced HAZ corrosion resistance in a sea water environment. The higher temperature heat-treatments fragmentise the lamellar phase, restricting any selective phase corrosion. However, this advantage can be compensated by the retention of the high temperature β phase, forming β’ phase. This phenomenon is more evident in the thinner sections of casting or welds, where cooling rates are higher, deteriorating the corrosion resistance. A lower tempering temperature of 675 ±15 °C combines all the desired microstructural features and the sufficient corrosion resistance, avoiding the risk of martensite formation. Nevertheless, these properties are achieved at the expense of the Charpy impact toughness and of the ductility, due to formation of the finer particle precipitation within the α phase. This can be overcome by heating at a slightly higher temperature of 710 °C for a similar time or by holding for longer periods (16 hours) at the conventional temperature (675 °C) [25].

4. EXPERIMENTAL PROCEDURES

4.1 CONSTRUCTION OF THE SPECIMENS

The core of the thesis is the investigation of the influence of the deposition parameters (wire feed rate, welding speed, and heat treatment) on the mechanical and corrosion properties of the material. To avoid the influence of the complexity of the geometry, rectangular blocks with different welding parameters have been constructed, consisting of overlapping sequential bead deposition. The facilities of Delft University of Technology (TU Delft) were used to produce single bead overlaps, see Figure 27 (left), whereas a bigger block with overlapping beads, in both vertical and horizontal direction, was constructed at the facilities of RAMLAB, see Figure 27 (right). The composition of the substrate and the filler material is evident in Table 8. The filler wire has 1 mm diameter, and the substrate has a thickness of 12 mm.

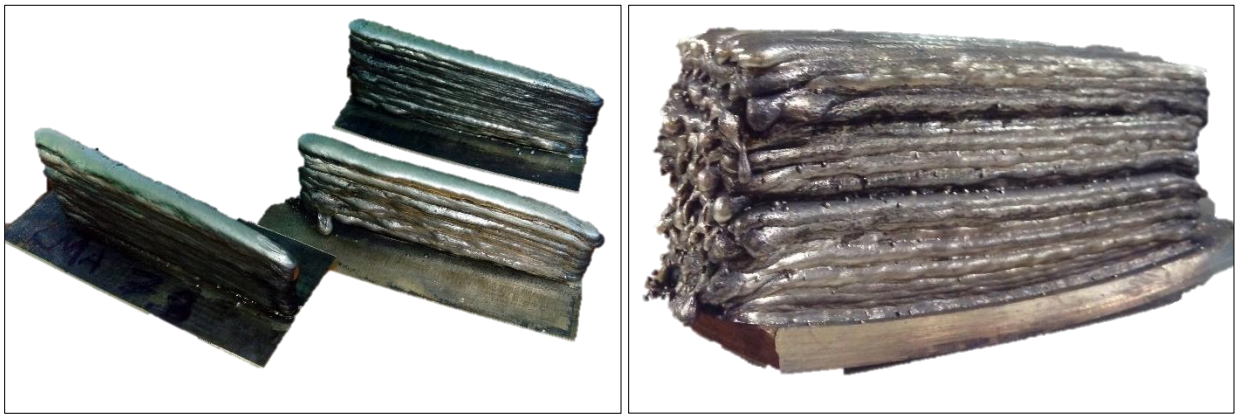

Figure 27: (left) The three blocks constructed at the facilities of TU Delft. (right) The block constructed at RAMLAB.

Table 8: Chemical composition (in wt%) of the substrate and the filler material based on XRF (X-ray Fluorescence Spectrometer) analysis.

	Cu	*Al*	*Ni*	*Fe*	*Mn*	*Cl*	*Si*	*Zn*	*P*	*K*	*S*
Substrate	79.72	9.07	4.87	4.82	1.17	0.10	0.08	0.07	0.02	0.02	0.01
Filler	73.66	6.68	2.40	2.64	11.09	0.20	0.26	2.97	0.02	0.03	0.02

4.1.1 SPECIMENS MADE AT TU DELFT

The 3D printing equipment at TU Delft consists of a GMAW torch, attached to x, y, z axis electrical motor actuators. The motors are computer controlled and the arc ignition by the controller of the welding machine (Fronius). The GMAW welding machine uses a pulsed synergic mode to decrease the heat input induced in the process. For the monitoring of the interpass temperature, which should be kept below 200 °C [21], [1], two type-K thermocouples were applied at the substrate and the arc ignition point. The experimental installation is presented in Figure 30 (right).

Three blocks (A, B, C) were deposited and cut in two equal parts. One part was investigated in as-deposited state, while the other half was subjected to a PWHT of 675 °C for 6 hours (Nabertherm). The heating rate was 100 °C/hour and was followed by air cooling. The filler material is the CMA alloy, whereas the substrate consists of the NAB alloy. The process parameters for every half-block are summarized in Table 9.

Table 9: Specifications of the block produced within the facilities of TU Delft and RAMLAB.

block	*feed rate (m/min)*	*travel speed (mm/sec)*	*PWHT*	*heat input[5] (J/mm)*	*length/width/height (mm)*	*number of beads*
A1	7.8	6.7	as-deposited	312	52 / 8 / 52	34
B1	9.6	6.7	as-deposited	351	59 / 8 / 52	34
C1	11.5	6.7	as-deposited	542	62 / 9.5 / 54	34
A2	7.8	6.7	675°C 6 h	312	53 / 8 / 44	34
B2	9.6	6.7	675°C 6 h	351	55 / 8 / 44	34
C2	11.5	6.7	675°C 6 h	542	57 / 9.5 / 47	34
RAMLAB	9.3	7.0	as-deposited	500	183/39.5/83.6	235

Subsequently, out of every half-block two thin cross-sections (thickness: 5 mm) were cut, one for microstructural investigation and one for corrosion testing, using a disco-tome and a micro-tome (Struers). The remaining material of every sub-block was then processed by electrical discharge machining (EDM) to produce sub-sized tensile specimens in longitudinal and vertical directions (workshop: Noukaris, Greece). The process steps of these specimens are illustrated in Figure 28.

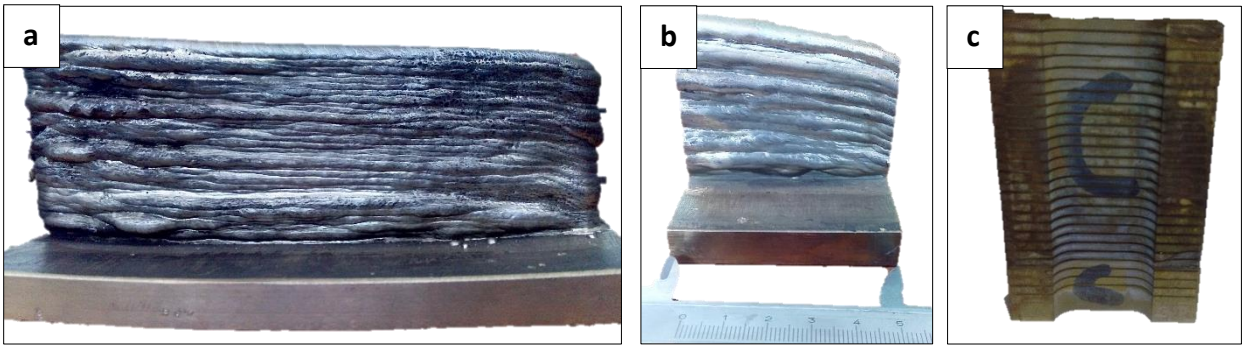

Figure 28: Pictures of the manufacturing process showing the location of the tensile specimens extracted from the blocks manufactured at TU Delft. (a) The as deposited 3D printed block. (b) The block is cut in two identical parts, one would be examined with no further process and one after the application of heat treatment. (c) Example of the block as received from the EDM workshop.

4.1.2 SPECIMENS MADE AT RAMLAB

RAMLAB 3D printer includes a Valk welding system integrated on a Panasonic welding robotic arm (Ya-series TM1400), and a welding table equipped with a cooling system, see Figure 30 (left). The welding parameters were programmed with a Panasonic robot control software, named as Desktop Programming and Simulation System (DTPS). A wavy travelling motion of the torch was chosen to increase the bead

[5] Heat input (h): $h = \frac{\eta V I}{u}$ [J/m], where η: efficiency of the welding machine, V: potential difference (V), I: current (A), u: travel speed (m/sec), see [46]. The average voltage and current value obtained from the welding machine were used for the calculations of the heat input.

width. Furthermore, the active wire mode decreased spattering. This feature controls the feeding rate of the filler, as schematically presented in Figure 29. After the ignition of the arc, the power drops and the filler approach the welding surface. Then, the filler drum rotates in the opposite direction to prevent a collision between the filler and the substrate. As the filler tip departs from the interface, the arc ignites again and the process repeats. Finally, the step-over distance of subsequent beads was chosen to be equal to $d = \frac{4.8}{7} = 0.685$, a value which is very close to the theoretical recommendation to achieve a flat top surface of the deposition, according to the literature [11].

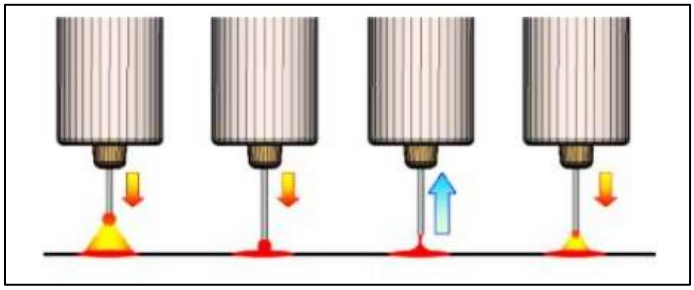

Figure 29: Schematic of the active wire mode. [35]

Figure 30: 3D printing equipment for the application of the WAAM method in RAMLAB (left) and in TU Delft (right).

The specimen produced with the above-mentioned procedure results in a block consisting of 235 welding beads, illustrated in Figure 31, with the welding parameters of Table 9. Every subsequent bead started at the opposite direction with respect to the previous one, minimizing the temperature inhomogeneity during the process. The block was machined afterwards with milling and lathing to produce subsized cylindrical tensile specimens and standard Charpy V-notched specimens. Moreover, a 5 mm thick cross-section of the block was kept intact for microstructural investigation purposes.

Figure 31: Pictures of the manufacturing process of the block produced at RAMLAB. (a) The as deposited block. (b) The block during milling. (c) The block after milling, ready for further machining, in order to produce tensile and Charpy specimens.

4.2 MICROSTRUCTURAL CHARACTERIZATION

4.2.1 SAMPLE PREPARATION

To reveal the microstructure of a specimen by means of optical microscopy, the sample must be mounted, ground, polished and etched. At first, the samples produced within TU Delft were investigated. The six cross-sections (from blocks A1, …, C2) were cut into two pieces, obtained from the bottom and the top part of the building height. In addition, the bottom part contained also the substrate material, Figure 32. In a similar way, the samples from the cross section of the block produced in RAMLAB were prepared. One sample was extracted from the first deposited layer, one from the middle section and one from the top layers. All samples are mounted using a phenolic hot mounting conductive resin (Polyfast).

Figure 32: Mounted specimens with conductive phenolic resin, ready for observation in optical microscope and scanning electron microscopy (SEM). (left) Block A1, (middle) Block B1, (right) Block C1.

The second stage includes grinding. Mounted specimens were ground with rotating discs of SiC paper, flushed with water as coolant to remove debris and dissipate the heat. The grinding procedure involves several stages, using a finer paper for each successive stage. Each grinding stage removes the scratches from the previous coarser paper. The following grinding sequence was followed: 180, 320, 800, 1200, 2000 and 4000 grit, according to FEPA P.

After grinding, the samples were polished. Before and after each polishing step, the sample was cleaned ultrasonically. The polishing was done using 3 µm and 1 µm polishing diamond paste on a rotating polishing cloth (Struers, type Mol for 3 µm and type Nap for 1 µm paste).

Etching is the last step of the preparation of the samples. This step is essential to reveal certain microstructural features, such as grain boundaries. During this process, the sample surface is immersed in an acidic solution for a certain time. The different phases and the grain boundaries exhibit different corrosion products, making them easily distinguishable. Initially, a solution of 5% $FeCl_3$ + 25% HCl + 70% distilled water was used, which was previously tested in the literature [2]. However, this solution

appeared to be strong and it was decided to use it in a diluted version, consisting of 25% of the above solution and 75% of distilled water.

4.2.2 OPTICAL MICROSCOPY (OM) AND SCANNING ELECTRON MICROSCOPY (SEM)

The microstructure was observed in a VHX-5000 KEYENCE optical microscope. The magnification used ranges from 50 to 2500 times. The smallest magnification assists in the macroscopic observation of the banded structure of the cross section, whereas the highest magnification allows for phases, precipitates and grain boundary recognition.

The scanning electron microscope (SEM) uses an electron beam to scan the sample surface and generate the image. The incident electrons (primary beam) interact with the atoms of the sample, generating electrons (detected beam) due to elastic and inelastic collision. The detected beam is characterized by the nature of the electrons contained. Usually, secondary, backscattered and Auger (only in UHV) electrons are analysed. These electrons come from different depths inside the material, as Figure 33 depicts. The secondary electrons result from inelastic collisions, happening near the surface. Thus, as part of the energy is lost during collision, they exhibit a lower energy than the primary beam or the backscattered electrons. The latter ones emerge due to the elastic collision of the primary beam with the atoms at greater depth inside the material than the secondary electrons. For this reason, their recorded energy is comparable with the energy of the primary beam. The energy differences are indicated also in Figure 33.

It can be easily concluded that the secondary electrons are usually used for high quality imaging of the surface of the sample, while the backscattered ones are mainly used during EDX (Energy-dispersive X-ray spectroscopy), chemical composition analysis. Finally, the Auger electrons provide information from only an extremely small depth of the surface and are rarely used in fractography. The SEM equipment used in this project is a JEOL JSM-IT 100. Furthermore, observation parameters, like the working distance and the magnifications, are illustrated as label at each SEM image.

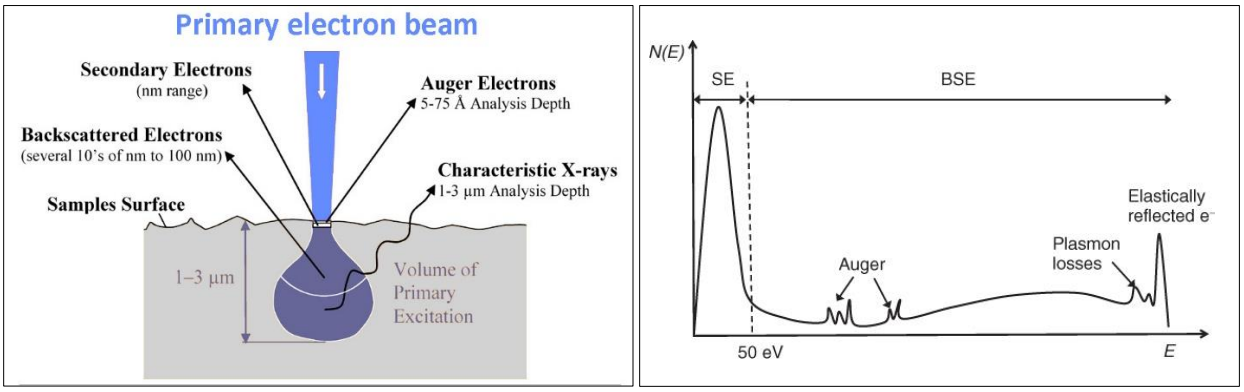

Figure 33: (left) Schematic showing the depth out of which each category of electrons emerges [36]. *(right) Qualitative graph representing the difference in energy and intensity between the detected electrons. SE: Secondary Electrons, BSE: Backscattered Electrons* [37].

4.3 MECHANICAL TESTING

4.3.1 HARDNESS

The Vickers hardness was obtained by a Struers DuraScan hardness test equipment, using a square based pyramidal diamond indenter. The angle of this indenter is 136°, which gives an angle of 22° with the horizontal, as shown in Figure 34.

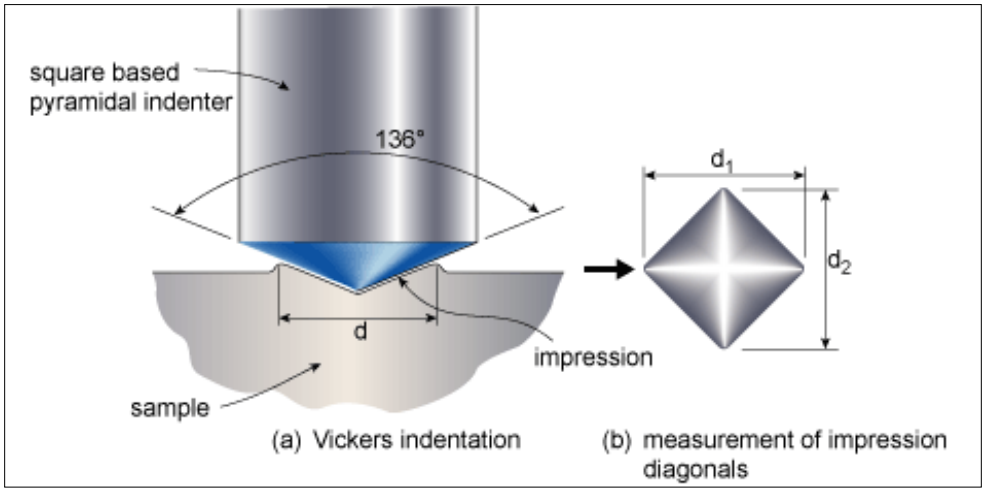

Figure 34: Schematic of the (a) indenter and (b) indentation shape of the Vickers hardness machine. [38]

The area of the indentation determines the hardness, which is equal to the force applied divided by the area of the indentation. This area can be calculated as follows:

$$A = \frac{d^2}{2\sin\frac{136°}{2}}$$

, where d is the average diagonal length, $d = (d_1 + d_2)/2$.

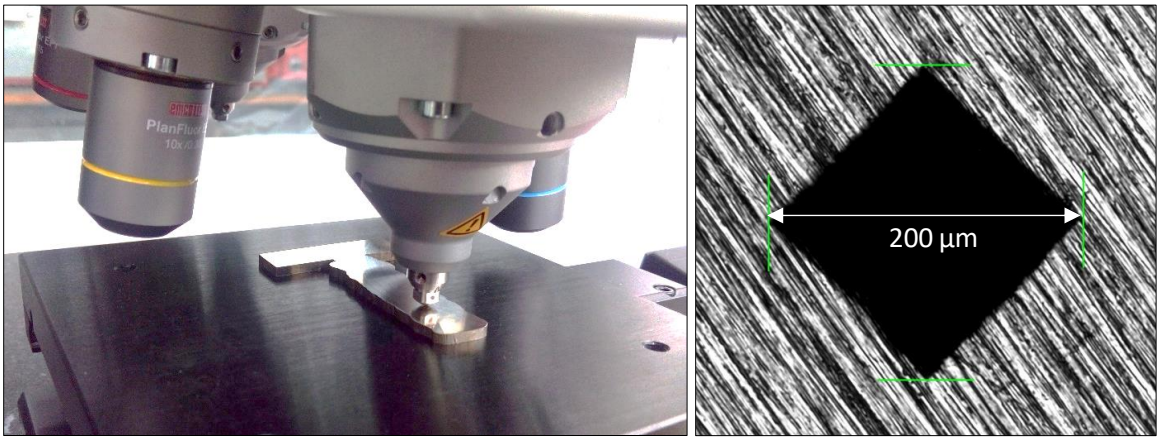

Figure 35: (left) Hardness testing process in one of the specimens obtained from the block produced at TU Delft. (right) Representative measurement showing the indentation.

The corresponding units of HV are kilograms-force per square millimetre (kg-f/mm²). In our case, 5 kg of force were used, resulting in an indentation with a diameter in the order of 200 µm, Figure 35.

The measurements were taking from both the TU Delft and RAMLAB samples. A series of hardness measurements were executed in a predefined path, obtaining 351 hardness values from the cross section of the block constructed at RAMLAB and 20 measurements along the deposition height from each block built at TU Delft, Figure 35 (left).

4.3.2 TENSILE TEST

Two categories of tensile specimens were considered in this study. The first category incorporates the specimens obtained from the blocks produced at TU Delft. These specimens are plate-like and 1.5 mm thick. Unfortunately, the small dimensions of the blocks did not allow us to follow international standards. Nevertheless, the geometry of the specimens has been chosen based on the general outlines of the standard [39], which imply that the gage length should be at least four times the width of the specimen. The specimens are oriented vertically and horizontally to the building direction. In this way, the effect of every layer can be examined together with the difference between the strength in the depositing and building direction, see Figure 38. In Figure 37 the design of the specimens is evident as well.

A tensile testing machine (INSTRON 5500R 4505) was used, where the software controls the movement of the head and records the data of the applied force and the resulted extension. The tensile speed is 0.5 mm/min and the extensiometer used is evident in Figure 36 (left).

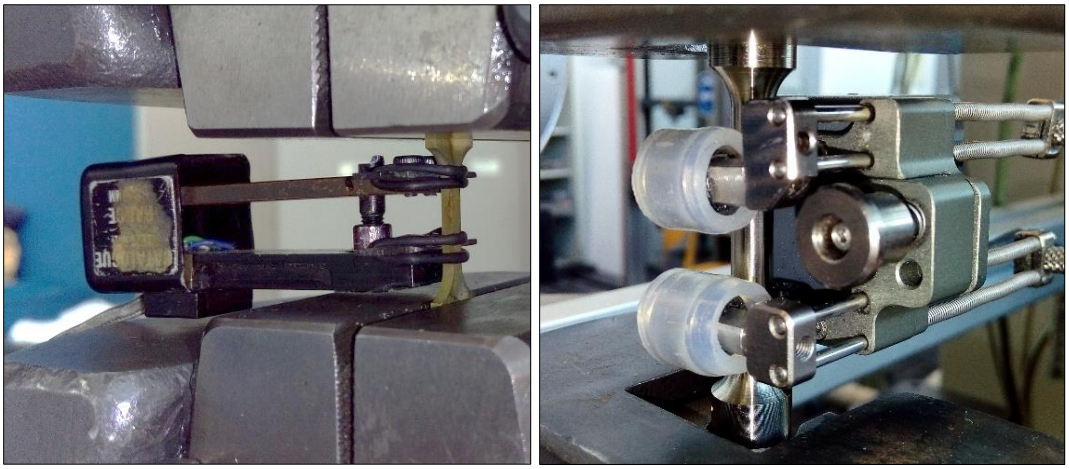

Figure 36: Extensiometer used during tensile testing of the specimens from the block produced at (left) TU Deft, (right) RAMLAB.

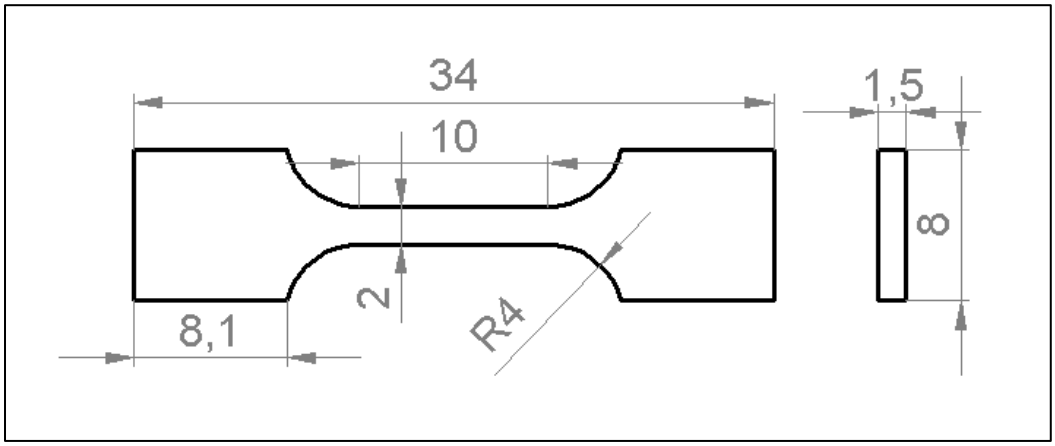

Figure 37: Design of the tensile specimens extracted from the block produced at TU Delft.

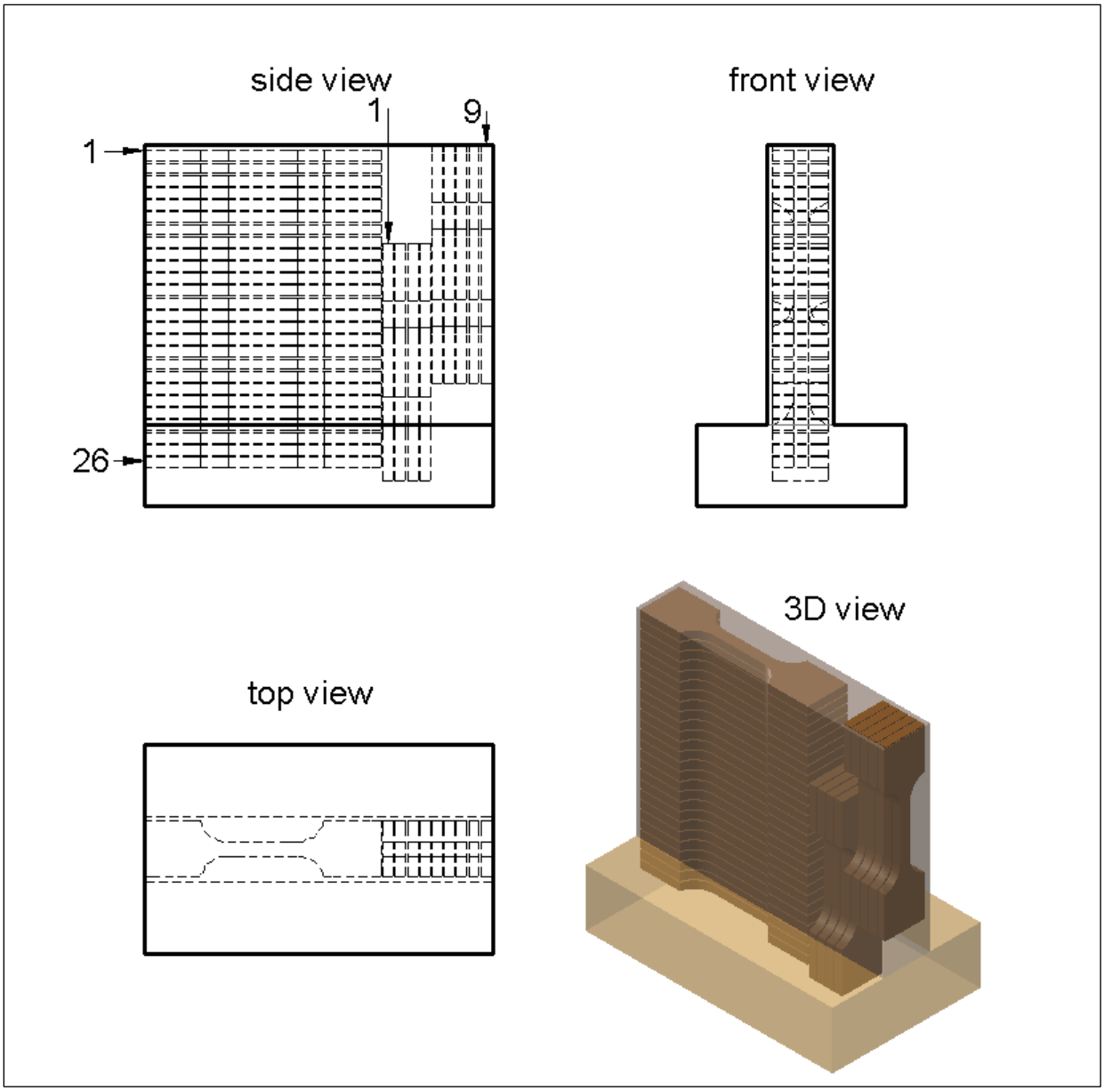

Figure 38: Graphical representation showing the location and the numbering of the tensile specimens extracted from the blocks manufactured at TU Delft.

The tensile specimens obtained from the block produced at RAMLAB are designed according to the ASTM E 8/E 8M – 08 standards [39]. Specifically, the dimensions are subjected to the small-sized category 3, round tension test specimens. The design is illustrated in Figure 39 (right). These specimens are oriented in both vertical and horizontal directions as well as Figure 39 and Figure 40 depict.

The tensile testing equipment (Zwick Z100) used for the testing of these specimens is also an electrical one. The tensile speed was set at 2.5 mm/min and the extensiometer used is presented in Figure 36 (right).

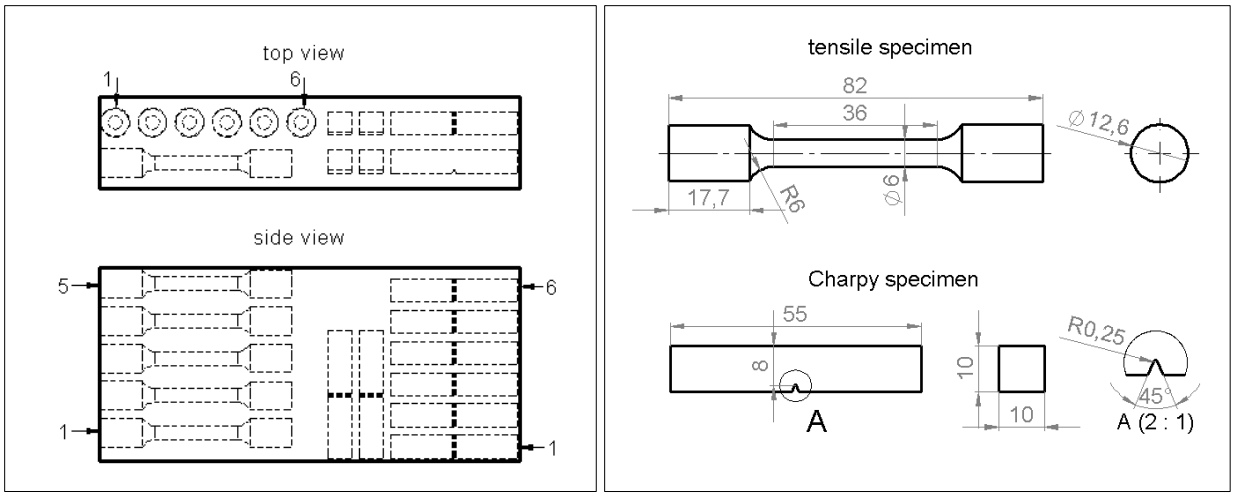

Figure 39: (left) Graphical representation showing the location and the numbering of the tensile and Charpy specimens inside the block produced at RAMLAB. (right) Design of the tensile specimens (upper part) and of the Charpy specimens (bottom part) in mm.

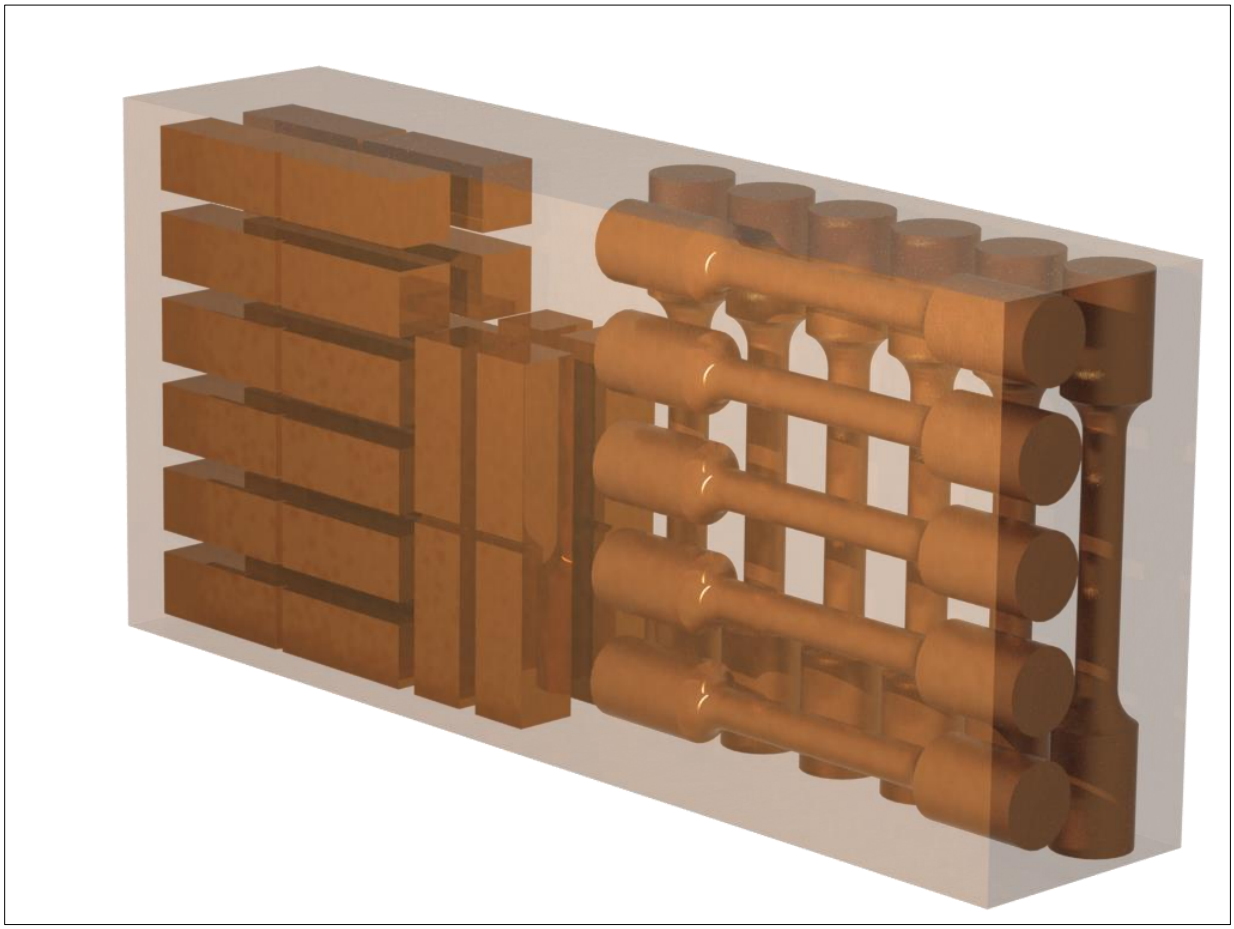

Figure 40: 3D representation of the design of the tensile and Charpy specimens inside the block produced at RAMLAB.

4.3.3 INSTRUMENTED CHARPY TEST

The instrumented Charpy test incorporates a strain-gage at the striker of the pendulum. This setup allows for recording the force at specific time intervals. Useful results which may be derived, include the general yield and the ultimate stress, the initiation and the arrest of an unstable fracture, and the test termination moment [40]. The testing machine is a MTS EXCEED Model E22 with a pendulum of 450 J, complying with the standards GB/T 229. More specific, the mass of the pendulum is 32.85 kg and the impact velocity is 5.234 m/s.

The Charpy specimens are machined out of the block produced at RAMLAB by conventional milling, and their geometry follows the ASTM E 23 – 07a standards, see Figure 39 (right). The orientation of the specimen lays also in the vertical and the horizontal direction, Figure 39 (left) and Figure 40. From the horizontal direction two kinds of specimens were obtained. The first category involves six specimens with their notch facing upwards, whereas in the second category the notch is facing sideways. The vertical specimens were used to examine the response of the material in three different temperatures, namely ambient temperature, -20 °C, and -60 °C. For the low temperature measurements, the specimens were submerged in liquid nitrogen until the desired temperature was reached. The temperature was measured by a thermocouple, which was placed between the sample and the grip.

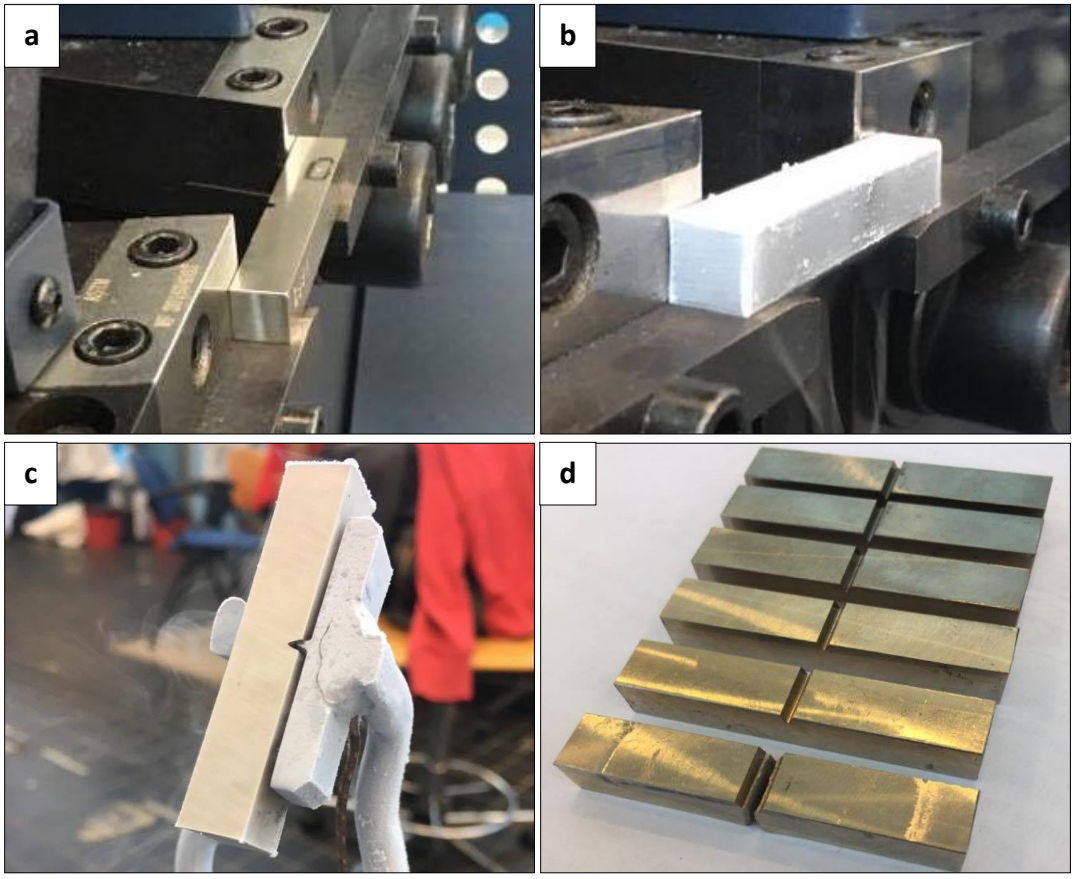

Figure 41: (a) Charpy specimen, placed between the anvils. (b) Charpy specimen at -60 °C, ready for testing. (c) Charpy specimen, after the immersion in liquid nitrogen. (d) The six horizontal Charpy specimens, with their notch facing sideways.

4.4 CORROSION TESTING

4.4.1 OPEN CIRCUIT POTENTIAL (OCP) AND POLARIZATION CURVES

Open circuit potential (OCP) refers to the electrical potential difference that exists between a working and a reference electrode, in the presence of an electrolyte. The V_{OCP} indicates the tendency of a metal to dissolve in a particular corrosive environment. On the contrary, the polarization experiments force the sample to behave as a cathode and subsequently as an anode, giving information on the corrosion rate. Performing the Tafel approximation at the results, which is explained in chapter 7, the corrosion current (i_{corr}) and the corrosion potential (E_{corr}) can be calculated. The corrosion rate increases with i_{corr}, while corrosion susceptibility increases with the drop of E_{corr}.

The OCP tests together with the polarization experiments were performed in six different areas of the cross-section of the deposited walls (4 in the deposited material, 1 in the interface and 1 in the substrate), see Figure 42 (left). These areas were selected in such a way that the whole building height was covered along with the substrate, and the interface between the substrate and the filler material. For reproducibility reasons, the same tests were performed at both sides of the cross sections. The immersion test took place in a galvanic cell, where the applied voltage to the aqueous solution was controllable. The cell consisted of a graphite counter electrode, a $Ag/AgCl_2$ reference electrode, an electrolyte solution, and the sample (reference electrode 2), see Figure 42 (right).

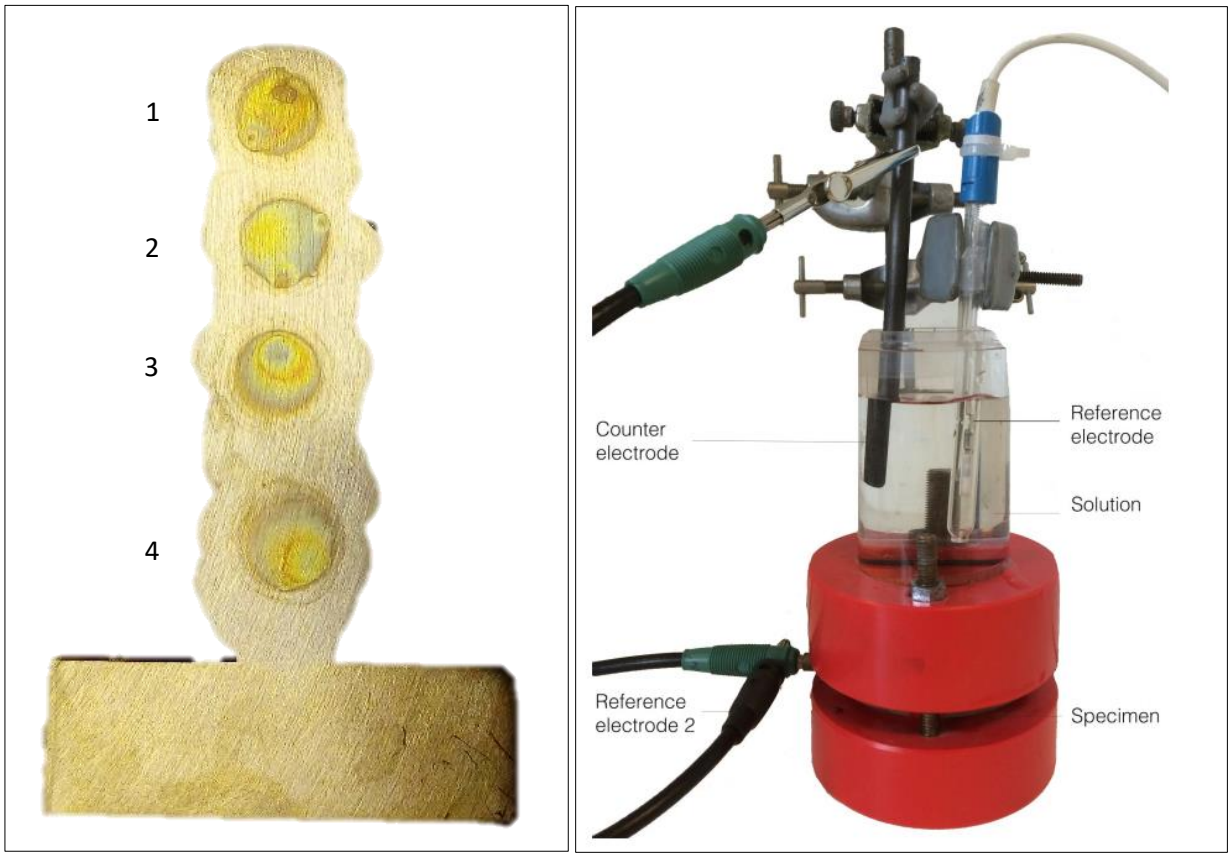

Figure 42: (left) Sample of the corrosion measurements. The test areas are evident due to the corrosion products. (right) The equipment used for the OCP and the polarization testing.

The electrolyte used had a composition of 3.5% NaCl and for the preparation a scale from Denver Instrument XP-3000 was used. The mixture of demi water and NaCl was homogenized by a magnetic stirring device (RETcontrol-visc, KIKA LABORTECHNIK).

As far as the samples are concerned, they are in the form of thin cross sections retrieved from the built blocks, see Figure 42 (left). In every test, the exposed area must be slightly bigger than that of the O-ring at the bottom of the immersion test apparatus (surface area: 38.46 mm^2). Moreover, the sample surface was ground up to 1200 grit paper and further cleaned with an ultrasonic device (Emmi-30HC from EMAC Technologies) for 10 min in acetone. The setup of the immersion apparatus is the final step of our experiment. The specimen is placed on the bottom of the device, centred on the rubber O-ring, with the clean surface faced up. The potential was applied by a potentiostat equipment (Autolab).

In this stage, the software controlling the procedure had to be calibrated. Nova 2.1 was the program controlling the experimental parameters, and the results were analysed in Nova 2.1 and in Excel. Two different experiments were performed sequentially. The first was an OCP procedure and the second was a polarization procedure. Analytically, in the OCP experiment the total measuring time of the experiment was 1 hour, with an acquisition rate of 1 Hz. Furthermore, the polarization experiments submitted the sample in a potential range of ±0.25 V from the V_{OCP}, which is the equilibrium potential obtained from the OCP measurements.

4.4.2 SCANNING KELVIN PROBE (SKP)

Originally, the SKP is a method for the measurement of the work function difference between a conductive sample and a vibrating tip. The work function is the smallest amount of energy needed to extract an electron from the outer shell of an atom. This value is a very sensitive indicator of the surface condition of the sample [41].

However, this method does not measure the work function directly. The investigated surface and the vibrating tip form a parallel plate capacitor, Figure 43 (a). Electrons are exchanged as the vibrating tip suspends above the specimen. Eventually, the work function difference is calculated by the addition of an external voltage, backing potential (V_b).

To explain the backing potential, an electrical circuit made between the two electrodes is assumed, Figure 43 (b). As a result, their potentials equalize, causing a flow of charge and producing a potential difference, V_c. Thus, the two surfaces become equally and oppositely charged. Finally, it is assumed that an external, backing, potential is applied at the capacitor (V_b), which permits biasing of one electrode with respect to the other, Figure 43 (c). At this unique point where V_b=-V_c the (average) electric field between the plates vanishes, resulting in a null output signal. Thus, by knowing the work function of the tip, the work function of the sample can be calculated.

The results extracted from the SKP method show the contact potential difference (CPD) between the sample and the tip. In the current study, the scope is to track any changes in the potential of different areas of the cross section of the blocks. Thus, the actual work function value is not of importance and the transformation of the CPD potential to work function value is out of the scope of the project.

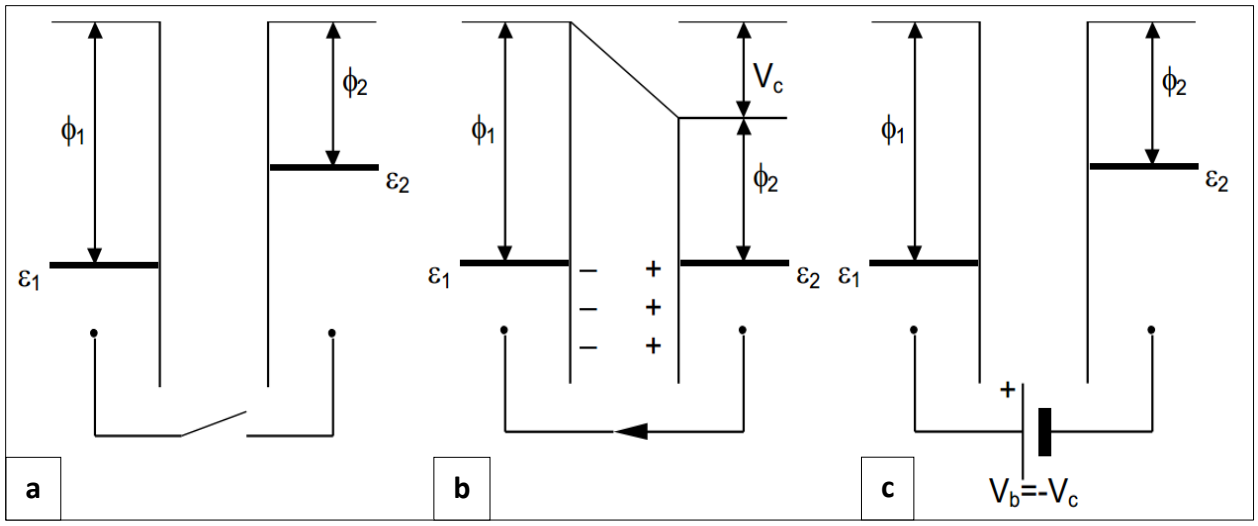

Figure 43: Schematic showing the fermi level (ε) and the work function (φ) for three cases. (a) Two conductive but isolated samples. (b) Two conductive and electrically connected samples. (c) Variable "backing potential" V_b in the external circuit permits biasing of one electrode with respect to the other. [41]

Initially, the sample was placed inside the SKP testing machine, see Figure 44, and the following parameters were chosen. The V_{ptp} (peak to peak) potential is equal to 960 mV, the backing potential is 7000 mV and the gradient 195. Line measurements were performed in the cross-sectional samples. Two representative specimens were chosen. The A1 and A2 cross sections were investigated to monitor the effect of heat treatment in the specimens with the same welding conditions. The samples used were the same as those prepared for the microstructural characterization, see Figure 32. However, in the SKP case, the samples were not etched.

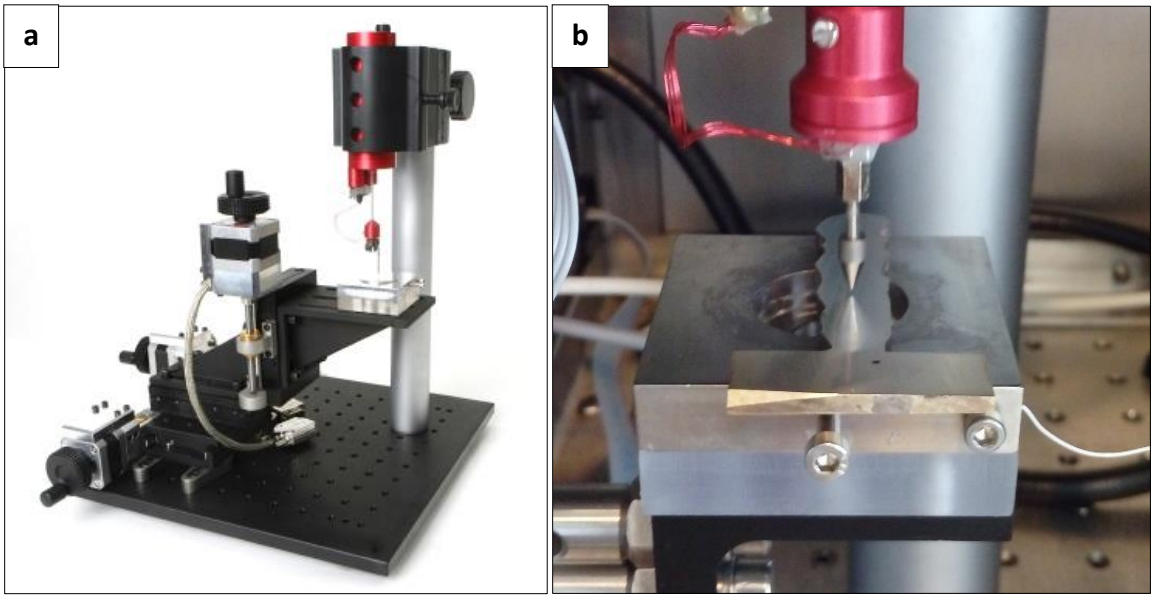

Figure 44: Testing of specimen in SKP apparatus. The cobalt-nickel tip is vibrating over the sample and can move only in z (vertical) axis. The sample holder can move in both x and y directions.

5. MICROSTRUCTURAL CHARACTERIZATION

This chapter deals with the microstructural investigation of the 3D printed blocks produced at TU Delft and at RAMLAB. Macroscopic pictures are presented (magnification x300), providing information on the macro-structure of the deposition layers. Furthermore, higher magnification images (x500, x1000, and x1500) are used to reveal the effects of the process parameters on the microstructure of the samples. The effect of heat input, temperature cycles, and heat treatment on the microstructure evolution will be presented. Figure 54 at the end of chapter (5.2) provides a useful map of the location of the most important microstructures presented in chapter 5.

5.1 SINGLE BEAD SPECIMENS (TU DELFT)

Figure 45 illustrates the banded structure of the three blocks produced with varying heat input at TU Delft. The left-hand pictures represent the structure of the block with the least heat input. The average layer width and height are 9.4 mm and 1.4 mm, respectively. In a similar way, the average layer width and height are 11.2 mm and 1.4 mm for the B block (intermediate heat input), and 13.5 mm and 1.8 mm for the C block, which has the greatest heat input. Concerning further geometrical characteristics, the penetration of the weld increases with the heat input, providing that the observed values are 0.9 mm, 1.3 mm and 1.7 mm for the three welding conditions. It should be highlighted that the misalignment of the layers also increases with the heat input, deteriorating the geometrical accuracy of the structure.

Subsequently, the top layer of each block was investigated. Figure 46 illustrates the heat treatment effect on the top deposited layer of the sample extracted from the A1 (as deposited) and A2 (heat treated) blocks. These blocks were manufactured with the least heat input. However, the reader may find in Figure A.100 of the Appendix A, similar figures for the case of the C1 and C2 blocks, which were built with the maximum heat input. The investigation of the banded structure follows in Figure 47 and Figure 48, showing C1 and C2 blocks, while similar pictures for the A and B blocks are presented in Appendix A. Finally, the microstructures of the first weld bead, the substrate, and of the RAMLAB block are provided.

5.1.1 TOP LAYER

The top layer of the deposited block does not experience a subsequent heat treatment, having no weld bead above. As a result, this layer should exhibit the same microstructure as an ordinary weld of the material under investigation, similar to the stable casting structure. Figure 46 illustrates the top layer microstructure of the A1 and A2 blocks, in two different magnifications. As mentioned before, Appendix A presents the respective images for the C1 and C2 blocks. In this way, the reader may observe the effect of heat input at every figure, comparing the microstructures of the sample with and without heat treatment, see Figure 46. At the same moment, the effect of heat input is evident as well, comparing Figure 46 with Figure A.100 of the Appendix A. Comparing these two figures, there are no major differences. The microstructure is identical, indicating that the heat input plays a secondary role on the resulted microstructure morphology of the top layer.

Figure 46 (a & b) show that phase α develops with a Widmanstätten morphology, both at the grain boundaries and at the interior of the β phase grains. However, grain boundaries are the preferred nucleation sites, having higher interface energy due to misorientation. The same trend is observed also in Appendix A.

Due to heat treatment at 675 °C for 6 hours, diffusion takes place. Figure 46 (c & d) depicts that the thickness of the Cu-rich grain boundary α phase increases, due to copper diffusion from β phase to α phase, increasing the concentration of alloying elements in β phase. Assuming that every alloying element has certain solubility in the β phase, it could be anticipated that the amount of precipitates would increase. It is evident that the stable cast structure is slightly affected by the tempering performed.

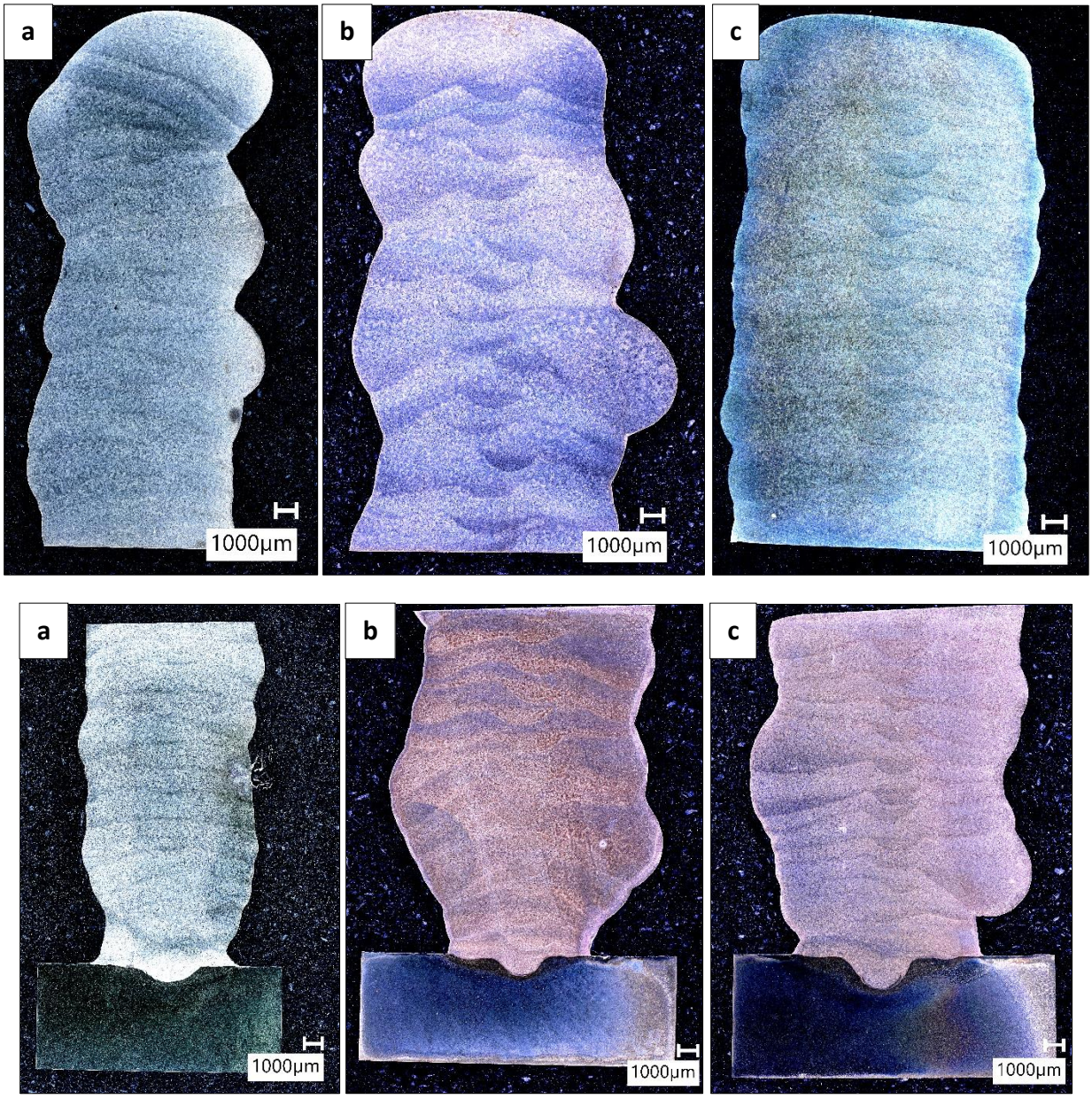

Figure 45: Low magnification micrographs of the 3D printed blocks produced at TU Delft, revealing the banded structure of the deposited material. (a upper) block A1 top part, (a bottom) block A2 bottom part, (b upper) block B1 top part, (b bottom) block B2 bottom part, (c upper) block C1 top part, (c bottom) block C2 bottom part.

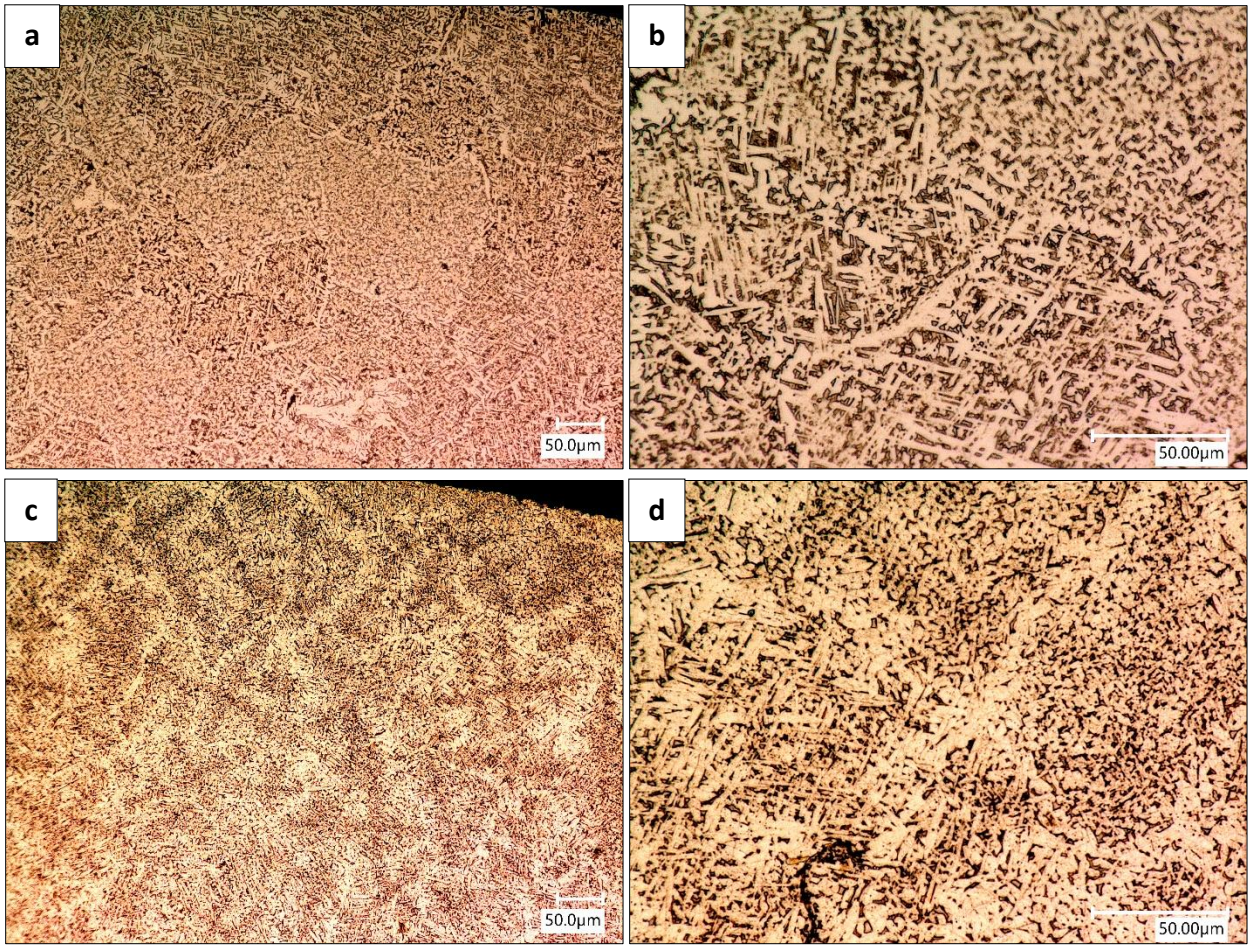

Figure 46: The top pictures illustrate the microstructure of top layer of block A1 (as deposited) at (a) x 500 and (b) x1500 magnification. The bottom two images represent the respective microstructure of top layer of block A2 (heat treated) at (c) x 500 and (d) x1500 magnification.

5.1.2 BANDS

Figure 45 revealed a banded structure of the deposited wall. This paragraph gives an insight of the microstructural features dominating these bands. Figure 47 illustrates the microstructure of blocks C1 and C2 (high heat input blocks) at different magnifications, showing the effects of heat treatment and the banded structure of the deposited material. Appendix A contains similar micrographs of A1, A2, B1 and B2 blocks.

Figure 47 (a) reveals that two distinctive microstructures are evident. At the centre of the picture, one of the deposited layers is presented. The prior β grains are visible, having a diameter within the range of 50 – 70 µm. The α phase forms a network at the grain boundaries and is finely dispersed inside the β grains. The top area of Figure 47 (a & b) represents the remelted part of the layer. The Widmanstätten α phase grows, making the grain boundaries indistinguishable.

The heat treated samples, see Figure 47 (c & d), indicate that the β phase is decomposed. This effect homogenizes the microstructure, eliminating the differences between the newly deposited, Figure 47 (d, left), and the remelted region, Figure 47 (d, right). Figure 48 shows the same features at even

greater magnification. In Figure 48 (a & b), the difference of the two regions are clearly evident, whereas the uniformity of the heat treated sample is illustrated at Figure 48 (c).

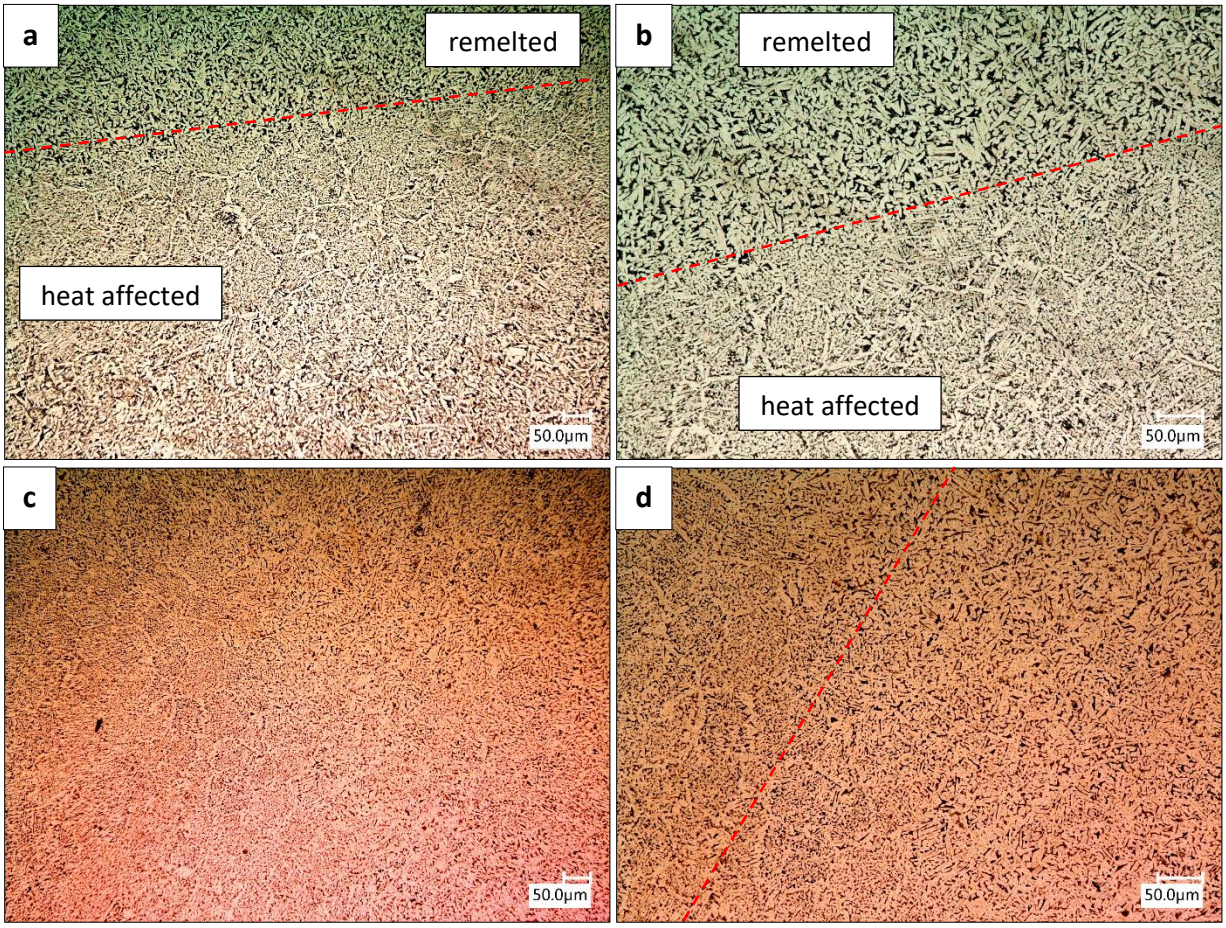

Figure 47: Microstructure of block C1 (upper) and C2 (bottom), at (left) x 300 and (right) x500 magnification.

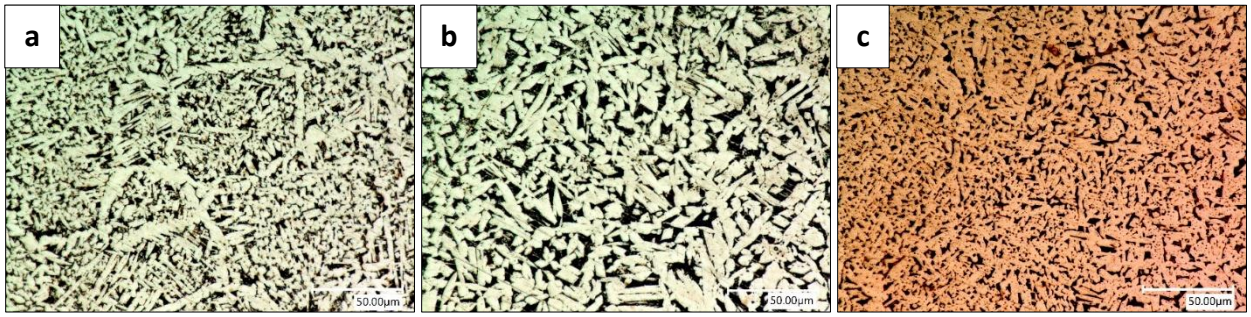

Figure 48: Microstructure of block C1 (a & b) and C2 (c) at x1500 magnification. (a) new layer, (b) remelted layer, (c) heat treated.

5.1.3 ROOT WELD

Figure 49 highlights the microstructural features at the interface of the first weld and the substrate. The upper two pictures show the as-deposited condition, whereas the bottom micrographs show the heat treatment effect. Moreover, these specific examples are extracted from the A1 and A2 blocks, but may serve as representative microstructures for the remainder of the cases. The main feature

changing at the rest samples, with higher heat inputs, are the geometrical characteristics, such as the penetration depth.

In Figure 49 (a), the cast structure is present at the weld pool. There is mixing between the two alloys and the penetration depth increases with heat input. The grains are elongated and their direction coincide with the maximum temperature gradient. Moving to the substrate region at Figure 49 (a and b), the microstructure of the heat affected zone (HAZ) is characteristic for the NAB alloys. The white etched α phase is surrounded by the dark etched martensitic β phase. More specifically, the microstructure consists of a partially transformed eutectoid structure, especially closer to the fusion line. It could be assumed that the heat input is high enough to elevate the temperature above the eutectic point, where the β phase is formed. Due to rapid cooling of the HAZ, retained β martensitic phase is formed.

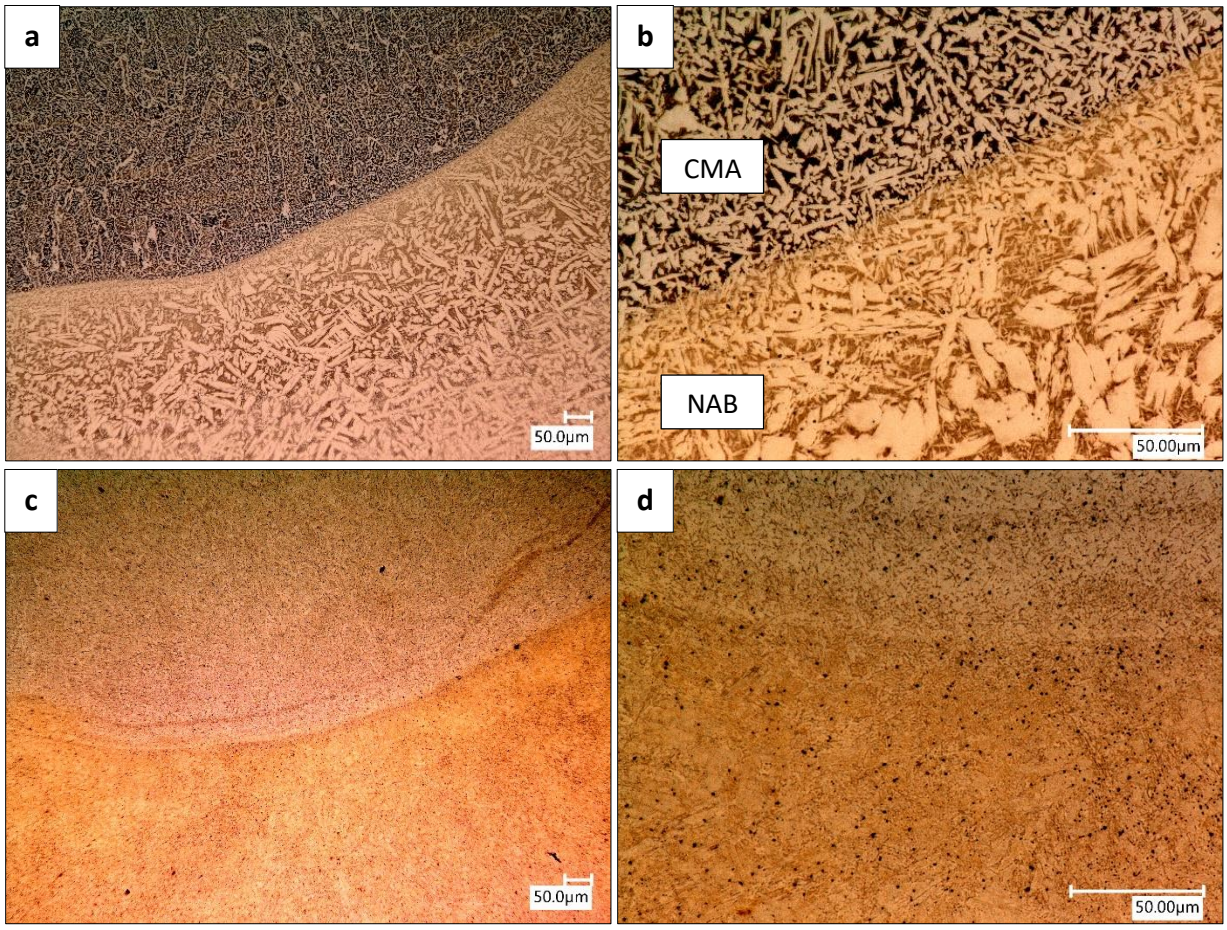

Figure 49: Microstructure of the first weld of block A1 (top) and A2 (bottom) at x300 (left) and x1500 (right) magnification.

5.2 OVERLAPPING BEADS SPECIMENS (RAMLAB)

This paragraph deals with the microstructural investigation of the 3D printed block produced at RAMLAB. At Figure 50, macroscopic pictures are presented, providing information on the macrostructure of the deposition layers. Specifically, samples were extracted from the top, middle and bottom part of the block, with the latter one incorporating the interface between the substrate and the filler material. Furthermore, higher magnification images are used to reveal the effect of the heat cycle, imposed by subsequent beads, on the microstructure of the samples.

Figure 50 reveals that in all three pictures the average bead height is within the range of 3 mm to 3.5 mm, whereas the width of the beads is 7 mm approximately. This constant behaviour indicates the reproducibility of the process if the interpass temperature is maintained below 200 °C. Of course, there is the phenomenon of remelting at each layer, according to which the subsequent layer melts a part of the previous deposition. Thus, the height gained after each layer is less than the actual height of the bead.

Figure 51, and Figures A.103 and A.104 in Appendix A present an overview of the microstructure of the top, middle and bottom layers, respectively. In more detail, Figure 51 (a) illustrates the banded structure of the top layer at low magnification, highlighting the re-melted region between the deposited beads. Similar features are also evident in Figures A.103 and A.104 in the Appendix A. Continuing with pictures b and c of these three figures, the reader may observe the deposited and the re-melted regions at higher magnification. Finally, Figure 52 (a & b) highlights the growth of the α phase at the grain boundary of the prion β grains.

The low magnification images reveal that the structure of the deposited layers varies, ranging from a structure similar to the top layer morphology of the TU Delft blocks to one with elongated prior β grains. In any case, the α phase is nucleated mainly at the grain boundaries of β phase but also in the interior of the β grains, as anticipated. The later morphology is called acicular α phase. The α phase at the grain boundaries form a network of α phase along the solidification direction, as Figures A.103 and A.104 (a & b) in the Appendix A indicate.

The higher magnification images show that the Widmanstätten α phase may grow towards the interior of the prior β grain. Furthermore, Figure 52 (a & b) depicts that the α phase may grow at a specific grain boundary. Probably, that boundary is characterized by higher mobility with respect to the other grain boundaries.

The weld at Figure 52 (c & d) shows that the heat affected zone is no larger than 300 μm. The substrate material at the heat affected zone has a coarser α phase than the bulk substrate microstructure. The dark etched phase is assumed to be the martensitic β’ phase.

The microstructure of the substrate is revealed in Figure 53. The upper two pictures present the non-heat treated version of the substrate. The martensitic β’ phase is evident along with the Widmanstätten α phase. The heat treatment results in the decomposition of the martensitic phase, which is evident in the bottom pictures of Figure 53, perhaps, giving rise to the amount of precipitates.

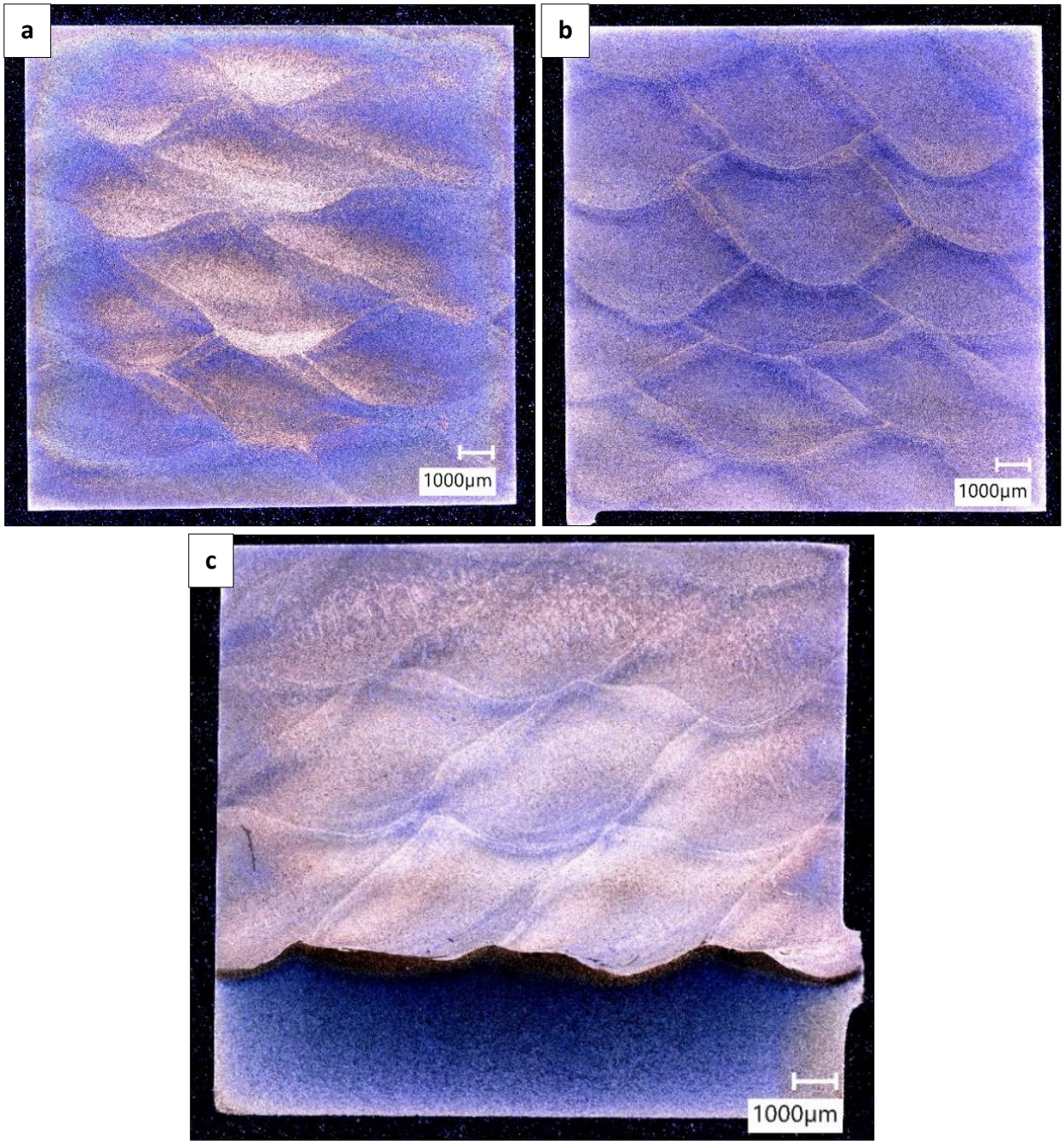

Figure 50: Macroscopic pictures of the 3D printed block produced in RAMLAB, revealing the banded structure of the deposited material. (a) top part, (b) middle part, (c) bottom part, including the first deposited bead and the substrate material.

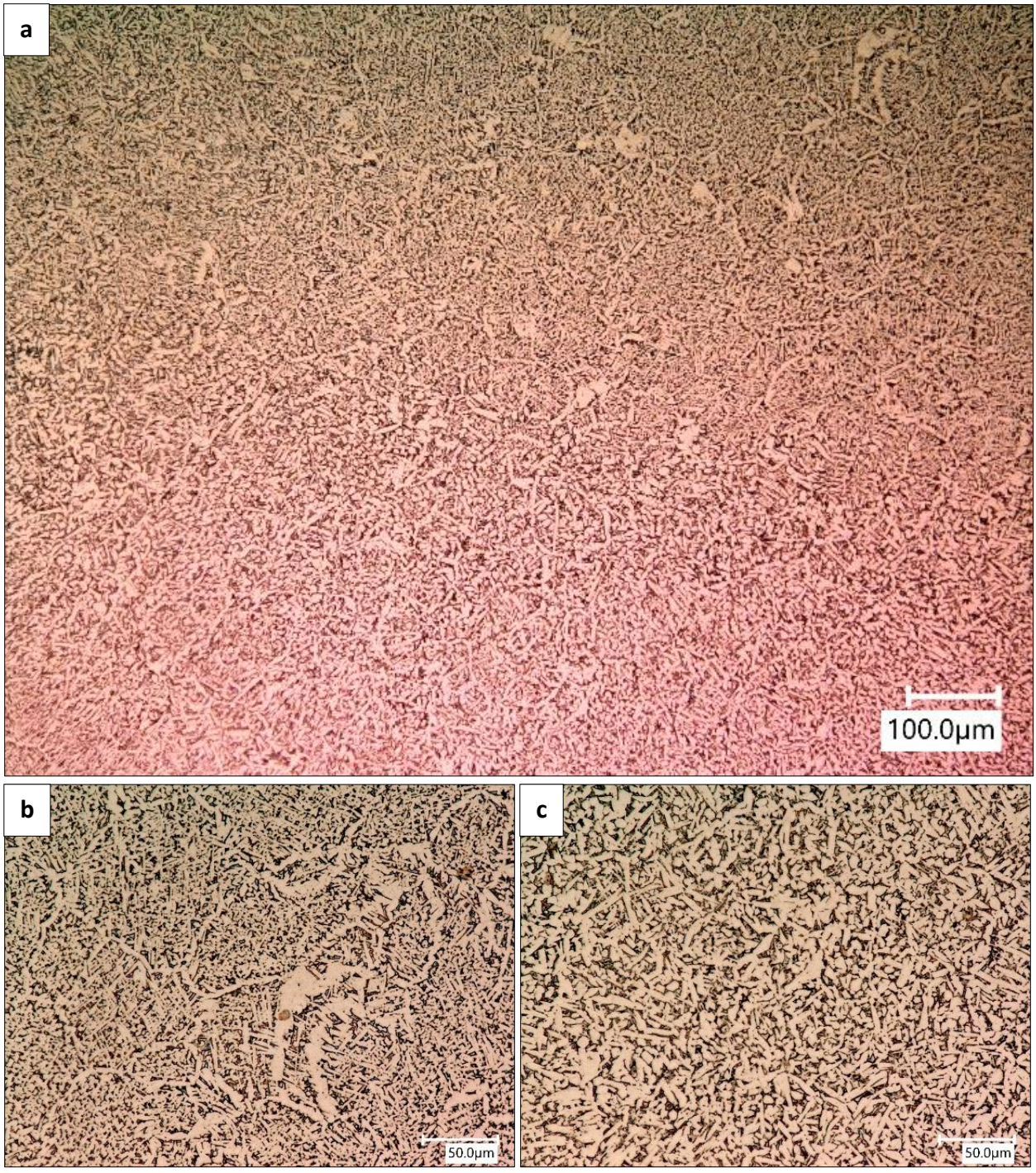

Figure 51: Microstructure of the top layers of the block produced at RAMLAB. (a) 300, (b) upper layer 1000, (c) bottom layer 1000.

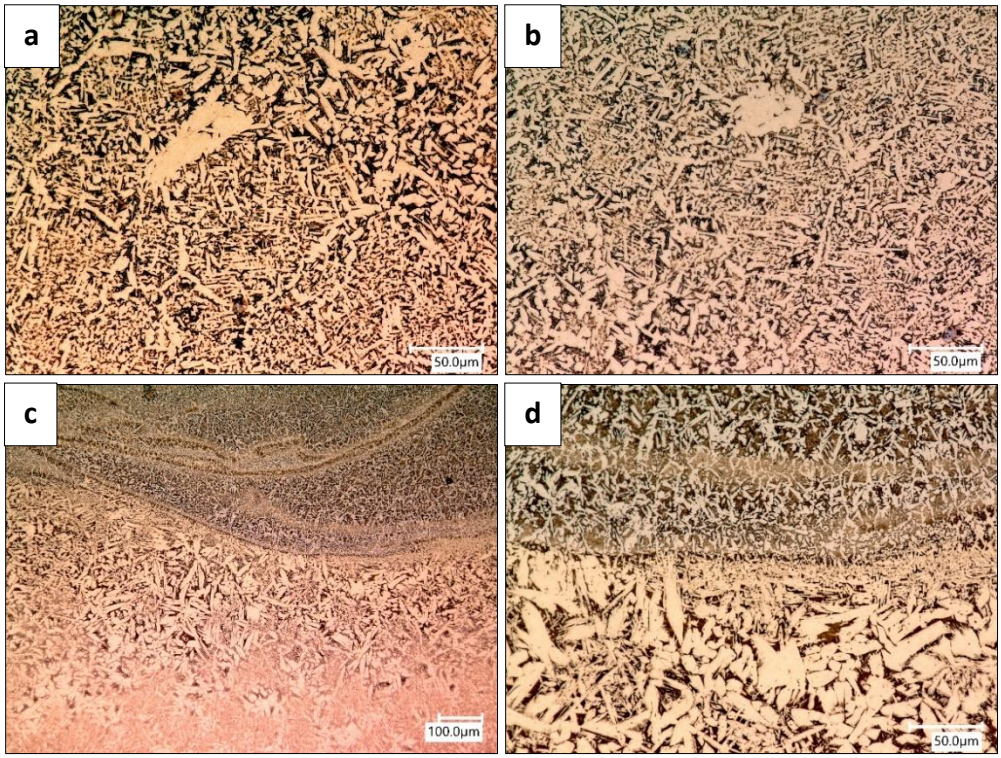

Figure 52: (a & b) Growth of α phase at the grain boundaries. (c & d) Microstructure of the weld of the block produced at RAMLAB. (left) x300, (right) x1000.

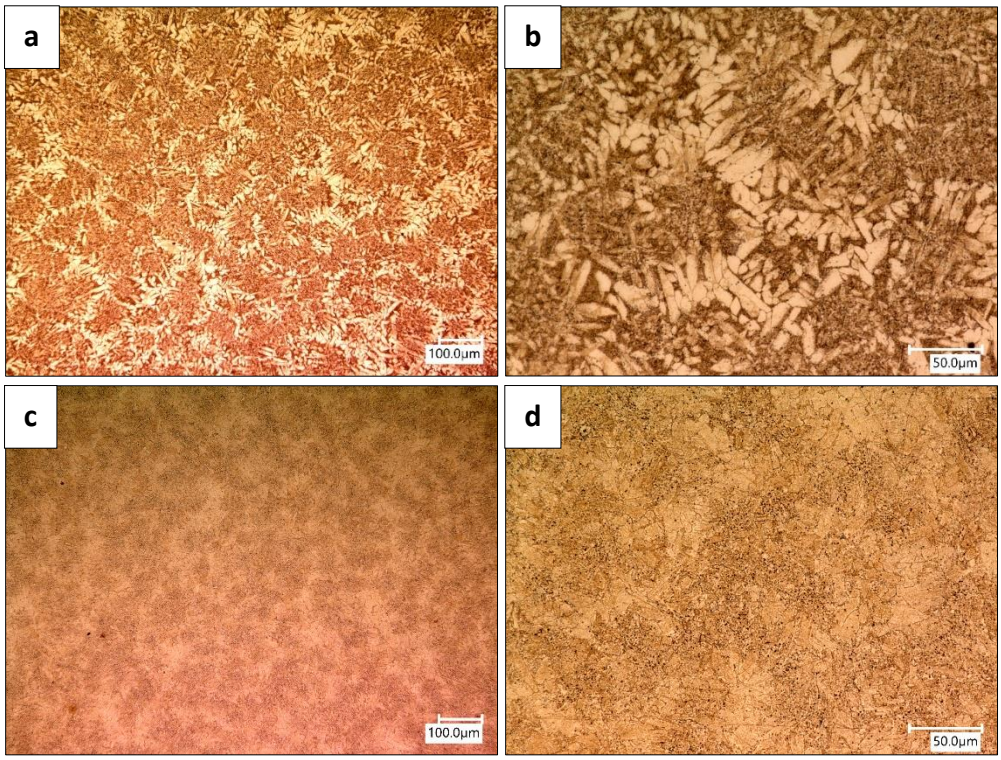

Figure 53: Microstructure of the non-heat treated (upper two pictures) and the heat treated (bottom two pictures) substrate material at (left) x300 and at (right) x1000 times magnification.

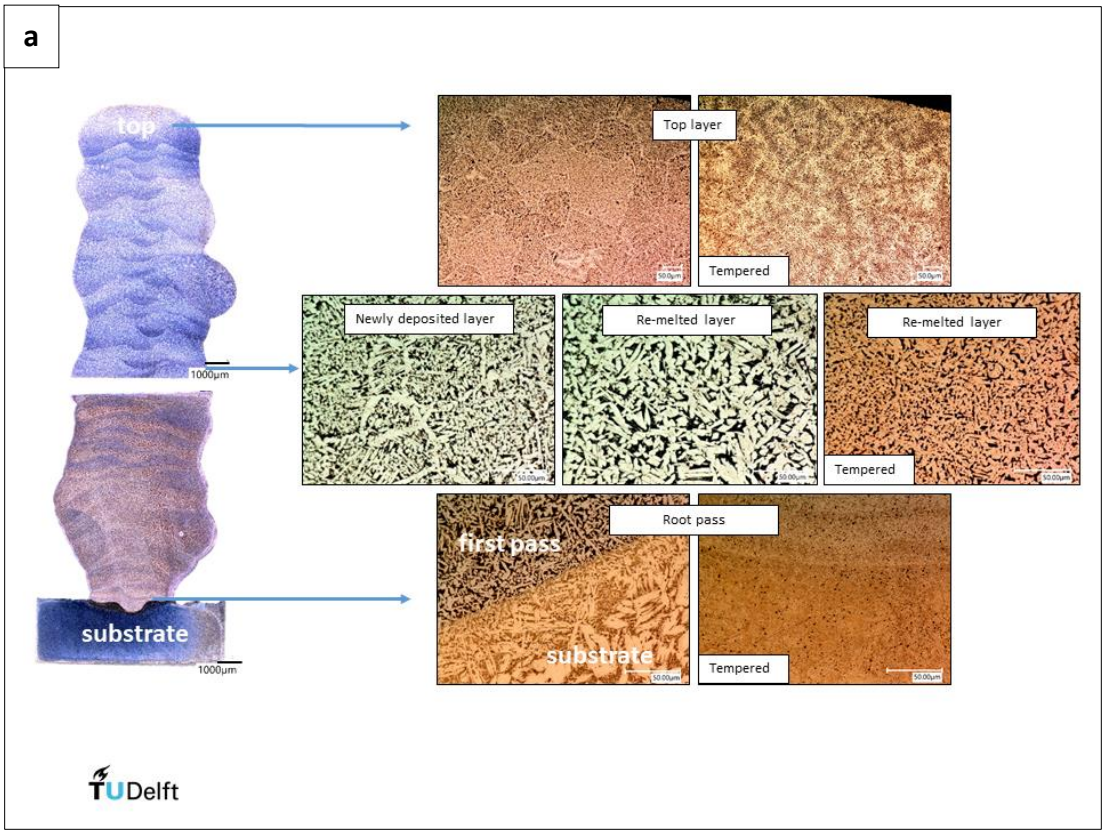

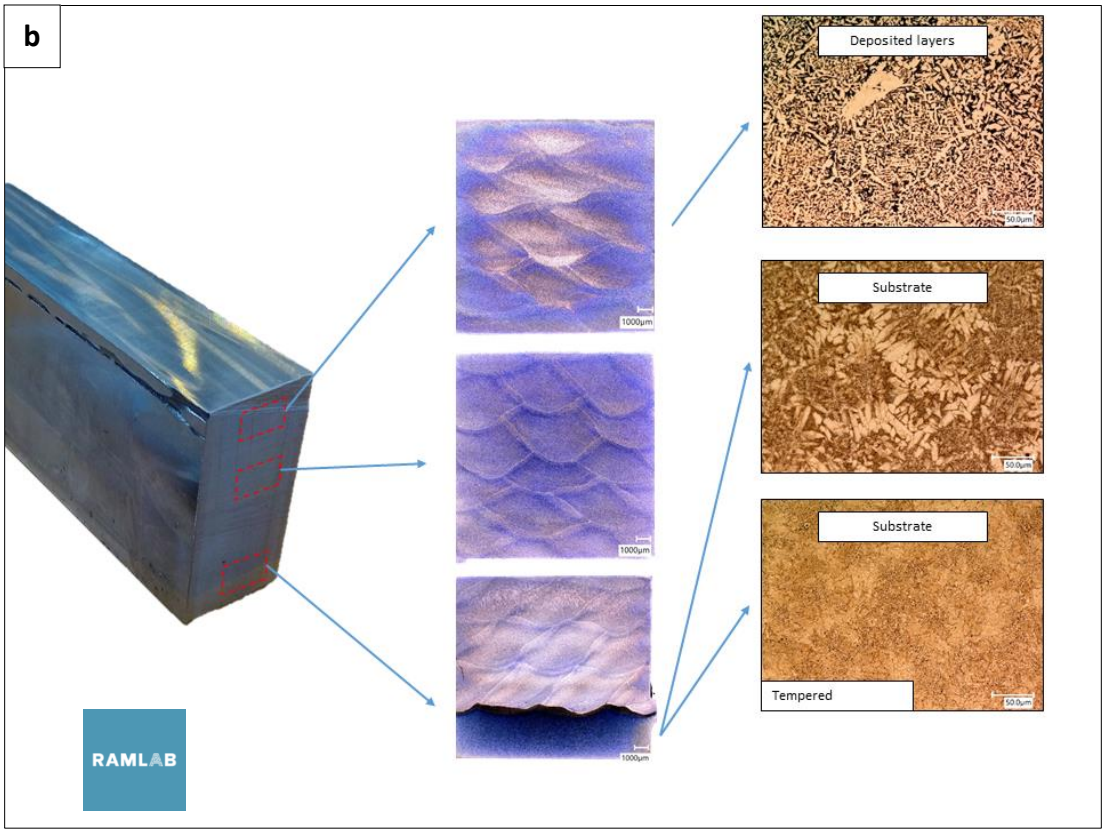

Figure 54: Overview indicating the location of the most important microstructures in case of (a) TU Delft block, (b) RAMLAB block.

5.3 SCANNING ELECTRON MICROSCOPY (SEM)

Scanning electron microscopy was used to reveal the precipitates, which might have formed in the samples. Figure 55 illustrates the chemical composition maps of the heat treated A2 block, while the reader can find in Appendix A the respective figures for the case of the substrate material and for the non-heat treated RAMLAB block. Table 10 contains the chemical composition of the different phases and was used for the identification of the constituent phases of the filler material.

In the top left picture of Figure 55, the reader can see the microstructure of the CMA alloy, consisting of the white etched α phase and the dark etched β phase. Most of the black spots in the picture are holes and not precipitates. This is evident by the fact that the chemical composition maps depict no irregularities in these areas. The aluminium content of the β phase is twice that of the α phase, which is in accordance with the data of Table 10. Furthermore, the content of copper is slightly higher in the α phase, which also confirms that the white regions represent the α phase, whereas the dark etched regions represent the β phase.

The significantly higher content of manganese and iron at certain spots in the respective maps of Figure 55 imply that at these regions precipitates are located. All the precipitates exhibit high amounts of these elements and without quantitative results of the chemical composition, it is difficult to indicate which precipitates are formed. However, judging from the size of the white spots of the composition maps (1 to 3 μm), the precipitates are most probably κ_2 particles. K_1 are one order of magnitude bigger, whereas κ_3 and κ_4 are one order of magnitude smaller [21].

Table 10: Chemical composition of the constituent phases of the CMA alloy [21].

Phases	*Composition, wt %*					
	Al	*Si*	*Mn*	*Fe*	*Ni*	*Cu*
α	5.9	0.2	12.1	2.4	1.4	78
β	12.5	0.3	13.5	1	2.2	70.5
κ_1	3.6	1.8	29.5	56.4	1.3	7.4
κ_2	15.9	3	25.1	47.1	1.2	7.8
κ_3	12.2	0.7	29.6	32.6	4.4	20.3
κ_4	8.2	0.6	28.9	36.7	2.9	22.6
"sparkle phase"	1.3	0.6	28.3	61	0.4	8.4
alloy composition	7.78	0.06	13.95	3.24	2.17	72.42

The situation is similar in Figure A.106 in Appendix A, regarding the non-heat treated filler material. However, the α phase is significantly smaller, as predicted from the microstructural investigation of the previous paragraphs.

Finally, Figure A.105 of the Appendix A presents the case of the non-heat treated substrate material, the NAB alloy. An extensive report of the chemical composition of the phases and the precipitates of these alloys is presented by Meigh [21]. In this case, the chemical composition of the white etched α phase and the dark etched β phase are similar. However, the α phase has a slightly higher copper and a lower aluminium content than the β phase. Regarding the precipitates, they are located at the grain boundary of the α phase and their diameter is approximately 1 μm. Most likely, these particles are small dendritic κ_2 rosettes or globular κ_3 particles.

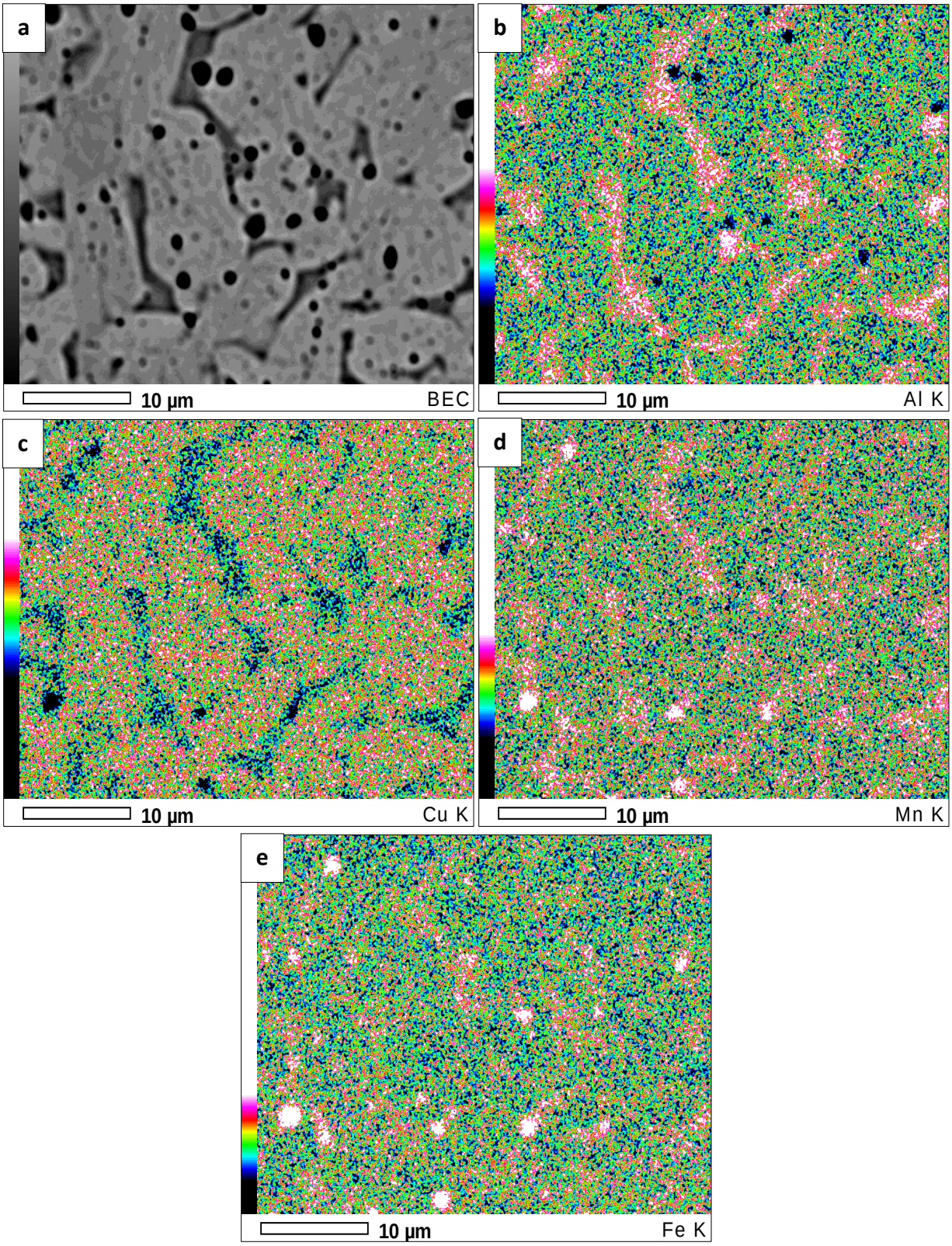

Figure 55: Picture (a) illustrates the microstructure of the PWHT A2 sample. The qualitative map of the distribution of certain elements (Al, Cu, Mn, Fe) is provided in (b) to (e).

6. MECHANICAL TESTING RESULTS

6.1 MACRO HARDNESS

The graphs in this paragraph present the measured hardness values obtained from both the blocks manufactured at TU Delft (A1, …, C2) and at RAMLAB. The macro hardness test is the easiest way to observe the mechanical behaviour of our specimens and predict the anticipated results in the tensile and Charpy tests. Of course, the values obtained for hardness and Charpy impact tests cannot be analytically correlated to the results of the tensile test, because the stress state at the first two experimental procedures is multiaxial and cannot be easily defined.

Figure 56 depicts that the hardness in all different welding parameters exhibits the same trend. The values below 10 mm represent the substrate and are in the order of 225 HV_{5kg}, 6% higher than the values of the deposited material. A maximum is observed at the interface, where metallurgical phenomena related with welding can be observed, such as the HAZ. The measurements at the top layers of the blocks are 7% elevated, showing the influence of the faster cooling rate and the absence of additional thermal cycles in comparison with the precedent beads. Moreover, the heat treatment affects the behaviour of both materials. The hardness of the substrate drops 5%, while the hardness of the filler drops 10%, approximately. As a result, the value of hardness of the deposited part is below 200 HV_{5kg}.

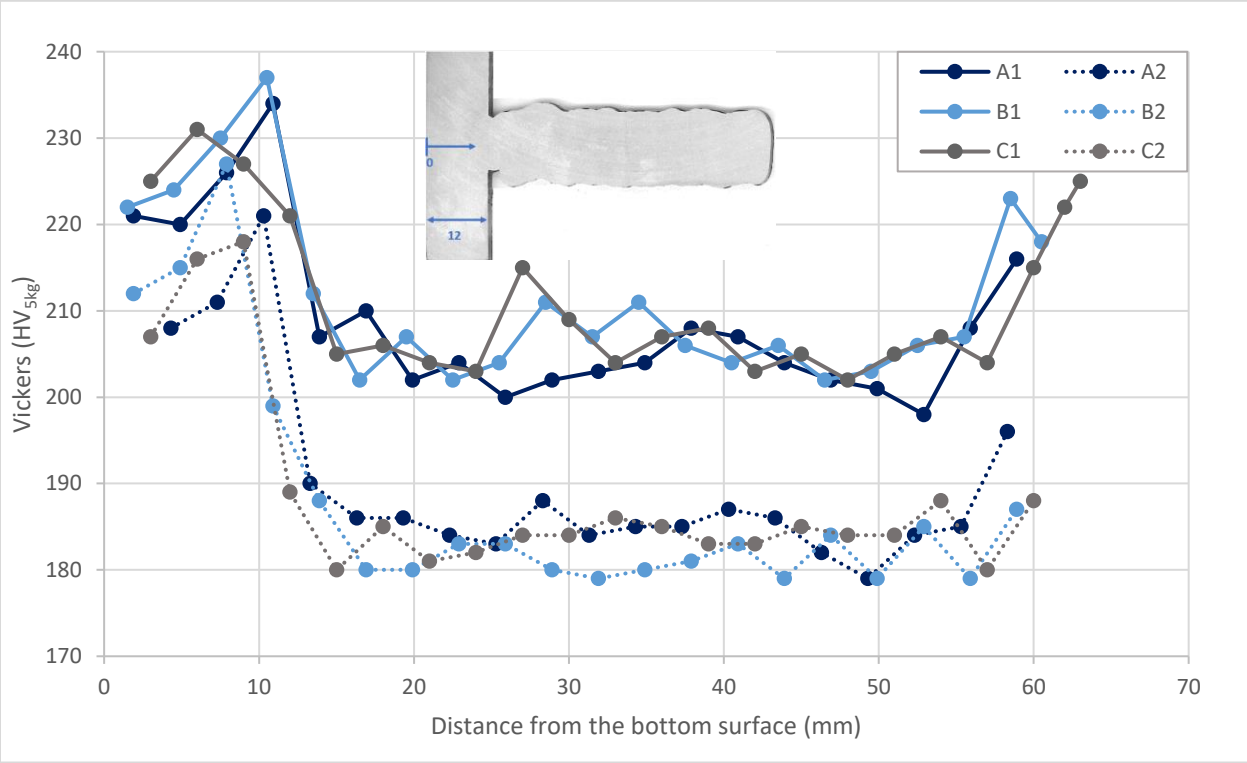

Figure 56: Vickers hardness measurements with 5 kg-f along the cross section of the block produced at TU Delft. All three heat input cases were investigated, with and without heat treatment.

The contour plot, shown in Figure 57, illustrates the distribution of hardness levels in the cross section of the block produced at RAMLAB. It should be mentioned that all the measurements are between the first and the top layer of the deposit, and no substrate is taken into account. The x-axis, representing the block width, has an interval of 6 mm, which is close to the interpass distance between subsequent beads. Obviously, the bottom beads exhibit the same behaviour as in the case of the blocks produced at TU Delft. Their chemical composition consists of a mixture of both the substrate and the filler material. This causes an increase in hardness of approximately 30% in comparison with the subsequent layers, reaching a magnitude of 270 HV_{5kg}. Also in a similar way to the previous plot, the values of the top layers show an increase in hardness. In more detail, this rise is not higher than 30% in comparison with the middle layers, and can be attributed to the faster cooling rates and the absence of subsequent thermal cycles at the top layer. The intermediate layers present slight variations in the order of 13%, which do not affect the mechanical behaviour of the structure, with values ranging between 200 and 230 HV_{5kg}. Finally, a pattern is observed along the building height, with very close values of hardness along the y-axis.

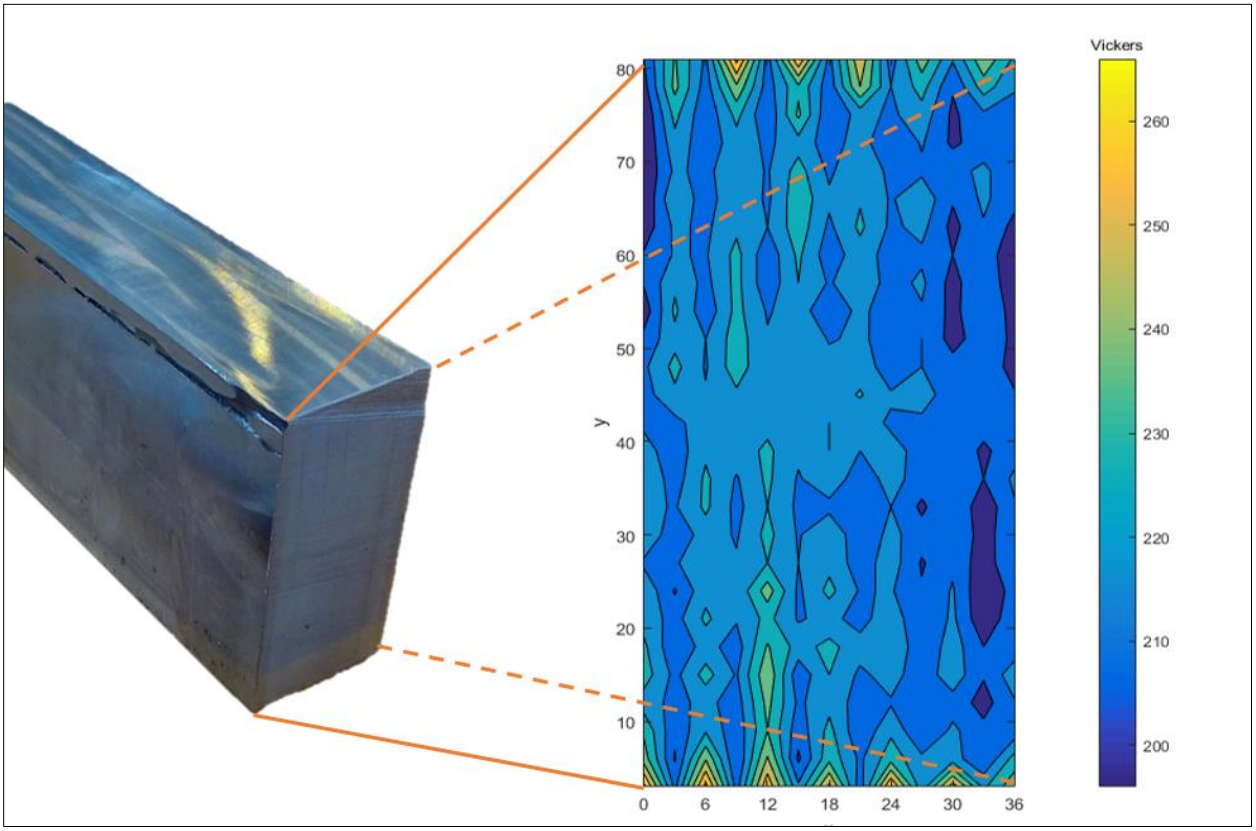

Figure 57: Vickers hardness measurements with 5 kg-f along the cross section of the block produced at RAMLAB. Every coloured area has a range of 10 HV. The x and y axis represent the width and height of the deposited block, respectively.

6.2 TENSILE TEST

6.2.1 SPECIMENS FROM THE TU DELFT BLOCKS

Tension testing is the most common procedure to estimate the strength and the ductility of materials. This paragraph is devoted to the results obtained from the tensile test measurements and includes the yield strength, the ultimate tensile strength and the total elongation [39]. The first parameter, the yield strength, indicates the onset of plastic deformation. However, in most cases this is not a well-defined transition at the stress-strain curve. Thus, this value is determined by the intersection of the stress stain curve and a parallel line to the elastic part of the stress-strain curve, which crosses the x-axis at 0.2% strain. The ultimate tensile strength is expressed by the highest value of stress recorded during testing and the total elongation is measured by the extensiometer at the moment of fracture. In all cases, the engineering stress and strain values are presented, meaning that the stress is calculated dividing the recorded force by the original cross section of the gage length, and the elongation is expressed as a percentage of the initial gage length.

The following graphs represent not only the most characteristic values of the results but also certain representative curves of the stress-strain measurements. Figure 58 to 60 illustrate the yield strength, the ultimate tensile strength and the total elongation of the horizontal specimens extracted from the block produced at TU Delft. Every diagram compares the results of all three different welding parameters with (A1, B1, C1) and without heat treatment (A2, B2, C2).

The curves show a similar behaviour to the ones obtained from the hardness measurements. Specifically, the substrate exhibits higher yield strength and ultimate strength values than the built material, having 550 MPa and 950 MPa yield and ultimate strength, respectively. The interface shows a sudden peak, reaching yield strength values close to 650 MPa and an ultimate strength above 1050 MPa. The filler material exhibits a yield strength in the range of 470 to 520 MPa and an ultimate tensile strength between 890 and 910 MPa.

Once more, heat treatment reduces the yield strength of the material up to 25%, but, simultaneously, narrows the spread of the values between different areas. The ultimate tensile strength is affected less, presenting a drop of 10%. It should be highlighted that the yield strength shows higher scattering than the ultimate tensile stress. This can be attributed to the fact that the yield load is calculated and not measured directly as in the case of ultimate tensile load. The calculated value of the yield strength depends on the accuracy of the determination of the slope of the elastic region of the stress-strain curve. As expected, the total elongation values exhibit the reversed behaviour of yield and ultimate tensile stress values. The strength is gained in expense of ductility, as in most cases.

The graph in Figure 61, incorporates all the above results for the case of 11.5 m/min wire feed rate, namely blocks C1 and C2. In this way, the relationship between yield and ultimate stress, and elongation can be easily compared. The values below 12.5 mm belong to the substrate and the interface of the substrate with the filler material. On the contrary, the values above 12.5 mm belong entirely to the 3D printed part. The consistency of the results obtained from the 3D printed part is highlighted, together with the reduction of ductility and the increase of hardness related to the results obtained from the interface and the substrate.

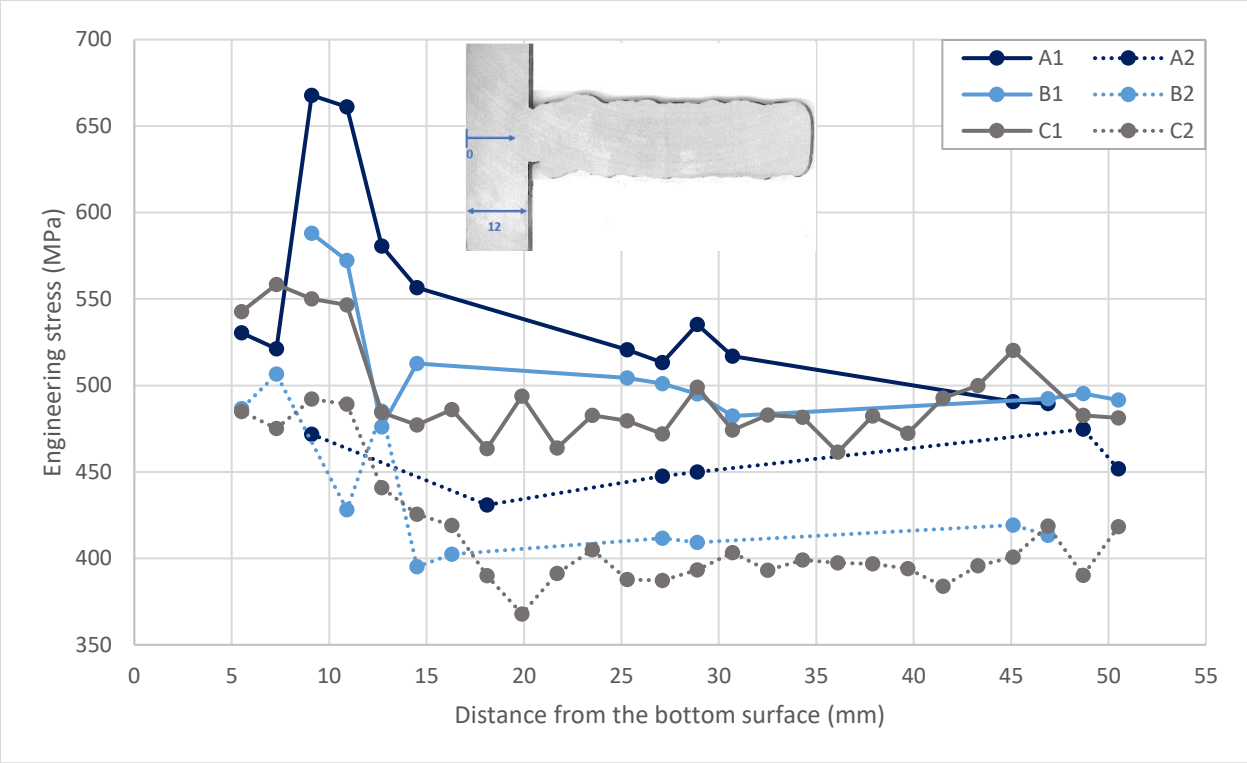

Figure 58: Yield strength values at 0.2 % elongation for different welding parameters of the horizontal specimens from the block produced at TU Delft, with (solid) and without (dashed) heat treatment. The values show the effect of built height on the strength of the material.

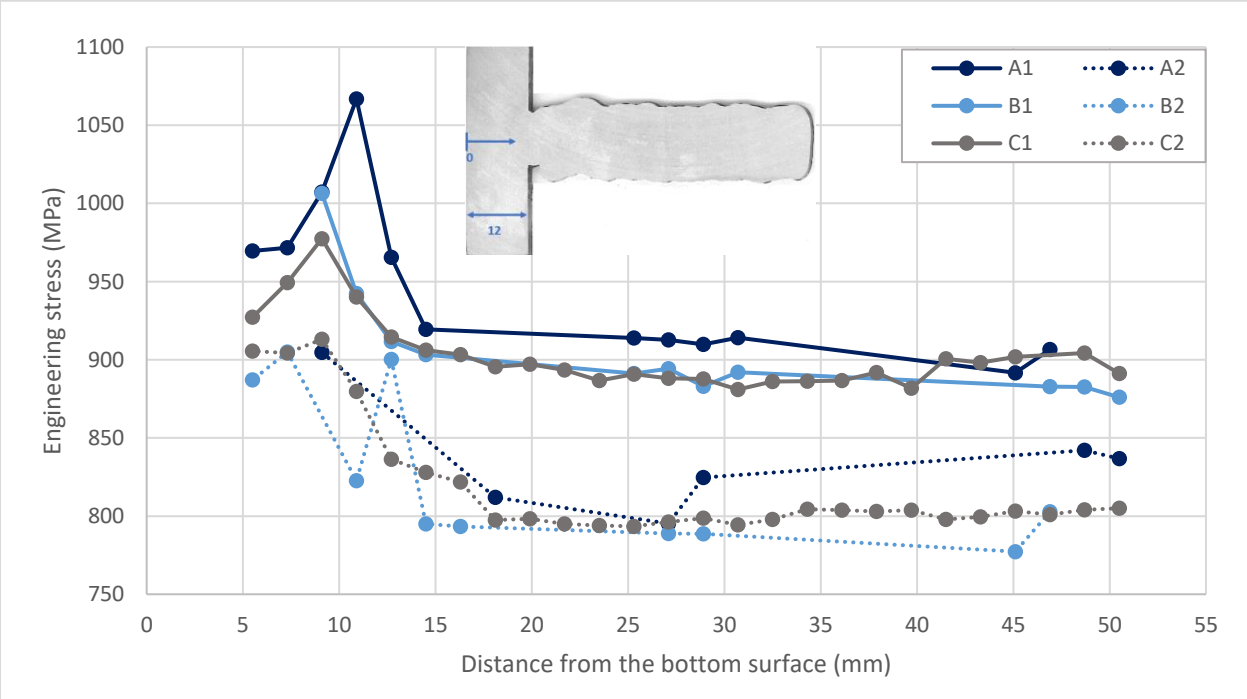

Figure 59: Ultimate tensile strength values for different welding parameters of the horizontal specimens from the block produced at TU Delft, with (solid) and without (dashed) heat treatment. The values show the effect of built height on the strength of the material.

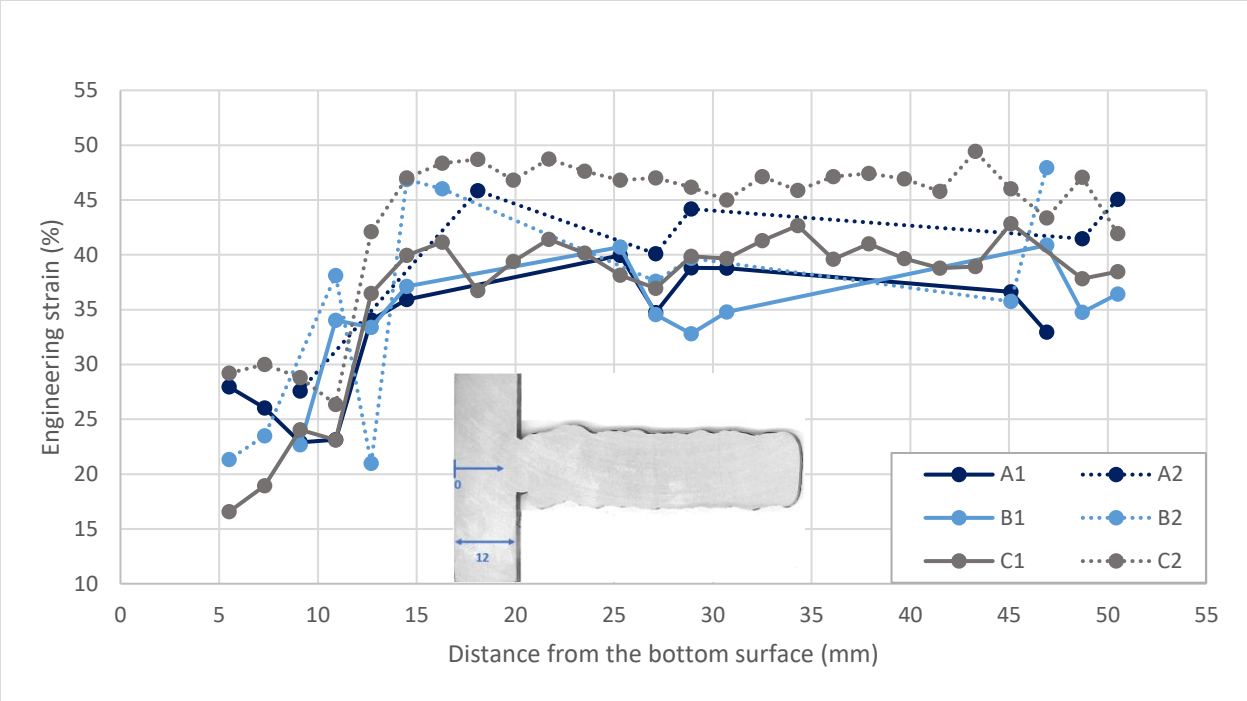

Figure 60: Total elongation for different welding parameters of the horizontal specimens from the block produced at TU Delft, with (solid) and without (dashed) heat treatment. The values show the effect of built height on the ductility of the material.

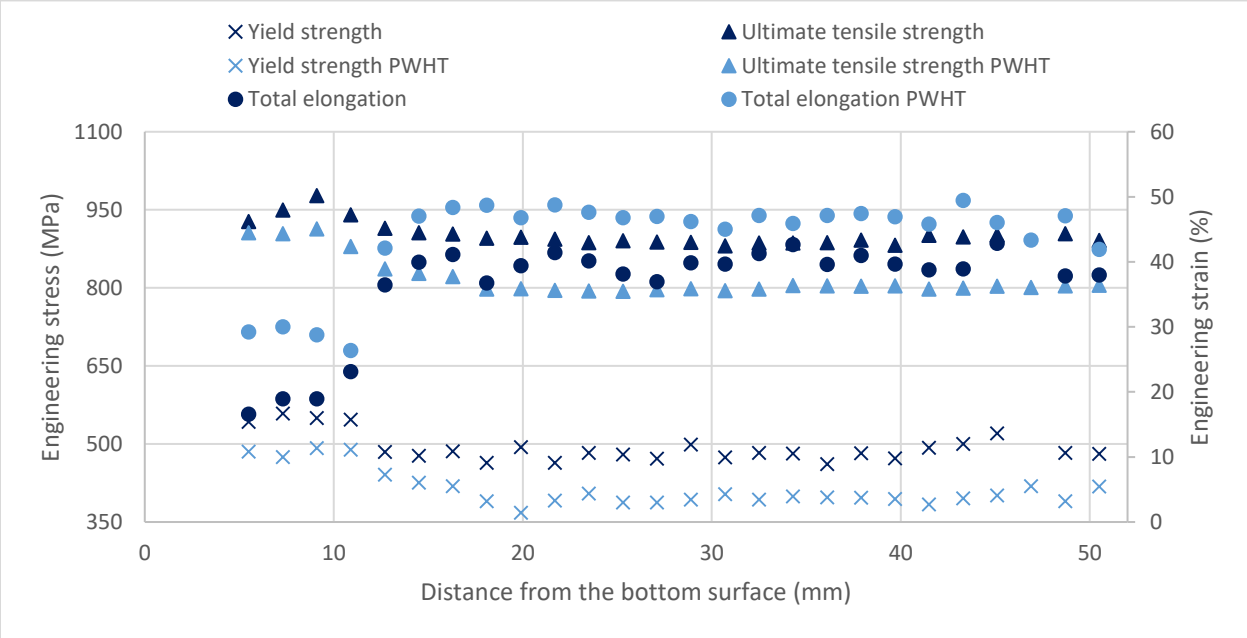

Figure 61: Diagram showing the yield strength, the ultimate tensile strength and the total elongation values, obtained from the horizontal specimens of blocks C1 and C2, produced at TU Delft.

Out of every block, (A1, …, C2), which was produced within the facilities of TU Delft, 26 tensile specimens were cut with electric discharge manufacturing. Firstly, the two sub-blocks with welding parameters 11.5 m/min wire feed rate and 6.7 mm/sec travel speed (C1 and C2) were chosen to be tested. All 52 horizontal specimens were tested and analysed. The consistency of the values showed that the rest

blocks could be tested by some representative specimens. These specimens were obtained from the top, middle and bottom layers and from the interface between the substrate and the deposited material.

In Figure 62 and 63, the stress strain curves for the horizontal specimens, without and with heat treatment, are presented. In these graphs, the characteristic values mentioned above can also been seen, such as the yield strength and the ultimate tensile strength.

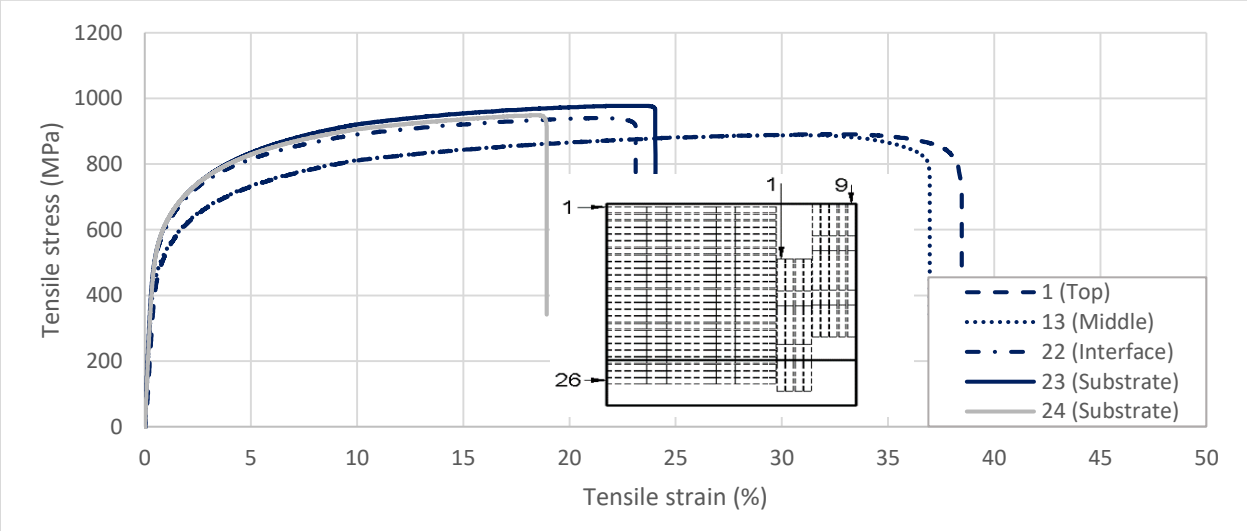

Figure 62: Engineering stress-strain curve for C1 block (no PWHT) obtained from horizontal tensile specimens from the top (1), middle (13), interface (22) and substrate (23,24) material.

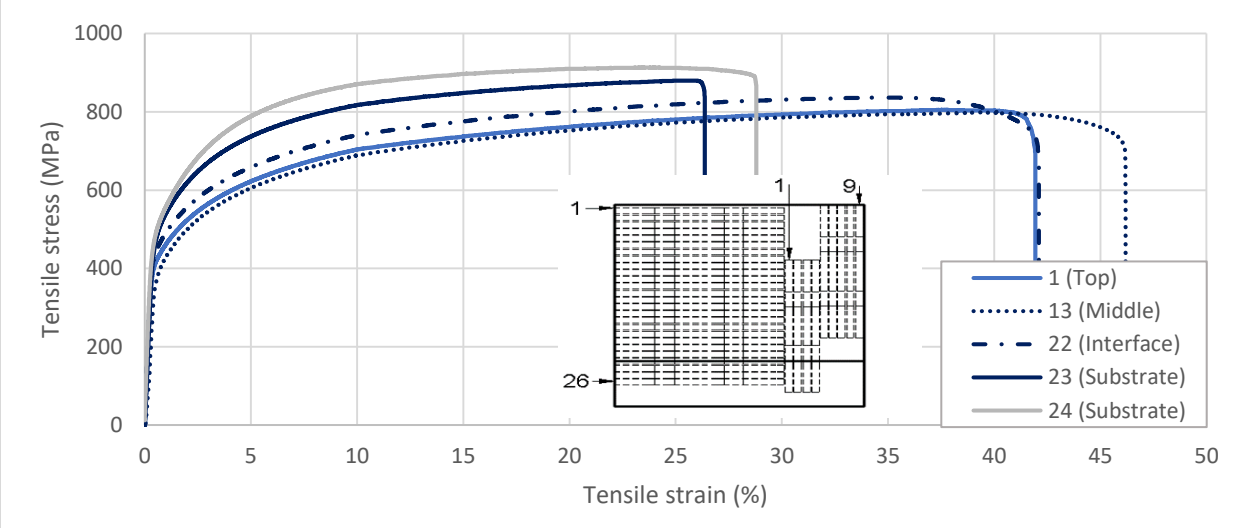

Figure 63: Engineering stress-strain curve for C2 block (PWHT) obtained from horizontal tensile specimens from the top (1), middle (13), interface (22) and substrate (23,24) material.

Initially, at low strain values, the specimen is within the elastic region. The elongation is reversible and the tensile energy can be recovered. Beyond the yield point, plastic deformation takes place, usually with the form of dislocation movement, but also additional mechanisms may contribute, such as twinning. Plastic deformation is irreversible and cause work hardening. These mechanisms are explained in chapter 8.

Figure 64 and 65 present the strength and elongation values for the vertical tensile specimens obtained from the blocks C1 and C2 respectively. As illustrated in Figure 38, specimens 1-4 are extracted from the bottom deposited layers, whereas specimens 5-9 belong to the top part of the blocks. In both cases, the gage length consists entirely of the deposited material.

For the non-heat treated case; the yield strength shows a 18% reduction in comparison with the average value of the horizontal specimens, obtained with the same welding parameters, while this reduction is 22% for the heat treated specimens. Furthermore, the same trend is observed in the ultimate tensile strength values, with a 22% reduction in the non-heat treated case, and 25% in the heat treated case.

The reader may find in Appendix B the tensile curves of all the specimens tested from both the TU Delft and the RAMLAB blocks.

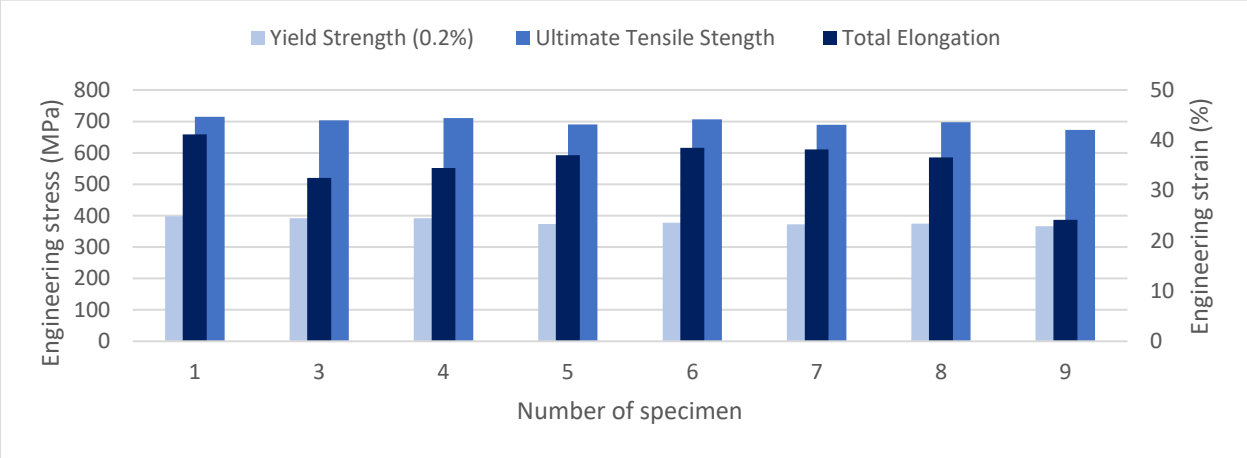

Figure 64: Yield and ultimate tensile strength, together with the total elongation for the vertical specimens manufactured from the non-heat treated block C1 produced at TU Delft. Specimen 2 was damaged during testing.

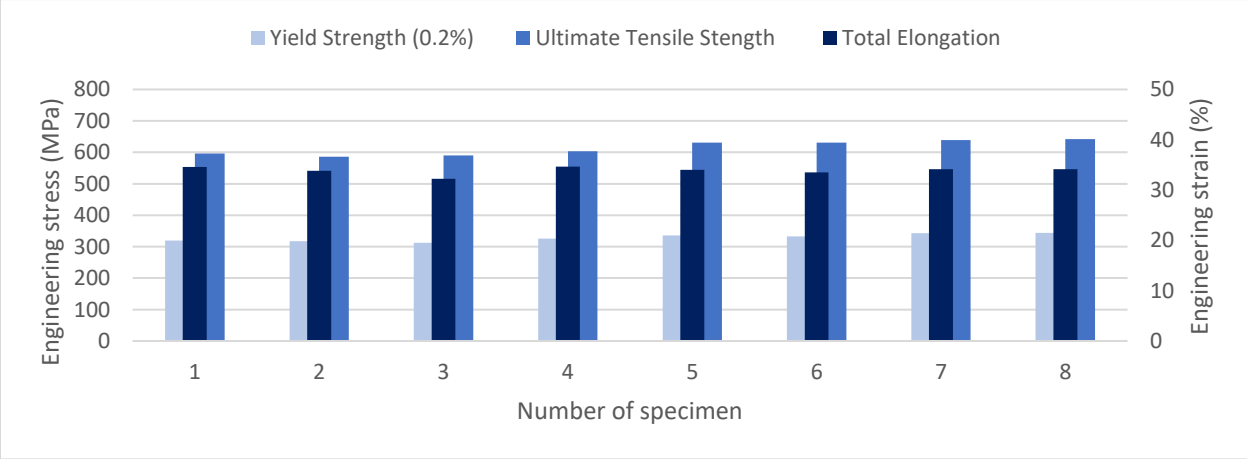

Figure 65: Yield and ultimate tensile strength, together with the total elongation for the vertical specimens manufactured from the heat treated block C2 produced at TU Delft. Specimen 9 was damaged during testing.

6.2.2 SPECIMENS FROM THE RAMLAB BLOCK

The following graphs in this chapter, Figure 66 and 67, deal with the results obtained from the tensile tests of the specimens of the block produced at RAMLAB. The graphs present the yield strength, the ultimate strength and the total elongation for the horizontal and vertical specimens, respectively.

The horizontal specimens exhibit a slight decrease with the built height in both the yield and the ultimate tensile strength. The total elongation shows the anticipated increase, as its trend is usually opposite to the ones of strength. The first specimen is machined from the bottom of the block and contains partly the substrate. Thus, its value cannot be compared to the rest results.

On the contrary, the vertical specimens, in Figure 67, present slightly lower but more uniform values than the horizontal specimens. This behaviour shows that the process of deposition was relatively steady, if the starts and the stops of the arc are discarded. The vertical specimen 6 was tested in two steps because of a software crash. During the first step, the specimen was loaded beyond the elastic region, but before necking. Thus, during the second attempt, work hardening was observed at the yield point, which was 13% higher. Nevertheless, the ultimate tensile strength and the total elongation remained unaffected.

Regarding the horizontal specimens produced at RAMLAB and at TU Delft, the yield strength values are similar, whereas the ultimate tensile strength of the RAMLAB specimens are approximately 10% lower than the TU Delft specimens. The elongation results present an interesting behaviour. The horizontal RAMLAB specimens have an elongation within the range of 20% and 26%, while the elongation of the TU Delft samples is between 35% and 45%. In a similar way, the vertical RAMLAB specimens show a 16% to 20% total elongation, whereas the respective range for the TU Delft vertical specimens is 35% to 40%. The reason for this difference will be discussed in chapter 8.

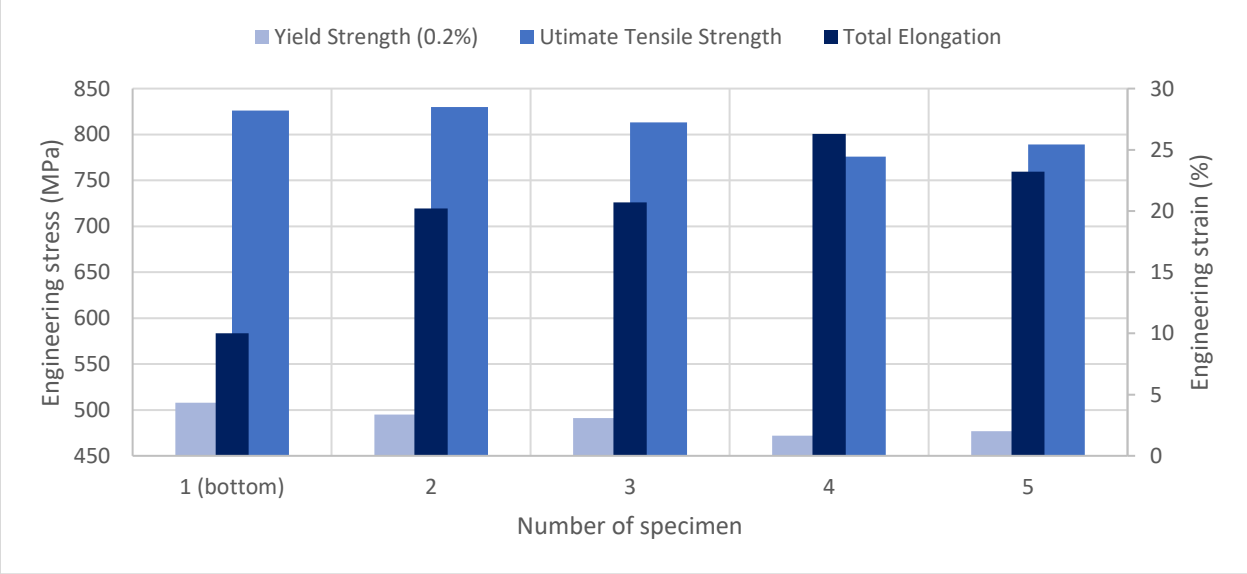

Figure 66: Yield and ultimate tensile strength, together with the total elongation for the horizontal specimens manufactured from the block produced at RAMLAB.

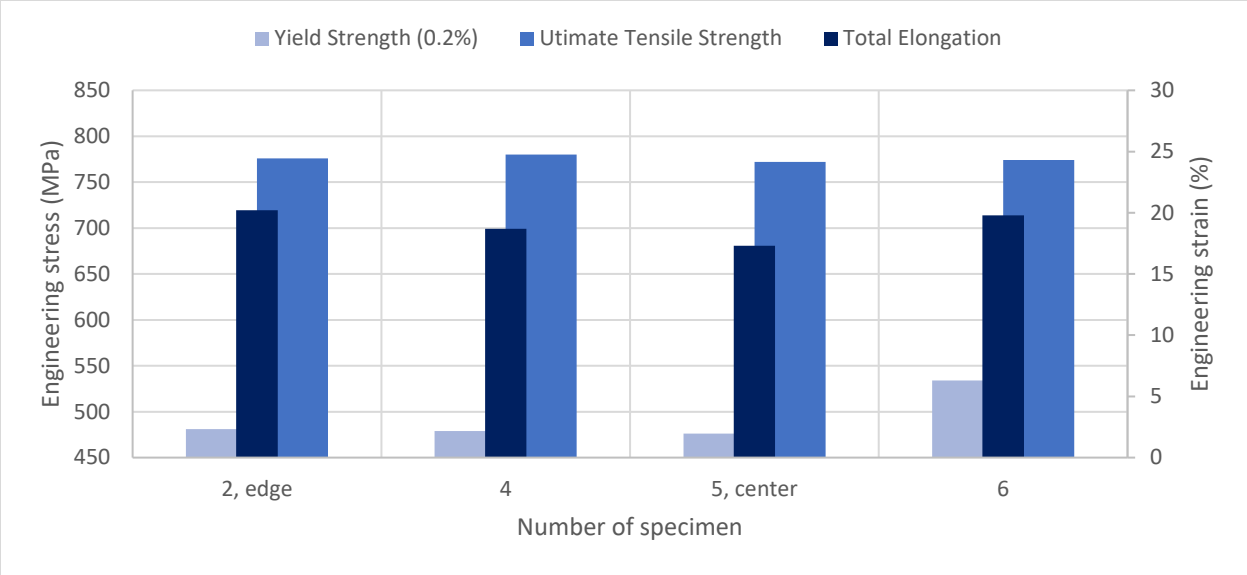

Figure 67: Yield and ultimate tensile strength, together with the total elongation for the vertical specimens manufactured from the block produced at RAMLAB.

The next graphs, Figure 68 and 69, illustrate the full stress-strain curve recorded during testing of the specimens from the block of RAMLAB. All of them show a smooth behaviour with no discontinuities. The work hardening of the vertical specimen 6, which was discussed previously, is evident in Figure 69 too.

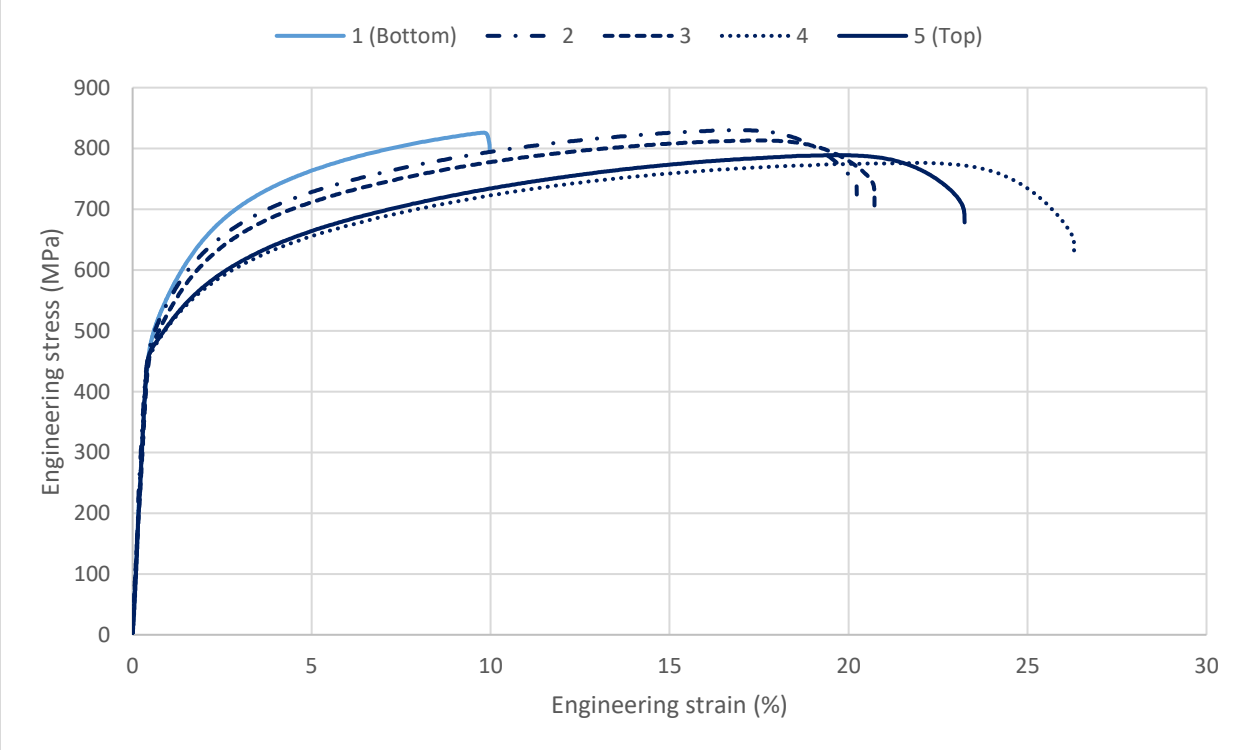

Figure 68: Engineering stress-strain curve of the horizontal specimens from the RAMLAB block.

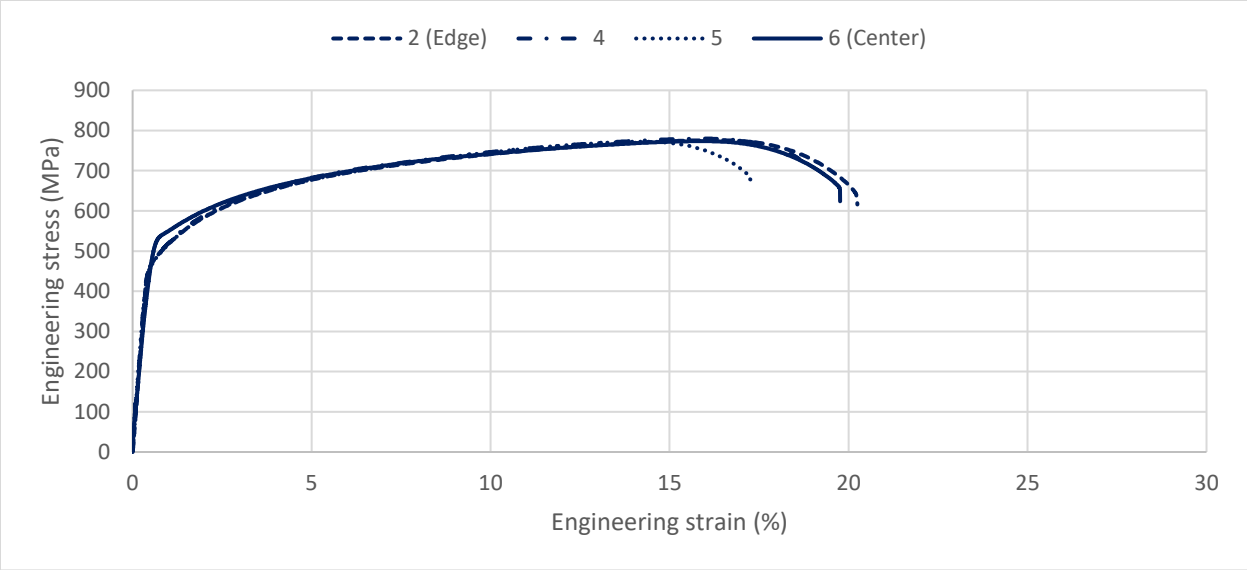

Figure 69: Engineering stress-strain curve of the vertical specimens from the RAMLAB block.

6.2.3 FRACTURE SURFACE

The fracture surfaces were investigated with the smallest magnification of the optical microscope. Figure 71 shows a horizontal fractured tensile specimen from the block produced at RAMLAB. In addition, Figure 72 shows on the left (a & c) the bottom parts, and on the right (b & d) the upper parts, of the vertical and horizontal fractured specimens. In both cases, the contraction of the cross-sectional area of the necking region is evident, along with the 45° inclination of the fractured surface relative to the central line of the axis. The central part of the cross section exhibits a horizontal fracture surface. The reason behind this morphology is elaborated in the discussion chapter 8.

A more in-depth analysis of the fracture surface, with the usage of SEM, is presented in Figure 70. There are regions showing cleavage, indicating brittle fracture, see Figure 70 (left), and others which clearly depict ductile behaviour, see Figure 70 (right). Details on these observations are reported also in the discussion part.

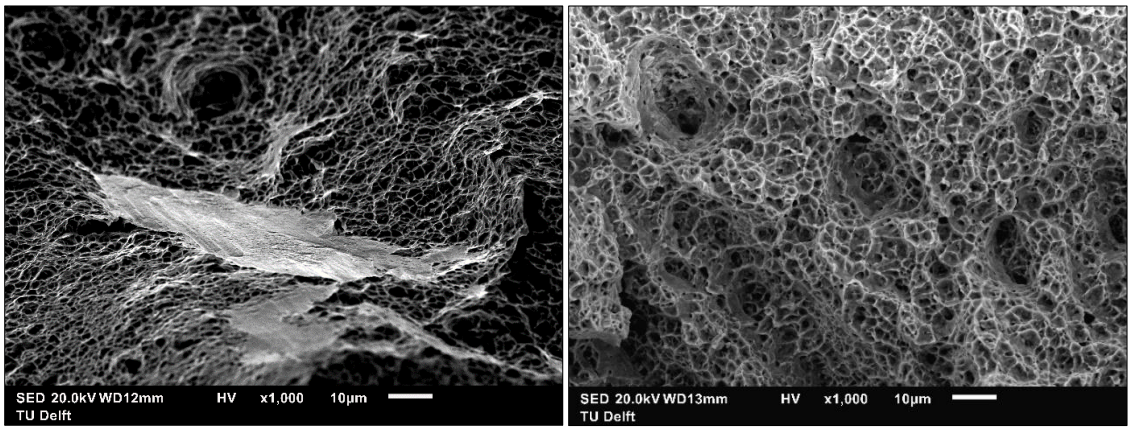

Figure 70: Fracture surfaces of the horizontal tensile specimen 3, of the block produced at RAMLAB, observed with SEM.

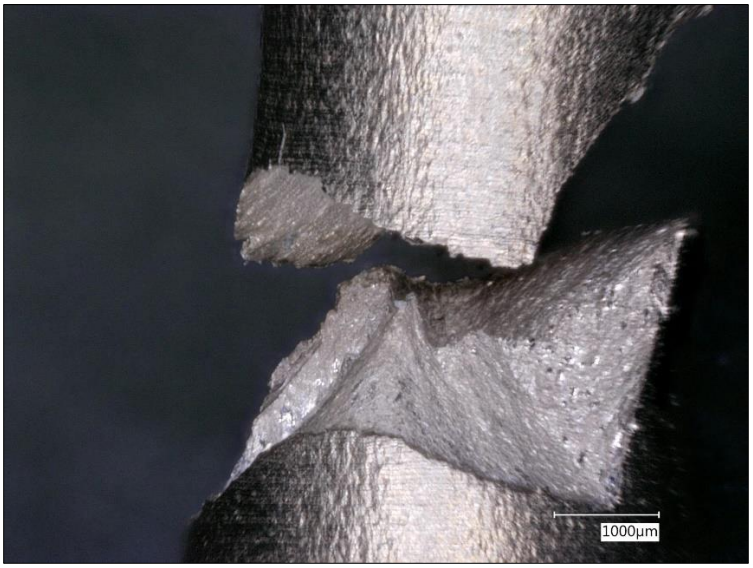

Figure 71: Macroscopic picture of the fracture area of a representative specimen of the block produced at RAMLAB.

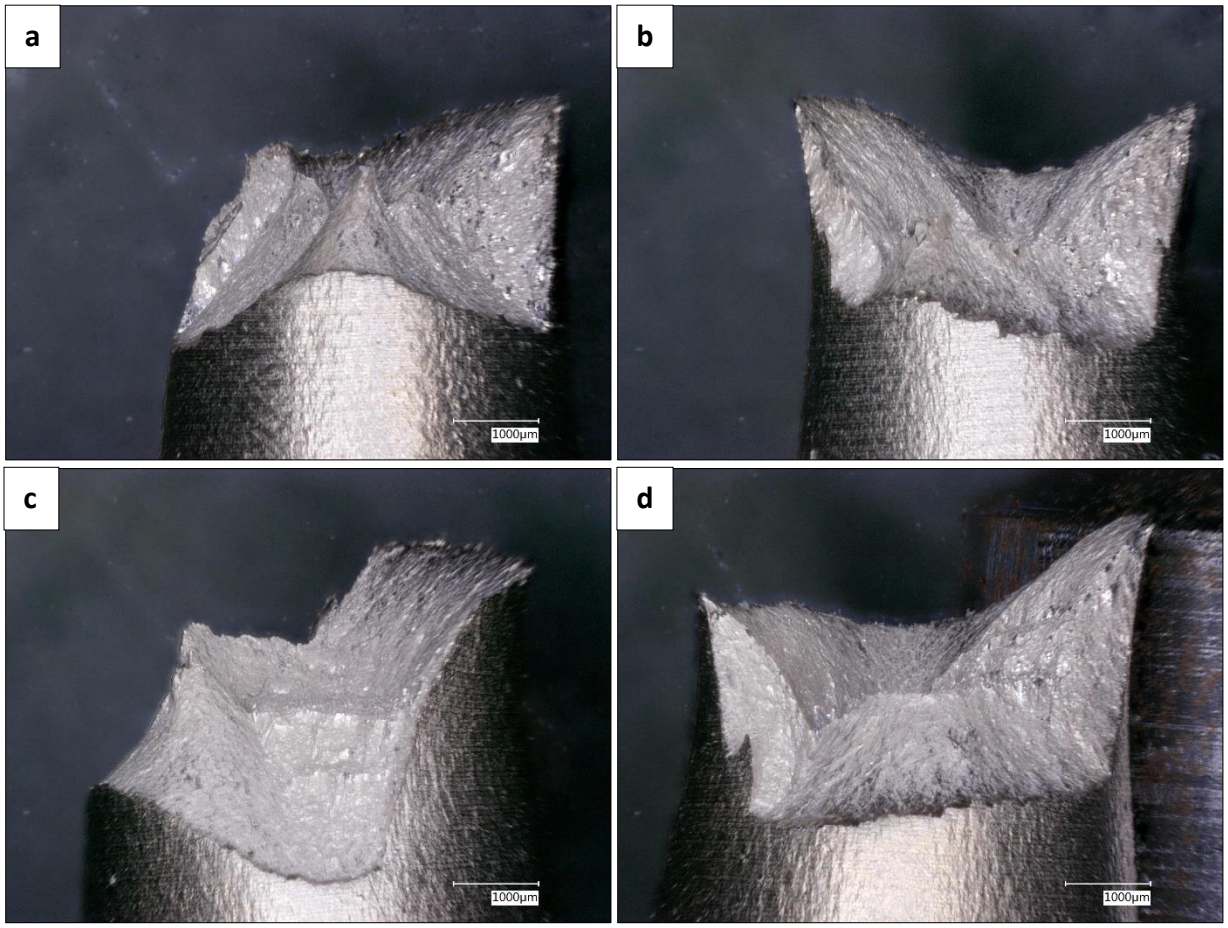

Figure 72: Macroscopic pictures of the fracture area of representative specimens of the block produced at RAMLAB. (a & b) Upper and bottom part of horizontal tensile specimen 3. (c & d) Upper and bottom part of vertical tensile specimen 4.

6.3 INSTRUMENTED CHARPY V-IMPACT TEST

6.3.1 ABSORBED ENERGY AND IMPACT STRENGTH

This paragraph deals with the results obtained from Charpy V-impact tests. These specimens are obtained from the block produced within the facilities of RAMLAB, as described in chapter 4.

At first, the absorbed energy, Figure 73, and the impact strength, Figure 74, are presented. These values can be extracted even from non-instrumented Charpy machines. The absorbed energy indicates the difference between the energy of the striker at the exact moment before the impact with the specimen and after the fracture of the specimen. The absorbed energy can be divided by the cross-sectional area of the specimen at the point of the notch, namely 80 mm^2, to calculate the impact strength.

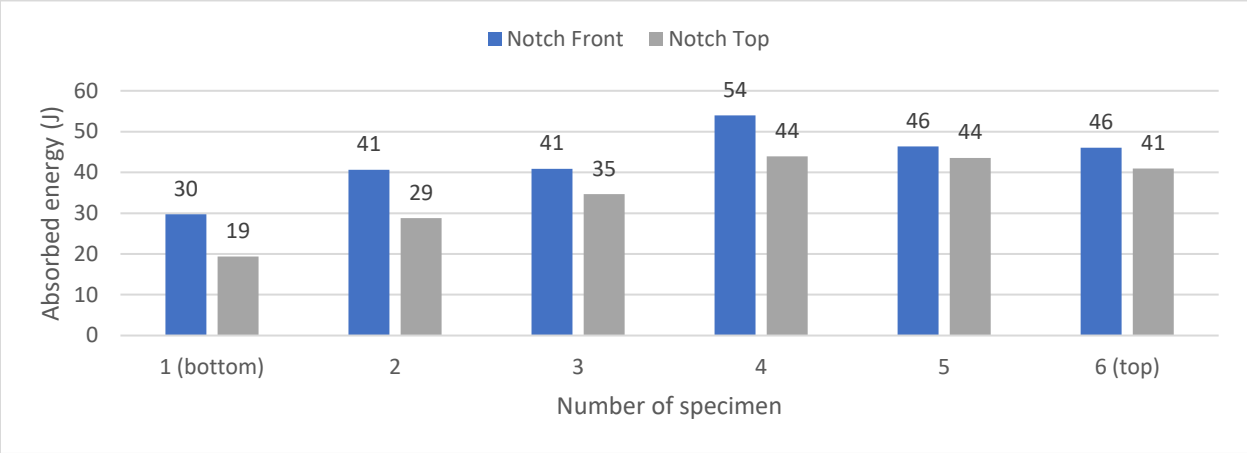

Figure 73: Absorbed energy values for the horizontal specimens with their notch facing sideways (blue) or top (grey). Specimens "1" are extracted from the bottom of the block, incorporating the interface and the built material, whereas specimens "6" were located at the top part of the block.

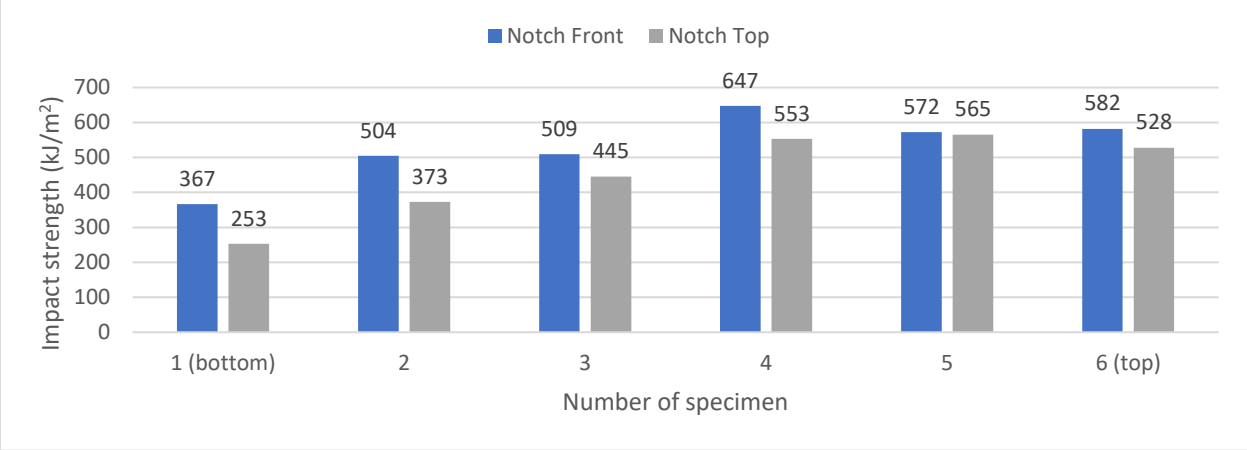

Figure 74: Impact strength values for the horizontal specimens with their notch facing sideways (blue) or top (grey). Specimens "1" are extracted from the bottom of the block, incorporating the interface and the built material, whereas specimens "6" were located at the top part of the block.

From the graphs above, two distinctive trends are evident. Firstly, the absorbed energy increases with the distance from the bottom of the wall. Secondly, the specimens with the notch facing sideways

exhibit higher absorption capability, up to 30%, than the ones with the notch facing top. It should be highlighted that the specimens "1" are extracted from the bottom of the block and consist of both the substrate and the built material. Therefore, these values cannot be compared with the other specimens.

Figure 75 shows the results of the vertical specimens at different testing temperatures. Unfortunately, due to geometrical constraints, only four specimens could be manufactured. The rest of the block produced at RAMLAB was used for the manufacturing of the tensile specimens. The value of absorbed energy at ambient temperature is the average of two measurements, and the remaining specimens were used to investigate the behaviour at -20 °C and -60 °C, respectively. Clearly, the impact strength of the material is deteriorated as the temperature drops. More specifically, the absorbed energy at -20 °C is 20% lower than the one at ambient temperature, whereas the value at -60 °C is 35% lower.

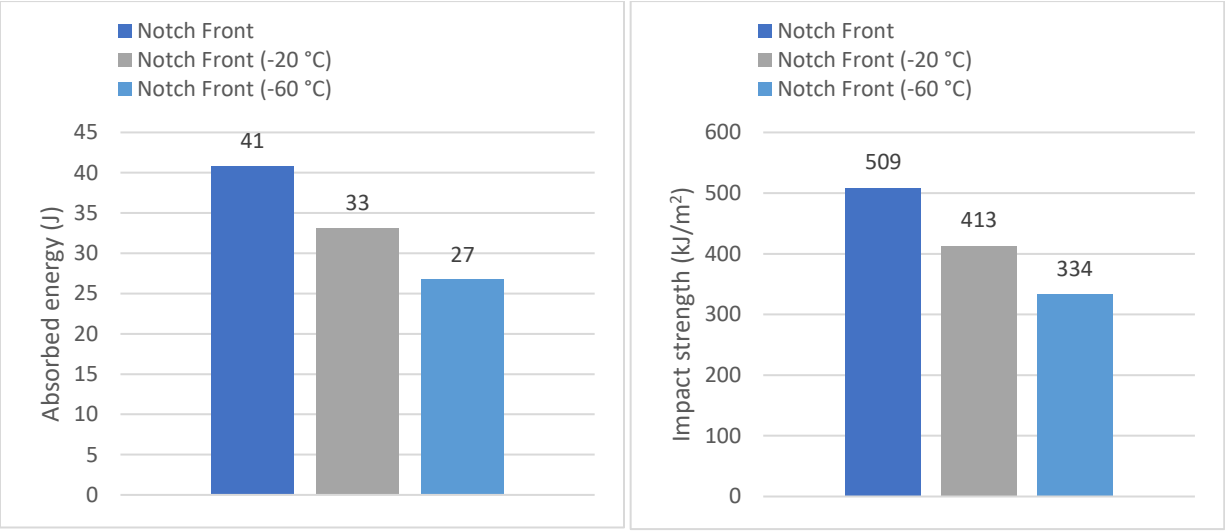

Figure 75: Absorbed energy (left) and impact strength (right) values for the vertical specimens at ambient temperature (dark blue), at -20 °C (grey) and at -60 °C (light blue).

6.3.2 LOAD MEASUREMENTS

The instrumented Charpy impact test provides data correlating the load at different moments during the fracture of the specimen. Plotting of these values not only represents the evolution of the process through time, but also gives information on characteristic values, such as the general yielding force, the maximum force, the force at unstable crack initiation and the crack arrest force, see Figure 76. Brittle specimens exhibit no general yielding. Thus, the maximum force is identical to the force at the initiation of the unstable behaviour, and the crack arrest force can be neglected. On the contrary, ductile materials exhibit a distinctive value for the above-mentioned forces [40].

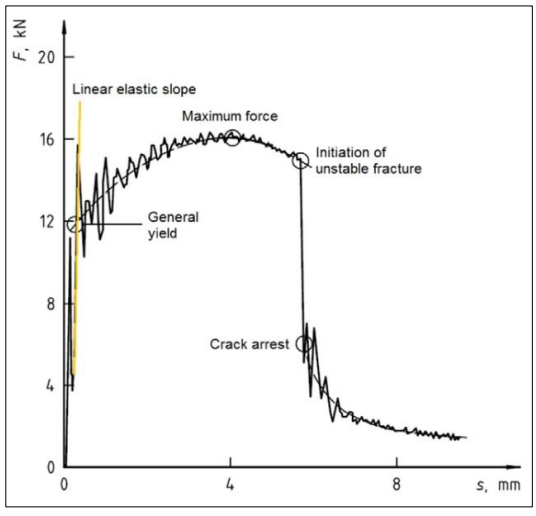

Figure 76: Characteristic load values during instrumented impact test [40].

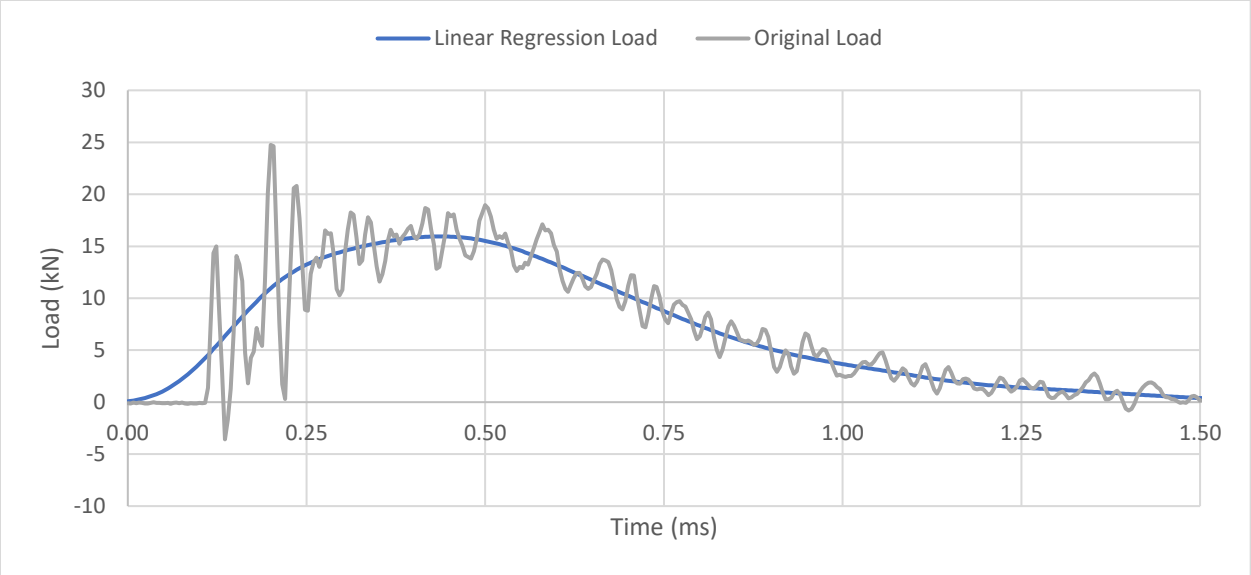

Figure 77: Record of the load during the impact test of the horizontal specimen 4 with the notch facing sideways. The grey line represents the original load data, as received from the sensor and the blue line shows a linear regression approximation.

The characteristic load values of all measurements are presented in Figure 78 to Figure 80. The general yield force, the maximum force and the force at unstable crack initiation present similar results in all specimens. Nevertheless, the crack arrest load exhibits the most interesting behaviour. This characteristic load exhibits the same trend for all the specimens as the absorbed energy (or as the fracture toughness). It may be concluded that the crack arrest load indicates at which extent the fracture is brittle or ductile in each case. The results present the same behaviour in all three categories of specimens, namely the ones with the notch facing sideways, Figure 78, towards the top, Figure 79, and the vertical specimens, Figure 80.

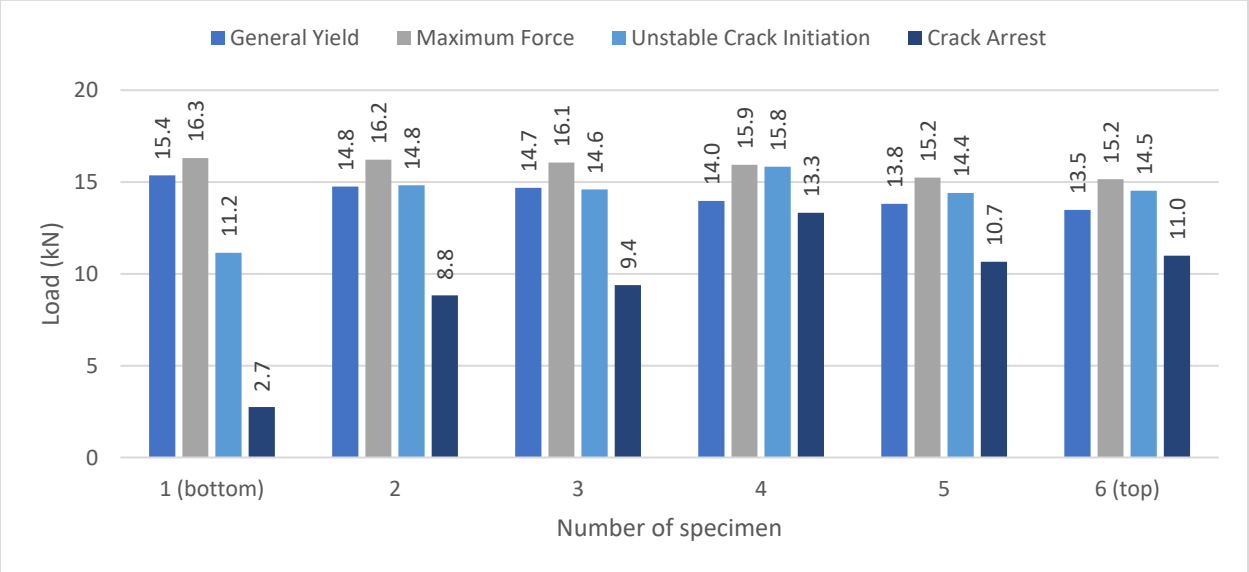

Figure 78: Characteristic load values during instrumented Charpy testing. The specimens are horizontal with their notch facing sideways.

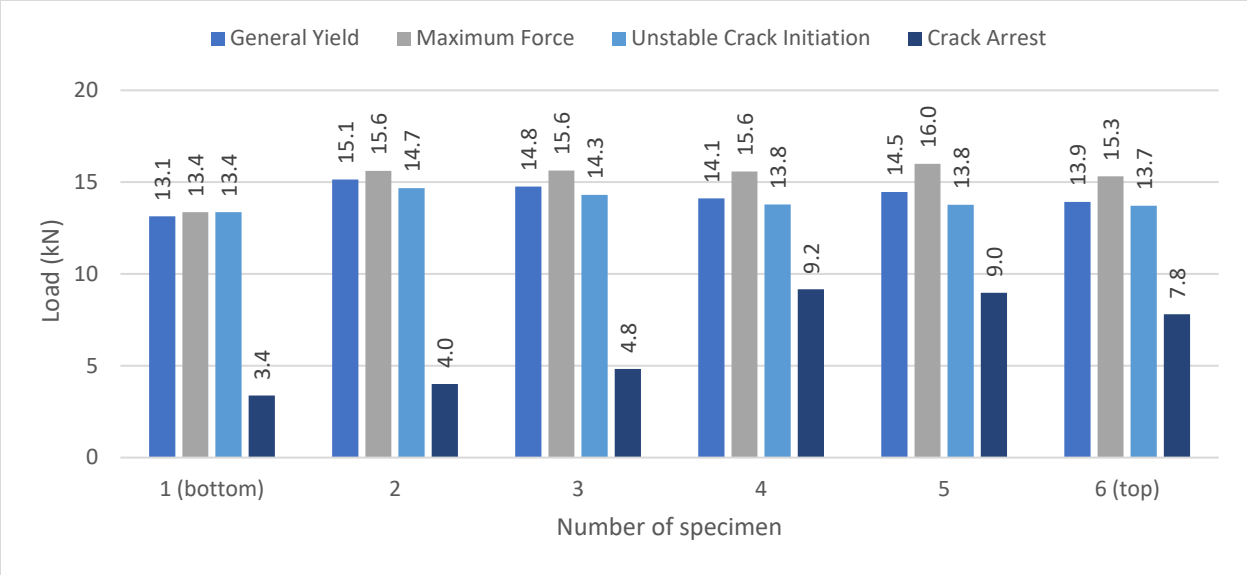

Figure 79: Characteristic load values during instrumented Charpy testing. The specimens are horizontal with their notch facing top.

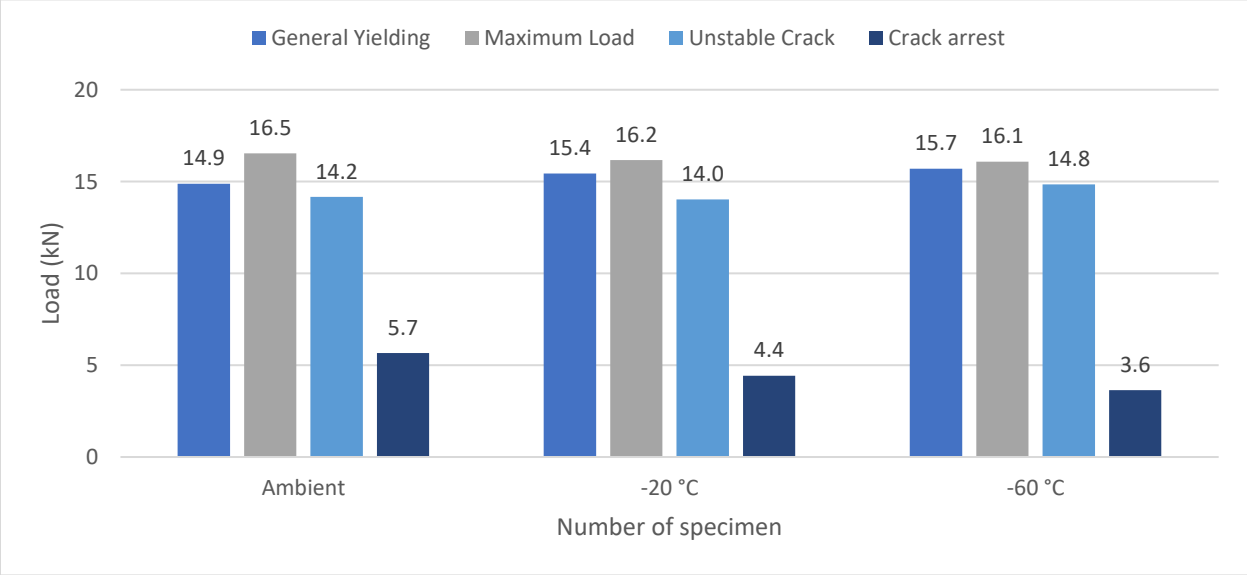

Figure 80: Characteristic load values during instrumented Charpy testing. The specimens are vertical and tested under different temperatures.

Another parameter that can be calculated is the dynamic yield strength. This value is of high importance in case an impact event is probable, as in propellers of ice-breaking vessels. For the calculation of the dynamic yield strength, certain parameters have to be defined according to Lucon [40].

At first, a constraint factor needs to be introduced, which expresses the ratio of load at general yielding to the force for yielding an unnotched specimen with the same cross section as the notched Charpy specimen.

$$C_{GY} = \frac{2M_{GY}}{\tau_{GY}(W-a)^2} \qquad (6.1)$$

, where

M_{GY}= bending moment at general yield per unit thickness
W= specimen width
α= notch depth
τ_{GY}= yield shear strength
σ_{GY}= yield tensile strength

The yielding criterion which will be used is the Von Mises criterion, involving the shear and tensile stresses at the onset of plastic deformation with the following equation.

$$\tau_{GY} = \frac{\sigma_{GY}}{\sqrt{3}} = 0.577\sigma_{GY} \quad (6.2)$$

Substituting equation (6.2) to (6.1), yields

$$\sigma_{GY} = \frac{3.732M_{GY}}{C_{GY}(W-a)^2} \quad (6.3)$$

The load case in Charpy specimen is a 3-point bending, because the specimen is supported at both sides at the anvils and the pendulum strikes at the midpoint. If the span to width ratio is equal to 4, then the bending moment per unit thickness is:

$$M = \frac{FW}{B} \quad (6.4)$$

, where B= width of the specimen and F= force. Substituting equation (6.4) to (6.3), yields

$$\sigma_{GY} = \frac{3.732F_{GY}W}{C_{GY}B(W-a)^2} \quad (6.5)$$

In our case, the instrumented striker has a tip of 8 mm radius, thus the C_{GY}=1.336 [40]. Moreover, B=10 mm and α=2 mm leading to:

$$\sigma_{GY} = 43.65F_{GY} \quad (6.6)$$

This value estimates the dynamic yield strength of the material at the uncracked ligament during the instrumented test.

The following graphs illustrate the calculated values of the dynamic yield strength, based on the general yield load measurements extracted from the instrumented Charpy test, for the horizontal, Figure 81, and the vertical specimens, Figure 82. The results depict that as the height of the block increases, the dynamic yield strength decreases. Furthermore, the specimens with the notch facing upwards exhibit slightly higher values than their counterparts with the notch facing sideways, up to 5%. The values of all the specimens are between 588 MPa and 661 MPa, neglecting specimens “1”. In general,

the calculated dynamic yield strength is 25% higher than the static yield strength. This behaviour may be attributed to the increased strain rate that accompanies the impact test.

The vertical specimens indicate once more the embrittlement that is caused by the decrease in temperature. As the testing temperature drops, the onset of general yielding is delayed. However, even in the extreme case, where ambient conditions and -60 °C are compared, the increase of dynamic yield strength is a mere 3%.

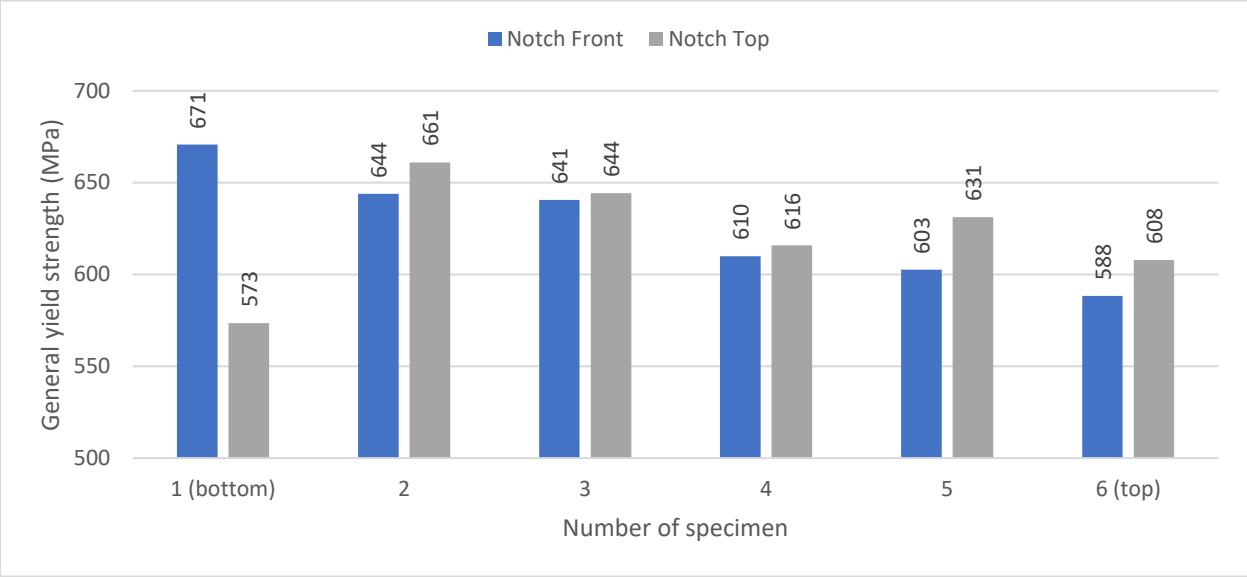

Figure 81: Dynamic yield strength for the horizontal Charpy specimens.

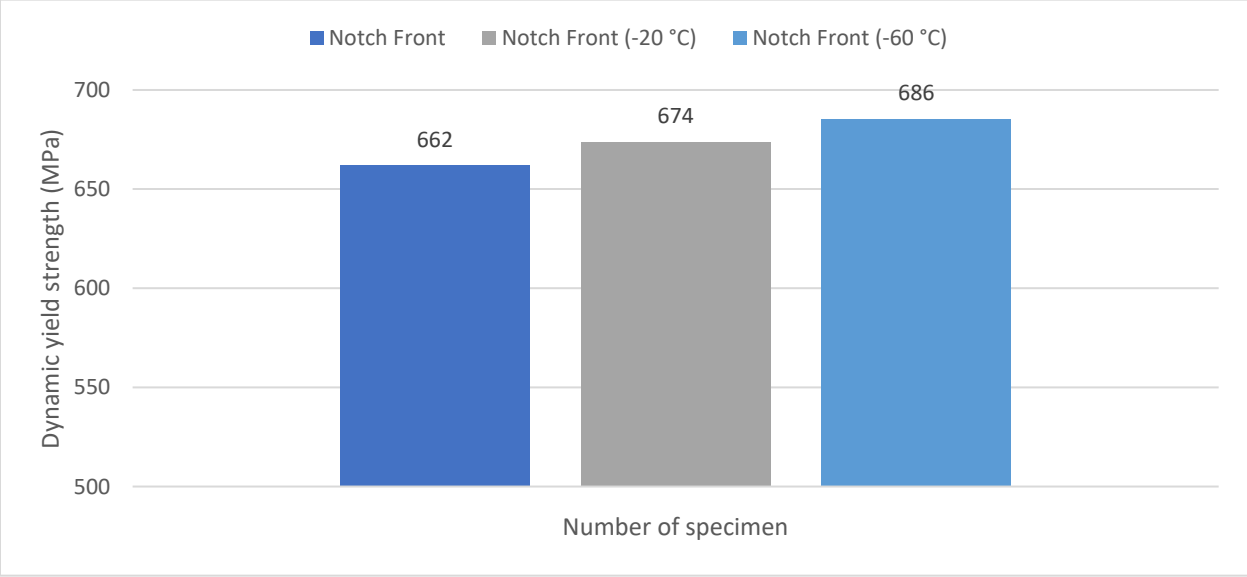

Figure 82: Dynamic yield strength for the vertical Charpy specimens.

6.3.3 FRACTURE SURFACES

The fracture surfaces were investigated initially by optical microscopy. Figure 83 shows different cases of horizontal and vertical tensile specimens, extracted from representative regions of the block manufactured at RAMLAB. In the pictures, there are annotations indicating several geometrical measurements, which are useful to estimate the extent of brittle or ductile behaviour. In all four pictures, the shear lips at the sides of the specimens are evident, and the geometrical characteristics are summarized in Table 11.

The pictures (a) and (b) of Figure 83 illustrate the fracture surface of the bottom specimens, near the base plate. The grey region is the filler material, whereas the tainted yellow areas represents the substrate. It is worth mentioning, that in Figure 83 (a), where the notch is facing sideways, the two parts of the specimen behave differently. The substrate exhibits greater shear lips, indicating a higher ductility. In addition, in Figure 83 (b), in which the notch is facing towards the top, the materials are deformed to a different extent. The shear lip at each side does not exhibit a continuous, bow-like shape. It has a double bow form, because the interface region has deteriorated ductility, as confirmed by the tensile testing results.

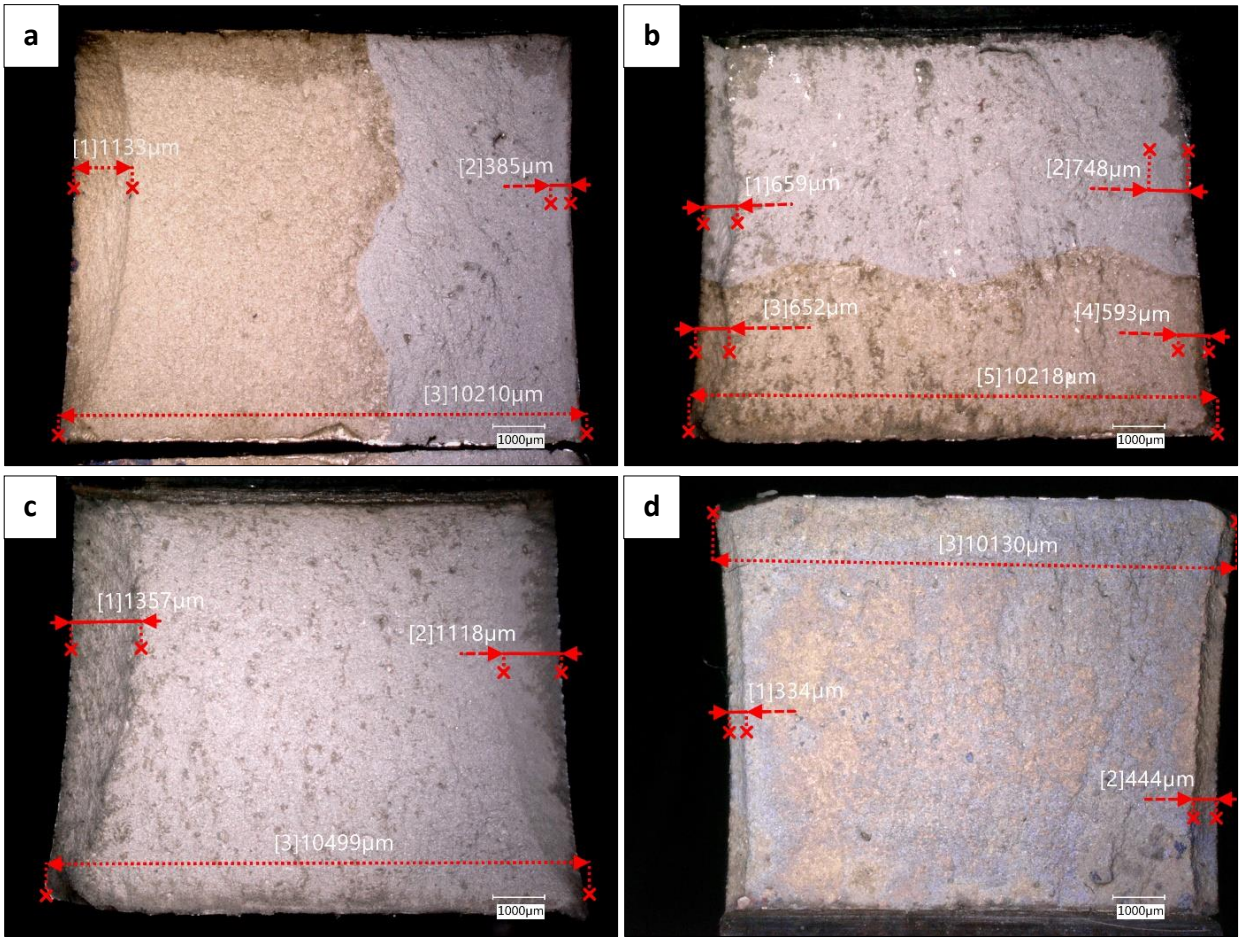

Figure 83: Fracture surfaces under the optical microscope for the following cases: (a) horizontal specimen 1, with the notch facing sideways, (b) horizontal specimen 1, with the notch facing top, (c) horizontal specimen 4, with the notch facing top, (d) vertical specimen, tested at -60 °C.

Subsequently, Figure 83 (c) and (d) illustrate the difference between a specimen tested at ambient temperature and at -60 °C. The contraction is significantly smaller at low temperatures, as Table 11 depicts. Moreover, the fracture surface has a shiny appearance in the case of brittle fracture, Figure 83 (d), whereas a dull appearance is evident for the ductile fracture, Figure 83 (c).

Concerning the data presented in Table 11, the lateral expansion is reduced for the vertical specimens, in comparison with the horizontal ones. Moreover, within the group of the vertical specimens, the lateral expansion reduces with the temperature. The interface specimens exhibit values similar to the vertical specimens which are tested at -20 °C.

Table 11: Average value of shear lip width and lateral expansion of six categories of Charpy specimens.

Specimen	*Shear lip (μm)*		*Lateral expansion (μm)*
Horizontal	1100		500
Vertical (ambient temp.)	860		300
Vertical (-20 °C)	660		240
Vertical (-60 °C)	400		120
	Shear lip 1 (μm)	*Shear lip 2 (μm)*	
Interface 1 (notch facing sideways)	1120	377	225
Interface 1 (notch facing top)	650	650	220

In Figure 84 (a & b), the fracture surfaces of Charpy specimens with the notch facing sideways or top are depicted. It appears that there are no major differences between the fracture mechanisms. In both cases, dimples are observed, indicating fracture by microvoid coalescence, a typical mechanism of ductile behaviour. Moreover, the dimples seem to be elongated parallel to the application of the force. This phenomenon indicates tensile tearing and is analysed in the discussion chapter 8. However, in Figure 84 (c) the situation is different. There is no distorted, elongated edge, showing a small amount of deformation. The flat, plate-like surfaces observed are typical examples of the cleavage mechanism. Thus, fracture in this case is governed by a brittle behaviour.

Moving on to Figure 85, the surface of the interface and the substrate area are illustrated. Specifically, in Figure 85 (a) the interface area is evident, if the reader focuses on the boundary between the white etched right region and the dark etched left region. Despite the colour difference, the fracture surfaces are similar at low magnification. However, at high magnification of the boundary of the two regions, Figure 85 (a, right), elongated dimples are observed on both sides of the substrate.

The fracture surfaces of the substrate are shown in detail in Figure 85 (b). Both straight and distorted surfaces are observed, confirming the decreased ductility of the substrate in comparison with the filler material. In addition, Appendix C contains graphs which present the energy absorption and the impact load records during the impact testing of all the Charpy V-notched specimens.

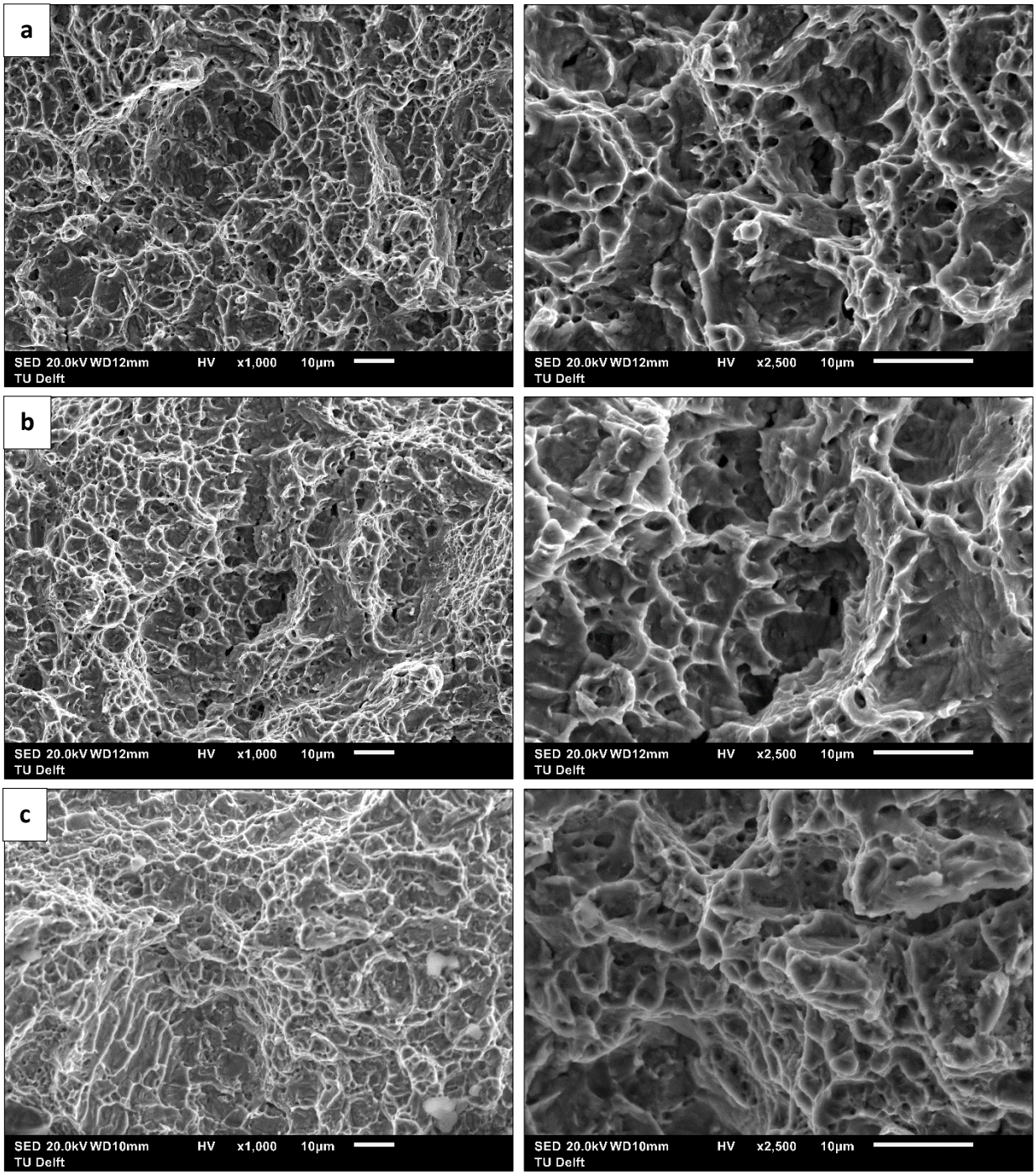

Figure 84: SEM photos at low magnification (left) and high magnification (right), of the following cases: (a) Horizontal Charpy specimen 4, with the notch facing top, (b) Horizontal Charpy specimen 4, with the notch facing sideways, (c) vertical Charpy specimen, tested at -60 °C.

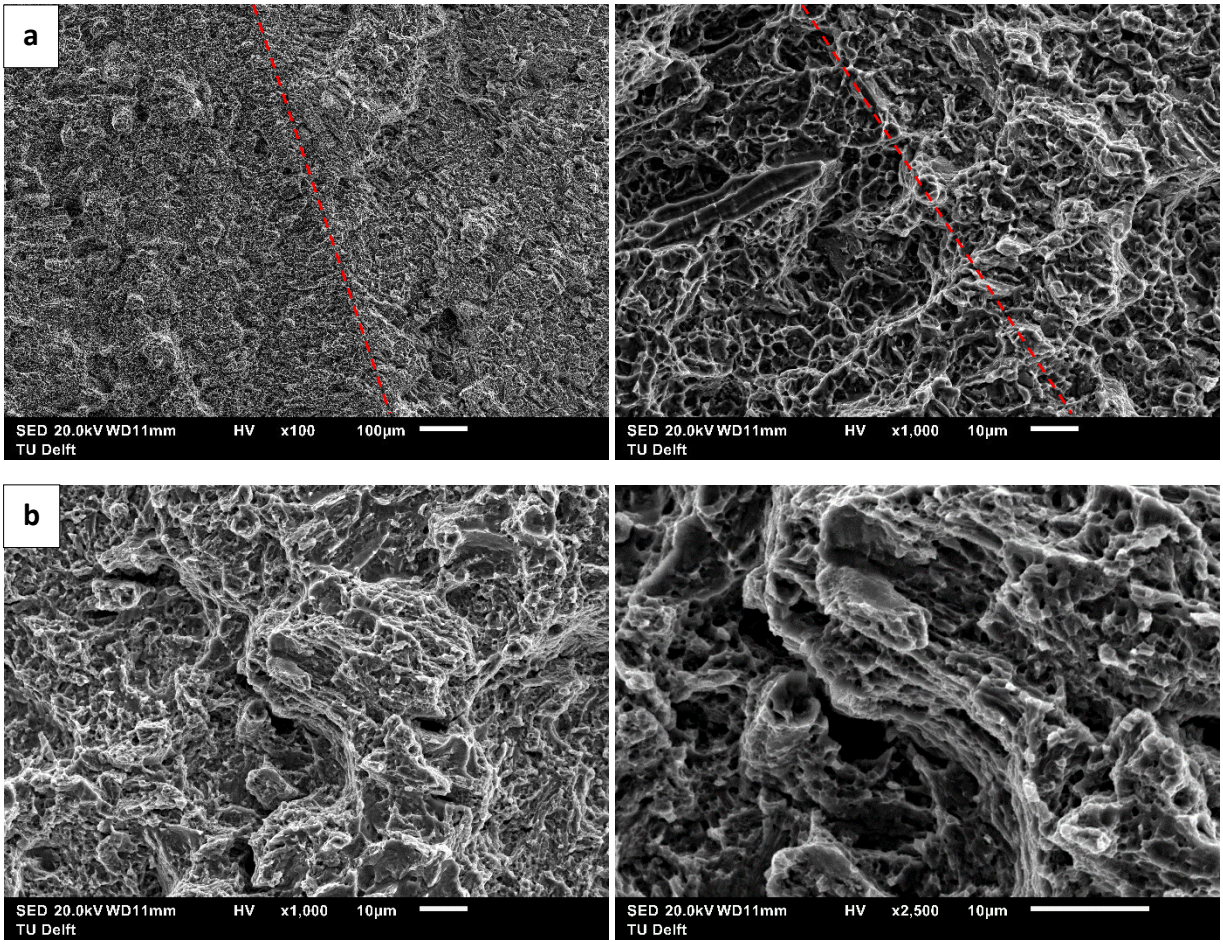

Figure 85: SEM photos at low magnification (left) and high magnification (right), of the following cases: (a) Interface between the substrate and the filler material of the horizontal Charpy specimen 1, (b) Horizontal Charpy specimen 1, at the side of the NAB alloy (substrate).

7. CORROSION TESTING RESULTS

7.1 OPEN CIRCUIT POTENTIAL (OCP) AND POLARIZATION CURVES

This paragraph presents the results obtained from the open circuit potential testing and the polarization experiments. As explained in chapter 4, the experiments were performed in four different areas of the built material, covering the whole height. Furthermore, results were also extracted from the interface of the first weld bead between the substrate and the filler and from the substrate.

Figure 86 illustrates the OCP measurements of the C1 block, whereas Figure 87 shows the polarization behaviour. Figure 88 and 89 show results of block C2, which is a heat-treated sample. The results of this set of experiments were chosen as representative examples of the majority of the tests performed. Similar graphs from the experiments conducted on blocks A1, A2, B1 and B2 are reported in Appendix D.

Focusing on the OCP test of Figure 86, the substrate presents the most positive equilibrium potential, if test 3 is ignored. OCP experiments are very sensitive to the surface finish of the sample. Thus, there are cases like test 3 presented below, where the result is misleading and does not reflect reality. Moreover, the polarization curve of area 3 at Figure 87 shows that the E_{corr} is between the values of area 2 and 4. Judging from the analysis of all the results, including the ones presented in Appendix D, the 3D printed material presents a corrosion behaviour which is slightly affected by the build height. The OCP value of the most specimens lies between -0.20 V and -0.25 V. However, in every specimen there is an area (1, 2, 3 or 4), which deviates significantly.

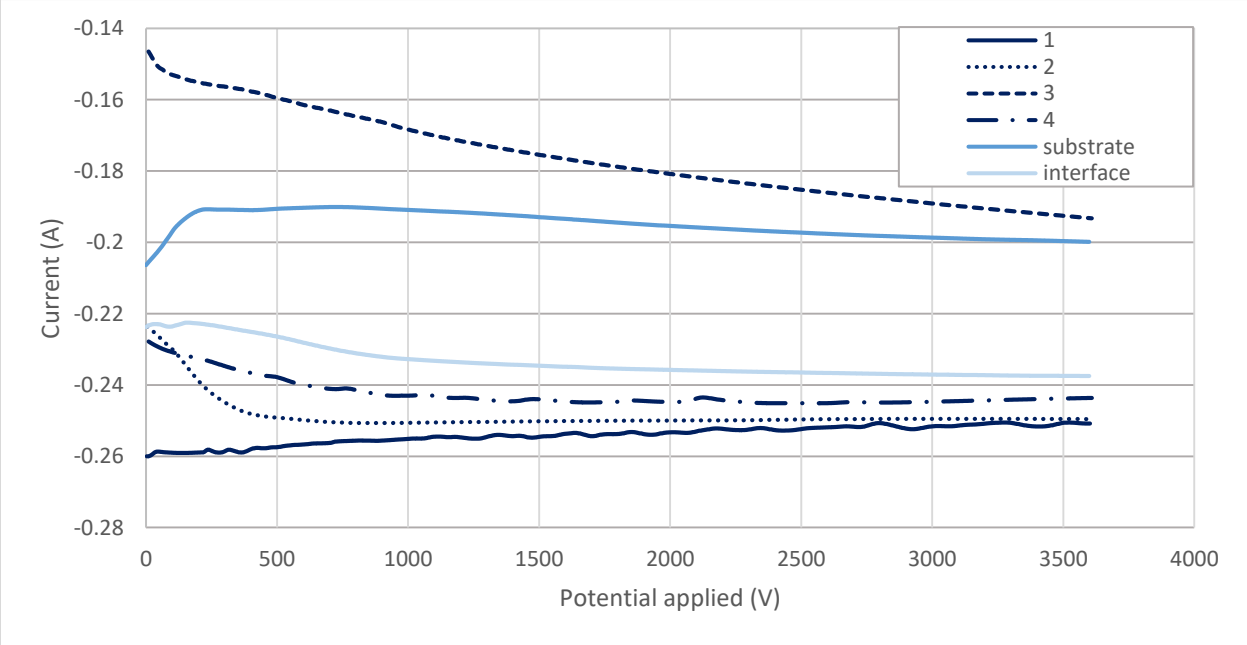

Figure 86: OCP results for the non-heat treated specimens, block C1 (feed rate: 11.5 m/min, travel speed: 6.7 mm/sec).

The polarization curves of Figure 87 show the anodic and cathodic reaction of the corrosion procedure. The cathodic (left) branch of the curves is a smooth line with no discontinuities, depicting that there is only one cathodic reaction taking place. However, the anodic branches present a step-wise curvature, indicating that there are more than one anodic reaction occurring.

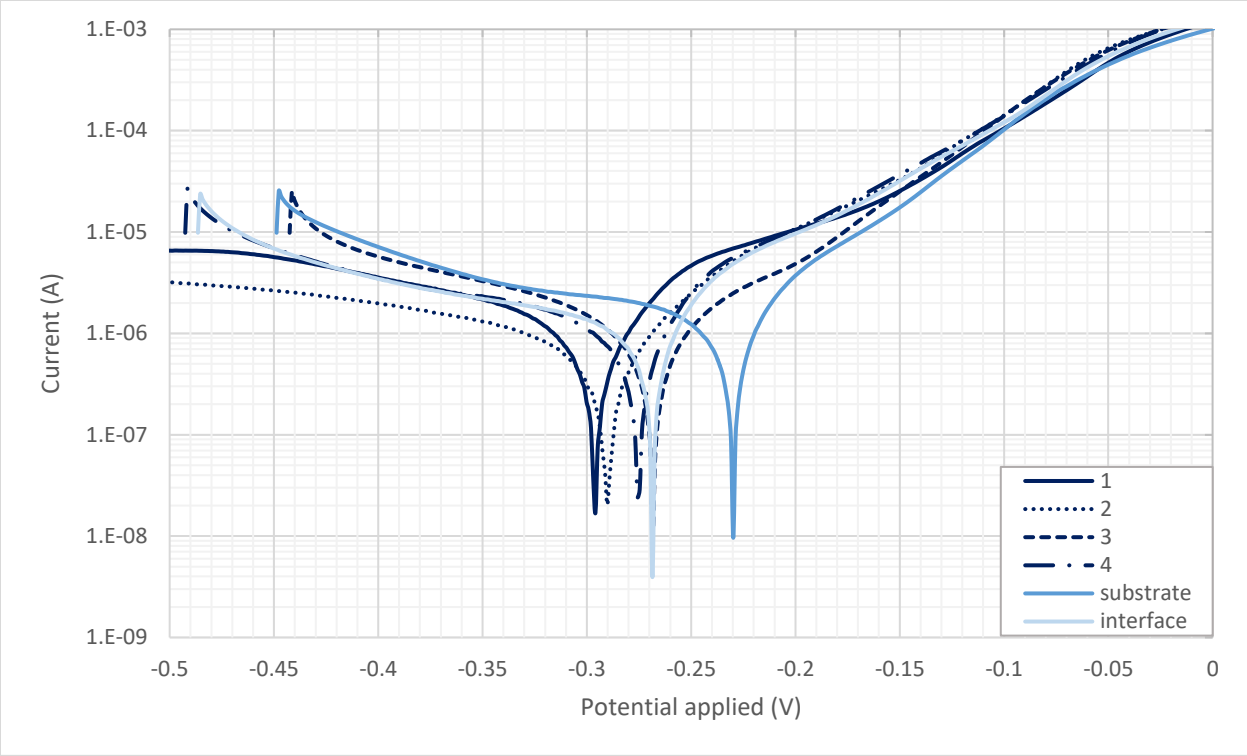

Figure 87: Polarization results for the non - heat treated specimens, block C1 (feed rate: 11.5 m/min, travel speed: 6.7 mm/sec).

In Figure 88, the reader may observe the OCP results of the filler material areas 1, 2, 3, and 4 of the heat-treated case. The microstructure of the heat-treated sample is more homogeneous and this leads to converging results. After one hour of experiment, all specimens show an OCP potential (V_{OCP}) close to -0.23 V. The same trend is also observed in the polarization curves of Figure 89, where the different lines are almost indistinguishable. The step-wise behaviour of the anodic part is even more evident in this case, than the results of the non-heat treated specimens of Figure 87.

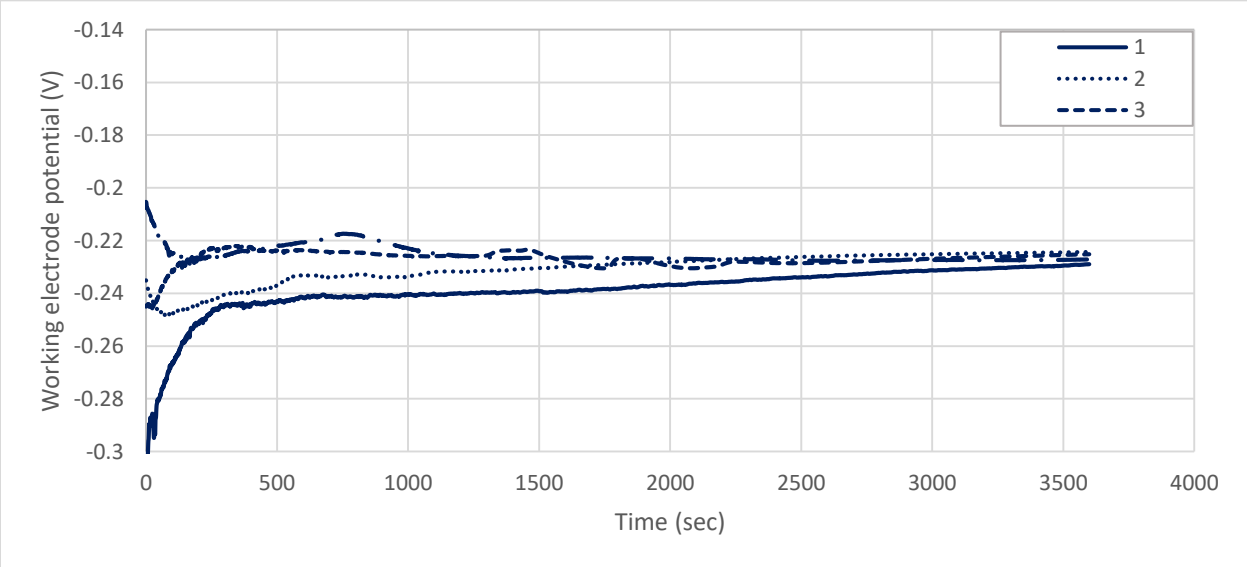

Figure 88: OCP results for the heat treated specimens, block C1 (feed rate: 11.5 m/min, travel speed: 6.7 mm/sec).

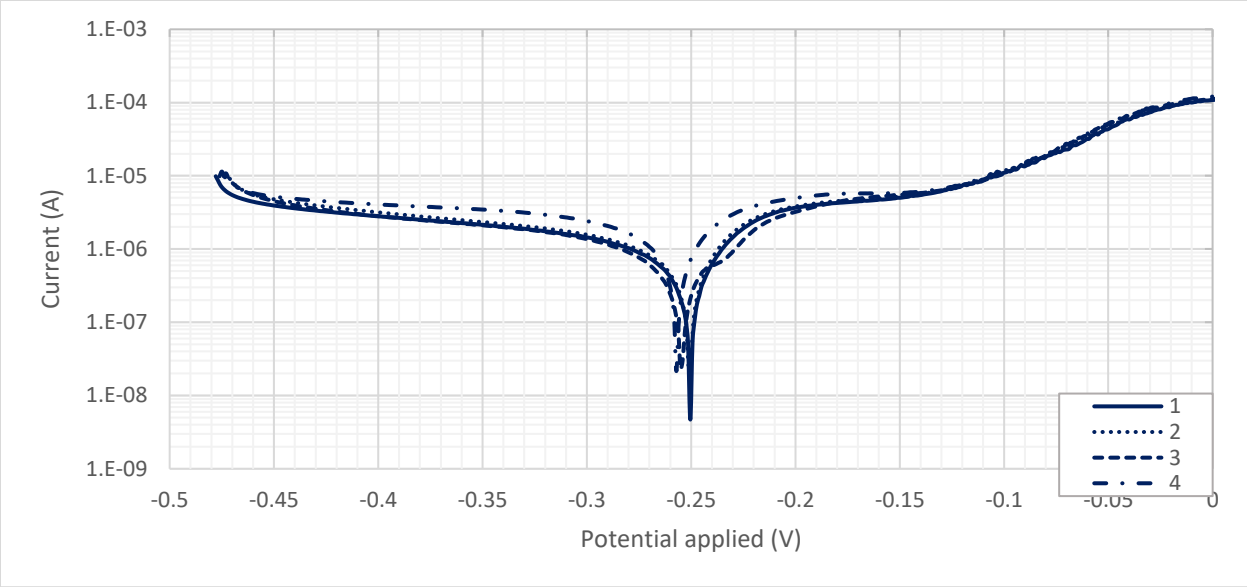

Figure 89: Polarization results for the heat treated specimens, block C1 (feed rate: 11.5 m/min, travel speed: 6.7 mm/sec).

For the quantification of the polarization results, the Tafel method was used. This method enables the approximate calculation of the current with a linear extrapolation of the two slopes of the polarization curves. The intersection coordinates are the corrosion current and the corrosion potential. Faraday's law is applied to calculate the corrosion rate [42], for a=60 g/mol, n=2, D=7400 kg/m^3.

$$r = \frac{ai}{nFD}\ [\frac{m}{sec}] \qquad (7.1)$$

, where

α= atomic number
n= number of electrons exchanged in reaction
F= faradays constant (96500 C/mol)
I= current density [A/m^2]
D= density [kg/m^3]

Figure 90 depicts that the corrosion rate results for the non-heat treated A1 specimen are reproducible, except for area 2, in which the one side of the specimen exhibits twice the value of the other side. Moving on to the specimens B1 and B2, Figure 91 illustrates that the non-heat treated samples show large deviations between the two sides in all the tested areas. Area 4 is an exception presenting values around 0.048 mm/year. The situation is changed in the case of the heat treated specimens. The areas 3 and 4 have similar values in both sides. However, the top and bottom areas 1 and 4, respectively, still exhibit large deviation.

The last case includes the C1 and C2 specimens and is presented in Figure 92. The non heat samples show less scattering than the samples of A and B blocks. The area 1 exhibits still the greatest difference between the corrosion rate of the two sides. The heat treated case show less scattering of the results, which are within the range of 0.034 and 0.063 mm/year. Areas 1 and 4 show again the largest difference between the two sides.

The above observations show no clear trend in the corrosion rate of the samples. However, it is evident that the material behaves satisfactory to this particular environment, exhibiting a lower corrosion rate than the commonly accepted rate of 0.15 mm/year [42]. Specifically, all measurements are in the range of 0.023 to 0.1 mm/year, whereas most of them lay in the vicinity of 0.05 mm/year. Furthermore, the top (1) and bottom (4) areas present the largest deviation between the two sides, even in the case of the heat treated samples.

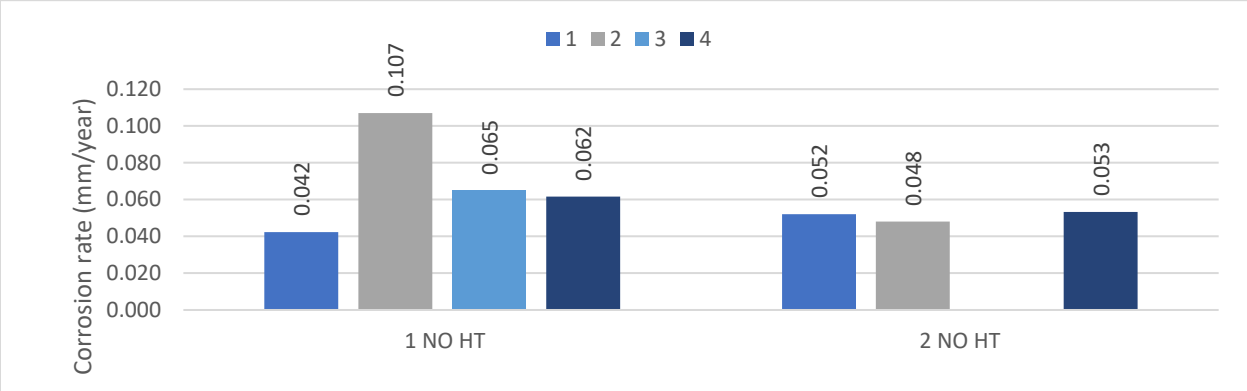

Figure 90: Corrosion rate results concerning the two sides of the sample from block A (non-heat treated).

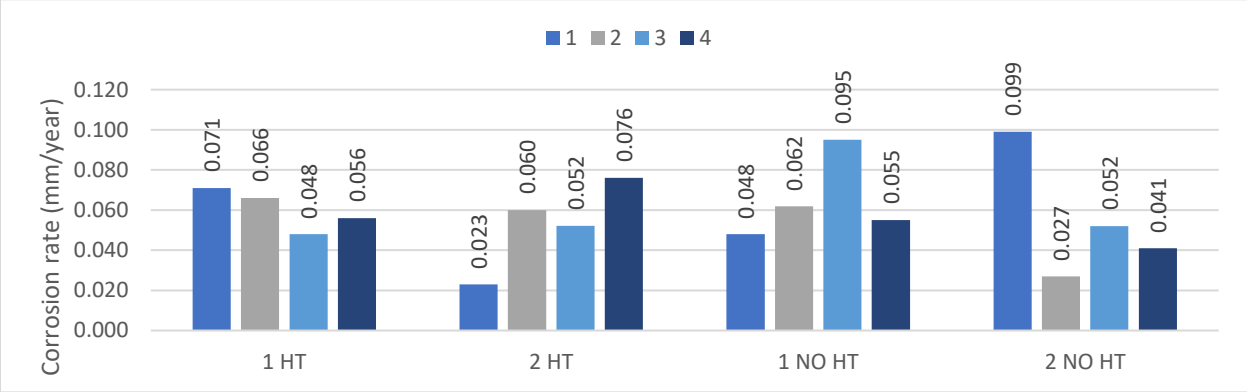

Figure 91: Corrosion rate results concerning the two sides of the sample from block B. The bar chart covers both the heat treated and the non-heat treated case.

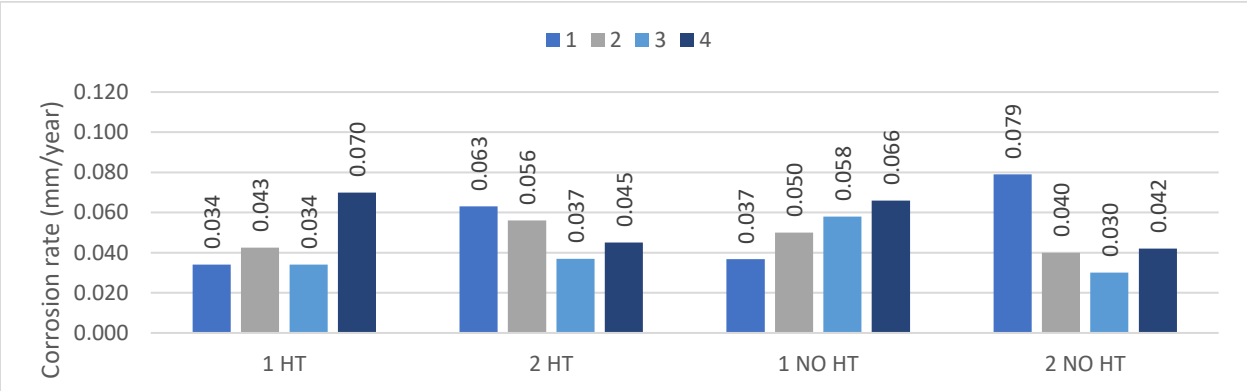

Figure 92: Corrosion rate results concerning the two sides of the sample from block C. The bar chart covers both the heat treated and the non-heat treated case.

7.2 SCANNING KELVIN PROBE (SKP)

The following graph, Figure 93, presents the results of the SKP experiments. Specifically, the dark blue lines, both continuous and dotted, show the contact potential difference (CPD) of the top part of the non-heat treated and the heat treated sample of the A block, respectively. In a similar way, the light blue line represents the bottom part. Furthermore, the first 10 data points belong to the substrate and the weld metal of the first bead, while the measurements 11 to 100 cover the remainder height with an interval of 200 μm. Finally, the measurements 101 to 200 illustrate the behaviour of the top part of the sample, with the last measurement recorded at the top layer of the block. The distance between these measurements is also 200 μm.

The graph depicts several trends of the CPD values. Starting with the non-heat treated sample, the substrate exhibits approximately 500 mV CPD, which is lower than the approximate values of the bottom part of the filler material, 650 mV. Moving to the top part, a gradual increase is observed, which results in a steep increase of the CPD at the top deposited layer. In any case, adjacent regions present similar values, within a range of 50 mV. The few extreme values should not be considered as indicative because the SKP method is remarkably sensitive to the surface condition of the sample.

As anticipated, the heat treatment of the sample homogenises the microstructure, leading to uniform CPD values throughout the deposited bock. It should be highlighted that at the bottom part, the heat treatment results in a 13% elevation of the recorded values, in comparison with the as received sample, while at the top part the measurements show a slight drop, in the order of 13% too.

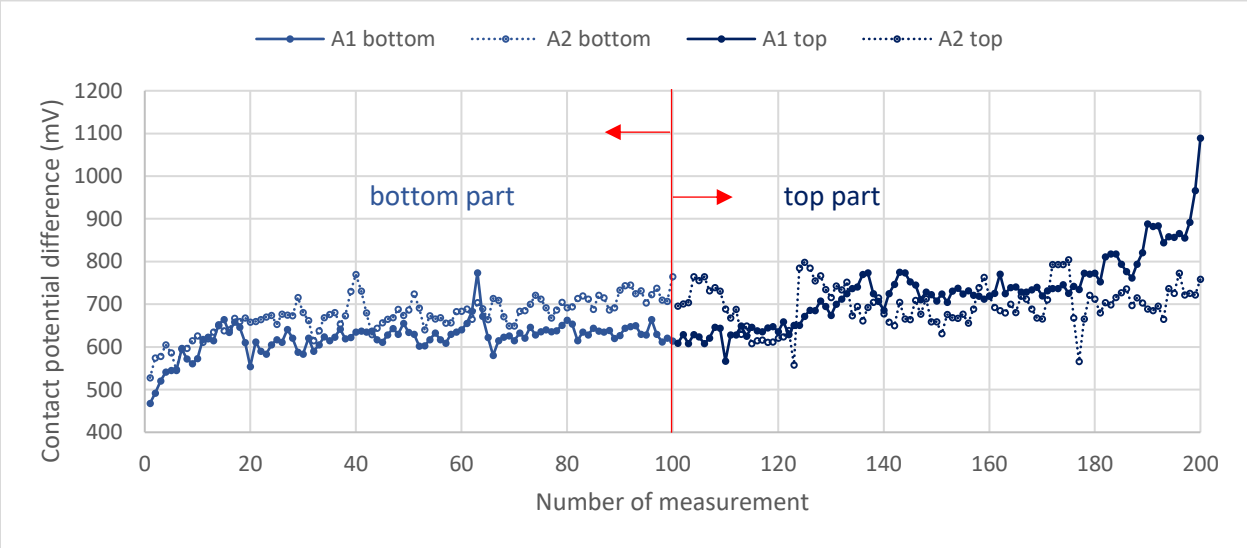

Figure 93: SKP results of the A block, with and without heat treatment. The contact potential difference is plotted for 200 measurements for the heat and the non-heat treated sample. The first 100 values belong to the bottom part and the rest 200 to the top part.

8. DISCUSSION

This chapter attempts to explain the mechanisms, responsible for the microstructural observations and for the mechanical and corrosion behaviour mentioned previously. Furthermore, the feasibility of the WAAM method, as an alternative to produce the aluminium bronze propellers, is evaluated.

8.1 MECHANICAL BEHAVIOUR

8.1.1 STRENGTHENING EFFECTS

The microstructure developed during the building of the constructions determine the mechanical behaviour. The CMA alloy consist mainly of two phases, α and β, along with certain precipitates. The percentage of the two phases outmatches the volume fraction of the precipitates and determines the mechanical behaviour of the material to a large extend. However, the precipitates cannot be ignored, because they have the ability to pin the dislocations. The α phase has an FCC structure, meaning that there are 12 slip systems, {111} <110> [43]. The preference of {111} as slip planes can be explained easily, if we consider that this family of planes is the most densely packed, providing a relatively smooth, frictionless slip surface. On the contrary, β phase has a BCC structure. Dislocation gliding in this case is not restricted to slip planes, because there is no match between the dense planes and the dense direction. More specifically, the (100) is the densest plane, but does not contain the <111> direction. Therefore, in BCC material the dislocation glide usually occurs at a defined direction, in which the Burger's vector is parallel to <111>, but not on certain plane (pencil glide mechanism) [43]. For comparison reasons, the HCP has only two independent slip systems, forcing the material to deform in the prismatic or the pyramidal planes, or by activating secondary deformation mechanisms, such as twinning [43]. It can be concluded that the α phase provides ductility, whereas the β phase together with the precipitates provide strength. This explains also the more ductile behaviour of the heat treated samples, where the α phase has grown, in comparison with the as deposited samples.

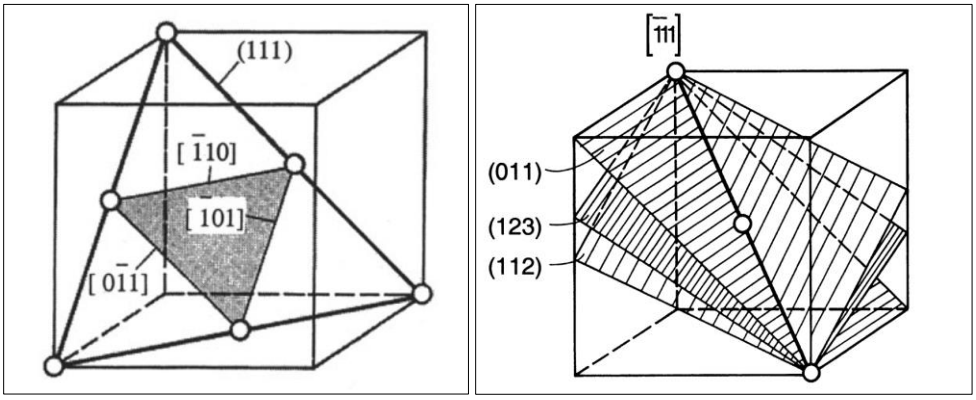

Figure 94: Schematics of the slip systems in case of FCC (left) and BCC (right) structure. In the FCC structure, the slip plane (111) is evident along with three slip directions. At the right picture, the BCC structure exhibits no definite slip plane. Thus, any slip plane, parallel to the [111] direction forms a potential slip system with this direction.

In the case where the material does not consist of a single element, the mechanism of solid solution hardening takes place. This phenomenon attributes its strengthening effect to the interaction between the alloying elements and the dislocations. There are three forms of interaction, namely the paraelastic, the dielastic and the chemical one. The first interaction is related to the compressive and

tensile stresses inside the lattice, which are caused by the atomic size difference between the constituent elements of the alloy. The second one is based on the shear modulus difference of the elements, which affects the energy density of the dislocations. Finally, the third mechanism is related to the stacking fault energy drop, as the solute concentration rises. The reason is that the solute atoms segregate to dislocations to reduce the stacking fault energy. If the dislocation is forced to move due to the application of stress, the solute atoms remain behind and the dislocation returns to its original composition, increasing the dislocation energy. As a result, we have the phenomenon of back stress, which resists the dislocation motion and strengthens the material.

Certain alloys, such as aluminium bronzes dealt with in this report, form precipitates. Dislocations are unable to penetrate hard particles and are forced to circumvent them by bowing out between the particles. The equation describing the phenomenon is given by Orowan [43]:

$$\tau = \frac{Gb}{l - 2r} \tag{8.1}$$

, where

$$l = \frac{r}{\sqrt{f}} \tag{8.2}$$

τ= shear stress, necessary to overcome the particle resistance
r= particles diameter
l-2r= average free dislocation segment length
f= volume fraction of dislocations

Combining equations 8.1 and 8.2, gives,

$$\tau_{OR} = \frac{Gb\sqrt{f}}{r} \tag{8.3}$$

, where G= shear modulus, b= Burgers vector.

Equation (8.3) indicates that given a certain volume fraction, the strengthening effect is more intense in the case of small particles. This could be the case for the κ_3 and κ_4 particles, which have a diameter of less than 0.5 μm.

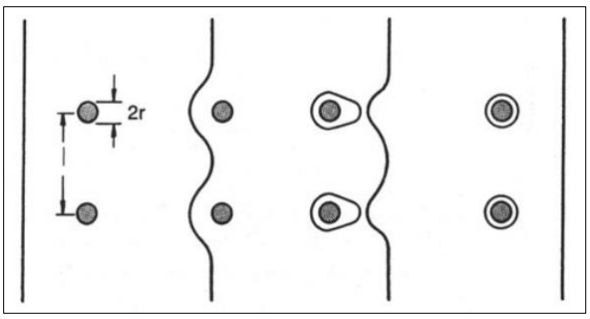

Figure 95: Schematic representation showing the process of dislocation movement through particles, according to Orowan [43].

Furthermore, precipitates may share an incoherent, semi-coherent or coherent interface with the matrix phase. The type of interface depends on how distorted the lattice is at the vicinity of the precipitate. Incoherent interfaces act as grain boundaries; thus, they are impenetrable. However, in any other case, the dislocation may cut through the particle.

Last but not least, the strength of a material is strongly correlated with the average grain size. This is a parameter of vital importance, because it can be tuned by carefully controlled heat treatment and cooling rate of the material, without the addition of extra alloying elements. As a result, the economic and the environmental impact are limited.

In this study, the top layer of the deposition exhibits higher strength than the rest of the layers, which is attributed to the existence of large dendritic β phase formations in the microstructure. As mentioned before, this phase contributes to the strength and deteriorates the ductility. The middle layers show a small scattering of their strength values. It may be concluded that every layer is mainly affected by the heat treatment caused by the next layer. Therefore, there is no significant difference in mechanical properties, if there are more than two subsequent layers. The interface between the substrate and the filler material is a mixture of the two alloys. The strength is elevated for different reason. First of all, the martensitic transformation of the NAB alloys enhances the brittleness, and secondly, the solid solution strengthening mentioned above is even more profound when more alloying elements are involved. All these conclusions are based on the mechanical behaviour of the subsized tensile testing specimens, in which every specimen consist only of a few layers. In the case of the RAMLAB specimens, where the cross-sectional area is considerably larger, the deposition height effect is eliminated.

The heat treatment applied deteriorated the mechanical properties of the alloy, without providing any significant gain in ductility. The α phase has developed, while the β phase was decomposed , see Appendix A, Figure A.100. In Figure A.102 of Appendix A, it is evident that the microstructure is homogenized, which explains the small scattering of the mechanical testing results of the A2, B2 and C2 blocks.

The above observations obtained from the tensile specimens are in close agreement with the hardness measurement of chapter 6. Hardness testing was performed in order to obtain a first approximation of the anticipated results of the tensile and Charpy V-impact testing. From the results, the following relationships between the hardness and the tensile values can be extracted:

for the horizontal tensile specimens $$\frac{\sigma_{UTS}}{HV} \approx 4 \quad (8.4)$$

for the vertical tensile specimens $$\frac{\sigma_{UTS}}{HV} \approx 3.3 \quad (8.5)$$

, where σ_{UTS}= ultimate tensile strength (MPa), HV= Vickers hardness.

8.1.2 MECHANICAL BEHAVIOUR IN UNIAXIAL TENSILE LOADING

This paragraph describes the reasons behind the shape of the stress-strain diagrams obtained from the tensile testing in chapter 6. As mentioned in chapter 6, the yield strength in not a well-defined point at the stress strain curve. This phenomenon implies the use of σ_{ys} at 0.2% elongation to determine the yield strength of our material. Beyond the yield point, the material is plastically deformed. The

following procedure describes the basic reasons behind the trend of the stress strain curve, beyond the elastic limit. At first, there is the easy glide regime (stage 1) which is characterized by a small hardening coefficient. The dislocation density is small, and therefore, dislocations can travel long distances until they become immobilized by other dislocations (Lomer-Locks) or grain boundaries [43]. As the stress rises, the secondary dislocations start moving by the activation of the conjugate slip systems. The dislocations must move to maintain the imposed strain during the tensile test. For each immobilized dislocation, a secondary one should be generated, causing a sudden rise in dislocation density during stage 2. The new dislocations are generated either from the surface or from Frank Read sources [43].

The last and longest hardening stage is stage 3. The characteristic feature in this stage is the cross slip of screw dislocations [43]. This kind of dislocation does not have a defined glide plane, and eventually slips on the plane with the largest shear stress. However, the Schmid factor (explained in the next paragraph) of the cross slip plane is smaller than the one in the primary slip plane, demanding high shear stress to achieve cross slip. The hardening coefficient in this stage is less than that of the one in stage 2, because there is a high possibility that a dislocation will meet an anti-parallel counterpart in the new, cross slip plane. As a result, the dislocation will be annihilated, a phenomenon called dynamic recovery. This mechanism should not be confused with the static recovery happening during annealing.

The stability of the plastic regime of the stress-strain is determined by the slope of the flow curve ($d\sigma_t/d\varepsilon_t$) and the geometrical softening, which is expressed by the slope ($dA_t/d\varepsilon_t$). The flow curve is a typical stress strain curve, but instead of engineering values, it has true stress and strain values (σ_t and ε_t) [43]. Moreover, A_t is the cross sectional area of gage length at any given moment. As described above, the hardening coefficient decreases as the imposed strain rises, while the geometrical softening becomes more evident as the cross-sectional area decreases. Thus, there is a critical strain value at which these two effects balance, indicating the ultimate tensile strength. Beyond this value, the softening effect dominates and the material fractures. It must be highlighted that during necking, as the cross sectional area reduces locally, the strain rate in this region is increased in comparison with the strain rate at the rest of the gage length, leading to a strengthening effect. Therefore, some tensile sample may fracture at a different location that the original necking was started. However, this behaviour was not observed in this project.

8.1.3 ELONGATION OBSERVATIONS

Chapter 6 presented the results of the experimental investigation of the uniaxial tensile tests. Among them, the tensile measurements exhibit a peculiar trend, regarding the elongation values. The specimens extracted from the RAMLAB block had an elongation in the order of 20%, which is close to the anticipated value in the literature. However, the miniature specimens, extracted from the TU Delft blocks presented twice as much elongation as the RAMLAB specimens. This behaviour can be explained by the size difference between the two samples. The cross-sectional area of the RAMLAB samples is 28.26 mm^2, while the one of the TU Delft block is 3 mm^2. Thus, the percentage of surface to the volume of a certain part of the gage length is significantly bigger in the case of the TU Delft sample. Consequently, there is a greater percentage of surface grains at these samples, relative to the RAMALAB specimens. A grain in the bulk is surrounded by twice as many grains than a grain located at the surface. The latter one is therefore easier to deform in order to follow the imposed strain. This phenomenon explains the elongation difference between the two samples.

8.1.4 CHARPY V-NOTCH RESULTS

The higher energy absorption capability of the specimens with the notch facing sideways should be correlated with the shape and orientation of the grains. No such detailed investigation was performed in this study. However, an attempt will be made to explain the difference between the Charpy specimens, concerning their notch orientation. Figure 96 illustrates the banded structure of the middle layers of the deposited blocks. The heat affected regions undergo a heat treatment after each deposition, while the remelted regions reach a temperature above the liquidus. If the notch is facing towards the top, then the crack tip propagates in a homogeneous microstructure in each layer and has to pass through remelted and HAZ regions alternately. This configuration consists of layer in series. As described in chapter 5, the microstructure of the deposited material has a casting structure composed of β phase, which is partially transformed to α upon cooling. The remelted region has a slightly different microstructure, with the α phase being developed and the β phase decomposed. The α phase enhances the ductility and deteriorates the strength, while the β phase has the adverse contribution to the mechanical behaviour, as explained in previous paragraph. Thus, the propagation through the remelted area is faster than in the heat treated region. On the contrary, if the notch is facing sideways, the crack tip is facing simultaneously both layers of remelted and heat treated regions. This configuration has the layers in parallel. In this case, there are no weak layers that the crack could penetrate easily. Of course, the above explanation is an approximation of the reality, where there is also a small remelted part between adjacent beads.

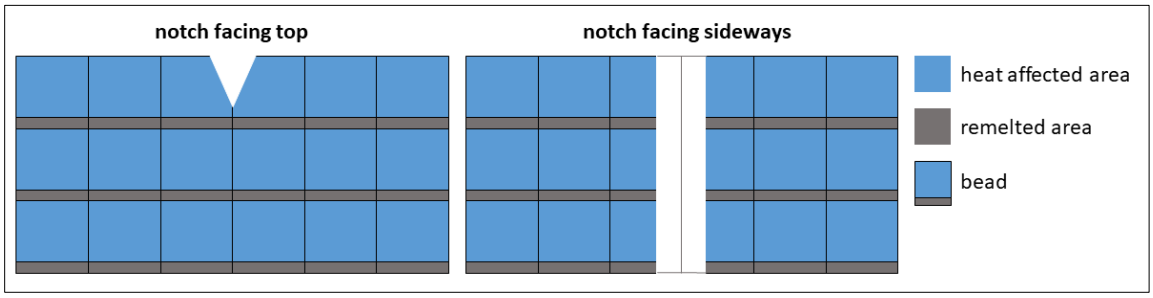

Figure 96: Schematic representation showing the orientation of the Charpy-V notch with respect to the banded structure.

8.1.5 DYNAMIC YIELD STRENGTH

The dynamic yield strength, measured via instrumented Charpy-V tests, is more than 25% higher than the static values. The dynamic yield strength exceeds the 600 MPa, while the static yield strength is approximately 480 MPa. This phenomenon is connected to the relation of the flow stress (true stress), σ, with the strain rate $\dot{\varepsilon}$, which is expressed by the following equations [43]:

$$m = \frac{d \ln \sigma}{d \ln \dot{\varepsilon}} \tag{8.6}$$

$$\sigma = K \dot{\varepsilon}^m \tag{8.7}$$

, where K= K(ε) and m= strain rate sensitivity.

As the strain rate rises, m increases, and as a result the true stress elevates. Thus, the material becomes stronger, exhibiting a higher value of the yield strength. The strain rate sensitivity is relatively low at ambient temperature. However, the impact test involves many orders of magnitude higher strain rates than a typical tensile test. In this case, the strengthening effect becomes profound even at ambient temperatures.

8.1.6 TENSILE FRACTURE SURFACE ORIENTATION

The vast majority of the tensile tests performed at both TU Delft and RAMLAB samples, presented a 45° inclination of the fracture surface to the axis parallel to the application of the tensile force. In order to explain this behaviour, the resolved shear stress has to be analysed. A dislocation moves along the slip plane under the application of a force, which has a component parallel to that slip plane. This component, the resolved shear stress, must have a high enough magnitude to overcome the internal friction forces, which restrict the motion of the dislocation. Figure 97 illustrates the transformation of the applied tensile load to resolved shear stress, which is described by the following equation.

$$\tau = \sigma \cos \kappa \cdot \cos \lambda = m\sigma \qquad (8.8)$$

, where

τ= resolved shear stress
σ= tensile stress
κ= angle between the tensile direction and the normal to the slip plane
λ= angle between tensile and slip direction
m= Schmid factor

It can be easily proven that the maximum resolved shear stress is observed at an angle of 45°. Thus, at small cross-sectional areas, as in the case of miniature tensile specimens of the TU Delft blocks, the crack initiates and propagates at this angle. However, the larger tensile specimens of the RAMLAB block exhibit a different behaviour. In some specimens, the crack initiates at 45° and then continues at 0°, until it approaches the edge of the cross section, where the orientation of the crack returns to 45°. A possible explanation to this phenomenon could be that a crack can propagate easier when the applied load is perpendicular to the crack surfaces. Thus, when the crack reaches a considerable length, it is difficult to continue propagating in the 45° direction and turns perpendicular to the applied load.

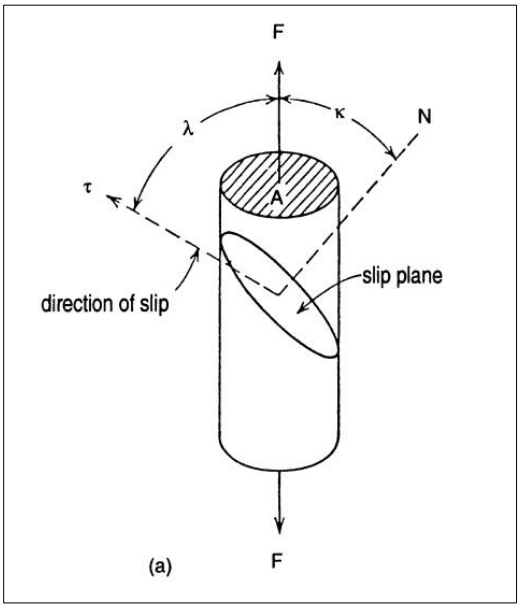

Figure 97: Schematic representation illustrating the geometrical relations at the resolved shear stress equation (8.8) [43].

8.1.7 FRACTURE SURFACE

Charpy specimens are characterized by a lack of constraint, thus the material is free to deform during impact. The form and the extent of deformation indicates how ductile or brittle the specimens is. The most common mechanism in a ductile fracture is the microvoid coalescence. The fracture surface exhibits dimples, which is the result of the merging of these voids. The edges of these features are the outcome of plastic failure of the ligaments between the voids. Furthermore, the morphology of the voids indicates the nature of the applied load, see Figure 98 (a). In our case, the nature of the loading can be represented by a 3-point bending test, resulting in tensile loads below the neutral line and compressive loads above the neutral line. As the crack starts from the notch and spreads towards the bulk, the tensile load acts as a tearing condition, perpendicular to the crack propagation. This stress field results in elongated dimples along the fracture surface [44].

On the contrary, a brittle fracture is characterized by a faceted fracture surface. This kind of surface is created by the rupture of atomic bonds along a well-defined crystal plane. In polycrystalline materials, the crack must change direction when it propagates from one grain to the neighbouring one. Depending on the misorientation between the grains, the fracture surface has distinctive features. River patterns and feather markings are among the most characteristic features, emerging from the step-wise geometry between parallel cleavage planes, see Figure 98 (b) [44]. These characteristics where used to characterize the fracture surfaces of chapter 6, where the Charpy specimens tested at -20 °C and -60 °C exhibit brittle fracture, while the ones at ambient temperature show ductile fracture characteristics.

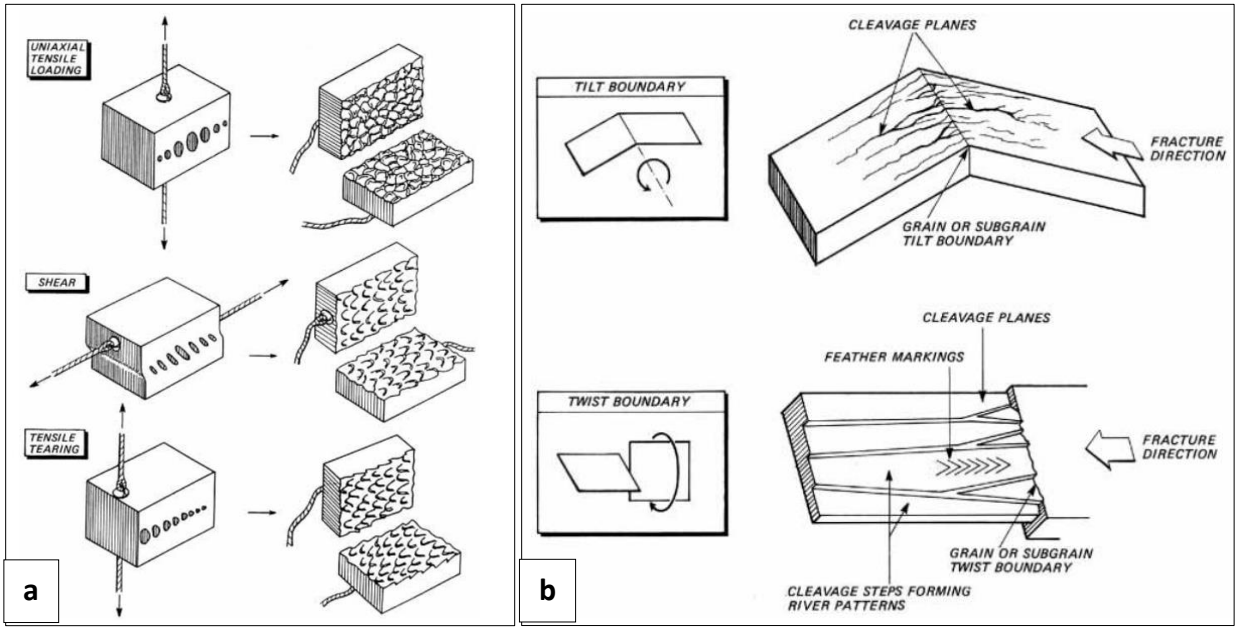

Figure 98: (a) Schematic representation of the dimple geometry, due to uniaxial tensile loading, shear and tensile tearing. (b) Schematic representation of the features related to cleavage fracture mechanism [44].

8.1.8 COMPARISON WITH THE REQUIREMENTS

No product can reach production level without meeting the certification requirements. Unfortunately, additive manufacturing is a relatively new process and the international standards have not managed to publish certain mechanical or corrosion properties requirements for the 3D printed products yet. Thus, up to now, costumers demand that the additive manufacturing products meet the performance of conventionally produced components. For instance, if a WAAM product attempts to substitute a cast propeller, then the requirement would be identical to the cast properties of the given material. Given the above situation, the results obtained in this project are compared with the ASTM specification for the C95700 cast alloy [21]. Table 12 presents the chemical composition of the CMA alloy, as specified by the ASTM standards, while Table 13 summarizes the most important mechanical testing results and compares them with the ASTM requirements.

It should be highlighted that almost all the specimens, regardless of the equipment by which they were produced (by RAMLAB or TU Delft gear), outmatch the ASTM requirements for the cast products of the same material. The non-heat treated samples exhibit approximately 100 MPa higher tensile yield strength than the requirement, which is equivalent with an increase of 36%. The standard even specifies the yield strength at 0.5% elongation, which is greater than the 0.2% elongation that was calculated during the experiments. Thus, the actual difference is even higher. Moreover, the PWHT samples show also a superior tensile yield strength to those of the ASTM standards, exhibiting 15% to 41% higher values.

The situation is similar when the ultimate tensile strength measurements are concerned. The horizontal tensile specimens, from both the TU Delft and the RAMLAB blocks, reach ultimate tensile strength values up to 810 MPa to 890 MPa, which is translated to 30% to 44% higher values than those of the ASTM. The respective percentage for the PWHT case is restricted to 30%. Moving on to the vertical sample, the strength drops, but still gives satisfactory results. The non-heat treated samples show 13% to 24% increase relative to the standards. However, the heat treated vertical samples constitute an exception of this study, exhibiting ultimate strength values very close to the desired ones.

As analysed previously, only the tensile specimens, extracted from the RAMLAB block are sufficient to provide reliable elongation values. They reached an average of 23% total elongation, which is equal to a 27% rise compared to the ASTM standards, approximately.

Finally, the absorbed energy and the hardness recorded values exceed the ASTM threshold in the vast majority of measurements. It should be reported that in the case of the impact specimens with the notch facing up, the average value of the absorbed energy in lower than the desired one. Of course, the same phenomenon holds for the specimens tested at low temperatures. The absorbed energy is lower than the one specified from the standards at ambient temperature, as anticipated.

Table 12: Chemical composition of the CMA alloys according to ASTM [21] *and to the results of XRF analysis.*

ASTM	*Nearest European CEN/TC 133 equivalent*	*Al*	*Fe*	*Ni*	*Mn*	*Si*	*Total other elements*	*Cu*
C 95700	CuMn11Al8Fe3Ni3-C	7.0-8.5	2.0-4.0	1.5-3.0	11.0-14.0	0.10	0.5	71
	filler wire (XRF analysis)	6.68	2.64	2.4	11.9	0.26		73.66

Table 13: Comparison between the required mechanical properties of the ASTM standards and the average experimental values recorded during hardness, tensile and impact testing at the 3D printed CMA alloy.

	ASTM[6] C 95700	*Horizontal TU Delft*		*Vertical TU Delft*		*RAMLAB*		
	As- Cast	*NO PWHT*	*PWHT*	*NO PWHT*	*PWHT*	*Horizontal*	*Vertical*	
Yield Strength (MPa)	275[7]	480	390	490	315	480	480	
Ultimate Tensile Strength (MPa)	620	890	800	700	**600**	810	770	
Elongation (%)	18	not reliable data				23	23	
		Horizontal RAMLAB				*Vertical RAMLAB*		
		Notch Up		*Notch Sideways*		*Ambient*	*-20 °C*	*-60 °C*
Absorbed Energy (J)	40	**38**		45		41	**33**	**27**
		TU Delft NO PWHT		*TU Delft PWHT*		*RAMLAB*		
Hardness (HV_{5kg})	180	205		185		215		

Furthermore, if the measured mechanical properties are compared to the results of Ding [2] for the case of 3D printed NAB alloy (CuAl10Ni5Fe5), the CMA alloy exhibits 140 MPa and 250 MPa higher yield and ultimate tensile strength, respectively. Nevertheless, when talking about an application of a material, the economical factor usually plays a crucial role. The price of the CMA alloy is approaching 50 Euro/kg, while the NAB alloy is cheaper and costs less than 30 Euro/kg. This significant difference in price should always be considered when a manufacturer selects the filler material of the 3D production of a marine propeller.

8.2 CORROSION SUSCEPTIBILITY

Corrosion is the deterioration of a material by the reaction with its environment. In our case, the samples were exposed to an aqueous solution (wet corrosion), thus the phenomenon of corrosion is purely an electrochemical reaction, meaning that one of the species involved undergoes a change in valency. As described in the experimental procedure session, the electrolyte used, contained 3.5% NaCl, resulting in a pH close to 6. This value of pH indicates that the cathodic process is limited by oxygen diffusion through the oxide and is described by the following chemical reaction:

Oxygen reduction $$O_2 + 2H_2O + 4e^- \rightarrow 4OH^-$$ (8.7)

[6] Nearest European CEN/TC 133 equivalent: CuMn11Al8Fe3Ni3-C

[7] 0.5% Proof strength (MPa), while the experimental measurements present the 0.2% Proof strength

For simplicity reasons, it is assumed that the material consists of 100% Cu, thus the anodic reaction is given by the equation:

$$Cu \rightarrow Cu^{2+} + 2e^{-} \quad (11.8)$$

The ionic carriers of charge in our solution are the following:

$$NaCl \rightarrow Na^{+} + Cl^{-} \quad (11.9)$$

A Pourbaix diagram illustrates the stable phases as a function of pH and potential. Furthermore, it is constructed with the use of the Nerst equation, which connects the electrode potential to the activity or for simplicity the concentration, of the ions in the solution. However, in this study, the Pourbaix diagram was retrieved from the site Material Project for the alloy CuMn11Al7 [45]. In the Pourbaix diagram below, the potential is defined with respect to the standard hydrogen electrode.

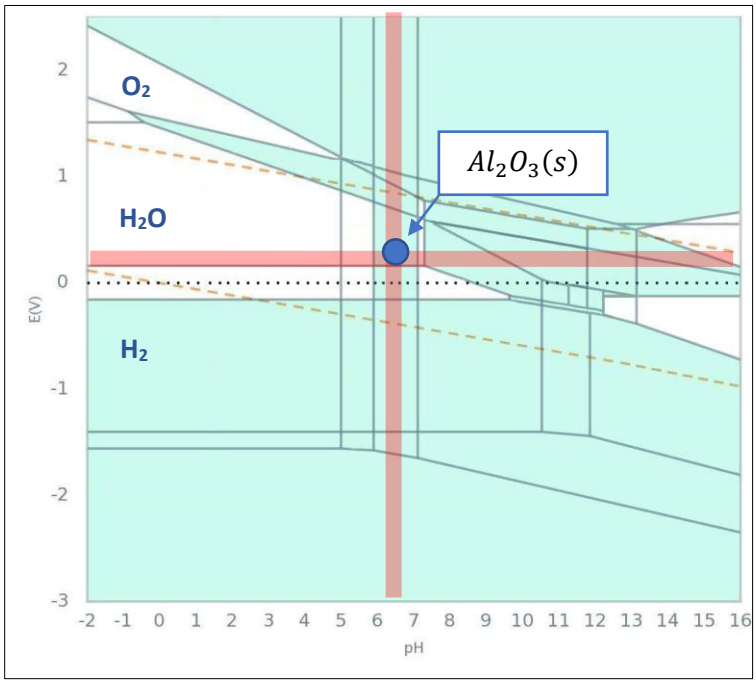

Figure 99: Pourbaix diagram of the CMA alloy, CuMn11Al7. The electrode potential is against the standard hydrogen electrode [45].

The recorded potential values during the OCP measurements exhibit an average of -20 mV against the Ag/AgCl electrode, which can be translated to 180 mV against the standard hydrogen electrode. Thus, knowing the x and the y axis of the Pourbaix diagram, it is concluded that corrosion leads to the formation of the following stable oxide: $Al_2O_3(s)$

Despite that the Pourbaix diagram gives information on which species are thermodynamically stable, it gives no information on the kinetics. This information can be obtained from the polarization curves experiments and the subsequent Tafel approximation, which gives an indication of the corrosion rate. During these experiments, the sample is polarized cathodically and then anodically, meaning that

there is an abundance or deficiency of electrons in the metal, resulting in a positive or negative charge built up, respectively.

The OCP results reported in chapter 7 and in Appendix D show that in most cases the samples reach a steady state, where equilibrium is reached. Some of them start with a high potential and subsequently their V_{OCP} value drops gradually, while others start from a low potential, which increases until the equilibrium value as time passes. The first phenomenon may be attributed to the dissolution of surface contamination, which impedes the corrosion process initially. The latter case is the outcome of the formation of the oxide layer at the top of the sample.

The polarization results indicate low corrosion rates, proving that the material is an ideal candidate of seawater applications. Furthermore, the corrosion rate results depict that the middle areas of the wall present greater consistency of the results, in comparison with the greater scattering of the results of the top and bottom areas. This behaviour does not change significantly even after tempering. Concerning the polarization curves, the form of the cathodic branch implies that the oxygen reduction takes place, equation (8.7). However, the step-wise behaviour of the anodic part may be attributed to a secondary anodic reaction. According to the literature review on chapter 3.5, the aluminium-rich anodic areas dissolve first and are followed by the copper areas.

The SKP results show clear differences of the CPD values along a line of the cross section length of the deposited blocks. The SKP graph in chapter 7 indicates the benefits of tempering, which reduces the scattering of the CPD values. As a result, the potential differences of adjacent areas are reduced, together with the susceptibility of galvanic cell formation.

9. CONCLUSIONS AND FURTHER INVESTIGATION

9.1 CONCLUSIONS

The conclusions extracted from the experimental observation can be divided into different categories. At a more generic level, the feasibility of the method was examined. The aluminium bronzes tested were weldable over a wide range of heat inputs with satisfactory results. The TU Delft blocks exhibit no porosity, while the RAMLAB block investigation revealed a small number of pores. However, the performance of the samples was identical in both cases. Moreover, the constructed blocks were not affected significantly by the deposition equipment. The TU Delft and the RAMLAB additive manufacturing experimental arrangements differ in every way, from the GMAW configuration to the way of movement of the welding torch. Nevertheless, the final products were similar concerning the properties and the quality. This behaviour implies that the material is tolerant to process parameters fluctuations. The absence of a martensitic transformation in CMA alloys, in the contrary to NAB alloys, contributes also to the above phenomenon, making the CMA properties less dependent on the cooling rate.

The microstructural investigation revealed that the 3D printed CMA block consisted of a banded structure. The different deposited layers depicted that the there are two phases, α and β, and a variety of precipitates. The Widmanstätten α phase mainly nucleates at the grain boundaries. The tempering promotes the α phase growth, making the grain boundaries indistinguishable, while the β phase decomposes.

With respect to the mechanical properties, the 3D printed blocks exhibit substantial strength and ductility. In almost all cases, they were superior to their cast rival, see Table 13. The mechanical properties exceed not only the requirements of ASTM for cast products, but also the properties achieved of similar 3D printed aluminium bronze products [2]. The interface area between the substrate and the filler material, together with the top layers of the deposition, exhibit higher strength and lower ductility than the average values measured at the main part of the 3D printed block. The perpendicular direction relative to the deposition is the weak one due to the banded nature of the microstructure. However, the deposition height plays no significant role in the mechanical properties. Furthermore, the heat treatment of 675 °C for 6 hours reduced the scattering of the mechanical properties but also resulted in softening. The result was 25% reduction of the tensile yield strength and 10% reduction of the ultimate tensile strength.

Regarding the corrosion results, the built height has little effect on the corrosion susceptibility, according to the polarization curves. The material exhibits a remarkably low corrosion rate, which justifies its use in marine applications. The SKP tests illustrated the beneficial aspect of the tempering heat treatment, which alleviates the large potential differences of adjacent deposited areas.

It may be concluded that the CMA alloys are prominent candidates for the emerging market of 3D printed marine propellers. These alloys superpass their rivals, namely stainless steels and the rest of the aluminium bronzes family, with respect to weldability and production parameters sensitivity. However, in many cases, the high cost of the CMA filler material may discourage its extensive use.

9.2 FURTHER INVESTIGATION

This thesis project proved the feasibility of the WAAM method to produce aluminium bronze products for marines applications. Furthermore, it quantified their most important mechanical and

corrosion properties, along with the most distinctive microstructural characteristics. However, as a novel technique, huge steps have still to be made in order to have reliable and reproducible results. Among them, temperature distribution is the most crucial factor that must be monitored and controlled.

In most metal alloys, the thermal cycles determine the microstructure of the material, and subsequently its performance. Thus, a Finite Elements Analysis (FEA) model predicting the temperature profile of each area would assist in the prediction of the resulted microstructure. For verification purposes, thermal cameras could monitor the deposition of weld beads and record the temperature distribution at each point within time. As an extension of the previous suggestion, the thermal model should be coupled to a mechanical model to predict the distortion of the structure, due to solidification and thermal shrinkage. Thus, the final product would be closer to the desired geometry.

Another aspect of the method to be improved is the reduction of the idle time between subsequent passes. Most metallic materials demand a certain interpass temperature in order to maintain their integrity and reduce the re-melting of the previous layers. Up to now, the problem has been tackled by special support tables, which incorporate a cooling system. Of course, these techniques provide sufficient cooling at the first steps of the deposition. However, as the height of the structure increases, the cooling rate drops dramatically. Consequently, a way of cooling the deposited layer in situ, and not through conduction of heat to the base, would be a game changing breakthrough.

LIST OF REFERENCES

[1] I. Richardson and C. Powell, “Guide to Nickel Aluminium Bronze for Engineers.” Copper Development Association, 2016.

[2] D. Ding, Z. Pan, S. Van Duin, H. Li, and C. Shen, “Fabricating Superior NiAl Bronze Components through Wire Arc Additive Manufacturing,” 2016.

[3] Y. Lv, L. Wang, X. Xu, and W. Lu, “Effect of Post Heat Treatment on the Microstructure and Microhardness of Friction Stir Processed NiAl Bronze (NAB) Alloy,” *Metals (Basel).*, pp. 1695–1703, 2015.

[4] H. Li, D. Grudgings, N. Larkin, and J. Norrish, “Optimization of Welding Parameters for Repairing NiAl Bronze Components,” pp. 2980–2985, 2012.

[5] A. Chakrabarti, A. Sarkar, T. Saravanan, A. Nagesha, and R. Sandhya, “Influence of Mean Stress and Defect Distribution on the High Cycle Fatigue Behaviour of cast Ni-Al Bronze,” *Procedia Eng.*, vol. 86, pp. 103–110, 2014.

[6] M. D. Fuller, S. Swaminathan, A. P. Zhilyaev, and T. R. Mcnelley, “Microstructural transformations and mechanical properties of cast NiAl bronze : Effects of fusion welding and friction stir processing,” *Mater. Sci. Eng. A*, vol. 463, pp. 128–137, 2007.

[7] C. Navy, C. Nab, F. S. Processing, F. S. Processing, T. Technical, C. Program, T. A. Zone, T. Nab, and G. Hooke, “Residual Stresses in Friction Stir Processed (FSP) Nickel Aluminum Bronze,” pp. 54–56, 2008.

[8] D. Nakhaie, A. Davoodi, and A. Imani, “The role of constituent phases on corrosion initiation of NiAl bronze in acidic media studied by SEM – EDS , AFM and SKPFM,” *Corros. Sci.*, vol. 80, pp. 104–110, 2014.

[9] J. Iqbal, F. Hasan, and F. Ahmad, “Characterization of phases in an as-cast copper-manganese-aluminum alloy,” *J. Mater. Sci. Technol.*, vol. 22, no. 6, 2006.

[10] William Adolph Nabach, “The effects of isothermal deformation and annealing on the microstructure of nickel-aluminium-bronze propeller material,” Naval Postgraduate School, 2003.

[11] D. Ding, Z. Pan, D. Cuiuri, and H. Li, “A multi-bead overlapping model for robotic wire and arc additive manufacturing (WAAM),” *Robot. Comput. Integr. Manuf.*, vol. 31, pp. 101–110, 2015.

[12] D. Ding, Z. Pan, D. Cuiuri, and H. Li, “Wire-feed additive manufacturing of metal components: technologies, developments and future interests,” *Int. J. Adv. Manuf. Technol.*, vol. 81, no. 1–4, pp. 465–481, 2015.

[13] M. Kathryn, G. Moroni, T. Vaneker, G. Fadel, R. I. Campbell, I. Gibson, A. Bernard, J. Schulz, P. Graf, B. Ahuja, and F. Martina, “Design for Additive Manufacturing : Trends , opportunities , considerations , and constraints,” *CIRP Ann. - Manuf. Technol.*, vol. 65, no. 2, pp. 737–760, 2016.

[14] F. Martina and S. Williams, “Wire + arc additive vs. traditional machining from solid: a cost comparison,” Cranfield, 2015.

[15] W. E. Frazier, “Metal Additive Manufacturing : A Review,” *ASM Int.*, vol. 23, no. June, pp. 1917–1928, 2014.

[16] A. S. Haselhuhn, “Design for Low-Cost Gas Metal Arc Weld-Based Aluminum 3-D Printing,” Michigan Technology University, 2016.

[17] D. Ding, Z. Pan, D. Cuiuri, and H. Li, “A practical path planning methodology for wire and arc additive manufacturing of thin-walled structures,” *Robot. Comput. Integr. Manuf.*, vol. 34, pp. 8–19, 2015.

[18] F. Montevecchi, G. Venturini, A. Scippa, and G. Campatelli, “Finite element modelling of Wire-Arc-Additive-Manufacturing process,” *Procedia CIRP*, vol. 55, pp. 109–114, 2016.

[19] D. Ding, Z. Pan, D. Cuiuri, H. Li, S. Van Duin, and N. Larkin, “Bead modelling and implementation of adaptive MAT path in wire and arc additive manufacturing,” *Robot. Comput. Integr. Manuf.*, vol. 39, pp. 32–42, 2016.

[20] J. Ding, P. Colegrove, J. Mehnen, S. Ganguly, P. M. S. Almeida, F. Wang, and S. Williams, “Thermo-mechanical analysis of Wire and Arc Additive Layer Manufacturing process on large multi-layer parts,” *Comput. Mater. Sci.*, vol. 50, no. 12, pp. 3315–3322, 2011.

[21] H. Meigh, *Cast and wrought aluminium bronzes, properties, processes and structure*. Leeds: Maney Publishing, 2000.

[22] C. D. Association, “Copper and its alloys.” [Online]. Available: http://copperalliance.org.uk/copper-and-its-alloys/alloys. [Accessed: 19-Jul-2017].

[23] F. Hasan, A. Jahanafrooz, G. W. Lorimer, and N. Ridley, “The Morphology , Crystallography , and Chemistry of Phases in As-Cast Nickel-Aluminum Bronze,” vol. 13, no. August, pp. 1337–1345, 1982.

[24] C. B. Fuller, M. W. Mahoney, W. H. Bingel, and M. Calabrese, “Tensile and Fatigue Properties of Friction Stir Processed NiAl Bronze,” pp. 3751–3756, 2007.

[25] G. M. Weston, “Survey of nickel-aluminium-bronze casting alloys on marine applications,” Melbourne, 1981.

[26] M. Hazra and K. P. Balan, “Failure of a nickel aluminium bronze (NAB) canned motor pump impeller working under polluted sea water – In fl uence of material selection , section thickness dependent microstructure and temper annealing heat treatment,” *EFA*, vol. 70, pp. 141–156, 2016.

[27] Z. Nishiyama, *Martensitic Transformation*. Academic Press, 1978.

[28] A. Jahanafrooz, E. Hasan, G. W. Lorimer, and N. Ridley, “Microstructural Development in Complex Nickel-Aluminum Bronzes,” vol. 14, no. October, pp. 1951–1956, 1983.

[29] R. Thomson and J.O. Edwards, “MRP/PMRL/76-28(J)” Ottawa.

[30] J.C. Rowlands and T.R.H.M. Brown, “4th International Congress on Marine Corrosion and Fouling,” 1976.

[31] E.A. Culpan and G. Rose, “No Title,” *J. Mater. Sci.*, vol. 13, pp. 1647–56, 1978.

[32] B. P. Pisarek, “Model of Cu-Al-Fe-Ni Bronze Crystallization,” pp. 72–79, 2013.

[33] C. D. Association, “Welding of Aluminium Bronze,” 1988.

[34] G. W. Lorimer, F. Hasan, J. Iqbal, and N. Ridley, “Observation of microstructure and corrosion behaviour of some aluminium bronzes,” *Br. Corros. J.*, vol. 21, no. 4, pp. 244–248, 1986.

[35] Panasonic, “TAWERS Active Wire Process (AWP).” Panasonic, Germany, 2012.

[36] “Scanning Electron Microscopy & Energy Dispersive X-Ray Spectroscopy,” *Vrije Universiteit Brussel*. [Online]. Available: https://www.surfgroup.be/semedx. [Accessed: 15-Jul-2017].

[37] “Low Voltage Electron Microscopy.” [Online]. Available: http://download.e-bookshelf.de/download/0000/7529/92/L-X-0000752992-0001829642.XHTML/index.xhtml. [Accessed: 15-Jul-2017].

[38] G. Mathers, “Hardness Testing Part 1,” *TWI*. [Online]. Available: http://www.twi-global.com/technical-knowledge/job-knowledge/hardness-testing-part-1-074/. [Accessed: 15-Jul-2017].

[39] ASTM E 8/E 8M - 08, “Standard Test Methods for Tension Testing of Metallic Materials,” 2008.

[40] E. Lucon, “Estimating dynamic ultimate tensile strength from instrumented Charpy data,” *Mater. Des.*, vol. 97, pp. 437–443, 2016.

[41] KPTechnology, “Software and Hardware Manual for Non-Scanning Ambient Kelvin Probe Systems.” 2014.

[42] D. A. Jones, *Principles and Prevention of Corrosion*, 2nd ed. Pearson, 1996.

[43] Günter Gottstein, *Physical Foundations of Materials Science*. Berlin: Springer.

[44] M. Janssen, J. Zuidema, and R. J. H. Wanhill, *Fracure Mechanics*, 2nd ed. Delft, Netherlands: VSSD, 2006.

[45] Sai Jayaraman, “Pourbaix Diagram.” [Online]. Available: https://materialsproject.org/. [Accessed: 02-Jul-2017].

[46] G. Ouden and M. Hermans, *Welding Technology*. Delft, Netherlands: VSSD, 2009.

APPENDIX A - MICROSTRUCTURAL INVESTIGATION

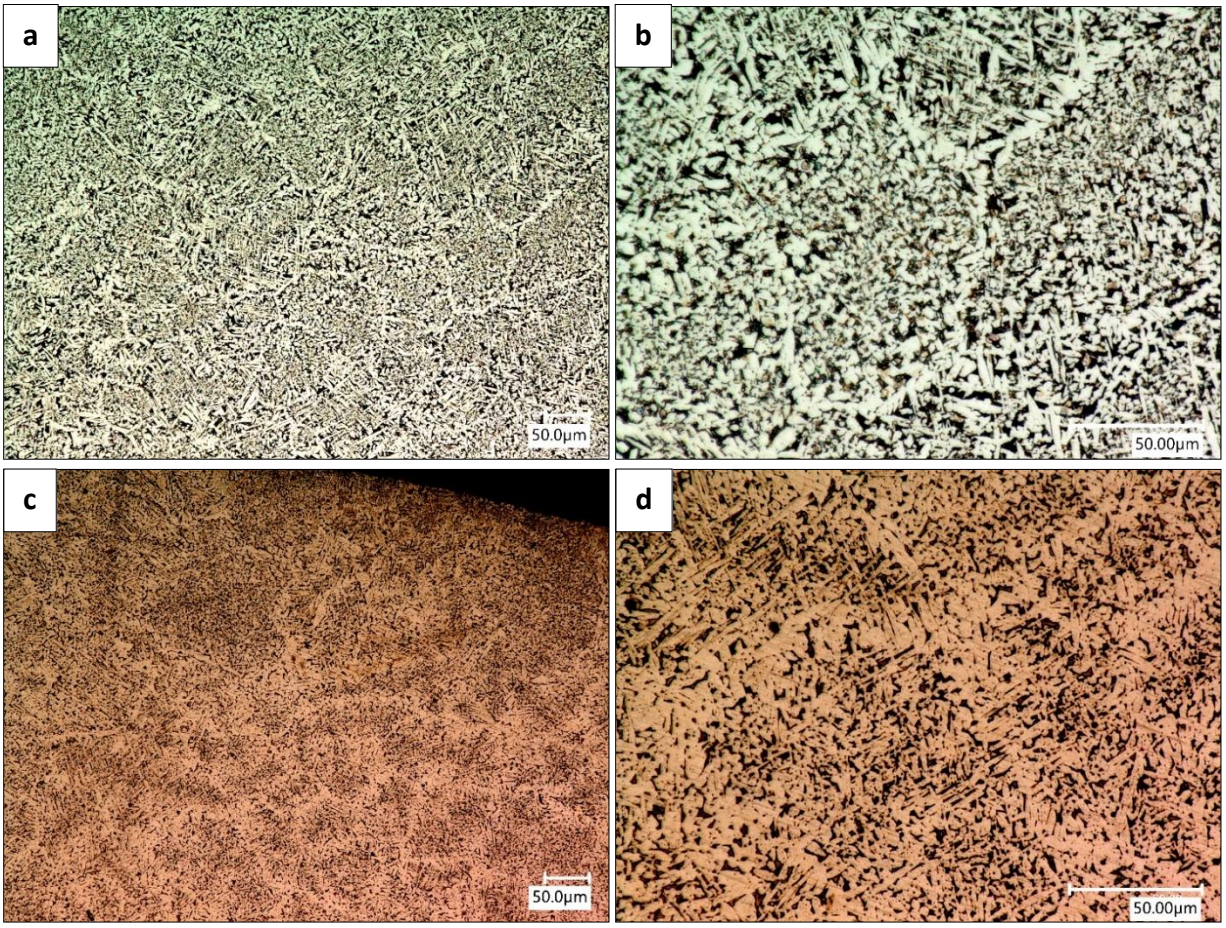

Figure 100: Microstructure of top layer of block C1 at (a) x 500 and (b) x1500 magnification. The bottom two images represent the respective microstructure of top layer of block C2 at (c) x 500 and (d) x1500 magnification.

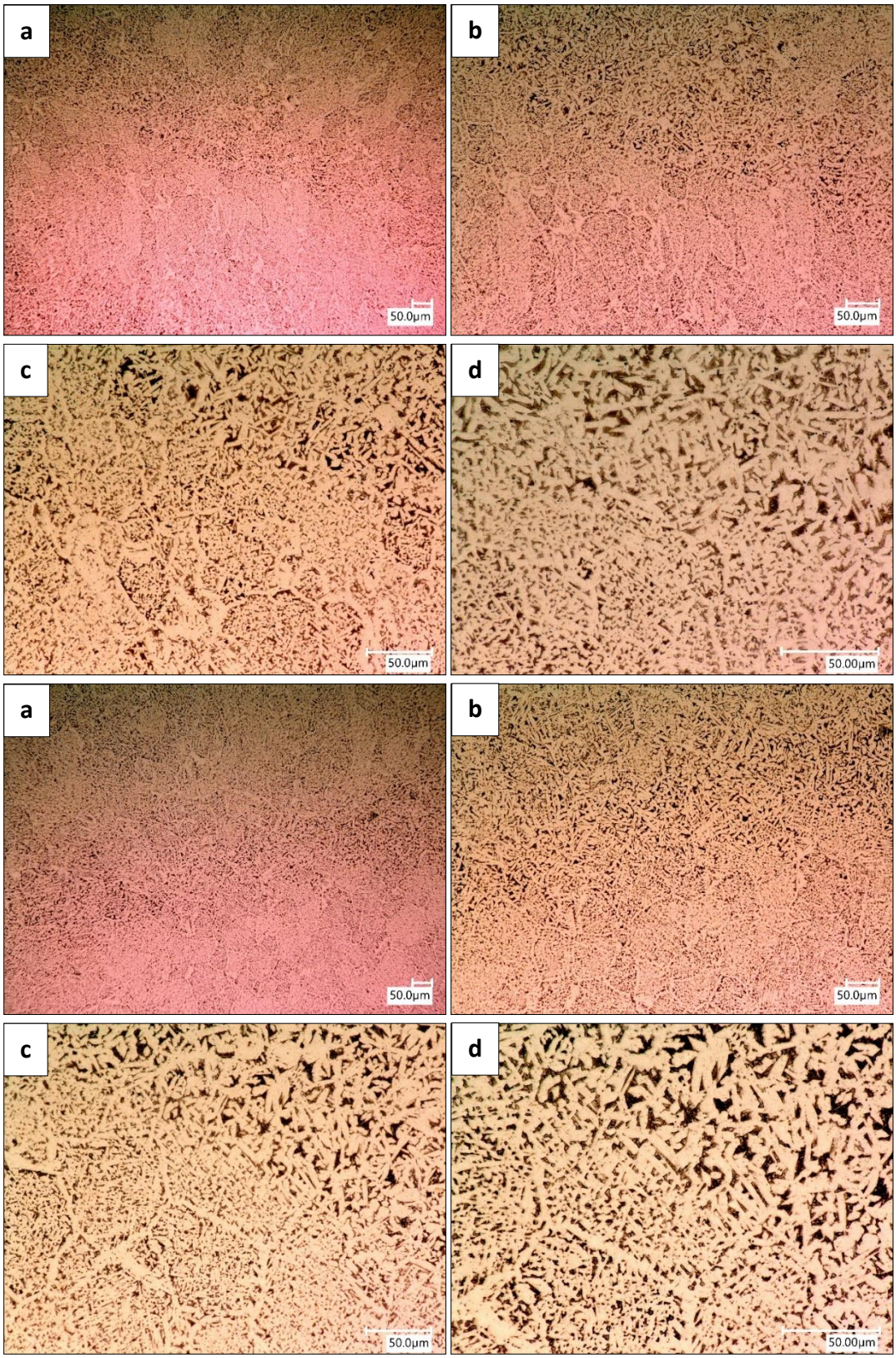

Figure 101: Microstructure of bottom (first 4 pictures) and middle (last 4 pictures) layers of block A1 at (a) x 300, (b) x500, (c) x 1000 and (d) x1500 magnification.

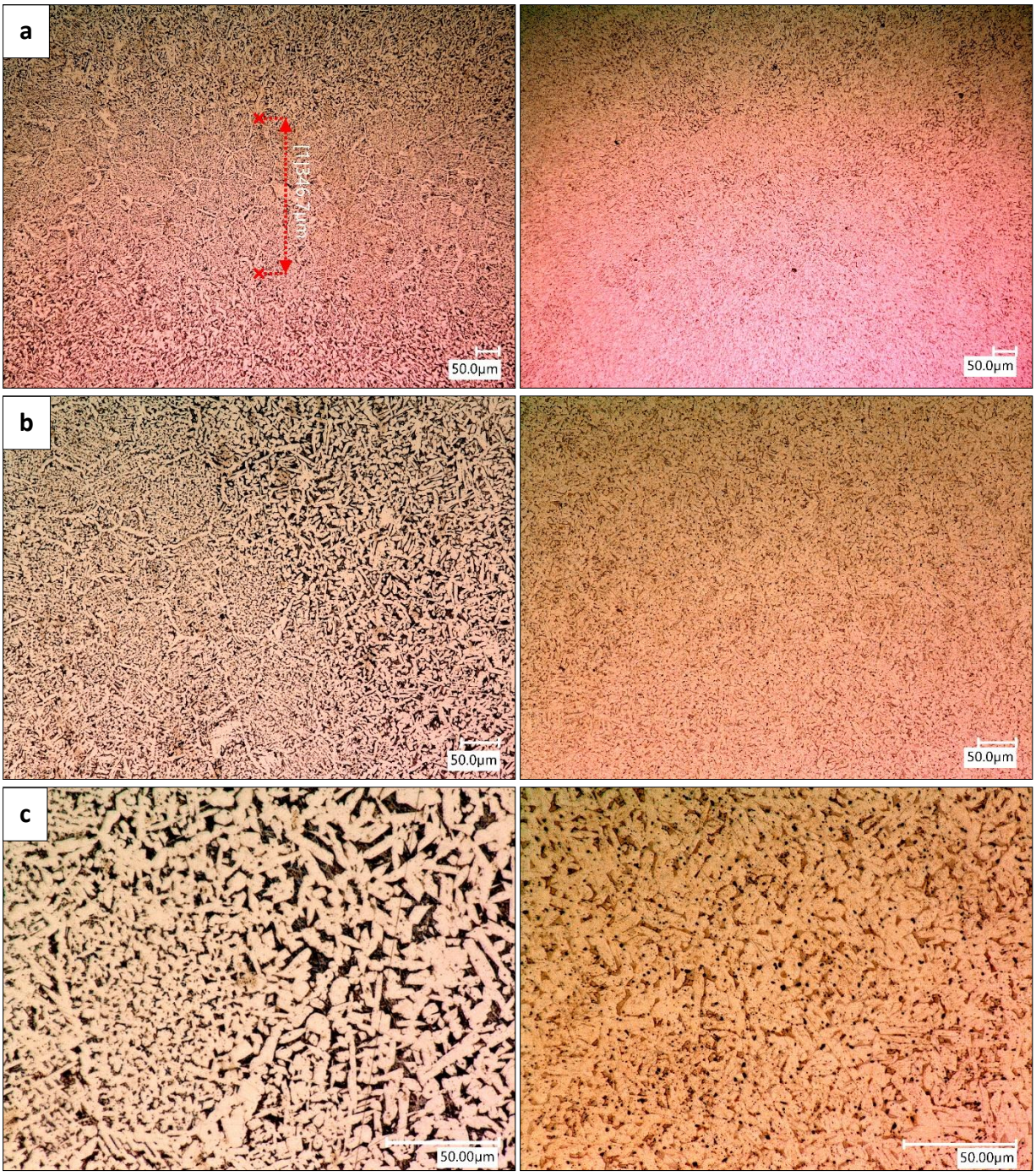

Figure 102: Microstructure of block B1 (left) and B2 (right) at (a) x 300, (b) x500 and (c) x1500 magnification.

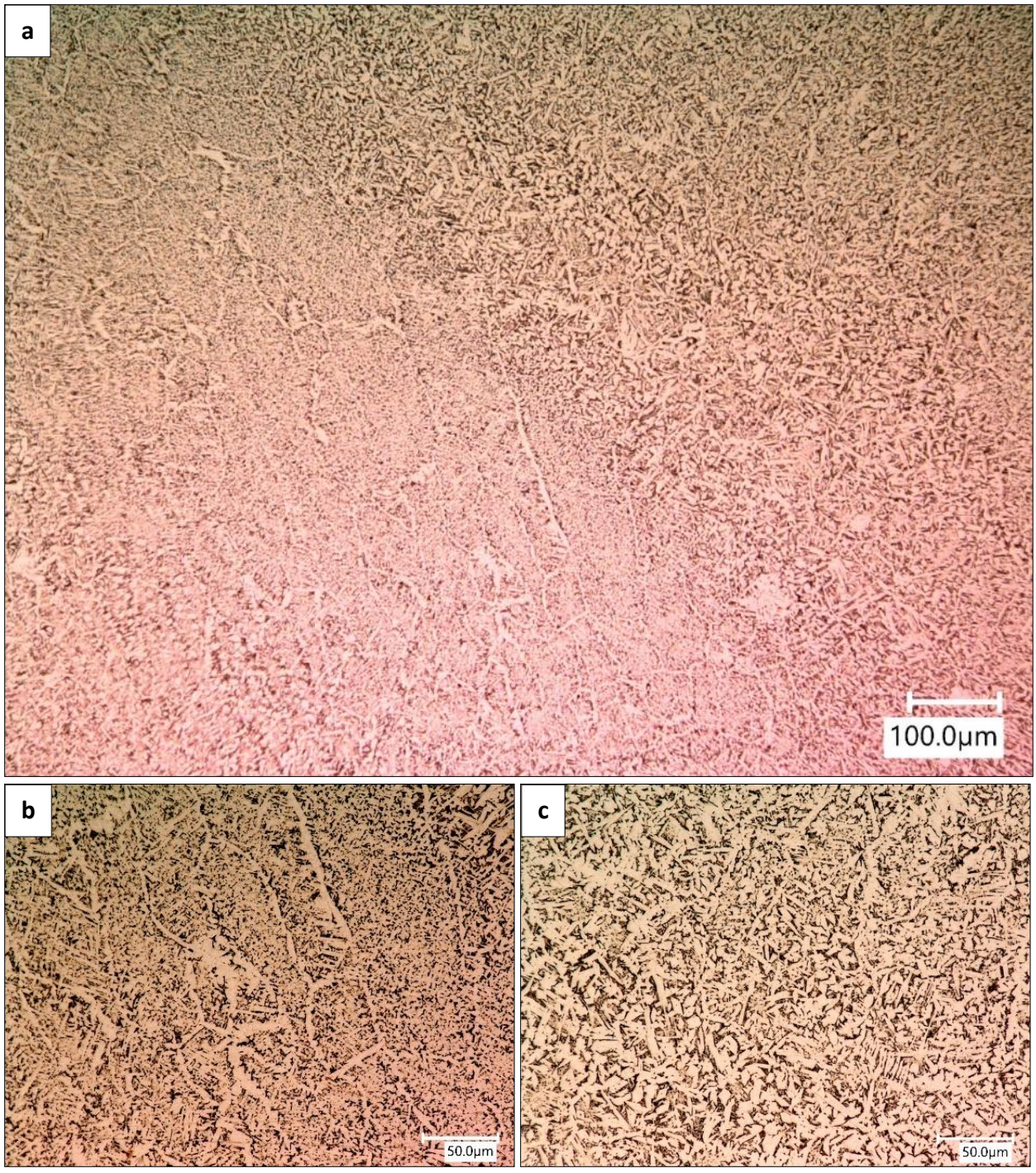

Figure 103: Microstructure of the middle layers of the block produced at RAMLAB. (a) 300, (b) upper layer 1000, (c) bottom layer 1000,

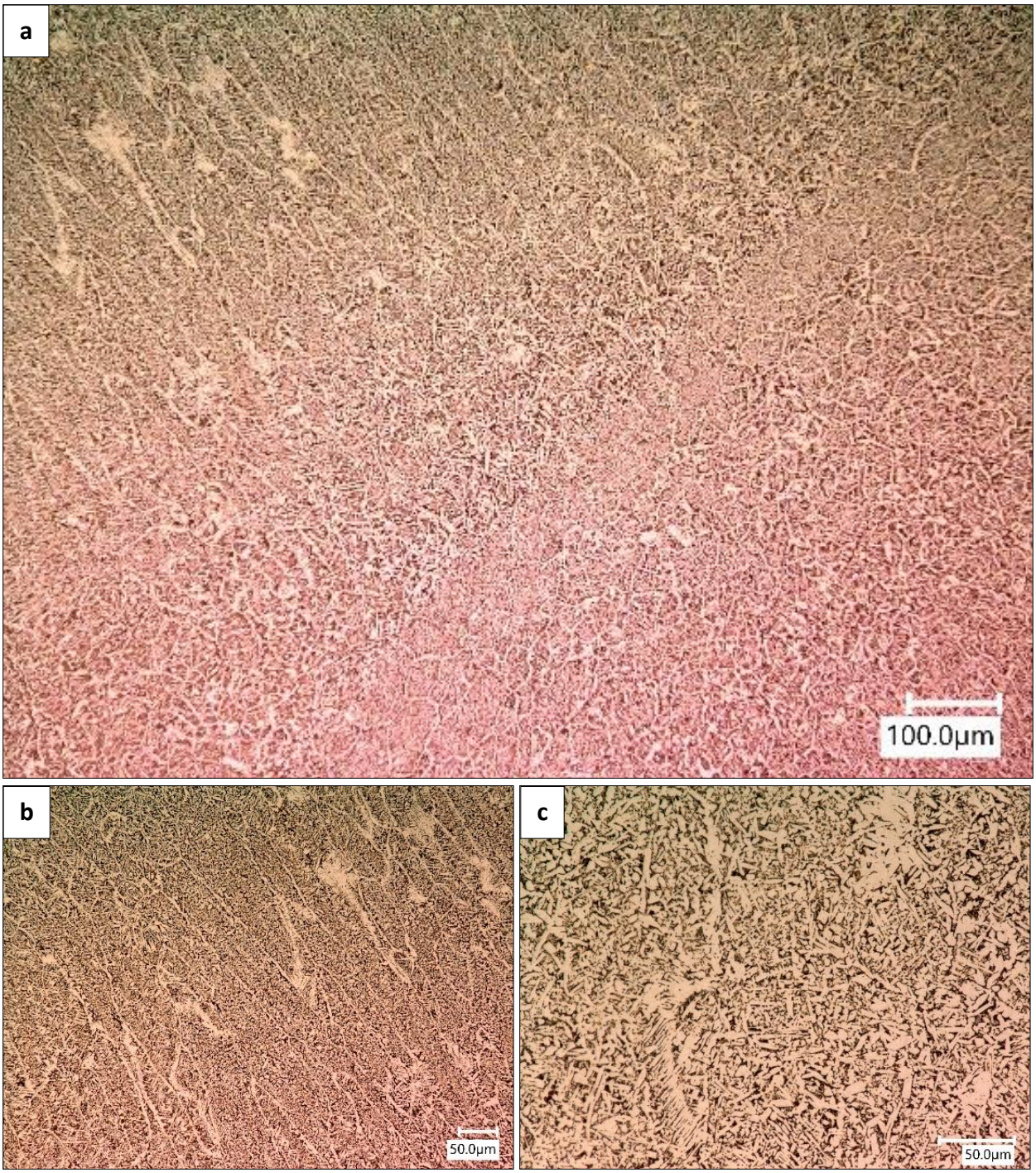

Figure 104: Microstructure of the bottom layers of the block produced at RAMLAB. (a) x300, (b) upper layer x500, (c) bottom layer x1000.

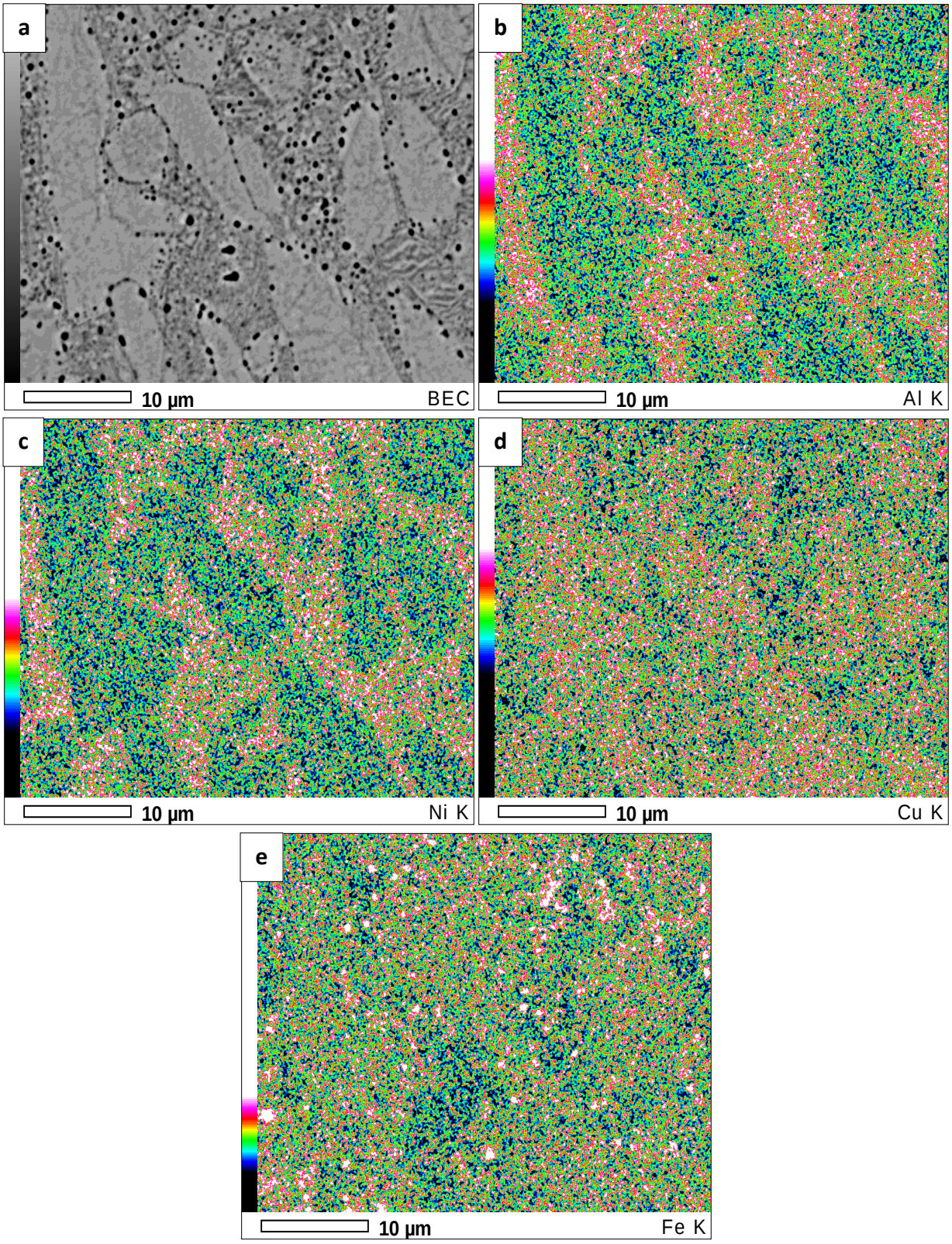

Figure 105: Picture (a) illustrates the microstructure of the substrate of the RAMLAB block. The qualitative map of the chemical composition is evident at the rest of the pictures for (b) Al, (c) Ni, (d) Cu, (e) Fe.

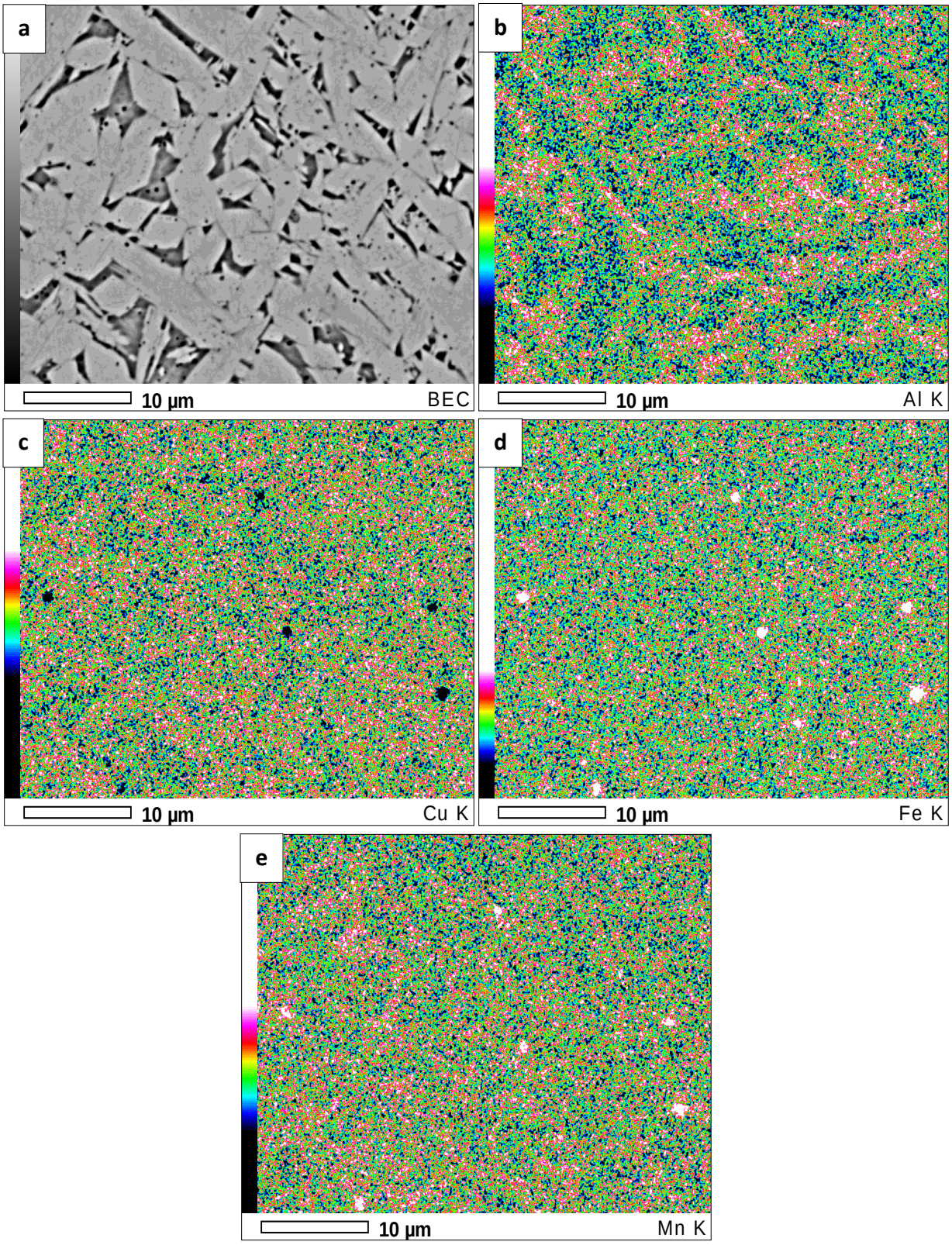

Figure 106: Picture (a) illustrates the microstructure of the deposited material of the RAMLAB block. The qualitative map of the chemical composition is evident at the rest of the pictures for (b) Al, (c) Cu, (d) Fe, (e) Mn.

APPENDIX B - TENSILE TESTING RESULTS

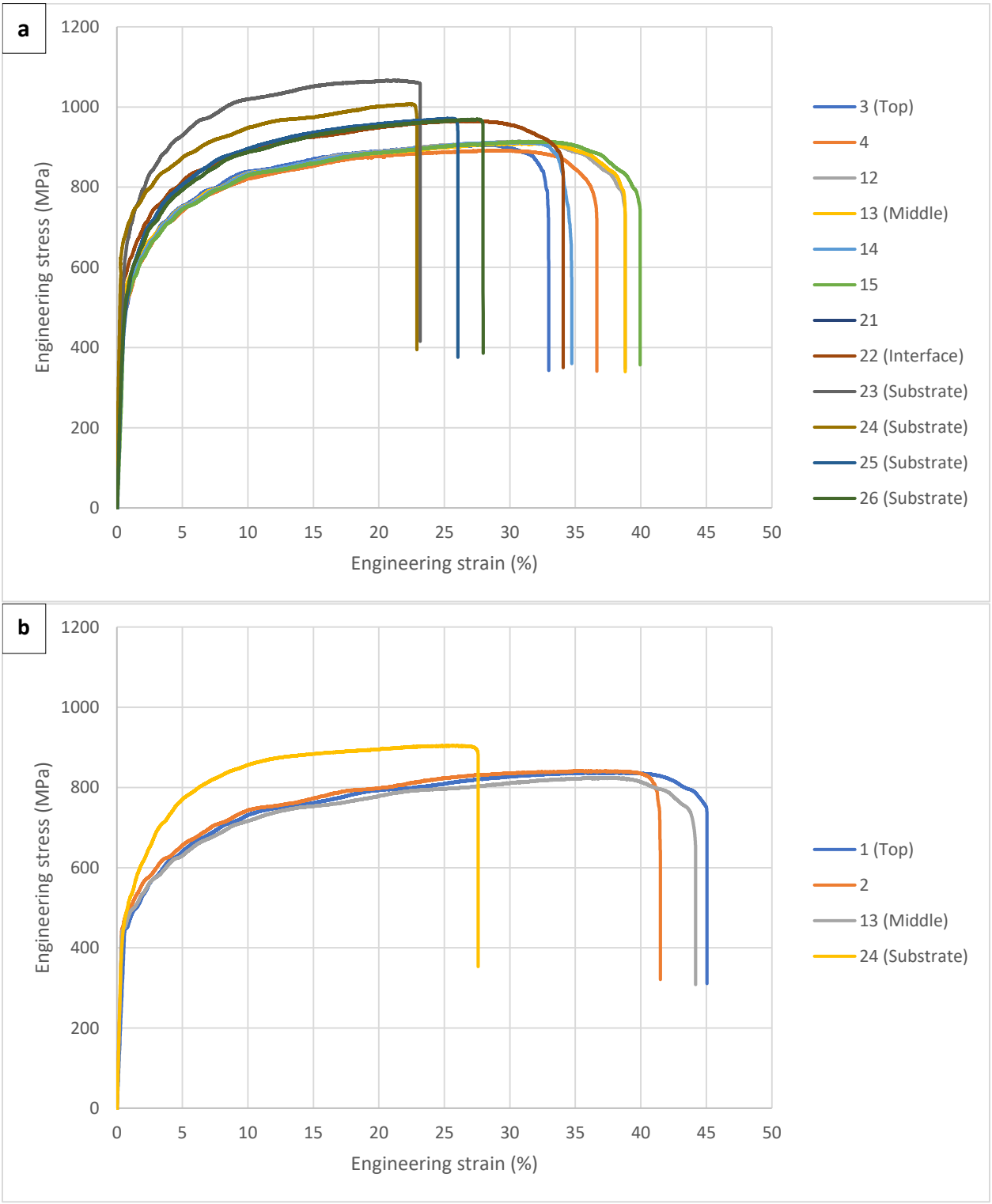

Figure 107: Tensile curves for the horizontal specimens of block A1 (a) and A2 (b).

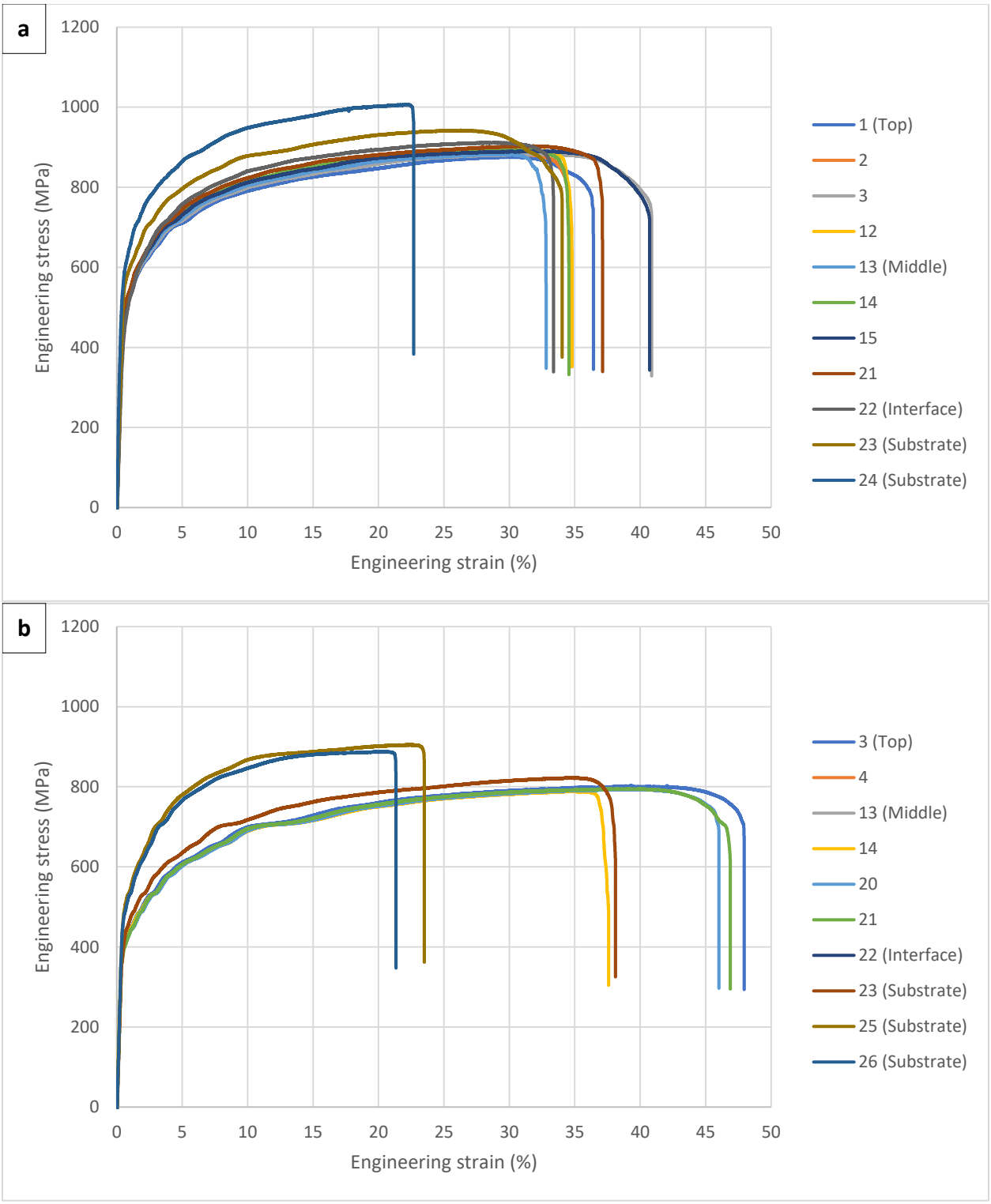

Figure 108: Tensile curves for the horizontal specimens of block B1 (a) and B2 (b).

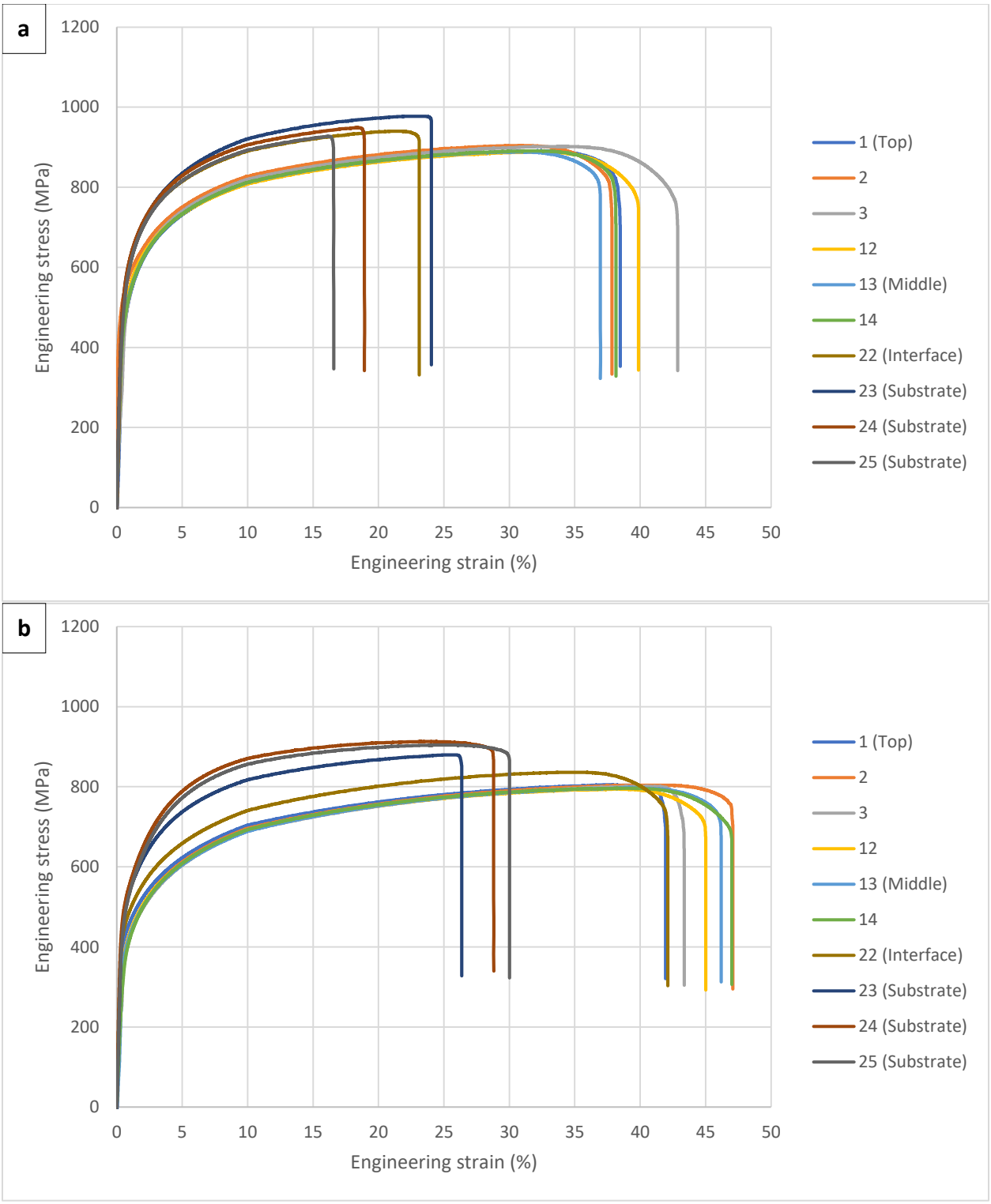

Figure 109: Tensile curves for the horizontal specimens of block C1 (a) and C2 (b).

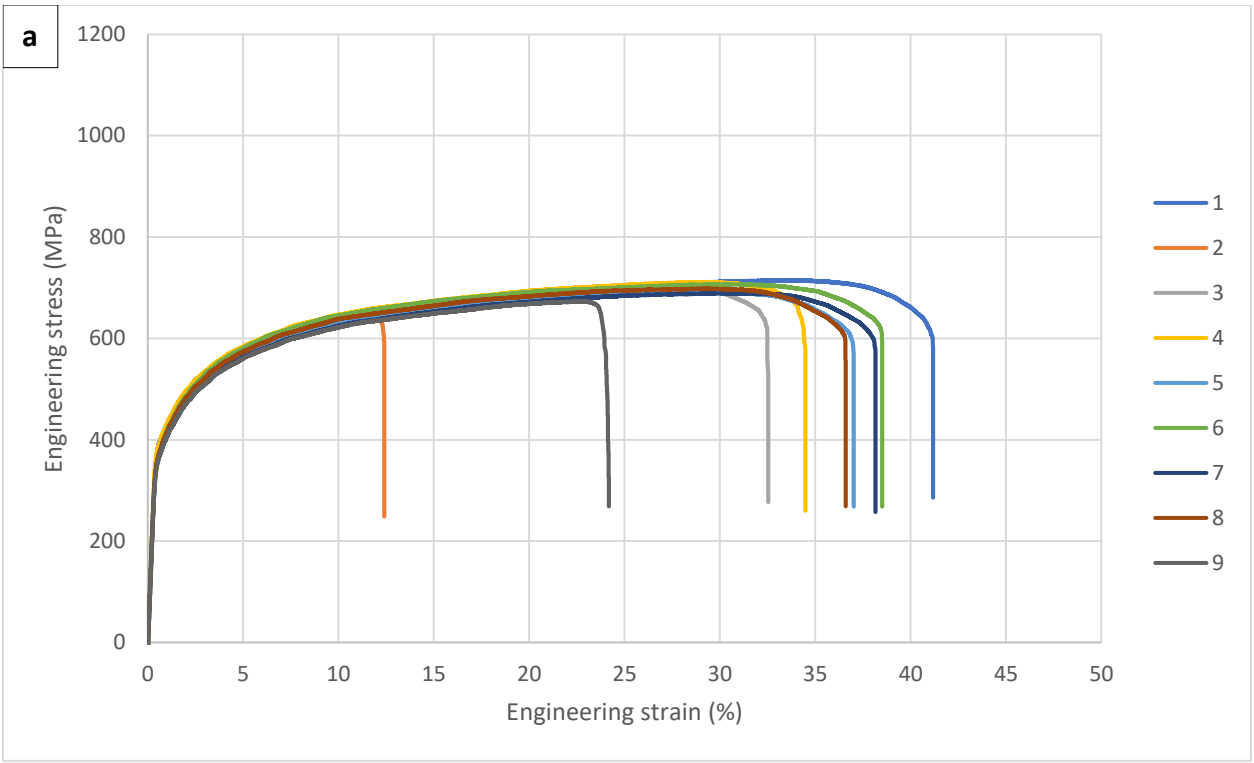

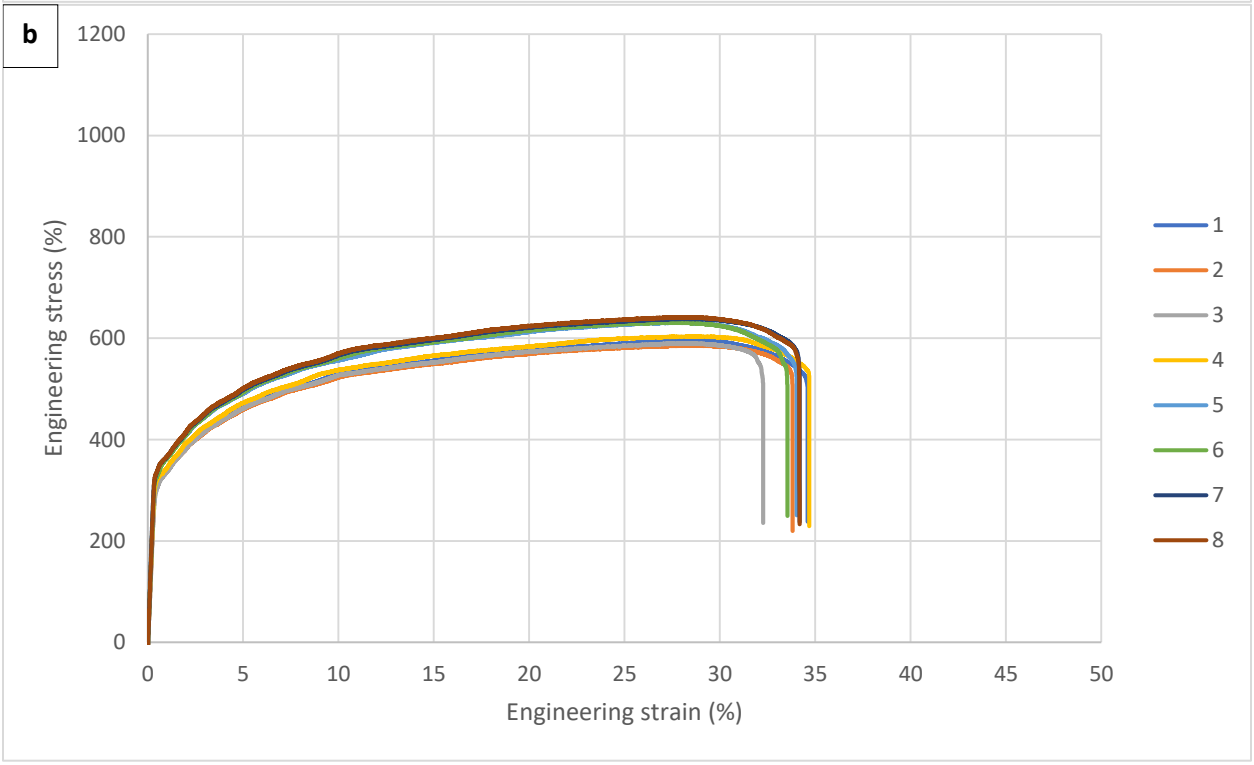

Figure 110: Tensile curves for the vertical specimens of block C1 (a) and C2 (b).

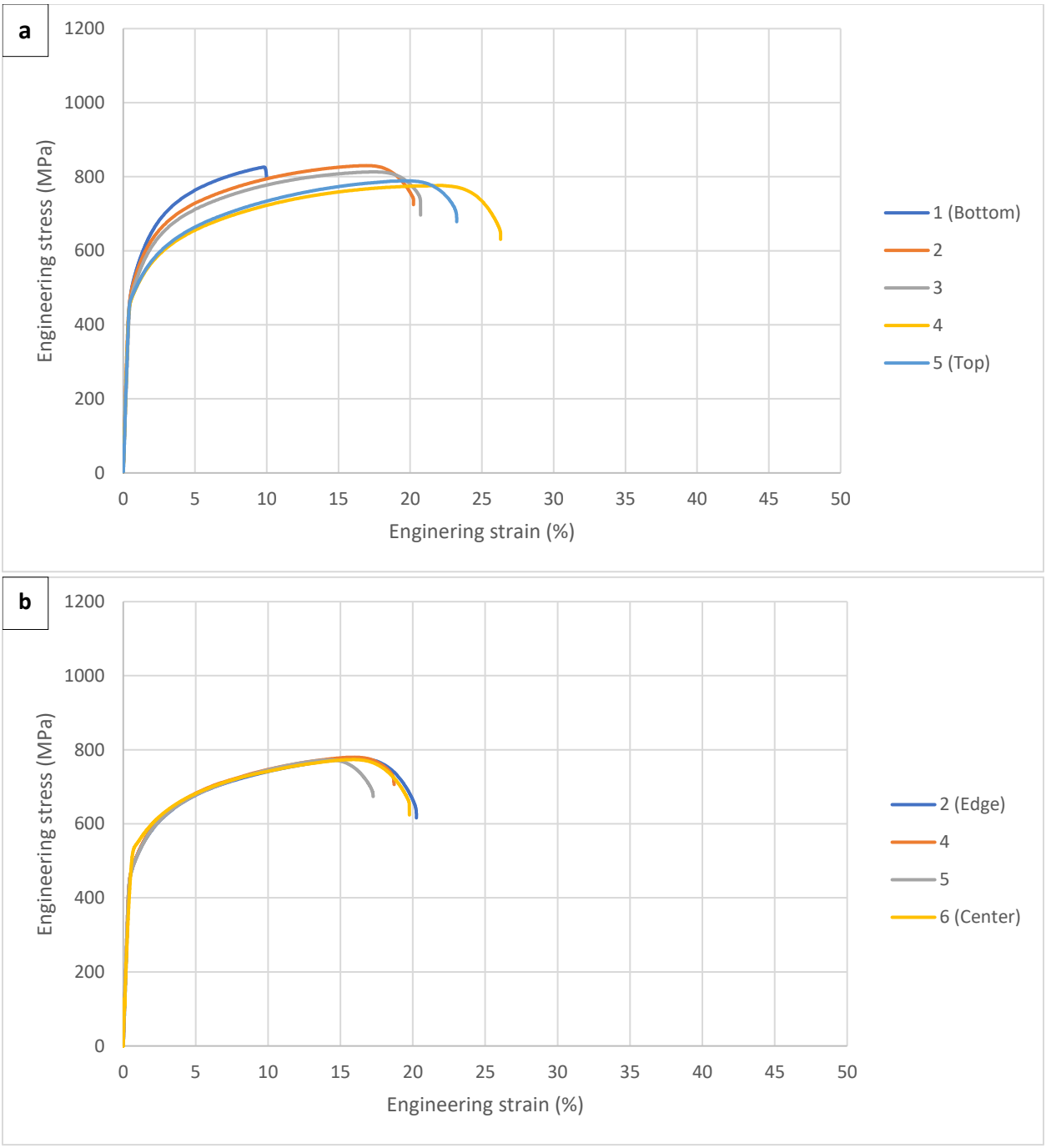

Figure 111: Tensile curves for the horizontal (a) and vertical (b) specimens of the block produced within the facilities of RAMLAB

APPENDIX C - CHARPY V-IMPACT TESTING RESULTS

1

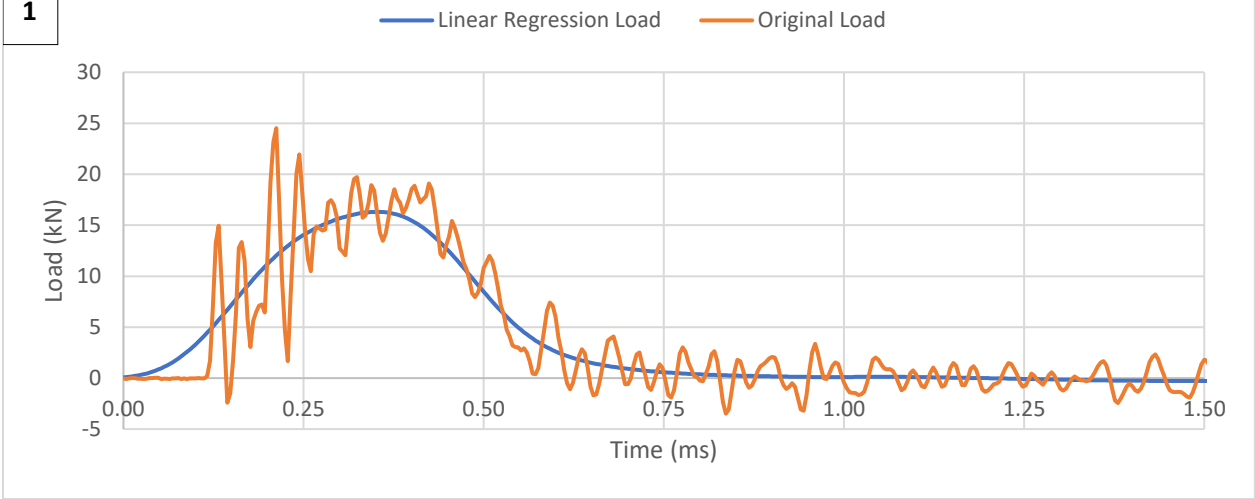

2

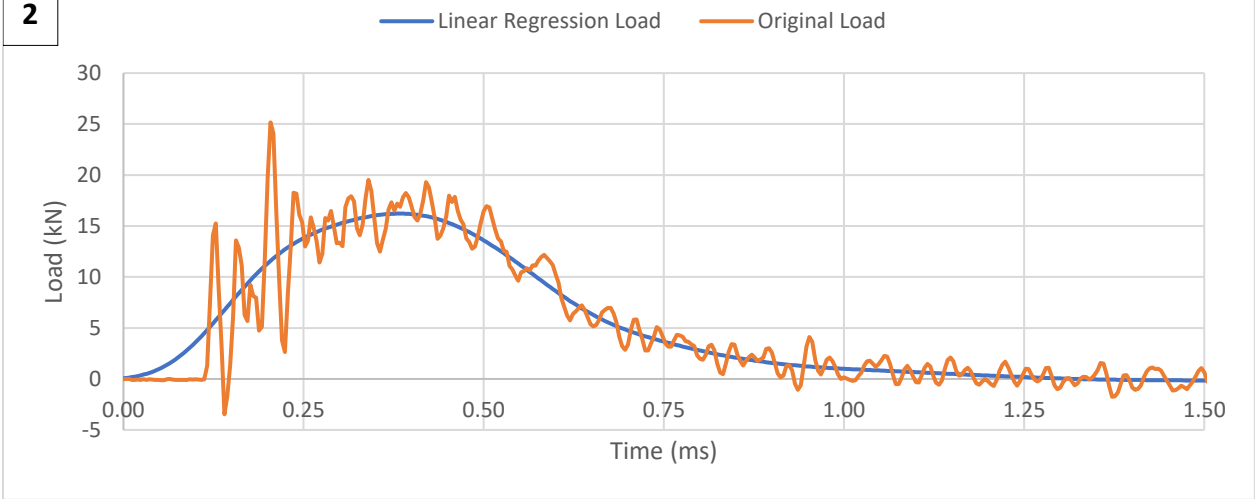

3

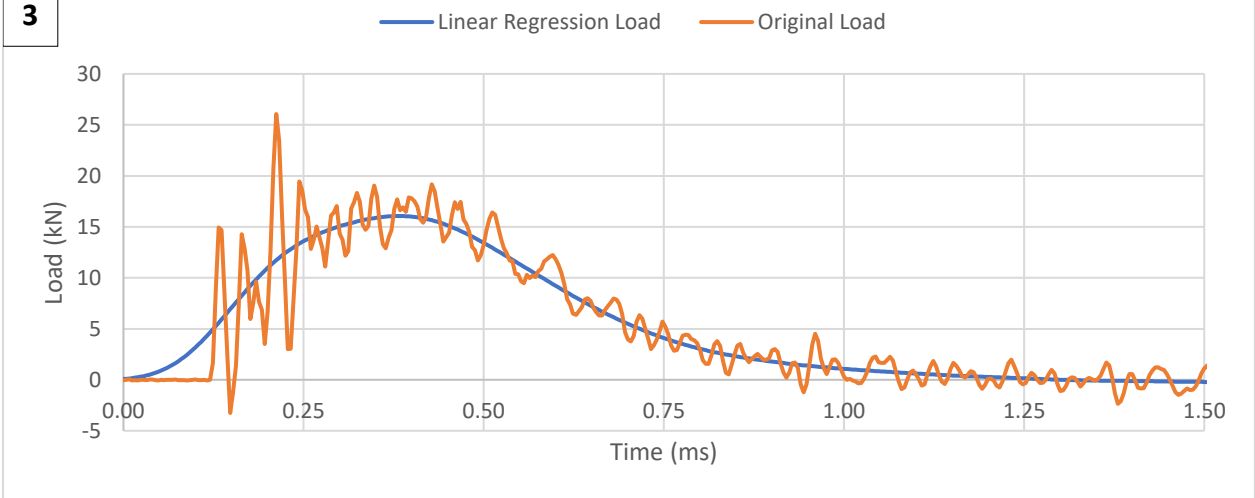

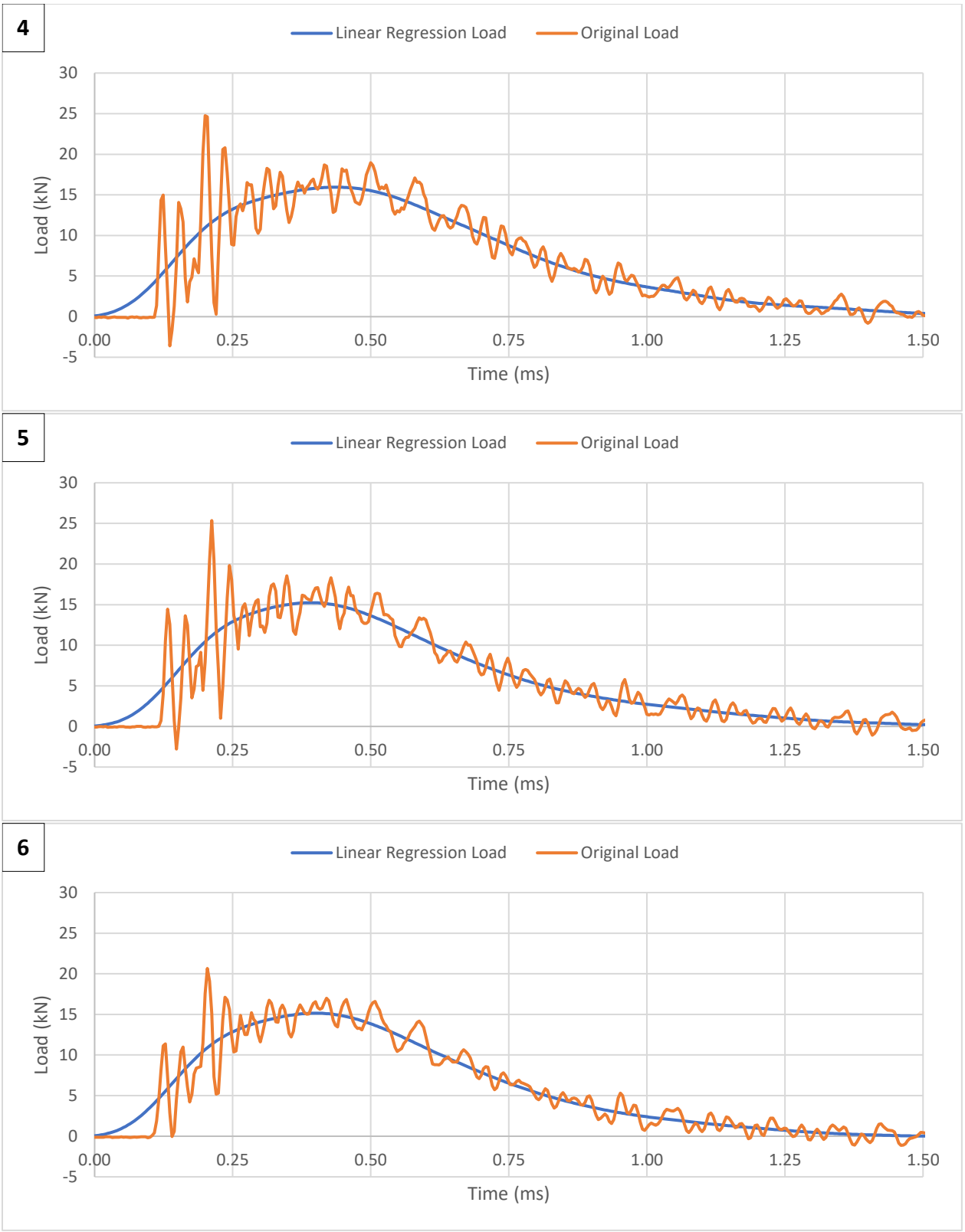

Figure 112: Record of the load during the impact test of the horizontal specimens 1-6 with the notch facing sideways. The orange line represents the original load data, as received from the sensor and the blue line shows a linear regression approximation.

1

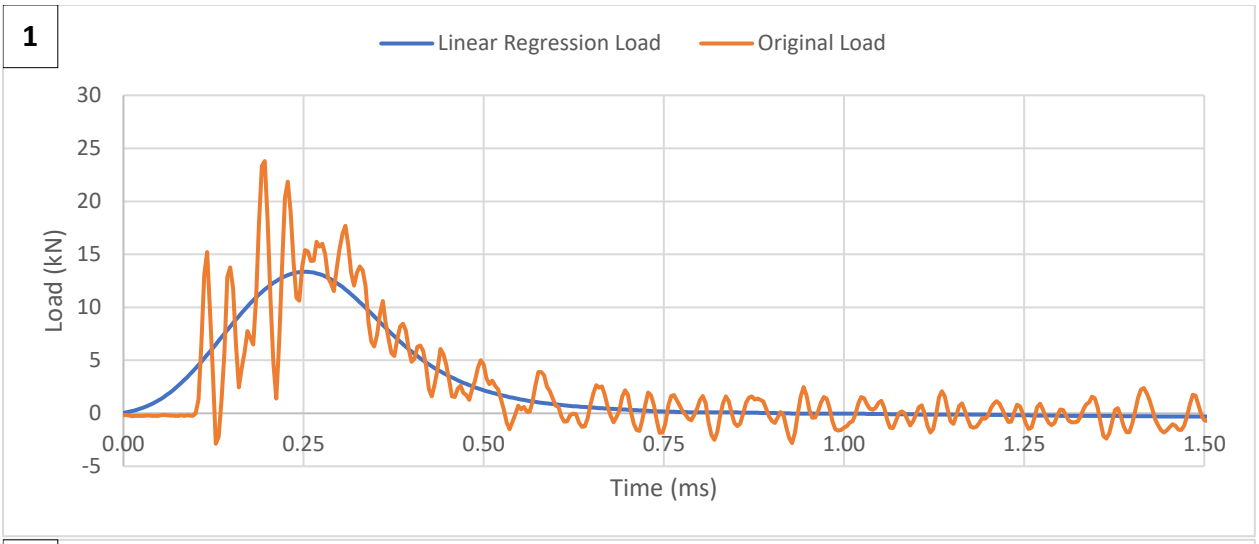
Linear Regression Load
Original Load
Load (kN)
Time (ms)
30
25
20
15
10
5
0
-5
0.00
0.25
0.50
0.75
1.00
1.25
1.50

2

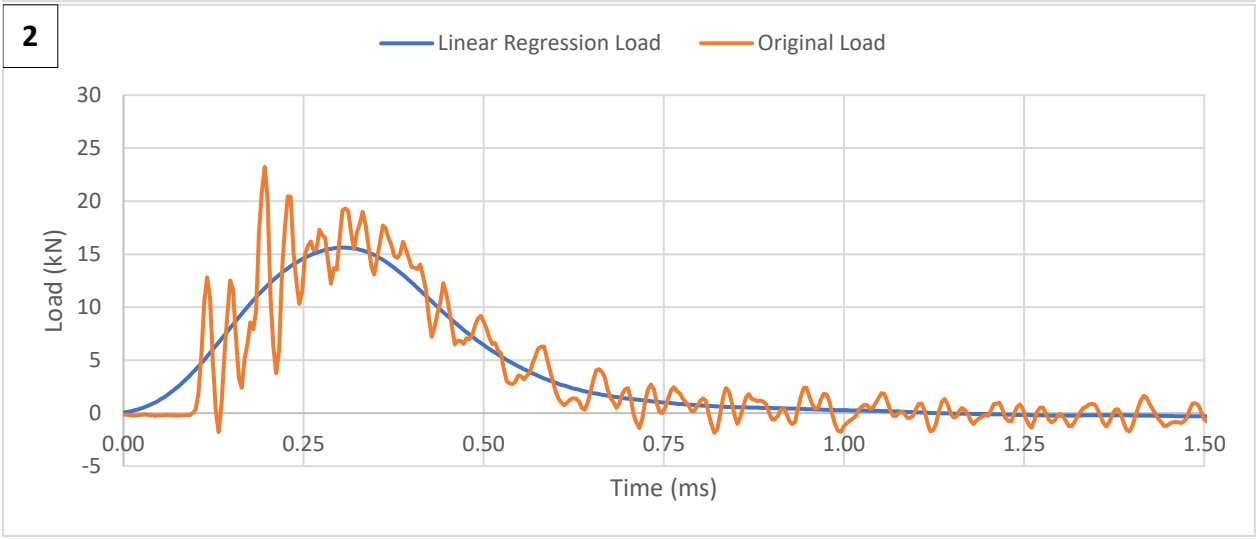
Linear Regression Load
Original Load
Load (kN)
Time (ms)
30
25
20
15
10
5
0
-5
0.00
0.25
0.50
0.75
1.00
1.25
1.50

3

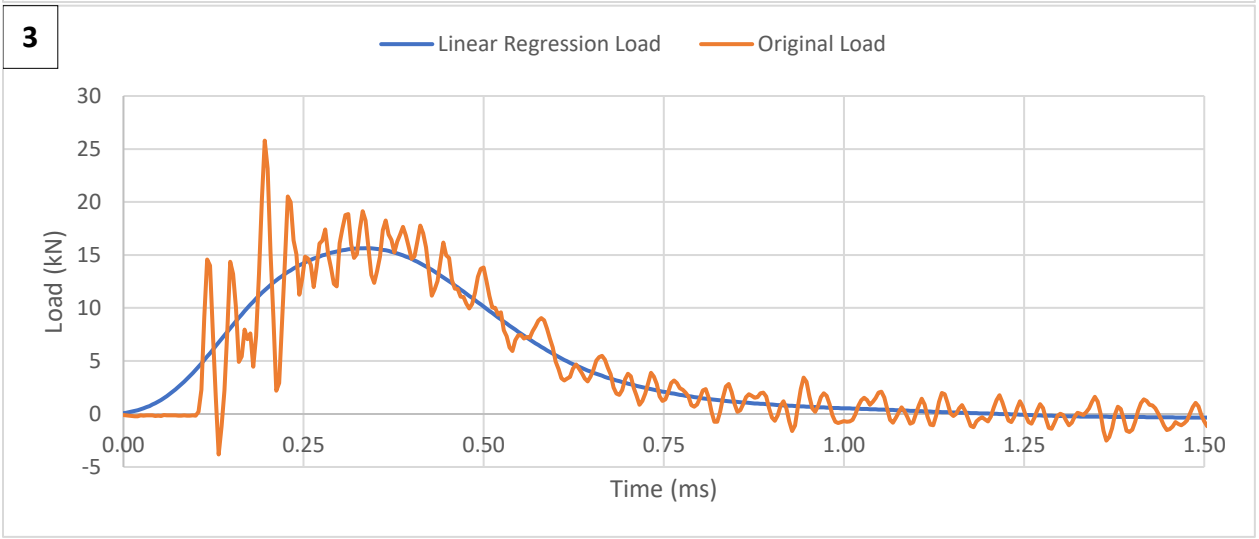
Linear Regression Load
Original Load
Load (kN)
Time (ms)
30
25
20
15
10
5
0
-5
0.00
0.25
0.50
0.75
1.00
1.25
1.50

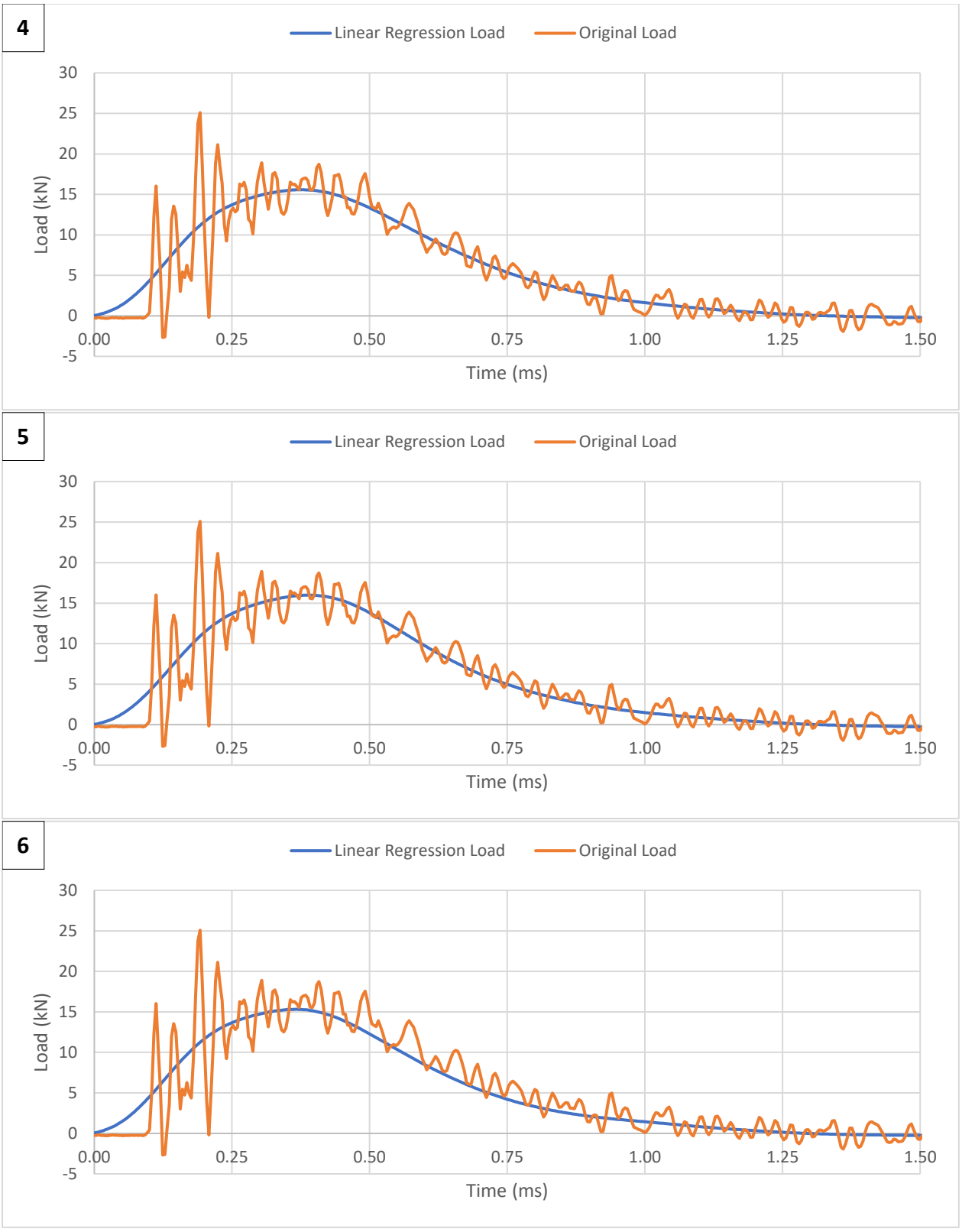

Figure 113: Record of the load during the impact test of the horizontal specimens 1-6 with the notch facing top. The orange line represents the original load data, as received from the sensor and the blue line shows a linear regression approximation.

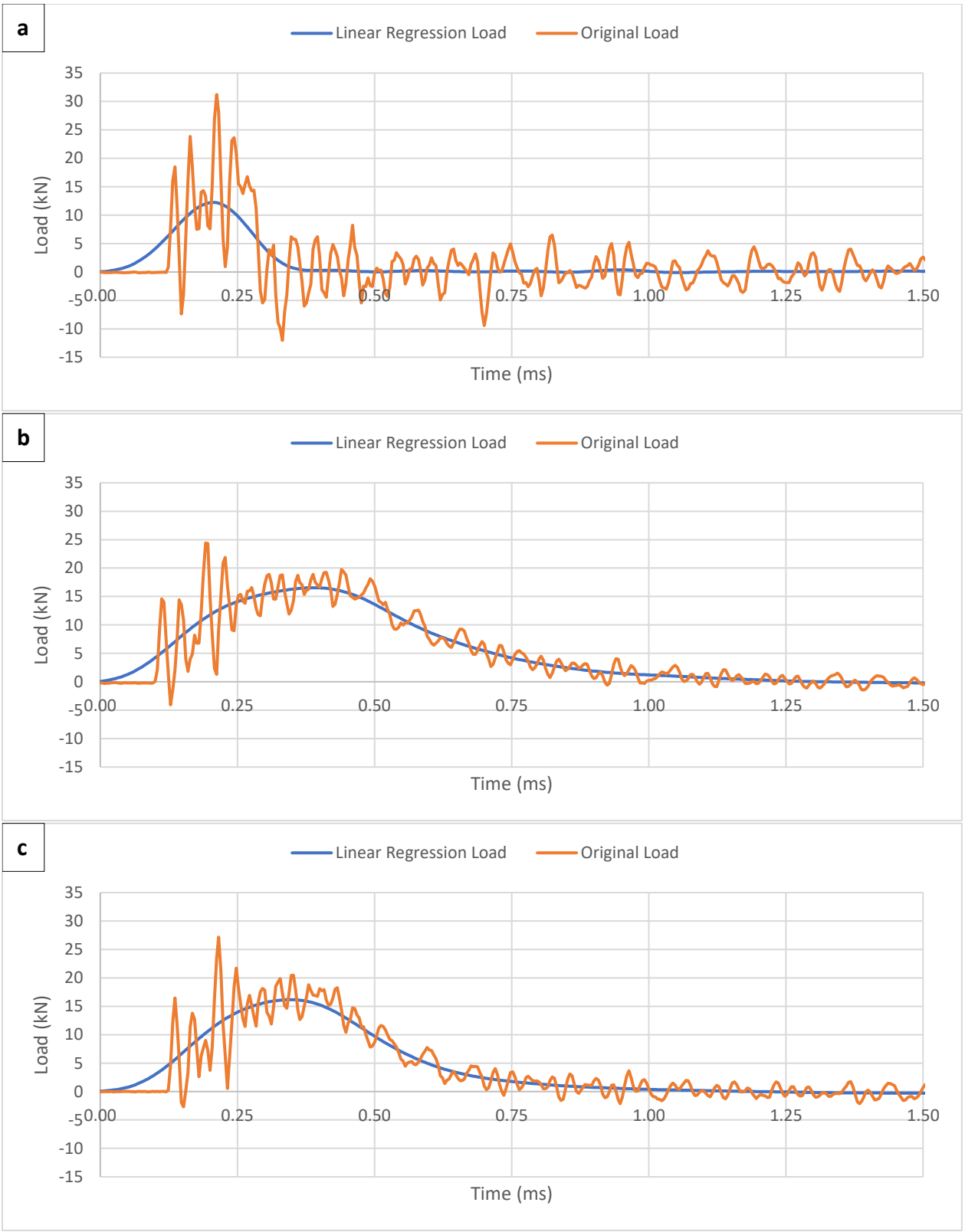

Figure 114: Record of the load during the impact test of the vertical specimens (a & b) at ambient temperature, (b) at -20 °C and (c) at -60 °C. The orange line represents the original load data, as received from the sensor and the blue line shows a linear regression approximation.

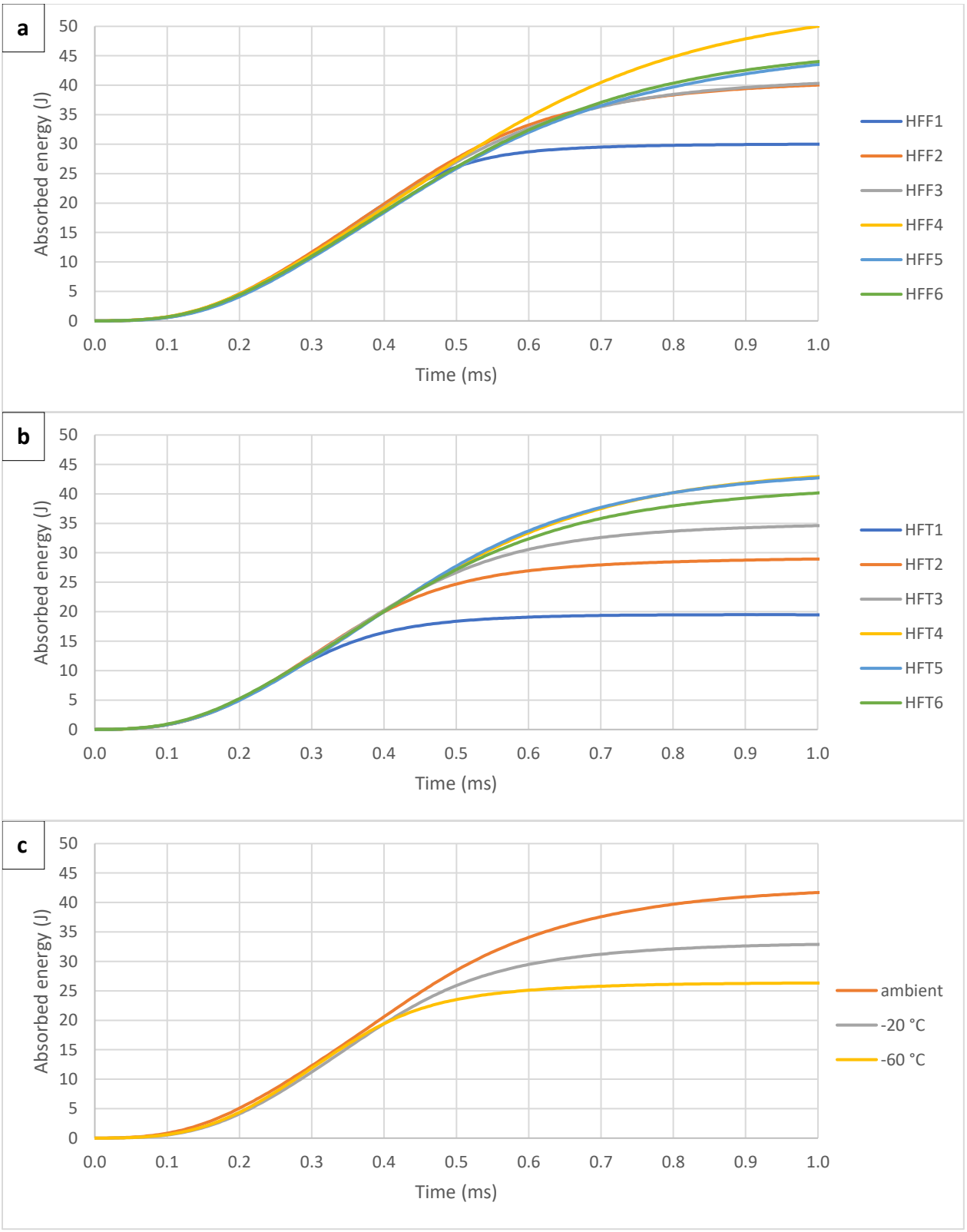

Figure 115: Recorded absorbed energy during the impact test for the (a) horizontal specimen with the notch facing front, (b) horizontal specimen with the notch facing top, (c) vertical specimens at ambient, -20 °C and -60 °C.

APPENDIX D - CORROSION TESTING RESULTS

a

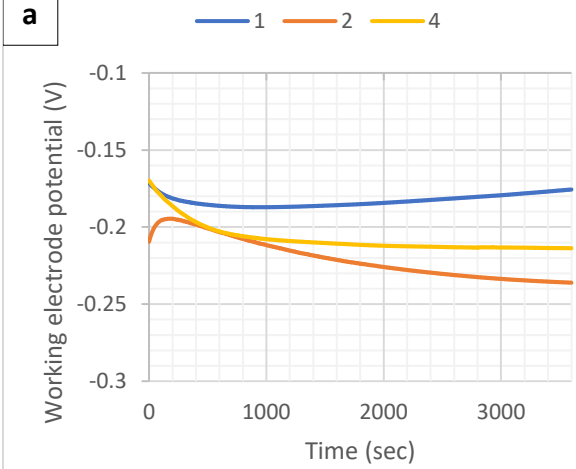

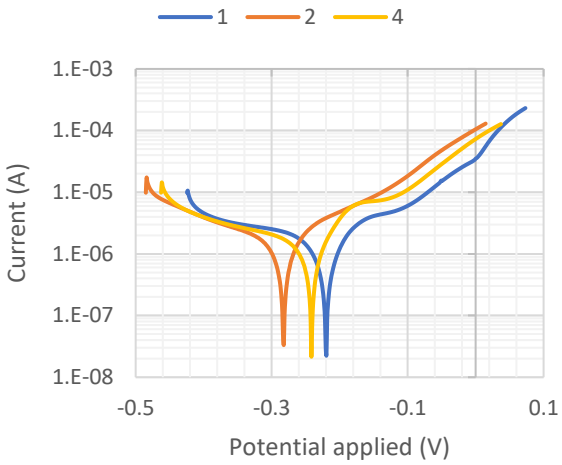

b

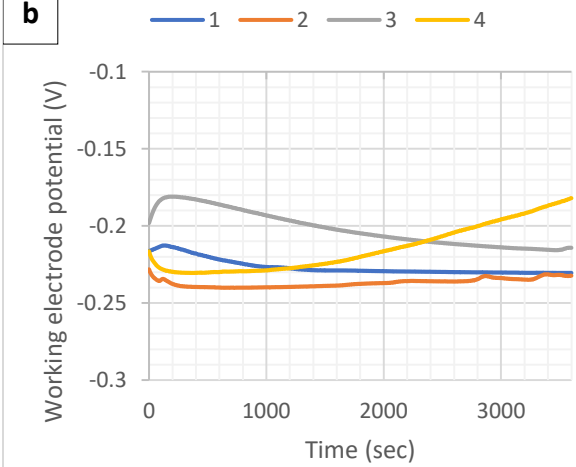

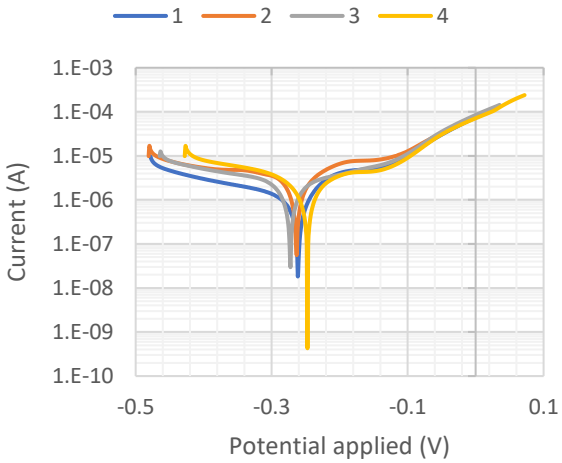

c

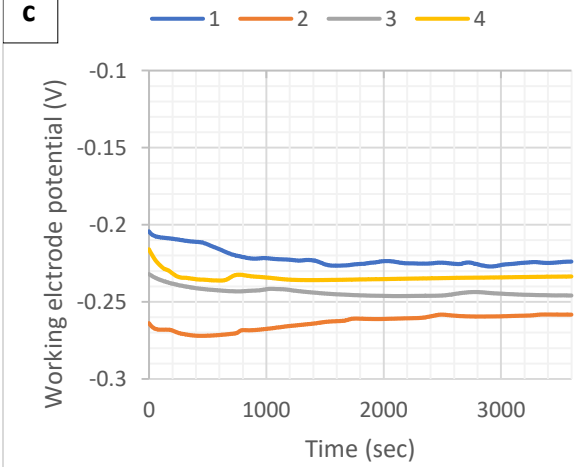

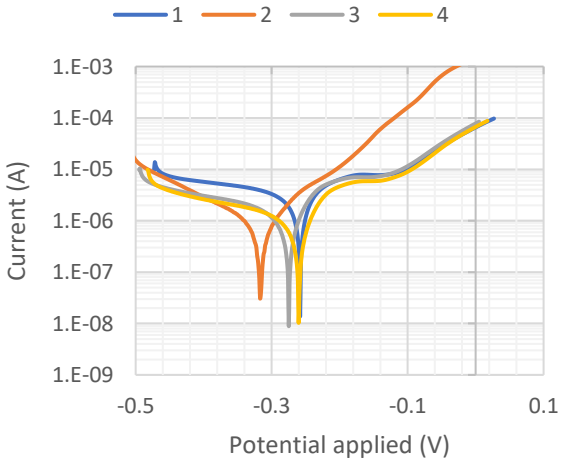

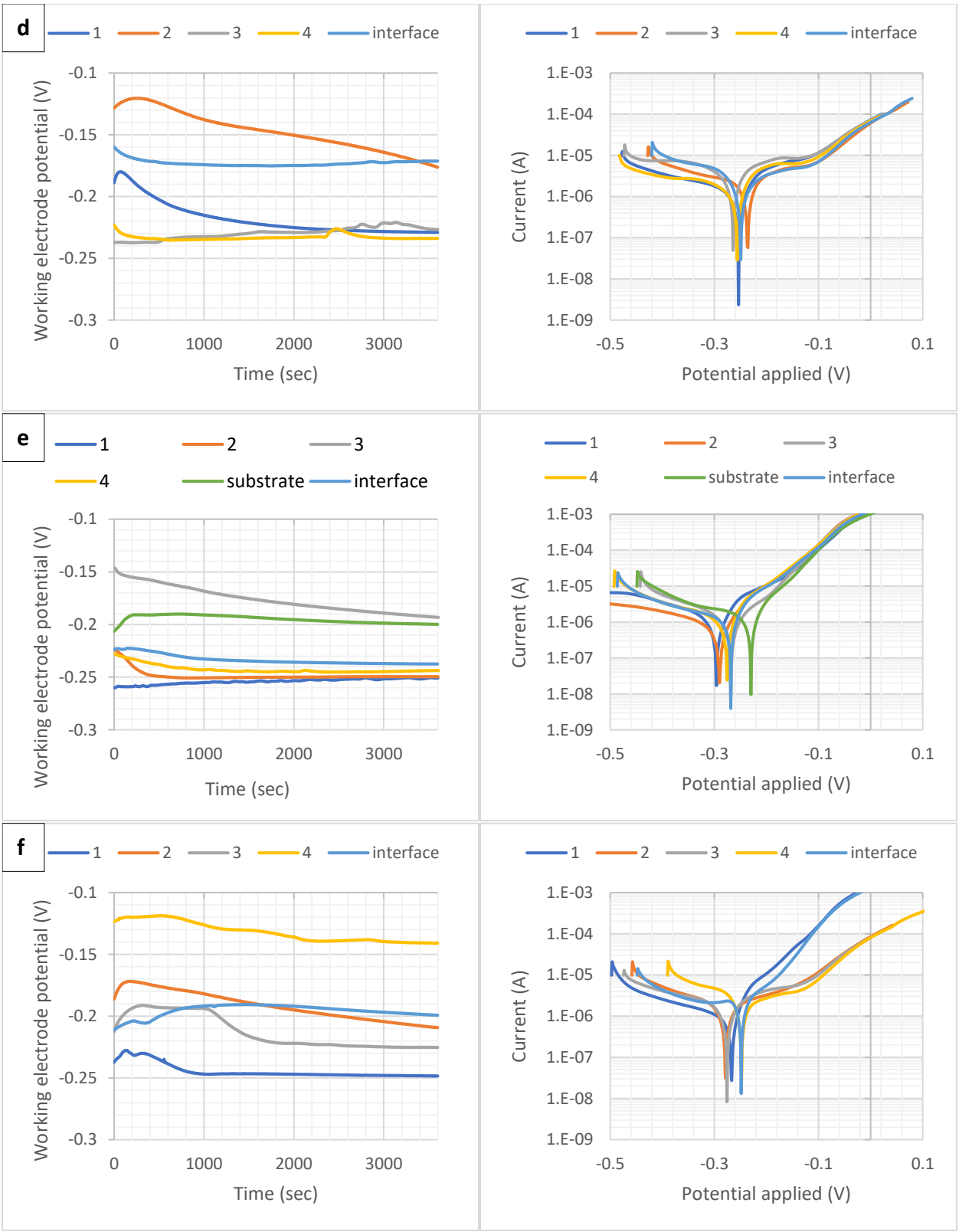

Figure 116: OCP (left) and polarization (right) results for the non - heat treated specimens, (a) block A1, 1st side, (b) block A1, 2nd side, (c) block B1, 1st side, (d) block B1, 2nd side, (e) block C1, 1st side., (f) block C1, 2nd side.

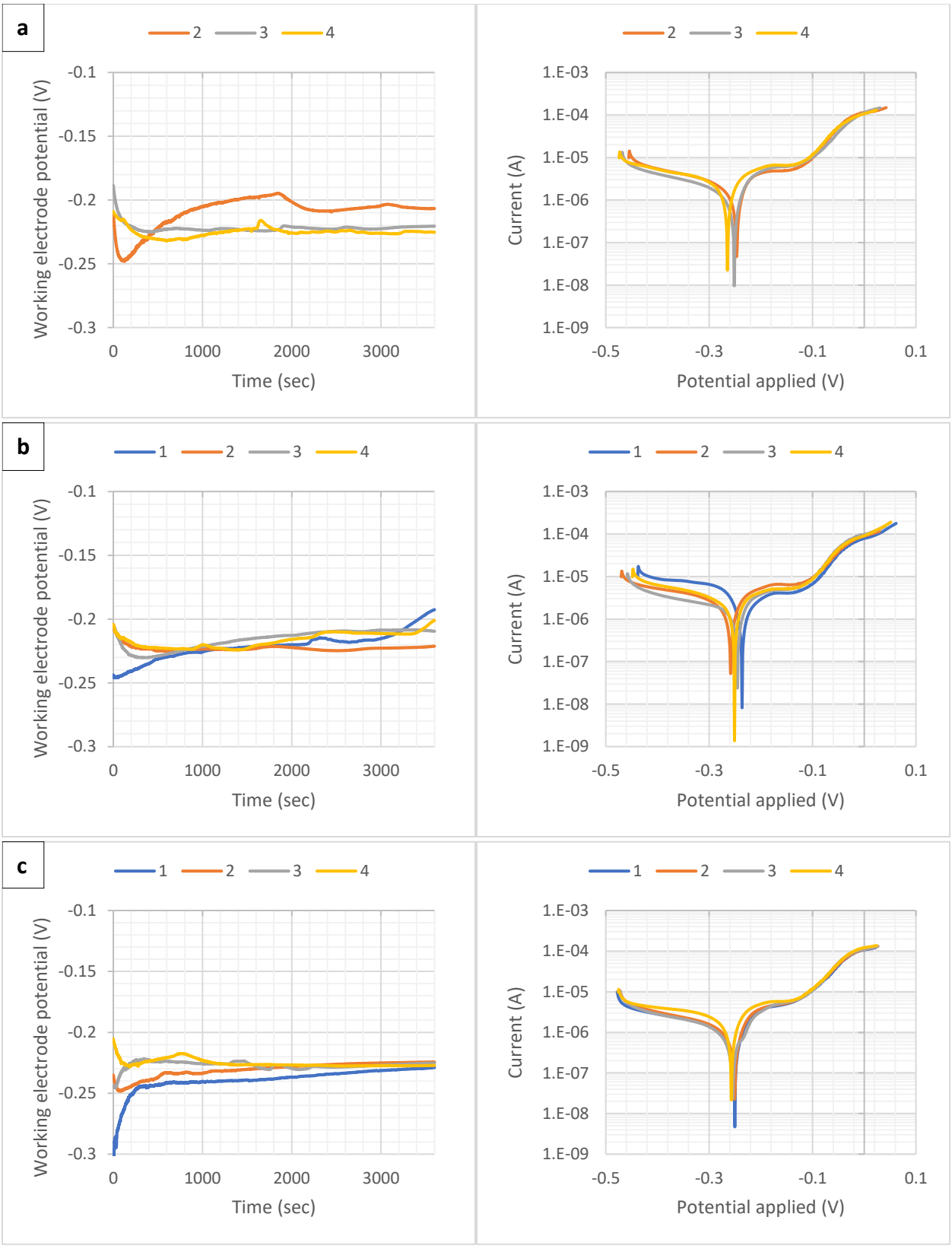

Figure 117: OCP (left) and polarization (right) results for the heat treated specimens, (a) B2, 1st side, (b) B2, 2nd side, (c) C2, 2nd side.